1-1-2018

Computational Modeling of Transcatheter Aortic Valves

Mostafa Abbasi
University of Denver

Computational Modeling of Transcatheter Aortic Valves

Abstract

Transcatheter aortic valve replacement (TAVR) is an established therapy alternative to surgical valve replacement in high-risk and intermediate-risk patients with severe aortic stenosis. Currently, although TAVR is an alternative and less-invasive treatment for high-risk and intermediate-risk patients, surgical aortic valves replacement (SAVR) was still considered as the gold standard for low-risk patients. TAVR could potentially be applied to lower-risk younger patients if the indications can be safely expanded to the patients and transcatheter aortic valve (TAV) long-term durability can match with that of surgical bioprostheses. In contrast to surgical aortic valves (SAVs), there have been limited clinical data on the long-term durability of TAV devices. In the absence of enough long-term valve durability data, accurate structural simulations and computational modeling become an integral part of the evaluation. Thus, the objectives of this dissertation were to employ in-vitro experiments and inverse finite element (FE) analyses to obtain accurate material properties of soft tissue employed in commercial available TAVs and then to implement them in computational simulations to determine leaflet stress and strain distributions for proper assessment of the TAVs long-term durability. Therefore, the main goal of this study was to develop an automated computational framework to minimize the peak stress on the leaflets under and optimize the TAV leaflet shape under physiological loading conditions. In addition, the impact of incomplete TAV expansion and thickness reduction on leaflet stress and strain distribution was assessed in this dissertation.

The results of this study showed that 2-3mm incomplete TAV stent expansion induced localized high stress regions within the TAV commissures, while 4-5mm incomplete stent expansion induced localized high stress regions within the belly of the TAV leaflets during the diastolic phase of the cardiac cycle. This study also presented three-dimensional anisotropic mechanical properties of leaflets used in Carpentier-Edwards PERIMOUNT Magna, Edwards SAPIEN 3 and Medtronic CoreValve. The optimized material parameters for each valve were implemented in FE simulations to assess the leaflet deformation and stress distribution. The results showed the CoreValve had the lowest peak stress value at the identical pressure value during diastole compared to the CE PERIMOUNT Magna and Edwards SAPIEN 3. Eventually, within the chosen design parameters in the optimization framework, we have achieved new designs for TAVs leaflet geometry in which the peak stress was 8.2% and 30.3% less than the corresponding surgical valves for 23 and 26 mm diameters, respectively. In addition, the leaflet peak stress of best TAV design obtained from the optimization framework showed the leaflet peak stress was 74.8% lower than the Edwards SAPIEN 3 TAV. The developed optimization framework may provide a more reliable TAV design with longer valve durability in comparison currently available designs. The present work presents a reliable approach to determine mechanical properties of pericardial valves and compare leaflet stress and strain distribution among different bioprostheses under physiological loading conditions.

Document Type

Dissertation

Degree Name

Ph.D.

Department

Mechanical Engineering

COMPUTATIONAL MODELING OF TRANSCATHETER AORTIC VALVES

A Dissertation

Presented to

the Faculty of the Daniel Felix Ritchie School of Engineering and Computer Science

University of Denver

In Partial Fulfillment

of the Requirements for the Degree

Doctor of Philosophy

by

Mostafa Abbasi

November 2018

Advisor: Ali N. Azadani, Ph.D.

Author: Mostafa Abbasi
Title: COMPUTATIONAL MODELING OF TRANSCATHETER AORTIC VALVES
Advisor: Ali N. Azadani, Ph.D.
Degree Date: November 2018

ABSTRACT

Transcatheter aortic valve replacement (TAVR) is an established therapy alternative to surgical valve replacement in high-risk and intermediate-risk patients with severe aortic stenosis. Currently, although TAVR is an alternative and less-invasive treatment for high-risk and intermediate-risk patients, surgical aortic valves replacement (SAVR) was still considered as the gold standard for low-risk patients. TAVR could potentially be applied to lower-risk younger patients if the indications can be safely expanded to the patients and transcatheter aortic valve (TAV) long-term durability can match with that of surgical bioprostheses. In contrast to surgical aortic valves (SAVs), there have been limited clinical data on the long-term durability of TAV devices. In the absence of enough long-term valve durability data, accurate structural simulations and computational modeling become an integral part of the evaluation. Thus, the objectives of this dissertation were to employ in-vitro experiments and inverse finite element (FE) analyses to obtain accurate material properties of soft tissue employed in commercial available TAVs and then to implement them in computational simulations to determine leaflet stress and strain distributions for proper assessment of the TAVs long-term durability. Therefore, the main goal of this study was to develop an automated computational framework to minimize the peak stress on the leaflets under and optimize the TAV leaflet shape under physiological loading conditions.

In addition, the impact of incomplete TAV expansion and thickness reduction on leaflet stress and strain distribution was assessed in this dissertation.

The results of this study showed that 2-3mm incomplete TAV stent expansion induced localized high stress regions within the TAV commissures, while 4-5mm incomplete stent expansion induced localized high stress regions within the belly of the TAV leaflets during the diastolic phase of the cardiac cycle. This study also presented three-dimensional anisotropic mechanical properties of leaflets used in Carpentier-Edwards PERIMOUNT Magna, Edwards SAPIEN 3 and Medtronic CoreValve. The optimized material parameters for each valve were implemented in FE simulations to assess the leaflet deformation and stress distribution. The results showed the CoreValve had the lowest peak stress value at the identical pressure value during diastole compared to the CE PERIMOUNT Magna and Edwards SAPIEN 3. Eventually, within the chosen design parameters in the optimization framework, we have achieved new designs for TAVs leaflet geometry in which the peak stress was 8.2% and 30.3% less than the corresponding surgical valves for 23 and 26 mm diameters, respectively. In addition, the leaflet peak stress of best TAV design obtained from the optimization framework showed the leaflet peak stress was 74.8% lower than the Edwards SAPIEN 3 TAV. The developed optimization framework may provide a more reliable TAV design with longer valve durability in comparison currently available designs. The present work presents a reliable approach to determine mechanical properties of pericardial valves and compare leaflet stress and strain distribution among different bioprostheses under physiological loading conditions.

ACKNOWLEDGEMENTS

There have been so many people around me who have directly or indirectly helped me complete my Ph.D study. First and foremost, I would like to express my deepest gratitude and appreciation to my advisor, Dr. Ali N. Azadani, for his continued support in this amazing field of research to help heart valve patients. I would also like to thank him for his mentoring, and financial support to finish my Ph.D. program. I believe that this dissertation would not be complete without his support and effort.

Additionally, I would like to express my sincerest acknowledgements to my oral defense committee Prof. Paul Rullkoetter, Prof. Peter Laz, and Dr. Rinku.Dewri for their for their assistance and advice to improve this dissertation.

I am also very grateful to all of my colleague and friends in the DU Cardiovascular Biomechanics Lab at University of Denver who have worked with me during my Ph.D. program, especially Mohammed Barakat, Koohyar Vahidkhah, Dong Qiu and Farhan Khodaee.

I must express my very profound gratitude to my mother, father, and my brothers, Behrouz, Bahman and Bahram; for their endless love, support, and encouragement throughout this process and my life. This dissertation is dedicated to them.

TABLE OF CONTENTS

LIST OF TABLES

LIST OF FIGURES

CHAPTER 1: INTRODUCTION

1.1 Anatomy and Physiology of the Heart

The heart pumps oxygenated blood through the body as the main part of the circulatory system is the human body. The heart is composed of two sides, right and left side. Each side is divided into two chambers. The atrium is the upper chamber which receives blood as it enters. The ventricle is the lower chamber with a thicker muscular wall than the atrium from which blood is pumped out. The heart has four chambers and four valves shown in Fig. 1.1. Chambers pump out oxygenated blood to the rest of the body and receive de-oxygenated blood from the body. The valves make sure that blood flow is always unidirectional in the right direction through the heart. One cardiac cycle can be divided into two parts - diastole and systole. At diastole, the left atrium receives oxygenated blood via pulmonary veins when the heart muscles are relaxed. During systole, the heart muscle contracts and left ventricle pressure significantly increases which pump the blood out of the heart. A typical pressure waveform through a cardiac cycle was shown in Fig. 1.2. At the beginning of systole, aortic pressure is about 80 mmHg whereas it is 120 mmHg near diastole. Transvalvular pressure gradient which is the net pressure difference between the ascending aorta and the left ventricle is large enough to make aortic valve leaflets open during systole.

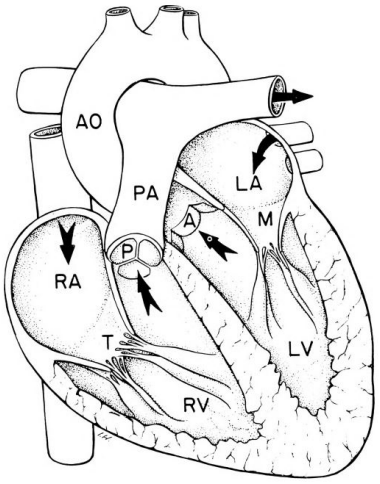

Figure 1.1: Anatomical structure of the human heart. RA: right atrium, RV: right ventricle, LA: left atrium, LV: left ventricle, T: tricuspid valve, P: pulmonary valve, M: mitral valve, A: aortic valve, PA: pulmonary artery, AO: aorta. Arrows indicate the path of blood flow, adapted from (Thubrikar 2018).

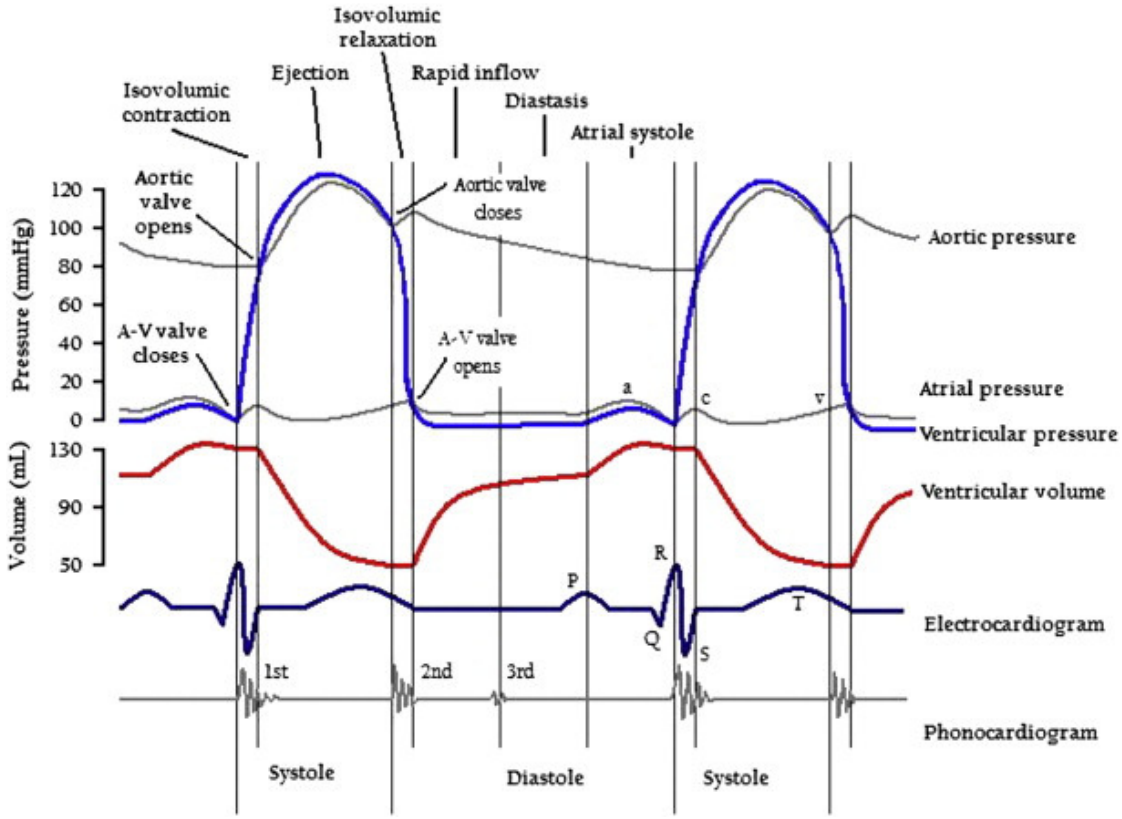

Figure 1.2: A Wiggers diagram and blood pressure waveforms during diastole and systole, adapted from (Sarazan 2014).

1.2 Heart Valve Diseases

The conditions that affect your heart including blood vessel diseases and congenital heart defects are called heart disease. Other conditions such as heart valve problems, irregular heartbeat and abnormal heart rhythms also are considered forms of heart disease. Among heart diseases, valvular diseases are the most significant cause of cardiac death among people in the world. When the heart valves do not function properly in opening all the way and closing tightly, it's called valvular heart diseases. There are number of causes of valvular heart diseases including congenital heart defect, infections, rheumatic fever and calcification in valves. Heart valves can be affected by two ways, stenosis and regurgitation. Stenosis is the term for narrowing of the valve that fails to open fully. A condition in which blood flows back through the valve in an inappropriate way is called regurgitation. In aortic valve regurgitation, leaflets do not seal properly during diastole which causes a failure of the one-way valve. In 2013, heart valve disease caused more than 50,000 deaths in the United States based on the American Heart Association report (Mozaffarian et al. 2015). According to the report, 67.5% of valvular heart diseases were because of aortic valve disorders.

1.3 Aortic Valve Stenosis

Aortic valve stenosis is one of the most prevalent type of cardiovascular disease among aortic valve disorders (Roberts and Ko 2005) . Either degenerative calcification in trileaflet aortic valves or a congenital heart defect called a bicuspid aortic valve can lead to aortic stenosis. In general, aortic stenosis is a problem for the aortic valve that prevents the valve to open fully due to calcified or defected leaflets. Especially in a narrowed aortic valve,

blood flow out from the heart is slow and that make the heart work very hard to pump blood through it. Aortic stenosis is categorized as mild, moderate, severe (Vahanian and Otto 2010). Symptoms of heart disease may not be present in most patients with mild to moderate aortic stenosis. However, people with severe aortic stenosis usually have classic symptoms such as angina, syncope, or dyspnea (Vahanian and Otto 2010). Based on the severity of aortic stenosis and patient's conditions, the most appropriate treatment is determined by a team of cardiologists and surgeons. Surgical options for aortic stenosis include aortic valve replacement (AVR), aortic valve repair and percutaneous aortic balloon valvuloplasty. However, AVR is the only definitive treatment which has relatively low mortality rate compared to other methods for patients with severe aortic stenosis (Aranki et al. 1993). Surgical aortic valve replacement (SAVR) via open-heart surgery, either with a mechanical or bioprosthetic heart valve, is a gold standard therapy for patients who have severe aortic stenosis (Walther et al. 2012). In addition, transcatheter aortic valve replacement (TAVR) is an established treatment alternative to SAVR in inoperable and high-risk patients (Cribier et al. 2002).

1.4 Surgical Aortic Valve Replacement

SAVR has been assumed the primary surgical therapy of patients who suffer from severe aortic stenosis. During this procedure, surgeons remove the degenerated aortic valve and replace it with one of two types of artificial aortic valves: mechanical valves and tissue valves (see Fig. 1.3). Because of some problems associated with mechanical valves such as thrombosis, bioprosthetic heart valve (BHV) replacements are recommended for patients who cannot take blood thinners or are below 60 years old, due to durability

concerns of bioprosthetic valves. Bioprosthetic valves are built with bovine or porcine pericardial tissues, which can be taken from animal tissue and be sewed to a metal frame, chemically treated with glutaraldehyde. It can imitate the one-way blood flow of the heart valve leaflets by sealing against each other. Stented and stentless common bioprosthetic surgical valves are shown in Fig. 1.4. Surgical bioprosthetic aortic valves (SAVs) have been reputed for their outstanding biocompatibility and hemodynamic performance (Laflamme et al. 2015). However, they have limited durability compared to mechanical valves. Among commercially available BHVs, the Carpentier-Edwards (CE) PERIMOUNT pericardial bioprosthesis (Edwards Lifesciences, Irvine, CA), shown in Fig. 1.4, has demonstrated a low rate of structural valve deterioration at 20 years which makes it as a reliable choice for SAVR (Jamieson et al. 2005). Despite the CE PERIMOUNT valve's long-term durability, SAVs may not be a suitable treatment method for patients who have severe aortic stenosis and considered high-risk to have open heart surgery.

Figure 1.3: (A) A mechanical valve (courtesy of www.heart-valve-surgery.com) (B) A tissue heart valve (courtesy of www.edwards.com).

Figure 1.4: (A) Stented pericardial bovine bioprosthetic valves. (B) Stented porcine aortic valve bioprostheses. (C) Stentless bioprosthetic valves. CE = Carpentier-Edwards; SPV = stentless porcine valve, adapted from (Piazza et al. 2011).

1.5 Transcatheter Aortic Valve Replacement

Transcatheter aortic valve replacement (TAVR) is an established therapy alternative to surgical valve replacement in high-risk and intermediate-risk patients with severe aortic stenosis (Leon et al. 2010). Considering the severity of aortic stenosis severity and the arterial system in patients, the TAVR procedure is performed using one of four different access approaches: transfemoral, transapical, transaortic and transcarotid (Thourani et al. 2015). During the transfemoral approach, transcatheter aortic valves (TAVs) are delivered via a catheter through the femoral artery using a tiny incision in the patient's leg. In the transapical approach, using a small incision in the chest, TAVs are delivered via a catheter through a large artery or through the tip of the bottom left chamber of the heart (left

ventricle) which is known as the apex. Alternatively, TAVs can be delivered through the ascending aorta via a catheter in the transaortic approach. For patients who have vascular anatomy issues that prevent transfemoral access, transcarotid arterial access may be an alternative. Although TAV manufacturers use a similar biologic leaflets as surgical bioprostheses and therefore it would be expected to degenerate via similar mechanisms, TAV design and implantation configuration are substantially different than surgical bioprostheses (Rodes-Cabau 2012, Bourantas and Serruys 2014).

In terms of recovery time, TAVR requires a shorter hospital stay (average 3-5 days) (Webb, Carere, and Lichtenstein 2007) compared to SAVR which is about three months. Several modern TAV designs were shown in Fig. 1.5. The use of this treatment has become increasingly common worldwide since 2002. When Cribier (Cribier et al. 2002) performed the procedure the procedure for the first time, to date, more than 350,000 patients have undergone TAVR across the globe (Barbanti et al. 2017). Currently, although TAVR is an alternative and less-invasive treatment for high-risk and intermediate-risk patients (Kodali et al. 2012), SAVR is still considered as the gold standard for low-risk patients. TAVR could potentially be applied to lower-risk younger patients if the indications can be safely expanded to the patients and TAV long-term durability can match with that of surgical bioprostheses. In contrary to SAVs, there have been limited clinical data on the long-term durability of TAV devices.

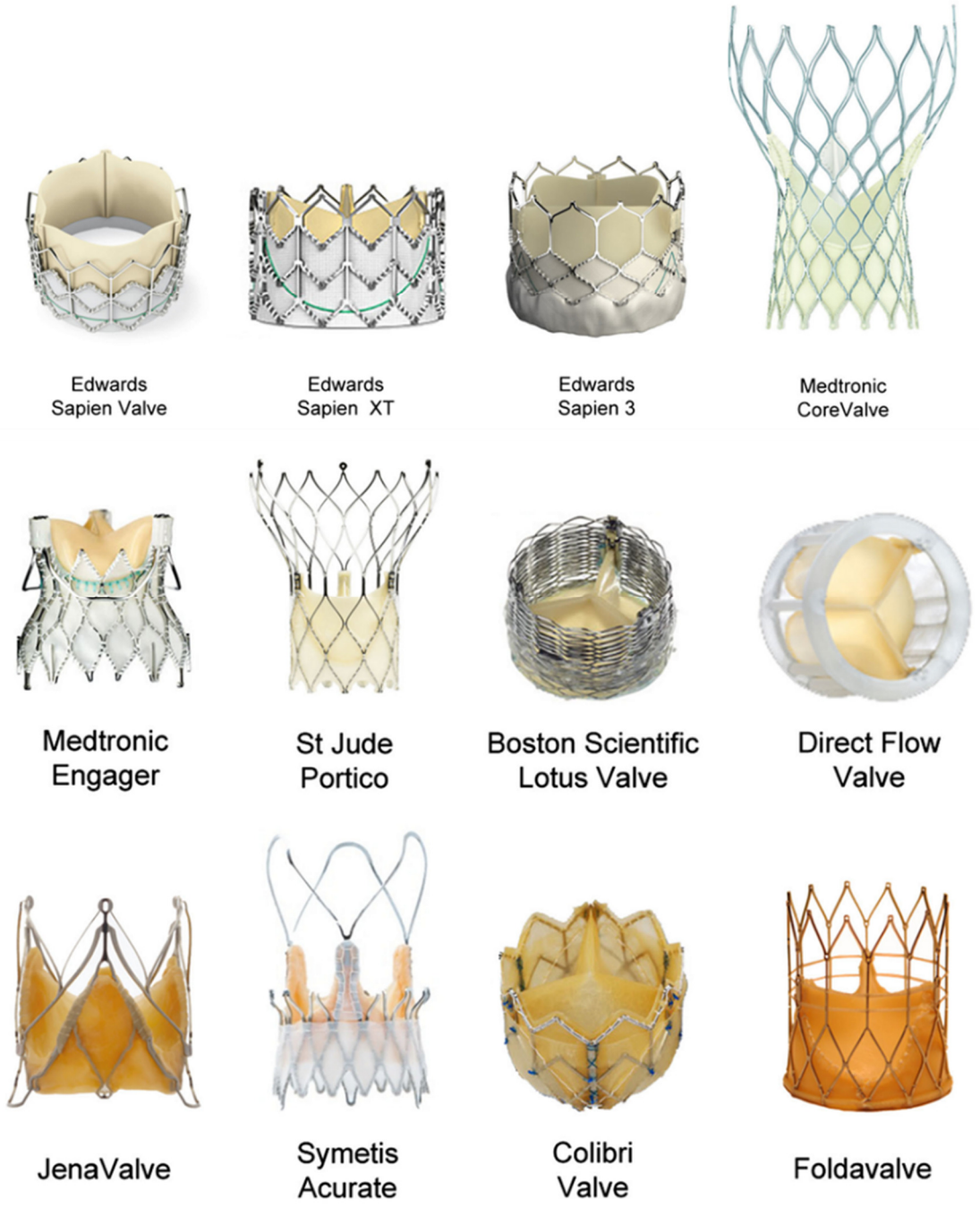

Figure 1.5: Several designs for transcatheter aortic valves, adapted from (Kheradvar et al. 2015).

1.6 Long-term Durability of Tissue Heart Valves

In the past few decades, the use of bioprosthetic valves for aortic valve replacement has increased considerably. To choose an appropriate bioprosthetic heart valve for aortic valve replacement, long-term durability of tissue heart valves is an important factor. Although more than 350,000 patients have undergone TAVR worldwide since 2002, to date, there have been limited publications on the long-term durability of TAVR. To expand TAV technology to lower risk younger patients for whom surgical results are excellent, TAV durability must match that of surgical bioprostheses. Therefore, proper evaluation of TAV longevity and tissue degeneration mechanism are crucial for potential expansion of TAVR to lower-risk patients.

Recently, the first long-term durability assessment of TAVs was conducted by Dvir and colleagues (Dvir et al. 2016). In their study, 378 patients who underwent TAVR including Cribier-Edwards, Edwards SAPIEN, and Edwards SAPIEN XT TAVs were followed up to 10 years. Based on their results, the estimated structural valve degeneration rate was approximately 50% at 8 years. In the absence of enough long-term valve durability data, accurate structural simulations and computational modeling become an integral part of the evaluation. Computational simulations can play a pivotal role in design and development of prosthetic heart valves considering appropriate material properties and boundary conditions, especially TAVs, by reducing the need to perform expensive pre-clinical tests.

Increased mechanical stress and flexural deformation on TAV leaflets may lead to accelerated tissue degeneration and diminished long-term durability (Ferrans et al. 1978a,

Levy et al. 1983, Sacks 2001, Sacks and Schoen 2002a, Schoen and Levy 1999a, Schoen et al. 1985, Thubrikar et al. 1983). Therefore, proper evaluation of the leaflet stress and strain distributions is required for further assessment of the TAVs long-term durability and to develop the next generation of heart valve prostheses. Numerous computational models have been developed to determine stress and strain distribution of the bioprosthetic heart valve leaflets under physiological loading conditions (Abbasi et al. 2016, Gunning, Vaughan, and McNamara 2014, Hsu et al. 2015, Martin and Sun 2015, Abbasi and Azadani 2015, Abbasi and Azadani 2017, Li and Sun 2010). These studies showed that minimizing the peak stress within a bioprosthesis leaflets is very crucial to maximize the long-term durability of a tissue heart valve. Therefore, the optimal valve designs in which the peak stress is reduced may provide improved long-term durability (Vesely 2003). Special considerations need to be made for minimizing the peak stress within TAVs leaflets. Incomplete TAV expansion, reductions in the thickness of TAV leaflets and leaflets geometry must be considered in our computational simulations to improve the long-term durability of TAVs. In addition, in computational modeling, considering accurate constitutive models is of the utmost importance to precisely capture mechanical properties of soft tissue and biomedical materials (Humphrey 2003).

1.7 Objectives

The objective of this study was to obtain accurate material properties of soft tissue employed in bioprosthetic heart valves and to develop an automatic computational framework to optimize the TAV leaflet shape under physiological loading conditions. In

addition, the impact of incomplete TAV expansion and thickness reduction on leaflet stress and strain distribution was assessed in this study.

To address the goals of this study in the development of TAVR, this dissertation is structured as follows: In chapter 2, computational simulations were developed to determine the impact of incomplete TAV stent expansion on TAV leaflet stress and strain distributions. The computational simulation results of incompletely expanded TAVs were compared to fully-expanded circular TAVs. In chapter 3, inverse FE methods were utilized to determine three-dimensional anisotropic mechanical properties of bovine pericardial leaflets of a surgical bioprosthetic heart valve under physiological loading condition. In chapter 4, the main objective of this chapter was to use finite element (FE) simulation to determine the impact of leaflet thickness on TAV leaflet stress and strain distribution under dynamic loading condition. In chapter 5, using a high-resolution three-dimensional digital image correlation (DIC) system, a side-by-side comparison of leaflet displacement and strain fields of three commonly used bioprosthetic heart valves: (i) Carpentier-Edwards PERIMOUNT Magna surgical bioprosthesis, (ii) Medtronic CoreValve, and (iii) Edwards SAPIEN 3 was performed. In chapter 6, we developed a non-invasive material characterization framework using integrated experimental and numerical methods to determine mechanical properties of soft tissue employed in bioprosthetic heart valves. Accordingly, I characterized three-dimensional anisotropic mechanical properties of leaflets used in two commercially available TAVs (i.e., Edwards SAPIEN 3 and Medtronic CoreValve), and compared the results to that of a commonly used and well-examined surgical bioprosthesis (i.e., Carpentier-Edwards PERIMOUNT Magna aortic heart valve).

In addition, the present dissertation provides a reliable approach to compare leaflet stress distribution among different bioprostheses under physiological loading condition. In chapter 7, we developed an automatic optimization framework to assess the impact of 3D leaflet shape on TAV maximum stress under dynamic physiological loading conditions. In Chapter 8, some conclusions and suggestions for future researches were presented.

CHAPTER 2: INCOMPLETE TRANSCATHETER AORTIC VALVE EXPANSION

2.1 Introduction

Although TAV manufacturers use a similar biologic leaflets as surgical bioprostheses and therefore it would be expected to degenerate via similar mechanisms, TAV design and implantation configuration are substantially different than surgical bioprostheses (Rodes-Cabau 2012, Bourantas and Serruys 2014). Unlike surgical valves, the degree of TAV expansion varies from patient to patient and depends upon annulus size and specific calcified valve geometry (Delgado et al. 2010). Furthermore, the current guidelines for TAVR are to upsize the TAV relative to the native annulus to secure the device and minimize paravalvular leakage. The range of annulus size for TAVR suggests that not all patients will achieve complete TAV expansion to the manufactured size, and some degree of incomplete stent expansion may exist (Binder et al. 2013, Schultz et al. 2009). Such alterations in the degree of stent expansion may lead to distorted leaflet cooptation which over time can negatively influence long-term durability. The impact of incomplete TAV expansion on leaflet stress distribution and ultimately long-term valve durability are not known. The objective of this chapter was to determine the impact of incomplete TAV stent expansion on TAV leaflet stress and strain distributions. Increased mechanical stress and flexural deformation on TAV leaflets may lead to accelerated tissue degeneration and

diminished long-term durability (Ferrans et al. 1978a, Levy et al. 1983, Sacks 2001, Sacks and Schoen 2002a, Schoen and Levy 1999a, Schoen et al. 1985, Thubrikar et al. 1983). In this chapter, computational simulation results of incompletely expanded TAVs were compared to fully-expanded circular TAVs.

2.2 Materials and Methods

2.2.1 Transcatheter aortic valve

A 23mm TAV was created based on the Edwards SAPIEN XT valve design (Fig. 2.1). Three leaflets were cut from a bovine pericardium patch (Edwards Lifesciences, Irvine, CA). The lateral sides of the leaflets were sutured together and then the leaflets were sutured at the base to a Dacron Sheet. A cylindrical stainless-steel stent (height 14 mm and thickness 0.34mm) was dilated to an external diameter of 23mm to hold the Dacron sheet and leaflets. The 23mm TAV was crimped and balloon-expanded to diameters ranging from 18 to 23mm in 1mm increments. A pre-drilled acrylic template was used to precisely expand the valve to the desired diameters (Fig. 2.2). TAV leaflet geometry was then obtained using NextEngine 3D Laser Scanner. Subsequently, surface reconstruction was performed using RapidWorks and SOLIDWORKS packages (See Fig. 2.3).

2.2.2 Biaxial testing system

A planar biaxial stretching system (CellScale, Waterloo, Canada) was used to determine mechanical properties of the bovine pericardium patch (Fig. 2.4). Three square samples were cut from the pericardium patch. Sample orientation was aligned such that

Figure 2.1: (Left) Edwards SAPIEN XT valve. (Center and right) Side and top view of homemade 23mm transcatheter aprotic valve; leaflet geometry was based on the SAPIEN XT valve design, adapted from (Abbasi and Azadani 2015).

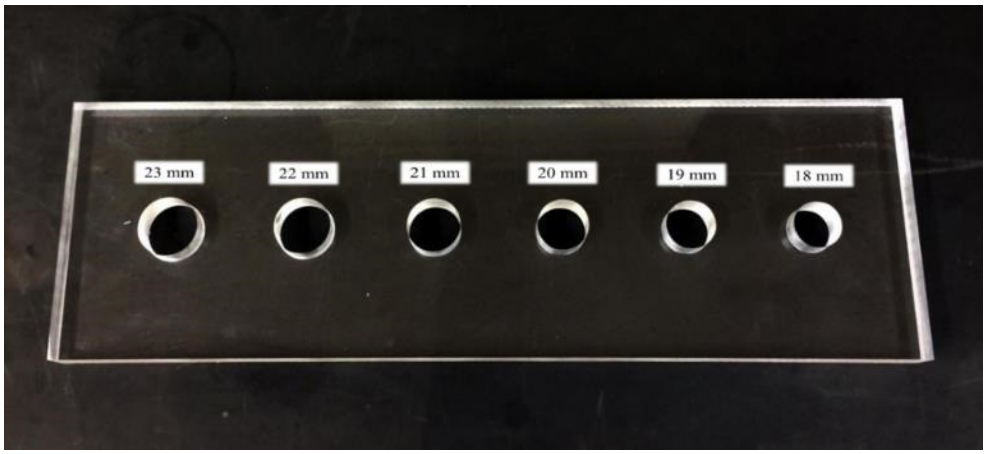

Figure 2.2: Pre-drilled acrylic template used to expand the TAV to the desired diameters, adapted from (Abbasi and Azadani 2015).

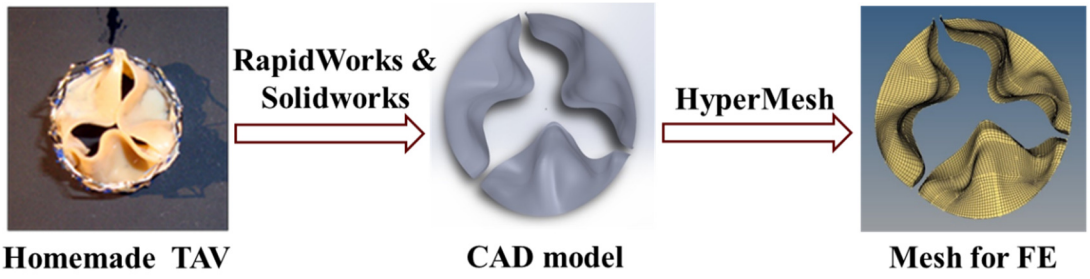

Figure 2.3: Overview of making a 3D geometry and mesh for FEM model.

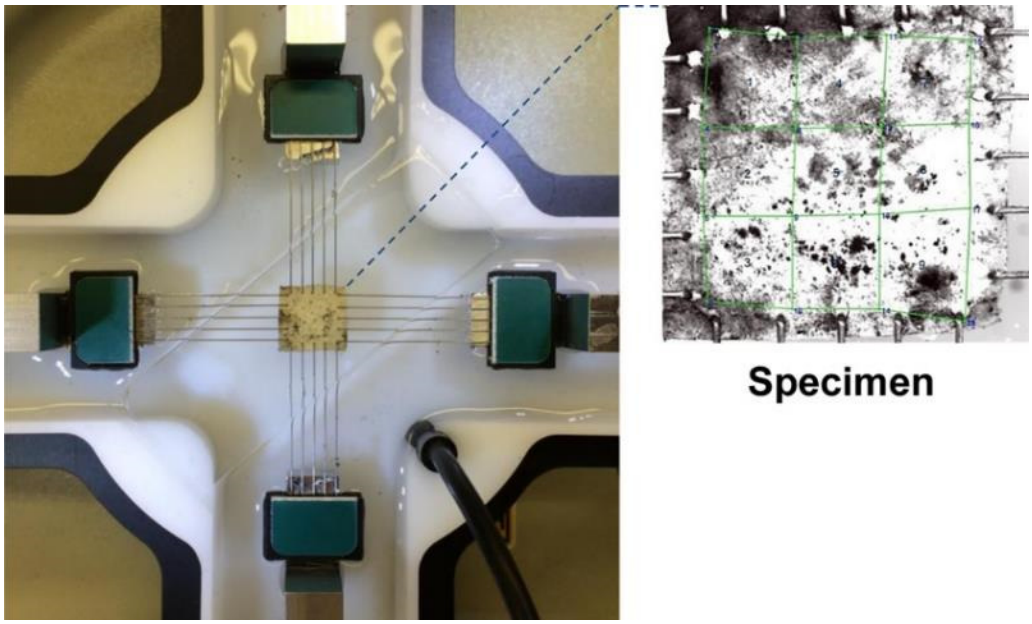

Figure 2.4: Planar biaxial stretching system used to determine mechanical properties of bovine pericardium, adapted from (Abbasi and Azadani 2015).

the circumferential edge of the square samples was parallel to the free edge of the TAV leaflets. The circumferential and longitudinal directions were considered as x and y directions, respectively. Specimen dimensions and thicknesses were measured using Mitutoyo Digital caliper and were stored in normal saline solution.

To obtain mechanical properties, the specimens were mounted on the biaxial system using a set of four CellScale BioRakes. The biaxial system equipped with two Honeywell 1,000g load cells located on two orthogonal arms. The load cells were zeroed after mounting the specimen. A temperature-controlled normal saline bath heated to 37°C provided a physiological environment. The top sides of tissue samples were sprinkled with graphite to create a textured surface for strain measurements. Real-time displacement of the graphite markers was obtained at a rate of 15Hz using a camera placed over the top

surface. Specimens were examined using the following equibiaxial displacement-controlled protocol. First, ten preconditioning cycles of 10% true strain were applied on both axes at 0.5Hz. Subsequently, each specimen was stretched to 100% strain on both axes with a 5s stretch and a 5s recovery. Furthermore, CellScale LabJoy image tracking software was used to obtain strain maps of the samples.

2.2.3 Constitutive modeling

Soft tissues are mostly comprised of water (Fung 1993); therefore, the pericardium samples were considered to be incompressible. Planar forces (F_{xx}, F_{yy}) measured by the two load cells were used to calculate Cauchy stresses (T_{xx}, T_{yy}) in the circumferential and longitudinal directions.

$$T_{xx} = \lambda_x \frac{F_{xx}}{t_0 l_{x0}} \tag{2.1a}$$

$$T_{yy} = \lambda_y \frac{F_{yy}}{t_0 l_{y0}} \tag{2.1b}$$

where t_0 is tissue thickness in the zero-stress state, and $\lambda = l/l_0$ is stretch ratio represents the ratio of deformed tissue length (l) to resting length (l_0). Components of Green strain (E) were calculated using the following equations:

$$E_{xx} = \frac{1}{2}(\lambda_x^2 - 1) \tag{2.2 a}$$

$$E_{yy} = \frac{1}{2}(\lambda_y^2 - 1) \tag{2.2 b}$$

A four parameter Fung's exponential strain energy function was fitted to the stress-strain data (Fung, Fronek, and Patitucci 1979)

$$W = \frac{C}{2}(e^{Q} - 1), \quad Q = c_{xx}E_{xx}^2 + 2c_{xy}E_{xx}E_{yy} + c_{yy}E_{yy}^2 \tag{2.3}$$

where E_x and E_y are the Green strains in x and y directions, respectively. c_{xx}, c_{yy}, $c_{xy,}$ *and* c are the material constants. Cauchy stresses can be obtained by the following equations:

$$T_{xx} = \lambda_x^2(c_{xx}E_{xx} + c_{xy}E_{yy})C\ exp(Q) \tag{2.4a}$$

$$T_{yy} = \lambda_y^2(c_{xy}E_{xx} + c_{yy}E_{yy})C\ exp(Q) \tag{2.4b}$$

A Levenberg-Marquardt least squares algorithm in MATLAB (v8.1.0.604) was used to fit the Fung's strain energy to the experimental data.

Although arm displacement rates were set equal for both circumferential and longitudinal directions, strain applied to the center of the specimen was not exactly equal in the two directions, mainly due to initiation and propagation of tears in the tissue at the boundaries where tungsten wires were anchored (Fig. 2.4). Therefore, stress-strain relationships in the equibiaxial strain state (E_{xx}=E_{yy}=E) were obtained as:

$$T_{xx}^{equi} = (2E + 1)E\big(c_{xx} + c_{xy}\big)Cexp\big\{\big(c_{xx} + c_{yy} + 2c_{xy}\big)E^2\big\} \tag{2.5a}$$

$$T_{yy}^{equi} = (2E + 1)E\big(c_{xy} + c_{yy}\big)Cexp\big\{\big(c_{xx} + c_{yy} + 2c_{xy}\big)E^2\big\} \tag{2.5b}$$

where the superscript *equi* denoted equibiaxial condition. The stress-strain curves converted to the equibiaxial stretch condition, and the anisotropic index, the difference in stiffness between the circumferential and longitudinal directions divided by the average stiffness, was calculated for each sample (Matsumoto et al. 2009). In the biaxial stretching system, although arm displacement rates were set equal for both circumferential and

longitudinal directions, strain applied to the center of the specimen was not exactly equal in the two directions. This is mainly due to initiation and propagation of tears due to stress concentration at the boundaries where BioRake tungsten wires are anchored, as shown in the Fig. 2.4. Therefore, we obtained stress-strain relationships in the equibiaxial strain state.

2.2.4 Finite element (FE) modeling

FE modeling was performed using ABAQUS/Explicit package (Dassault Systemes Simulia Corp., RI, USA). In the simulations, leaflets were only modeled, and the stent was considered to be rigid. IGES format of the leaflets were imported into HyperMesh (Altair Engineering, Troy, MI), and leaflet geometry was discretized with mapped mesh (See Fig. 2.3). The mesh was then imported to ABAQUS to perform a large deformation analysis. S4 shell elements with general frictionless contact were used to discretize the valve geometry. Element type S4 is a fully integrated finite-membrane strain shell element and it does not have hourglass modes in either the membrane or bending response of the element. Therefore, we used element type S4 because the element does not require hourglass control and it improves stress calculation accuracy.

A mesh of approximately 8,000 elements was enough to assure that the results are independent of mesh density. A transvalvular pressure waveform measured from repeated in-vitro tests conducted in our custom-built pulse duplicator (BDC Labs, Wheat Ridge, CO) was applied to the leaflets (Fig. 2.5). The pulse duplicator input parameters were matched with ISO-5830 and FDA standards for testing heart valves: heart rate of 70 beats/min, mean aortic pressures of 100 mm-Hg, and cardiac outputs 5 L/min. In the

dynamic FE analysis, density of 1,100 kg/m^3 was used for the leaflets(Jermihov, Jia, Sacks, Gorman, Gorman III, et al. 2011, Kim et al. 2006).

It has been observed that neglecting viscous damping in modeling of bioprosthetic valves may cause instability in FE models (Jermihov, Jia, Sacks, Gorman, Gorman III, et al. 2011, Kim et al. 2006). Therefore, to mimic viscous damping effects of surrounding fluid, a Rayleigh damping coefficient of α=20000 1/s was considered in the simulations (Jermihov, Jia, Sacks, Gorman, Gorman III, et al. 2011, Kim et al. 2006). Two cardiac cycles were simulated to guarantee cycle invariance.

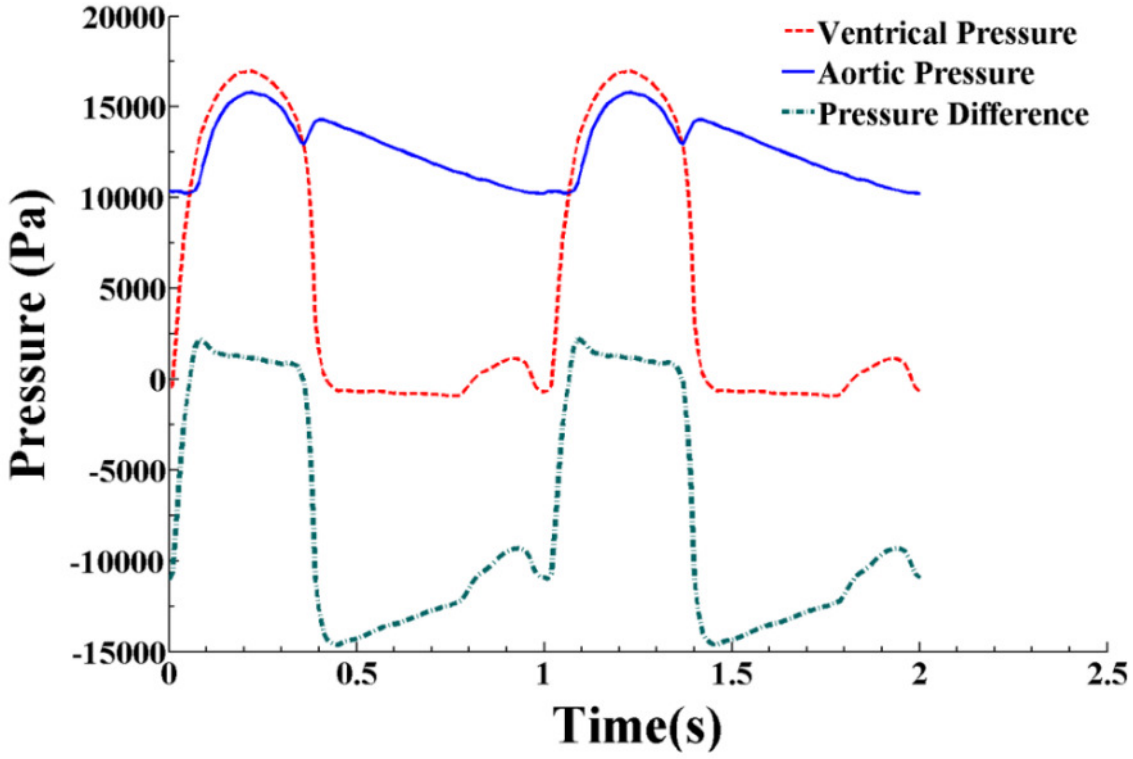

Figure 2.5: The variation in pressure in the left ventricle (red dashed line) and the aorta (blue solid line) over two cardiac cycles. The wave pressure (green dash-dot line) is defined as the pressure difference between the left ventricle and the aorta, adapted from (Abbasi and Azadani 2015).

2.3 Results

2.3.1 Biaxial stretching data

Square samples of consistent size were cut from the bovine pericardium patch, and length and thickness of each sample are shown in Table 2.1. Experimental raw data obtained from biaxial testing of the three specimens are shown in Fig. 2.6. Stress-strain data were fit to the Fung's strain energy function and material constants for each specimen are shown in Table 2.1. In addition, using Eq. (2.5), the stress-strain curves were converted to the equibiaxial stretch condition. As shown in Fig. 2.7, the difference between the equibiaxial stress-strain curves in the circumferential and longitudinal directions for each one of the samples was found to be minimal which is 19%. It appears that the entire extracellular matrix of the bovine pericardium is highly bonded due to chemical fixation and anti-calcification treatment, and therefore the tissue behaves nearly like an isotropic material over the examined strain range.

As a result, in the computational modeling, TAV leaflets were assumed to be isotropic nonlinear hyperplastic material, and a fourth-order reduced polynomial strain-energy function as shown below was fitted to the average curve of each sample:

$$W = \sum_{i=1}^{4} C_{i0} \, (\bar{I}_1 - 3)^i \tag{2.6}$$

Table 2.1: The Dimensions of bovine pericardium specimens and coefficients of Fung-strain energy function fitted to the raw data.

Specimen Number	Thickness (mm)	Length (mm)	C(kPa)	c_{xx}	c_{yy}	c_{xy}	Anisotropic index
1	0.433	13.36	133.84	4.48	2.53	12.16	0.124
2	0.426	13.34	74.43	10.36	6.28	23.70	0.127
3	0.430	13.35	42.69	36.36	25.95	21.48	0.198

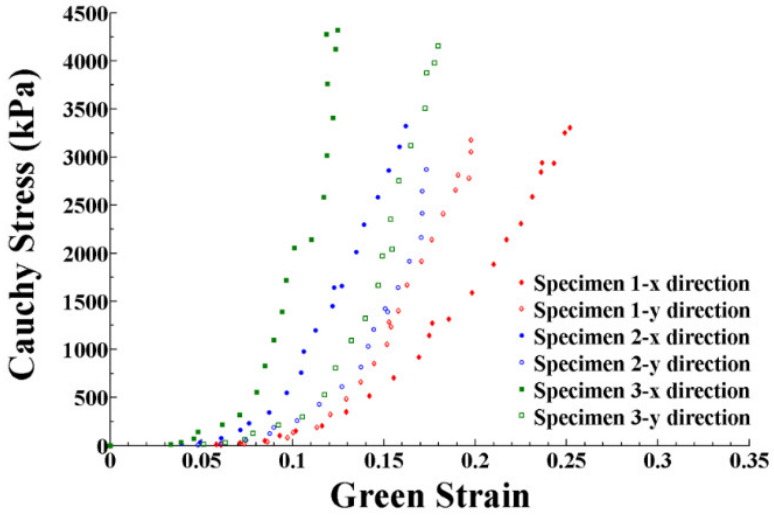

Figure 2.6: Raw biaxial data of three squared specimens cut from bovine pericardium in the circumferential (filled marks) and longitudinal (blank marks) directions, adapted from (Abbasi and Azadani 2015).

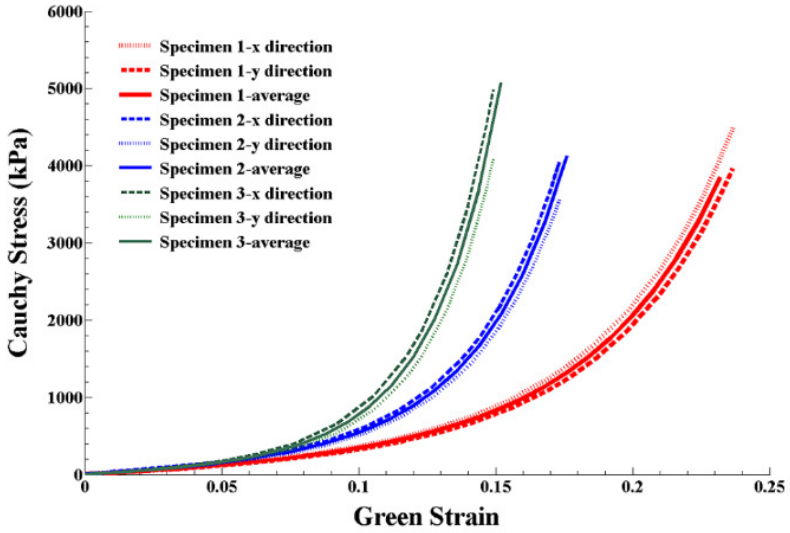

Figure 2.7: Raw data were converted to equibiaxial stretch condition (dashed lines: circumferential, dotted lines: longitudinal, and solid lines: average), adapted from (Abbasi and Azadani 2015).

$$W = \sum_{i=1}^{4} C_{i0}\,(\bar{I}_1 - 3)^i \tag{2.6}$$

where C_{i0} are constants and $\bar{I}_1$ is the first principal invariant of the left Cauchy–Green deformation tensor.

In the simulations, the average mechanical property of specimen number 1 was considered as material property of the three TAV leaflets. In this way, our simulations would capture the highest stress levels that may exist in TAV leaflets. The coefficients of the reduced polynomial strain-energy function fitted to the average curve of specimen number 1 are shown in Table 2.2.

2.3.2 Leaflet stress and strain distributions

The maximum principal stress and strain distributions of the 23mm TAV expanded to diameters ranging from 18 to 23mm are plotted in Fig. 2.8 and Fig. 2.9 at the peak of systole and early in the diastole. As shown in the figures, TAV leaflet stress and strain distributions were dependent on the diameter of the inflated TAV. After complete expansion of the TAV to 23mm, high stress regions were observed primarily in the boundary edge during systole, and the maximum principal stress reached 1.04MPa in the fully-open position. During diastole, however, high stress regions were observed primarily in the commissures, and the maximum stress reached 2.52MPa, early in diastole right after complete valve closure. In addition, the maximum principal logarithmic strain exhibited a similar distribution during valve opening and closing. The peak strain value reached to 0.28 at the boundary edge in the fully-open position, and the peak strain value reached to 0.36 at the commissures in the diastole.

Table 2.2: Coefficients of fourth-order reduced polynomial strain-energy function fitted to the average curve of specimen number 1.

C10	C20	C30	C40
1.56941E+5	8.59024E+5	-6.50847E+5	5.59565E+6

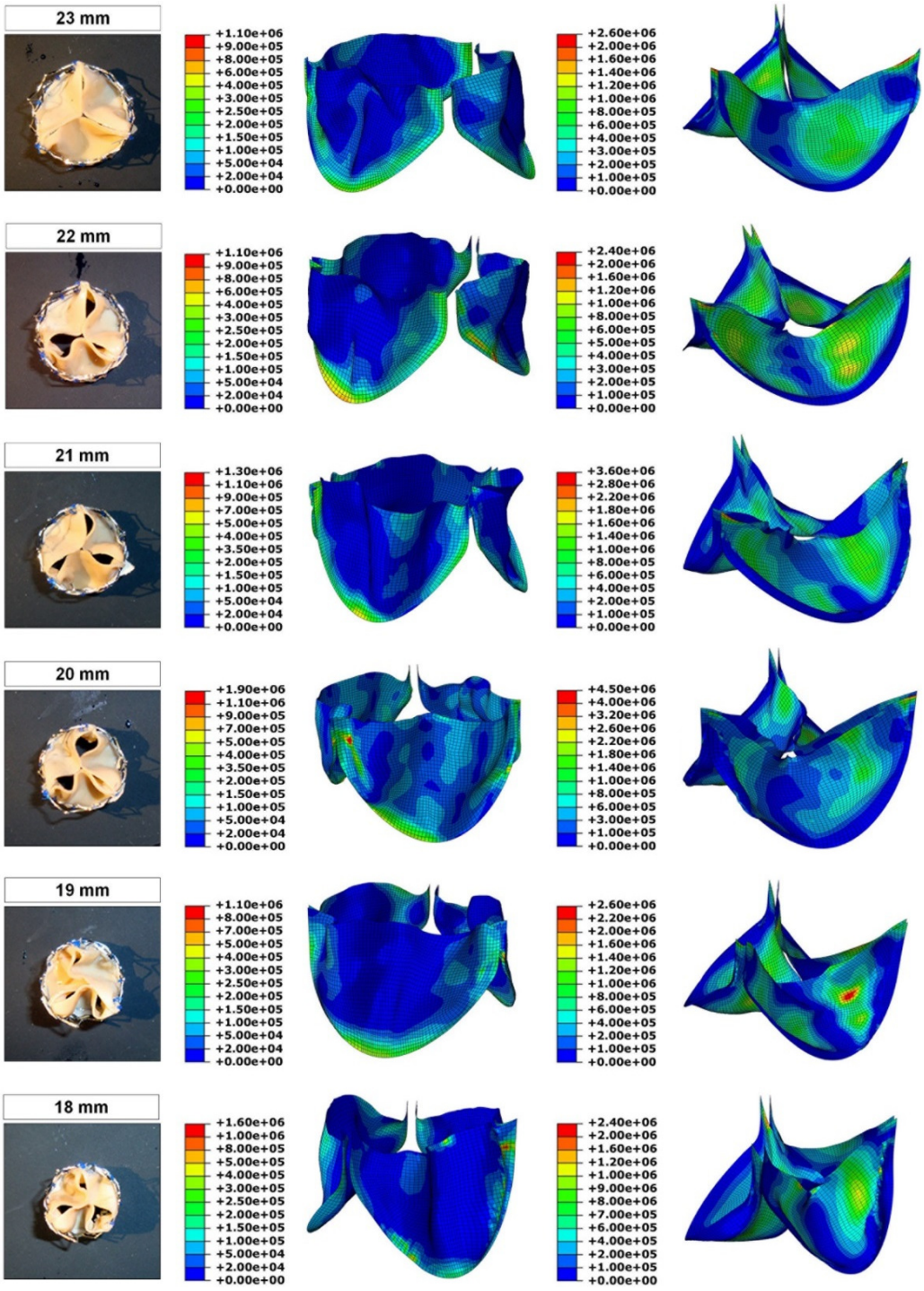

Figure 2.8: (Left column) 23mm TAV expanded to diameters ranging from 18 to 23 mm in 1 mm increments. (Middle column) 1st principal stress of TAV leaflets (MPa) in the fully-opened position. (Right column) 1st principal stress of TAV leaflets (MPa) in the diastole, adapted from (Abbasi and Azadani 2015).

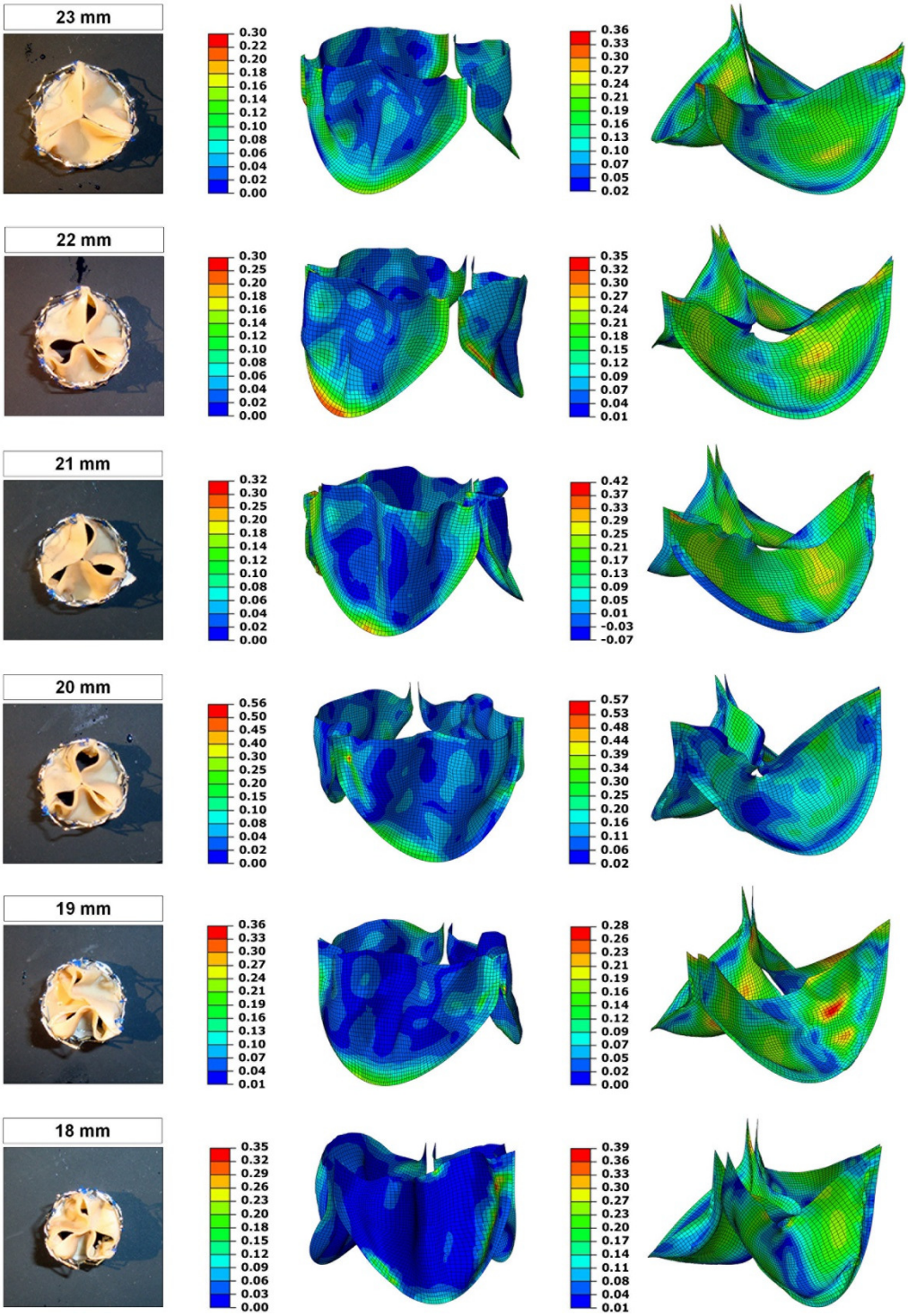

Figure 2.9: (Left column) 23mm TAV expanded to diameters ranging from 18 to 23 mm in 1 mm increments. (Middle column) 1st principal logarithmic strain of TAV leaflets in the fully-opened position. (Right column) 1st principal strain of TAV leaflets in the diastole, adapted from (Abbasi and Azadani 2015).

As presented in Fig. 2.8 and Fig. 2.9, incomplete expansion of TAV for 2mm or more induced localized high stress and strain regions within the leaflets. Incomplete expansion of the 23mm TAV to diameters of 21 and 20mm induced sharp bending at the commissures and consequently created localized high stress regions (Fig. 2.8). After incomplete expansion of the 23mm TAV to diameters of 21 and 20mm, the maximum principal stress in the fully-open position reached to 1.28 and 1.33MPa, respectively; however, early in the diastole, the maximum principal stress reached to 3.53 and 4.49MPa, respectively. Furthermore, the maximum principal logarithmic strain after incomplete expansion of the 23mm TAV to diameters of 21 and 20mm reached to 0.31 and 0.56 respectively in the fully-open position and reached to 0.42 and 0.57 respectively in the diastole.

In contrast, incomplete expansion of the 23mm TAV to diameters of 19 and 18mm shifted high stress and strain regions from the commissures to the belly region in the diastole. Expansion of the 23mm TAV diameters to 19 and 18mm induced sharp leaflet bending within the belly of the TAV leaflets and consequently created pockets of high stress regions in the belly region in the diastole (Fig. 2.8). The maximum stress within the belly region was reached to 2.60 and 3.00MPa after incomplete expansion of the 23mm TAV to diameters of 19 and 18mm, respectively. In the fully-open position, however, the maximum stress was observed in the vicinity of boundary edges, and the maximum stress reached to 1.06 and 1.58MPa, respectively. The maximum principal logarithmic strain showed similar distribution to the maximum principal stress during valve opening and closing. After incomplete expansion of the 23mm TAV to diameters of 19 and 18mm, the maximum principal logarithmic strain reached to 0.35 and 0.40, respectively early in the

diastole, and during systole, the maximum principal logarithmic strain reached to 0.28 to 0.35, respectively.

In diastole, as shown in Table 2.3, the average principal stress of the commissures was increased as the post-inflation diameter increased. In contrary, the maximum principal stress in the belly region was decreased as the post-inflation diameter increased. Furthermore, incomplete expansion of the 23mm TAV to diameters of 21 and 20mm induced sharp bending at the commissures and consequently created localized high stress regions within the commissures as presented in Table 2.3. However, expansion of the 23mm TAV diameters to 19 and 18mm induced sharp leaflet bending within the belly of the TAV leaflets and created pockets of high stress regions.

2.4 Discussion

2.4.1 Summary

In this chapter, we examined the impact of incomplete TAV stent expansion on leaflet stress and strain distributions to understand the impact of oversizing on deformation and mechanical performance of TAV leaflets. Through dynamic simulations of a 23mm TAV expanded to diameters ranging from 18 to 23mm, we found that the maximum principal stress was significantly higher in the diastolic phase of cardiac cycle than the systolic phase. Furthermore, we found that TAV leaflet stress and strain distributions were dependent on the diameter of the inflated TAV. After complete expansion of the TAV to 23mm, high stress regions were observed primarily in the commissures during the diastole. However,

Table 2.3: 1st principal stress of 23mm TAV leaflets expanded to diameters ranging from 18 to 23 mm in the diastole.

TAV inflated diameter	**23mm**	**22mm**	**21mm**	**20mm**	**19mm**	**18mm**
Average principal stress of all the *commissures* (MPa)	1.56	1.32	1.23	1.19	0.87	0.37
Maximum 1st principal stress in the *commissure* region (MPa)	2.52	2.31	3.53	4.49	1.91	1.83
Maximum 1st principal stress in the *belly* region (MPa)	1.16	1.24	1.36	2.26	2.60	3.00

2-3mm incomplete TAV stent expansion induced localized high stress regions within the commissures due to sharp tissue bending at the commissures. The peak stresses were increased by 40.1% and 78.2% after incomplete expansion of the 23mm TAV to diameters of 21 and 20mm, respectively. In contrast, 4-5mm incomplete stent expansion induced localized high stress regions within the belly of the TAV leaflets. The peak stresses were increased by 124.1% and 158.6% within the belly region after incomplete expansion of the 23mm TAV to diameters of 19 and 18mm, respectively. Increased mechanical stress and flexural deformation on TAV leaflets may lead to accelerated tissue degeneration.

2.4.2 Oversizing in TAVR procedure

In TAVR procedure, valve oversizing is crucial to achieve proper anchoring. Currently, Edwards SAPIEN valve and Medtronic CoreValve are widely available and used. TAV size recommendations are based on native valve annulus size, as measured by transesophageal echocardiography (TEE) or computed tomography (CT). According to Edwards Lifesciences instructions for use, 23mm Edwards SAPIEN XT valve is recommended for native valve annulus size of 18-22mm measured by TEE, and native

valve annulus area of 314-415mm^2 measured by CT. On the other hand, CoreValve is slightly more oversized than SAPIEN valve. Based on Medtronic instructions for use, 23mm CoreValve is recommended for annulus size of 18-20mm, and 26mm CoreValve is recommended for annulus size of 20-23mm. The range of annulus size for TAVR suggests that not all patients will achieve complete TAV expansion to the manufactured size, and some degree of incomplete stent expansion may exist. Incomplete stent expansion has been commonly observed following TAVR with Medtronic CoreValve in native calcified aortic valves, and following TAVR with Edwards SAPIEN valve within degenerated stented bioprostheses, the valve-in-valve procedure (Bapat et al. 2013, Jilaihawi et al. 2011, Schultz et al. 2009, Willson et al. 2012). In native calcified valves, incomplete expansion of the Medtronic CoreValve stent is common and has been observed in 62% of patients undergoing TAVR (Jilaihawi et al. 2011, Schultz et al. 2009). Nevertheless, incomplete stent frame expansion has also been observed in TAVR with Edwards SAPIEN valves. Willson et al. reported 8% of patients undergoing TAVR with SAPIEN valve in the study cohort had under-expanded stent frame (Willson et al. 2012). Incomplete expansion of SAPIEN frame is typical because of the existence of highly calcified native leaflets, inaccuracy of annulus sizing prior to TAVR procedure, or specific valve anatomy (e.g. bicuspid aortic valve). In the contrary to native valves, in the valve-in-valve procedure within degenerated bioprosthetic valves, incomplete stent expansion is more common in TAVR with Edwards SAPIEN valves. This is due to the fact that SAPIEN valves are implanted within the rigid bioprosthetic frame, in contrary to the supra-valvular positioning

of CoreValve. Therefore, incomplete stent expansion is a common phenomenon in both Edwards SAPIEN valve and Medtronic CoreValve Revalving system.

Unlike surgical stented bioprosthetic valves where leaflets are attached to a rigid frame and their motion is highly consistent, optimal TAV function requires full circular deployment of the valve to its nominal dimensions(Azadani, Jaussaud, Matthews, Ge, et al. 2009, Azadani and Tseng 2011, Gunning, Vaughan, and McNamara 2014). Under-expanded TAVs will function suboptimally with impaired coaptation of the leaflets and increased valvular pressure gradient (Azadani et al. 2011, Azadani, Jaussaud, Matthews, Chuter, et al. 2009). It has previously determined that incomplete TAV expansion due to oversizing negatively impacts valvular hemodynamics, leading to increased pressure gradient and transvalvular energy loss (Azadani et al. 2010). Therefore, fully-expanded circular stent deployment is essential to achieve optimal hemodynamic outcomes following TAVR. In this chapter, we assumed an identical pressure wave across all the simulations for consistency. However, incomplete TAV expansion leads to increased transvalvular pressure gradients, and increased valvular gradients will induce even higher localized stresses on leaflets of the under-expanded TAVs during systole.

The degree of TAV expansion varies from patient to patient based on annulus size and specific calcified valve geometry. As a result, non-circular eccentric stent deployment may also occur in TAVR patients (Delgado et al. 2010, Morganti et al. 2014, Schultz et al. 2009, Zegdi et al. 2008). Sun and Siroios (Sun, Li, and Sirois 2010) have shown that distorted, elliptical shape of TAVs induced a significant increase in leaflet peak stresses and strains compare to those of fully-expanded circular TAVs under the same loading conditions. They

proposed a FE model to simulate elliptical bioprosthetic valve deformation under quasi-static loading condition by applying a uniform pressure of 120mmHg to the leaflets. They reported that maximum stress and strain of a distorted TAV with an elliptical eccentricity of 0.68, increased significantly by 143% and 17%, respectively, as compared to a fully-expanded circular TAV. Clinical importance of TAV under-expansion or eccentricity and their impact on the long-term valve durability is unknown. There is indirect evidence, observed in stentless surgical bioprostheses, to suggest that valve distortion may lead to accelerated calcification and fibrosis in an animal model (Mohammadi et al. 2006, van Nooten et al. 1999). Therefore, increased mechanical stress due to incomplete or eccentric stent deployment may lead to diminished long-term durability.

2.4.3 Study limitations

In this chapter, initial leaflet geometry was based on a homemade TAV. Although, the TAV leaflet geometry was similar to SAPIEN XT, by using precise leaflet geometry of SAPIEN valve or CoreValve, accurate leaflet stress and strain distributions of the two devices that are widely used in clinics can be obtained. In addition, the effects of crimping on the mechanical properties of tissue were not considered in this FE analysis. Alavi et al. (Alavi, Groves, and Kheradvar 2014c) reported the crimping may induce structural damage to bovine pericardial leaflets. Furthermore, the three TAV leaflets were assumed to be isotropic nonlinear hyperplastic material. Although tissue anisotropy was minimal, a nonlinear anisotropic material model may provide more accurate simulation results. Alteration in the material properties induces significant changes in the mechanical behavior of the leaflets, as highlighted by Auricchio et al. (Auricchio et al. 2014) . Finally, viscous

damping was implemented in the FE simulations to mimic surrounding fluid. However, a more accurate simulation may involve fluid–structure interaction (FSI) simulation.

2.5 Conclusions

In summary, computational models were developed to study the impact of incomplete TAV stent expansion on leaflet stress and strain distributions. We found that TAV leaflet stress and strain distributions were dependent on the diameter of the inflated TAV. We found that 2-3mm incomplete TAV stent expansion induced localized high stress regions within the TAV commissures, while 4-5mm incomplete stent expansion induced localized high stress regions within the belly of the TAV leaflets during the diastolic phase of the cardiac cycle. In TAVR, valve oversizing is essential to secure the valve and prevent paravalvular aortic regurgitation. However, if oversizing leads to incomplete expansion of the stent, it will induces localized high stress regions within the TAV leaflets which overtime may lead to premature tissue degeneration.

CHAPTER 3: MATERIAL CHARACTERIZATION OF HEART VALVE TISSUE

3.1 Introduction

Design and development of the life sustaining implantable medical devices such as heart valves in the current regulatory framework require extensive and expensive pre-clinical and clinical testing. The existing process limits opportunities to thoroughly refine current designs, and explore novel high-risk, high-payoff ideas (Keefe et al. 2010). However, in the past few years, the role of computational modeling is becoming increasingly important in design and verification of medical devices. Computational modeling provides a framework for quantitative description of device function and provides greater consistency and predictability in the development of new devices. Furthermore, computational modeling can yield significant cost savings by mitigating the need to perform time consuming bench-top and pre-clinical animal testing. As a result, computational modeling and simulations are becoming an integral part of research and development in medical device industry, considering that the U.S. Food and Drug Administration (FDA) and CE Mark regulatory requirements are a major driving force behind it (Stewart 2013).

In computational modeling, considering accurate constitutive models is of the utmost importance to precisely capture mechanical properties of soft tissue and biomedical materials (Humphrey 2003). Constitutive models are needed to accurately predict and

simulate mechanical response of biomedical materials under a verity of multi-axial loading conditions that may exist under physiological conditions. However, lack of comprehensive three-dimensional material models limits the utility and effectiveness of computational models in research and development of medical devices. Some of the reasons accountable for the absence of comprehensive three-dimensional soft tissue constitutive models are: (1) Majority of experimental testing used to estimate material parameters such as in-plane biaxial testing cannot capture the out-of-plane displacements of soft tissue, required to determine 3D anisotropic mechanical properties of soft tissue (Holzapfel and Ogden 2009). In addition, technical difficulties in interpreting biaxial test results have been previously reported that may impact the experimental outcome (Eilaghi et al. 2009, Nolan and McGarry 2016, Waldman and Lee 2002), (2) Biological soft tissues are viscoelastic in nature and often approximated as pseudo-hyperelastic models; however, the pseudo-hyperelastic models commonly fitted to experimental data that were not collected at strain-rates comparable to physiological conditions.

Extensive intra-specimen and inter-specimen variations exist in mechanical properties of soft tissue; therefore, mechanical properties of examined materials in experimental setting may be significantly different from the actual materials used in the implanted devices. Thus, using optimized material coefficients to represent specimen-specific behavior is crucial in computational modeling and simulations. Inverse finite element (FE) analysis is a valuable tool that can be used to accurately estimate mechanical properties of heart valve tissues on subject-specific basis. The procedure is a numerical approach in which an optimization algorithm is coupled with a FE method to find optimal values for a

set of parameters such as material parameters in a constitutive equation. In the optimization process, experimental data is often used as reference input to the parameter estimation algorithm. In recent years, in particular with the advent of transcatheter aortic valve replacement for the treatment of patients with aortic stenosis, utilization of computational models is an emerging trend for demonstrating the effectiveness of new valve designs (Kheradvar, Groves, Falahatpisheh, et al. 2015). Currently, the commercially approved transcatheter heart valve leaflets are made from chemically treated bovine or porcine pericardium (Kheradvar, Groves, Goergen, et al. 2015). In addition, chemically treated bovine pericardium has been extensively used in the fabrication of surgical bioprostheses. It has been demonstrated that chemically treated bovine pericardium is an anisotropic biocomposite material (Sacks and Chuong 1998, Zioupos, Barbenel, and Fisher 1992), with intra-specimen and inter-specimen variability and distinct collagen fiber architecture (Sacks, Chuong, and More 1994). During the past few decades, a number of computational studies have attempted to determine stress distribution of valve leaflets and correlate high flexural stresses during valve opening and high tensile stresses during valve closure to regions of tissue degeneration. However, the accuracy of the simulations may be limited due to the use of simplistic isotropic or simplified non-subject-specific anisotropic material models for bovine pericardial leaflets.

The main objective of this chapter was to use inverse FE methods to determine three-dimensional anisotropic mechanical properties of bovine pericardial leaflets of a surgical bioprosthetic heart valve under physiological loading condition. The FE simulations were validated using experimental in-vitro measurements, and the impact of different

generalized Fung-elastic constitutive models (generalized anisotropic vs. orthotropic) in ABAQUS software was investigated on leaflet deformation and stress distribution. Furthermore, the Rayleigh damping coefficient that was introduced to the FE simulations to simulate viscous damping effects of surrounding fluid was assessed in the inverse parameter estimation. Lastly, this chapter presents an approach for utilizing commercial FE software packages for quantitative description of heart valve function under physiological loading conditions and mitigating the need to perform time consuming bench-top and pre-clinical animal testing.

3.2 Materials and Methods

3.2.1 Theoretical Background

3.2.1.1 Constitutive Modeling

A constitutive law should approximate physical behavior of soft tissue under specific conditions of interest. Biological soft tissues are viscoelastic in nature, and their mechanical behavior is dependent on the history of deformation. However, biological soft tissue are often approximated as pseudo-hyperelastic materials (Fung 2013a). A hyperelastic material is defined as a subclass of elastic materials in which there exists a *strain-energy function* Ψ which is exclusively a function of the deformation gradient tensor $\boldsymbol{F}$.

$$\boldsymbol{P} = \frac{\partial \Psi(\boldsymbol{F})}{\partial \boldsymbol{F}} \tag{3.1}$$

Where $\boldsymbol{P}$ denotes the *first Piola-Kirchhoff stress tensor* which is a measure of the force acting on the deformed configuration per unit undeformed area.

The strain-energy function can also be expressed as a function of Green-Lagrange strain tensor $\boldsymbol{E}$ in the form of

$$\boldsymbol{S} = \frac{\partial \Psi(\boldsymbol{E})}{\partial \boldsymbol{E}} \tag{3.2}$$

Herein, $\boldsymbol{S}$ is the *second Piola-Kirchhoff stress tensor*. The *second Piola-Kirchhoff stress tensor* can be defined in another way

$$\boldsymbol{S} = J\,\boldsymbol{F}^{-1}\boldsymbol{\sigma}\boldsymbol{F}^{-T} \tag{3.3}$$

where $\boldsymbol{\sigma}$ is the *Cauchy stress tensor*, and $J = \det \boldsymbol{F}$ is the *Jacobian of the deformation*. Cauchy (or true) stress is a measure of force per unit area in the deformed configuration. For additional information regarding strain and stress tensors, the reader is referred to (Holzapfel 2000, Lai et al. 2009).

Soft tissues are primarily comprised of water and therefore have negligible permeability (Fung 2013a). Materials that keep their volume constant through deformation are characterized by incompressibility constraint $J = 1$. For additional information regarding enforcing incompressibility constraint on the strain energy function, the reader is referred to (Fung and Tong 2001, Sun and Sacks 2005b).

3.2.1.2 Elasticity Tensor

An *elasticity tensor* $\mathbb{C}$ describes properties of the continuum and shows how variations in strain will affect the stress tensor.

$$\mathbb{C} = \frac{\partial \boldsymbol{S}}{\partial \boldsymbol{E}} \tag{3.4}$$

Elasticity tensor is a tensor of rank four with 81 components. However, the number of coefficients can be reduced to 21 independent components by making arguments of symmetry (Holzapfel 2000, Lai et al. 2009). It is also important to note that the convexity of strain energy functions should be always satisfied to guarantee the stability of elastic body equilibrium while deforming. If the elasticity tensor $\mathbb{C}$ is positive definite, then the strain energy function will be convex. The elasticity tensor $\mathbb{C}$ is said to be a positive definite if (1) all diagonal elements are positive; (2) the determinant of $\mathbb{C}$ is positive, and (3) its inverse exists, and is symmetric and positive definite (Holzapfel 2000).

3.2.1.3 Generalized Fung Hyperelastic Constitutive Model

The Fung strain-energy function, introduced more than three decades ago, has been shown to properly describe the nonlinear mechanical behavior of many biological soft tissue (Fung, Fronek, and Patitucci 1979). A generalized three-dimensional Fung strain-energy function proposed by Humphrey (Humphrey 1995) is available in ABAQUS/Explicit in the form of

$$\Psi = \frac{c}{2}(e^{\mathcal{Q}} - 1) + \frac{1}{\mathcal{D}}(\frac{{J_{el}}^2 - 1}{2} - \ln J_{el}) \tag{3.5}$$

where Ψ is the strain energy per unit of reference volume. $\mathcal{D}$ and c describe the temperature-dependent material parameters, J_{el} stands for the elastic volume ratio which is equal to J in the absence of thermal strains, and $\mathcal{Q}$ is given by

$$\mathcal{Q} = \boldsymbol{E}\colon(\mathbb{b}\boldsymbol{E}) \tag{3.6}$$

where $\mathbb{b}$ is a non-dimensional symmetric fourth-order tensor of anisotropic material constants, and $\boldsymbol{E}$ is the Green-Lagrange strain tensor, under the assumption of tissue incompressibility.

Considering incompressibility assumption ($J_{el} = 1$), the Fung strain energy function is reduced to

$$\Psi = \frac{c}{2}(e^{Q} - 1) \tag{3.7}$$

If $\mathbb{b}$ is positive definite, then Ψ is strictly convex, and the numerical solution will be stable. The number of components of $\mathbb{b}$ that must be determined is similar to the elasticity tensor $\mathbb{C}$. ABAQUS supports generalized anisotropic and orthotropic forms of the generalized Fung model, and therefore the number of independent components of $\mathbb{b}$ has to be specified based on the level of anisotropy: 21 for the fully anisotropic and 9 for the orthotropic materials.

$$\mathbb{b}_{\text{anisotropic}} = \begin{bmatrix} \mathbf{b_{1111}} & \mathbf{b_{1122}} & \mathbf{b_{1133}} & \mathbf{b_{1123}} & \mathbf{b_{1113}} & \mathbf{b_{1112}} \\ & \mathbf{b_{2222}} & \mathbf{b_{2233}} & \mathbf{b_{2223}} & \mathbf{b_{2213}} & \mathbf{b_{2212}} \\ & & \mathbf{b_{3333}} & \mathbf{b_{3323}} & \mathbf{b_{3313}} & \mathbf{b_{3312}} \\ & & & \mathbf{b_{2323}} & \mathbf{b_{1323}} & \mathbf{b_{1223}} \\ & & \text{Symmetric} & & \mathbf{b_{1313}} & \mathbf{b_{1213}} \\ & & & & & \mathbf{b_{1212}} \end{bmatrix},$$

$$\mathbb{b}_{\text{orthotropic}} = \begin{bmatrix} \mathbf{b_{1111}} & \mathbf{b_{1122}} & \mathbf{b_{1133}} & 0 & 0 & 0 \\ & \mathbf{b_{2222}} & \mathbf{b_{2233}} & 0 & 0 & 0 \\ & & \mathbf{b_{3333}} & 0 & 0 & 0 \\ & & & \mathbf{b_{2323}} & 0 & 0 \\ & & \text{Symmetric} & & \mathbf{b_{1313}} & 0 \\ & & & & & \mathbf{b_{1212}} \end{bmatrix} \tag{3.8}$$

3.2.2 Biaxial Testing System

To characterize mechanical properties of bovine pericardium of a surgical bioprosthetic valve based on the generalized Fung constitutive model using inverse FE simulations, appropriate initial estimate values were needed. To obtain the initial values, a bovine pericardial patch was obtained from Edwards Lifesciences Inc. and a planar biaxial stretching device (CellScale Biomaterials Testing, Waterloo, Canada) was used to determine the patch in-plane mechanical properties (Fig. 3.1A). Details of the biaxial testing procedure have been previously described in chapter 2. Briefly, three square samples were cut from the pericardium patch for biaxial testing. The specimens were mounted on the biaxial stretching system by using a set of four CellScale BioRakes. A normal saline bath heated to 37° C provided a physiological environment. The top sides of specimens were sprinkled with graphite to create a textured surface for strain measurements. Samples were tested over a large strain range using the following equibiaxial displacement-controlled protocol. First, ten preconditioning cycles of 10% true strain were applied on both axes at 0.5 Hz. Subsequently, each specimen was stretched to 100% strain on both axes with a 5 s stretch time. Real-time displacement of the graphite markers was obtained using a camera placed over the top surface at a rate of 15 Hz.

CellScale LabJoy image tracking was used to capture displacement field (Fig. 3.1A). Relative movements of the center-element nodes were used to calculate deformation gradient and green strain in MATLAB (v8.1.0.604, Natick, MA). To analyze kinematics, we restricted our analysis to planar homogenous deformations in the form of

$$x_1 = \lambda_1 X_1 + k_1 X_2$$

$$x_2 = k_2 X_1 + \lambda_2 X_2 \tag{3.9}$$

$$x_3 = \lambda_3 X_3$$

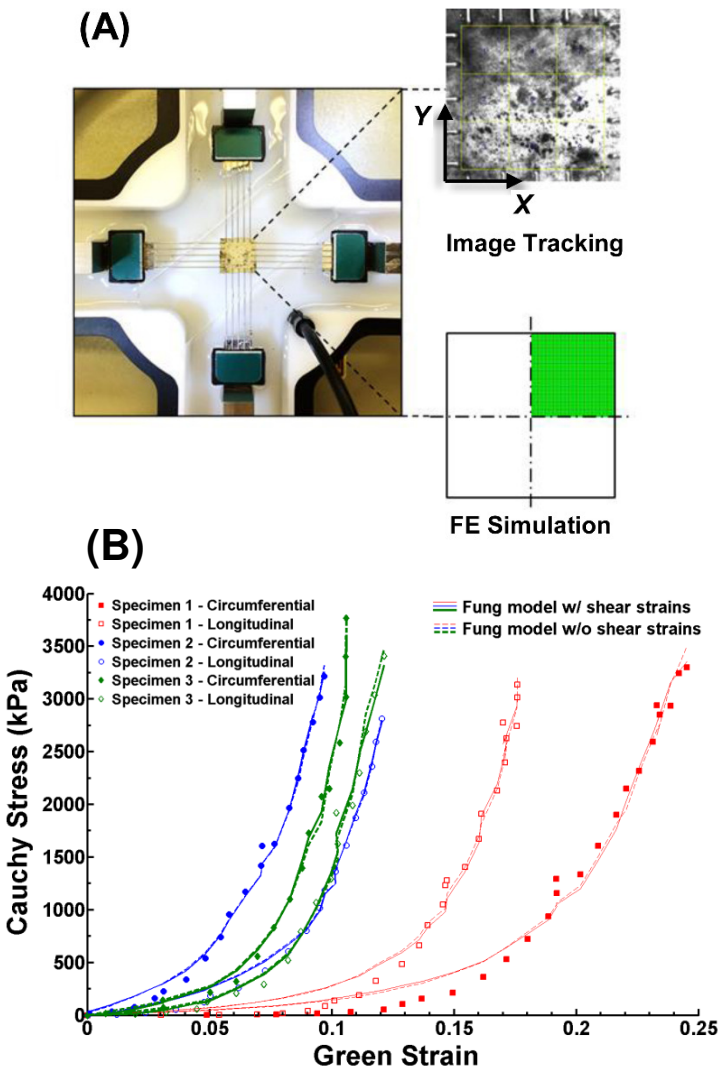

Figure 3.1: (A) Planar biaxial stretching system used to determine mechanical properties of bovine pericardium, and (B) The raw data were fit to two-dimensional Fung constitutive model (solid lines: Fung model with in-plane shear strains and dashed lines: Fung model without in-plane shear strains), adapted from (Abbasi et al. 2016).

where X_i and x_i are material points in the reference configuration and deformed configuration, respectively, λ_i are the axial extension ratios and k_i are measures of in-plane shear. Since bovine pericardium has negligible permeability ($J = 1$), the out-of-plane extension ratio was calculated as $\lambda_3 = 1/(\lambda_1\lambda_2 - k_1k_2)$.

In addition, data from load cells was used to determine stress during deformation. Planar forces (f_1, f_2) measured by the two load cells were used to calculate the non-zero components of the first Piola-Kirchhof $\boldsymbol{P}$ stress (P_{11}, P_{22}) in the two orthogonal directions.

$$P_{11} = \frac{f_1}{t_0 \ell_{01}} \quad \text{and} \quad P_{22} = \frac{f_2}{t_0 \ell_{02}} \tag{3.10}$$

where t_0 is tissue thickness in the zero-stress state, and ℓ_0 is the length of undeformed tissue. For the biaxial planar homogeneous deformation, out of plane normal and shear stresses were considered to be zero. Using the components of the first Piola-Kirchhof stress, the associated second Piola-Kirchhof and Cauchy stress were calculated.

For constitutive modeling, Fung constitutive model was considered with full expansion of quadric terms of Q to account for in-plane shear strains (Sacks 1999)

$$Q = \mathrm{b}_{1111}\mathrm{E}_{11}^2 + \mathrm{b}_{2222}\mathrm{E}_{22}^2 + 2\mathrm{b}_{1122}\mathrm{E}_{11}\mathrm{E}_{22} + \mathrm{b}_{1212}\mathrm{E}_{12}^2 + 2\mathrm{b}_{1112}\mathrm{E}_{12}\mathrm{E}_{11} + 2\mathrm{b}_{2212}\mathrm{E}_{12}\mathrm{E}_{22} \tag{3.11}$$

The experimental data from the biaxial mechanical stretch testing was fitted to the two-dimensional Fung model using a nonlinear regression interior-point algorithm in MATLAB. Convexity of the constitutive model was enforced as descried previously(Sun and Sacks 2005b). Since the regression algorithm is sensitive to the starting parameters,

several wide-ranging initial starting guesses were used to obtain optimized material parameters. In addition, to obtain initial estimate values for the orthotropic model, the experimental data were fit to Fung constitutive model without in-plane shear strains.

3.2.3 In-Vitro Testing System

A custom-built pulse duplicator system (BDC Labs, Wheat Ridge, CO) was used for functional testing of a 23mm Carpentier-Edwards bioprosthetic aortic valve (Fig. 3.2). The pulse duplicator input parameters matched ISO 5840 and FDA standards for testing heart valves: heart rate of 70 beats/min, mean atrial and aortic pressures of 10 and 100mmHg, and cardiac output of 5 L/min. Recirculating fluid of 37% by volume glycerin solution in normal saline solution was used as a blood analog fluid. Transvalvular pressure waveform and flow rate were measured from repeated in-vitro tests. Furthermore, the leaflet motion was captured by a Casio Ex-FH25 high-speed camera during the entire cardiac cycle at a rate of 1000 frames per second. The images were digitized in MATLAB, and the center of each leaflet was tracked and its distance with respect to the center of the valve was calculated through the entire cardiac cycle.

To match the motion, shape, and deformation leaflet in the FE simulation with the experimental measurements in the pulse duplicator, we didn't filter transvalvular pressure waveform were measured from repeated in-vitro tests and used the experimental raw data in our simulations. Although the reproducing physiological hemodynamic conditions in vitro pulse duplicator system was tried in our experiments, due to the lack of adequate compliance in the cardiac chamber, the peak systolic transvalvular pressure obtained in the experiment was higher than the physiological value. In most previous studies, to acquire

physiological hemodynamic conditions, the transvalvular pressure waveforms obtained from in-vitro tests were filtered.

3.2.4 Finite Element Modeling

Leaflet geometry of the 23mm Carpentier-Edwards bioprosthesis was obtained using NextEngine 3D Laser Scanner (NextEngine, Inc., Santa Monica, CA). Surface reconstruction was performed using RapidWorks and IGES format of the leaflets were obtained for FE simulations (See Fig. 3.4). For mesh generation, the leaflets were imported to HyperMesh (Altair Engineering, Inc., Troy, MI), and the geometry was discretized using a mapped mesh. The mesh was subsequently imported to ABAQUS/Explicit solver, and S4 shell elements with a thickness of 0.513 mm were used to discretize the valve geometry. Material orientation for each one of the elements was uniformly aligned parallel and normal to the free edge of the leaflets using a home-made MATLAB script (See Fig. 3.5). Density of the leaflets was considered to be 1,100 kg/m^3 and bioprosthetic frame was considered to

Figure 3.2: Custom-built pulse duplicator system (BDC Labs, Wheat Ridge, CO)

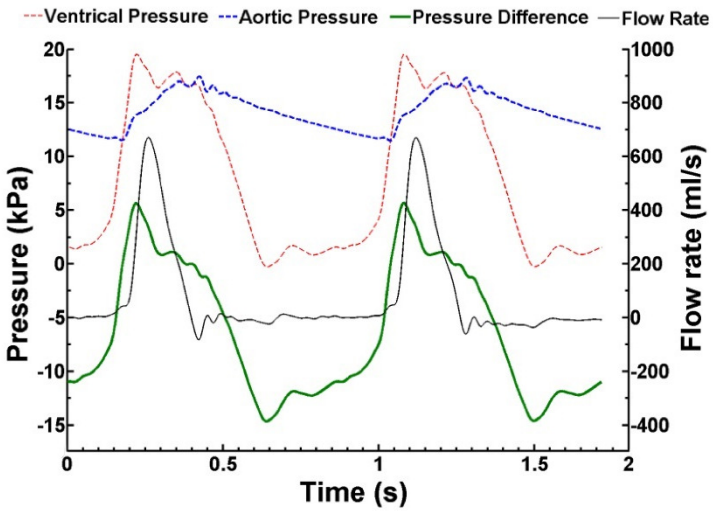

Figure 3.3: Custom-built pulse duplicator system (BDC Labs, Wheat Ridge, CO), and (B) Bioprosthetic pressure and flow rate waveforms, adapted from (Abbasi et al. 2016).

be rigid and fixed. Furthermore, no boundary condition was applied to the upper edge of the leaflets. Furthermore, the transvalvular pressure waveform obtained from the in-vitro experiments was applied to the leaflets to model the dynamic loading. Moreover, a Rayleigh damping coefficient α was introduced to the simulations to mimic viscous damping effects of surrounding fluid.

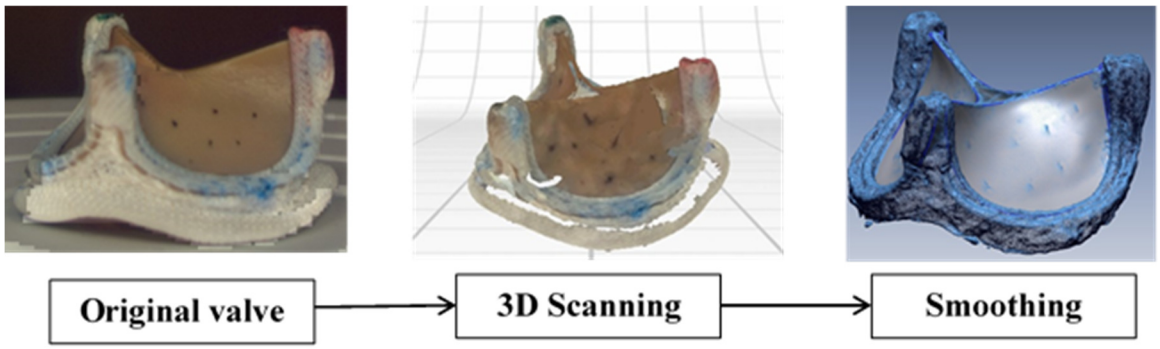

Figure 3.4: Overview of making a 3D geometry for the 23mm Carpentier-Edwards bioprosthesis.

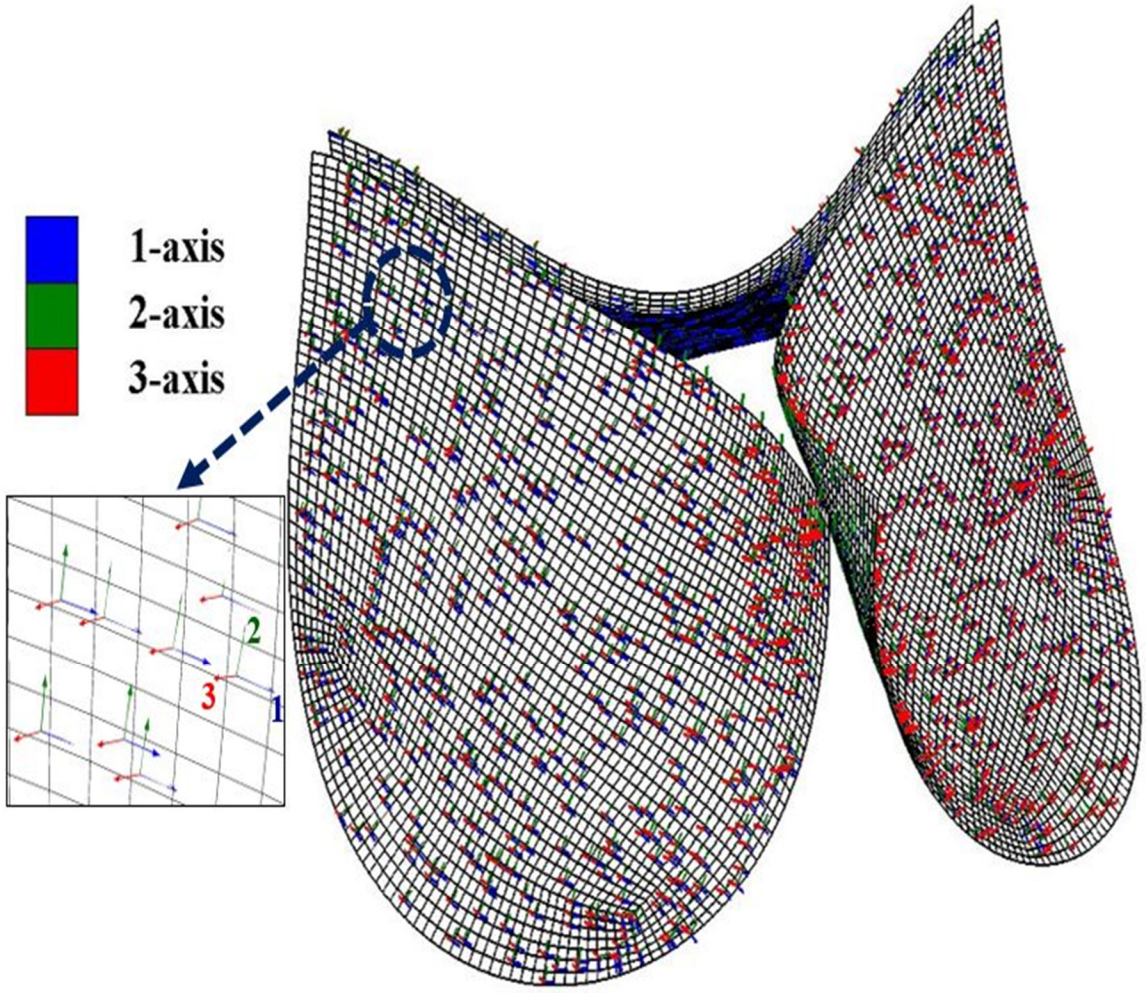

Figure 3.5: Material orientation axes defined in the circumferential (1-axis; blue), radial (2-axis; green) and normal (3-axis; red) directions.

Note that the number of elements discretizing the leaflet geometry was chosen based on the study of the independence of numerical solution, specifically the distribution of principal stress contours on the leaflets, from the computational grid (Fig. 3.6). In these simulations, leaflets were assumed to be isotropic nonlinear hyperplastic material, and a fourth-order reduced polynomial strain-energy function. Details of the material model have been previously described in chapter 2.

3.2.3 Optimization Framework

We utilized a two-step global optimization technique to determine 3D mechanical properties of the bioprosthetic leaflets as well as the Rayleigh damping coefficient. The flowchart in Fig. 3.7 shows how the target parameters were determined. First, equi-biaxial tensile test was simulated to obtain appropriate initial estimate values for the out-of-plane material coefficients in both generalized anisotropic and orthotropic forms of the Fung model. Considering the symmetry of the specimen geometry, only one quarter of the specimen was simulated (Fig. 3.1A). Out-of-plane material coefficients of the specimen were obtained by minimizing the error norm of displacement field between biaxial measurements and FE simulations of the central element using particle swarm optimization (PSO) method implemented in Isight (Simulia, Providence, RI). The optimization process terminated when the change of the objective function is less than the set tolerance of 10^{-6}. Second, bioprosthetic leaflets were simulated and the material parameters obtained from the previous step were used as initial estimate values in the second round of optimization. In this step, the material parameters plus the viscous damping coefficient were optimized using PSO method in Isight. Twenty-three and eleven input parameters were included in the optimization procedure for generalized anisotropic ($\mathbb{b}_{anisotropic}$, c, and α) and orthotropic ($\mathbb{b}_{orthotropic}$, c, and α) Fung models, respectively. The middle point distance of leaflets with respect to the center of the valve in the FE simulation was matched with the experimental measurements as shown in Fig. 3.8A. To reduce computational cost, only one leaflet motion was considered in the optimization procedure during the valve opening in the systole. The optimization process terminated when the change of the objective

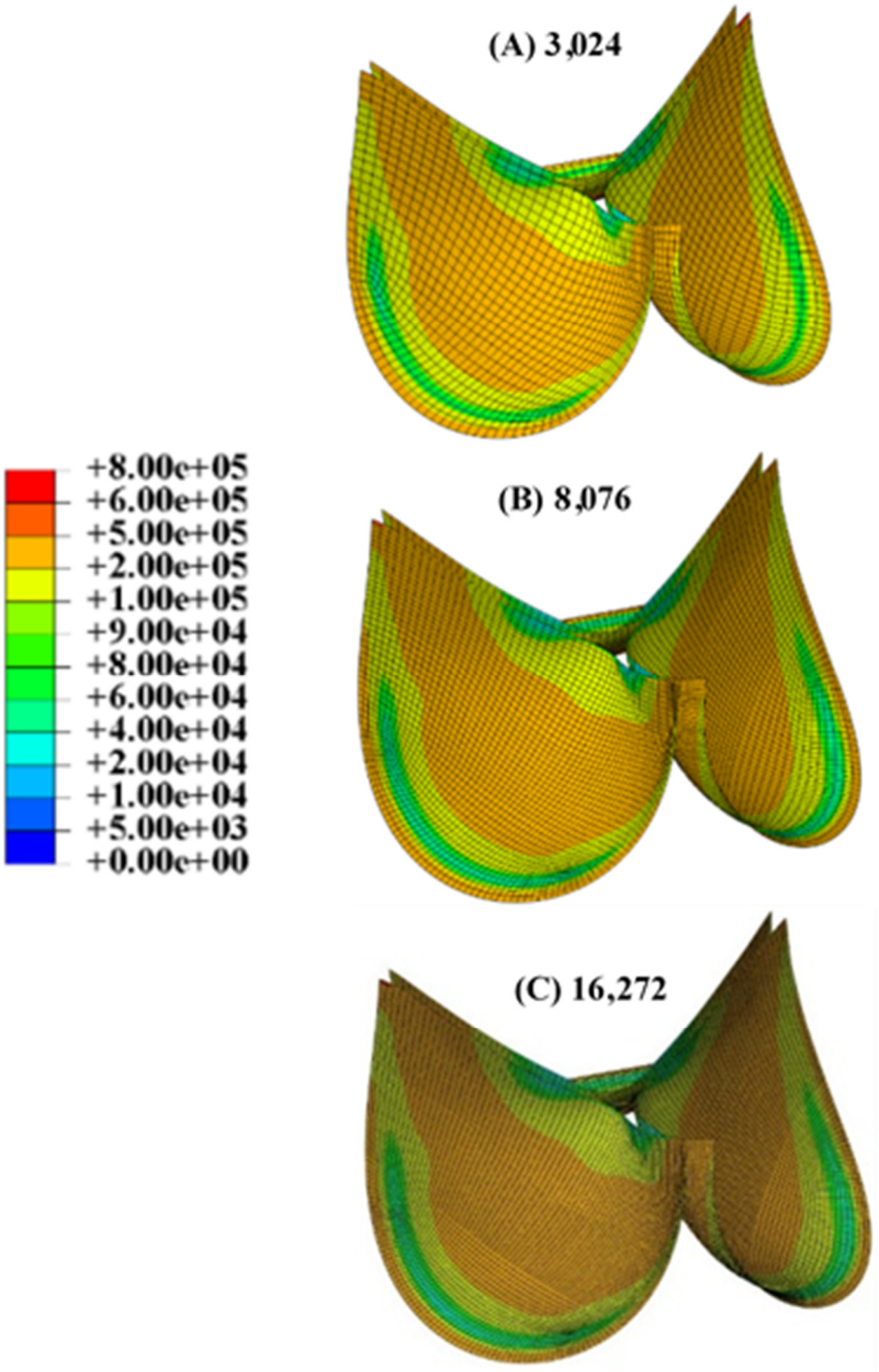

Figure 3.6: Independence of the numerical FE solution from the computational grid. The contours are showing the distribution of the maximum principal stress on the valve leaflets. The difference in maximum stress and displacement during diastole between (B) and (C) was less than 0.7%.

function is less than the set tolerance of 10^{-6}. Positive definiteness of elasticity tensor and incompressibility constraint were imposed by the solver during the optimization iterations.

3.3 Results

3.3.1 Biaxial stretching data

Three square samples were cut from the bovine pericardium patch and stretched in the biaxial testing machine. Length and thickness of each square sample are shown in Table 3.1. The average length of the square samples was 13.35±0.01 mm and the average thickness of the bovine pericardium samples was 0.430±0.004 mm. Experimental raw data obtained from biaxial testing of the three specimens are shown as Cauchy stress-Green strain plots in Figure 3.1B. Stress-strain data were fit to the Fung's strain energy function in the absence and presence of in-plane shear strains. Material parameters of the bovine pericardium samples in the absence of in-plane shear strains were shown in Table 3.1. The parameters were obtained as initial estimate values for the orthotropic Fung model. Furthermore, material parameters of the bovine pericardium samples considering in-plane shear strains were shown in Table 3.2. The parameters were obtained as initial estimate values for the generalized anisotropic Fung model. Material coefficients presented in both tables satisfied the convexity constraints.

Table 3.1: Dimensions of bovine pericardium specimens and coefficients of Fung strain energy function fitted to the raw data without in-plane shear strains.

Specimen	**Thickness (mm)**	**Length (mm)**	$\boldsymbol{c}$ **(kPa)**	$\mathbf{b_{1111}}$	$\mathbf{b_{2222}}$	$\mathbf{b_{1122}}$	$\boldsymbol{r^2}$	**Anisotropic index**
1	0.433	13.36	31.64	15.22	16.57	12.68	0.986	0.124
2	0.426	13.34	85.93	46.03	30.30	25.25	0.995	0.127
3	0.430	13.35	26.78	58.61	47.05	39.21	0.992	0.198

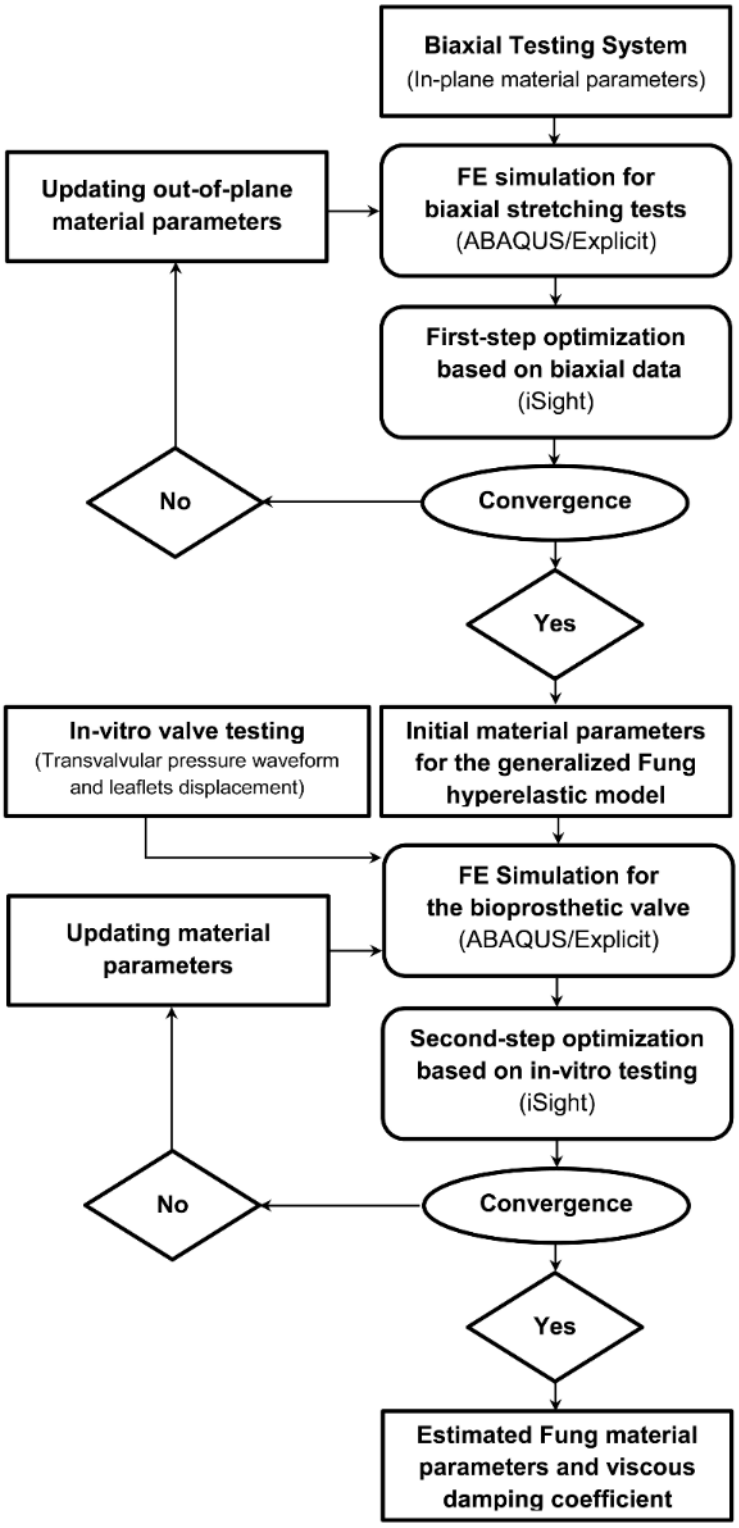

Figure 3.7: Flowchart for parameter estimation algorithm, adapted from (Abbasi et al. 2016).

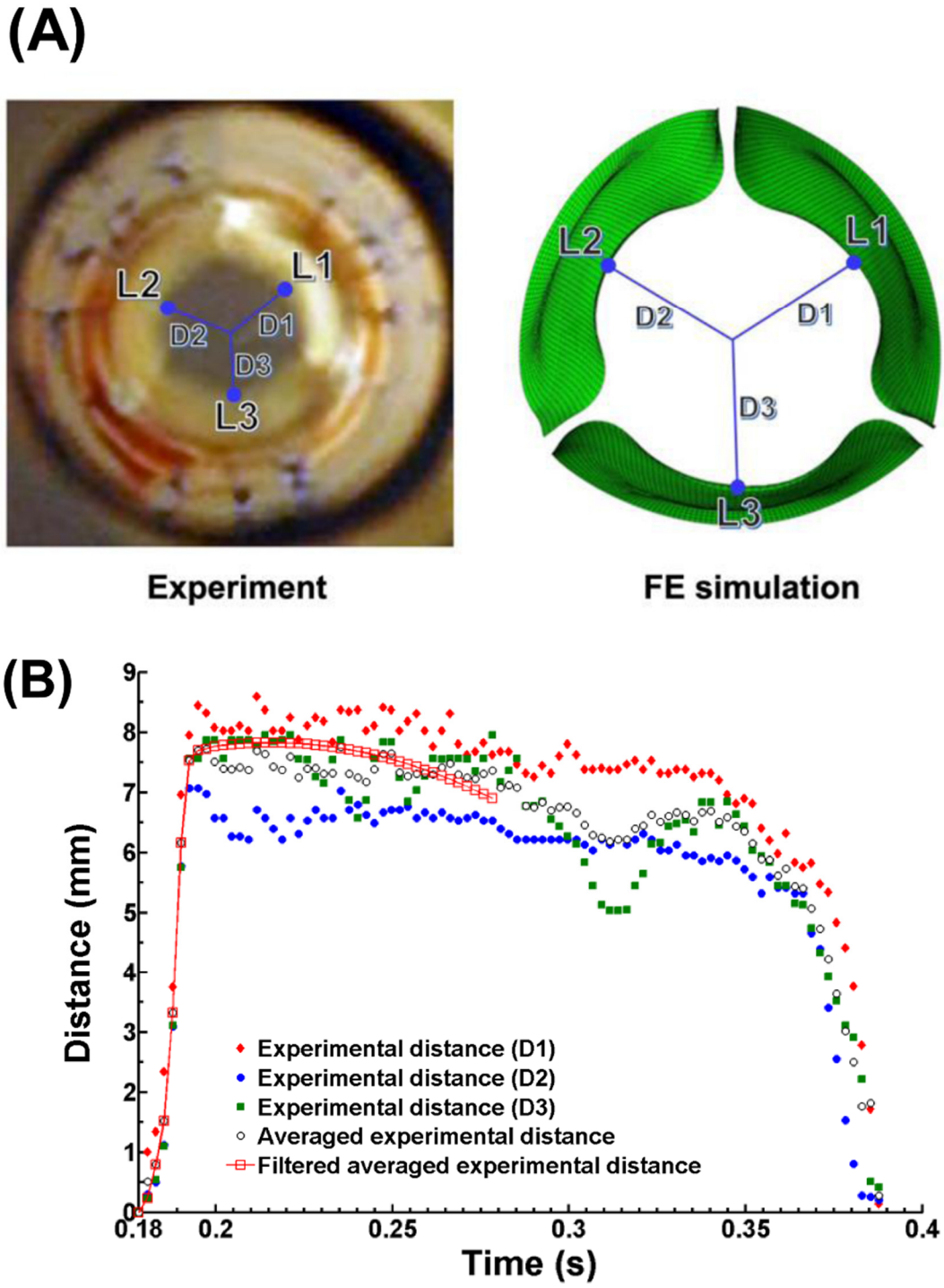

Figure 3.8: (A) Deformation measures (D1, D2, and D3) in the actual valve and FE simulation, and (B) Image processing of the three quantitative measures during systole, adapted from (Abbasi et al. 2016).

Table 3.2: Material coefficients of Fung strain energy function fitted to the raw data considering in-plane shear strains.

Specimen	c (kPa)	$\mathbf{b}_{1111}$	$\mathbf{b}_{2222}$	$\mathbf{b}_{1122}$	$\mathbf{b}_{1212}$	$\mathbf{b}_{1112}$	$\mathbf{b}_{2212}$	r^2
1	75.21	11.62	13.00	8.12	10.15	-8.19	-11.38	0.987
2	96.00	28.28	27.51	22.92	79.21	-20.68	7.15	0.996
3	34.22	69.75	56.49	47.07	1526.36	155.02	141.05	0.994

3.3.2 In-vitro experimental testing data

The 23mm Carpentier-Edwards Perimount bioprosthesis was tested in the pulse duplicator to obtain hemodynamic data for testing heart valves. The transvalvular pressure gradient waveform obtained from the in-vitro test was used as dynamic loading in the FE simulations (Fig. 3.3). In addition, for the optimization process, bioprosthetic leaflet motion was analyzed during the systole and the middle-point distance of the three leaflets with respect to the center of the valve was obtained from image processing (Fig. 3.8A). Average distance of the three leaflets was obtained during the valve opening. The curve was filtered in MATLAB and used in the optimization procedure as described previously (Fig. 3.8B).

3.3.3 Estimated Material Parameters of Bovine Pericardial Leaflets

We used a two-step optimization procedure to determine 3D mechanical properties of the bioprosthetic leaflets, as well as the Rayleigh damping coefficient introduced to simulate viscous damping effects of the surrounding fluid. First, equi-biaxial tensile test of the bovine pericardium specimens was simulated to obtain appropriate initial estimate values for the out-of-plane material coefficients in both generalized anisotropic and orthotropic forms of the Fung model. Specimen number 3 was arbitrarily chosen for the optimization procedure (Fig. 3.1B). Out-of-plane material coefficients of the bovine pericardium sample were obtained by minimizing the measured and simulated

displacement vector of the central element in the two orthogonal directions, X_1 and X_2 (Fig. 3.9). The result of material optimization is shown below

$$\mathbb{b}_{\text{anisotropic (initial estimate)}} = \begin{bmatrix} 69.75 & 47.07 & 23.29 & 6.21 & 28.79 & 155.01 \\ & 56.49 & 19.35 & 27.29 & 41.23 & 141.03 \\ & & 27.97 & 37.67 & 12.96 & 10.91 \\ & & & 43.25 & 43.99 & 15.28 \\ & & \text{Symmetric} & & 31.04 & 9.20 \\ & & & & & 1526.26 \end{bmatrix},$$

$$\mathbb{b}_{\text{orthotropic (initial estimate)}} = \begin{bmatrix} 58.61 & 39.21 & 32.32 & 0 & 0 & 0 \\ & 47.05 & 32.57 & 0 & 0 & 0 \\ & & 40.32 & 0 & 0 & 0 \\ & & & 10.66 & 0 & 0 \\ & & \text{Symmetric} & & 38.73 & 0 \\ & & & & & 42.36 \end{bmatrix}.$$

Subsequently in the second step of the optimization procedure, bioprosthetic leaflets deformation was simulated under the dynamic loading. Inverse parameter estimation was performed by considering a relatively wide range of initial values in the optimization framework: $1 \leq b_{ijkl} \leq 1.6 \times b_{ijkl\,(intial\ estimate)}$ and $900 \leq \alpha \leq 9000$. Material parameters and viscous damping coefficient of the bioprosthetic leaflets were then estimated under dynamic loading using PSO method in Isight, by matching the middle point distance of leaflets in the FE simulation with the experimental measurements as shown in Fig. 3.10. The estimated material parameters of the bovine pericardial leaflets based on generalized anisotropic and orthotropic Fung model are listed below

$$\mathbb{b}_{\text{anisotropic (estimated values)}} = \begin{bmatrix} 62.95 & 36.39 & 54.14 & 17.13 & 45.45 & 41.72 \\ & 61.88 & 45.64 & 68.15 & 67.97 & 23.42 \\ & & 65.98 & 38.70 & 63.95 & 56.17 \\ & & & 14.40 & 16.26 & 27.56 \\ & & \text{Symmetric} & & 42.57 & 17.61 \\ & & & & & 60.66 \end{bmatrix},$$

$$\mathbb{b}_{\text{orthotropic (estimated values)}} = \begin{bmatrix} 66.56 & 39.36 & 42.29 & 0 & 0 & 0 \\ & 51.58 & 24.73 & 0 & 0 & 0 \\ & & 79.56 & 0 & 0 & 0 \\ & & & 9.51 & 0 & 0 \\ & & \text{Symmetric} & & 28.12 & 0 \\ & & & & & 22.19 \end{bmatrix}.$$

In addition, the estimated values for c and α, the viscous damping coefficient, are presented in Table 3.3.

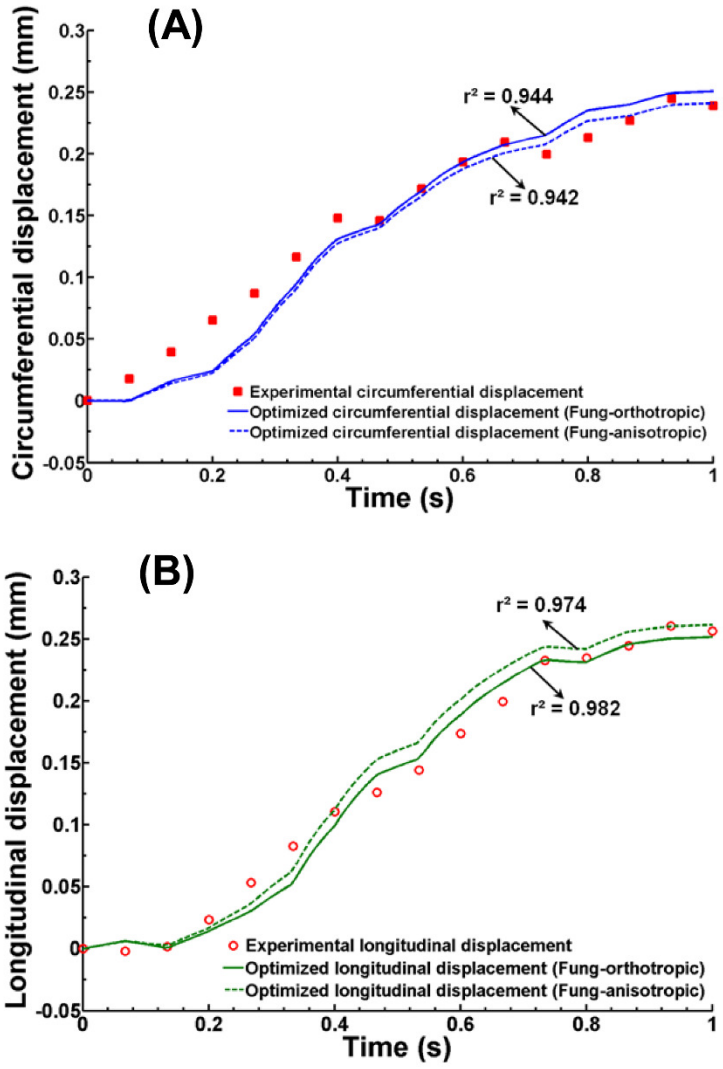

Figure 3.9: Experimental and optimized (A) circumferential (X_1) and (B) longitudinal (X_2) displacement data, adapted from (Abbasi et al. 2016).

Table 3.3: Material parameter and viscous damping coefficient for the Fung model.

Fung model	c (Material parameter, kPa)	α (Viscous damping, 1/s)
Orthotropic	26.03	2191
Anisotropic	24.62	2148

The magnitude of viscous damping coefficient controls the opening characteristics of the aortic valve. Figure 3.11 shows how different values of viscous damping coefficient would influence on the opening characteristics of bioprosthetic leaflets for the Fung-orthotropic model. Considering an identical material coefficient for the leaflets, a higher value for viscous damping coefficient leads to slower valve opening.

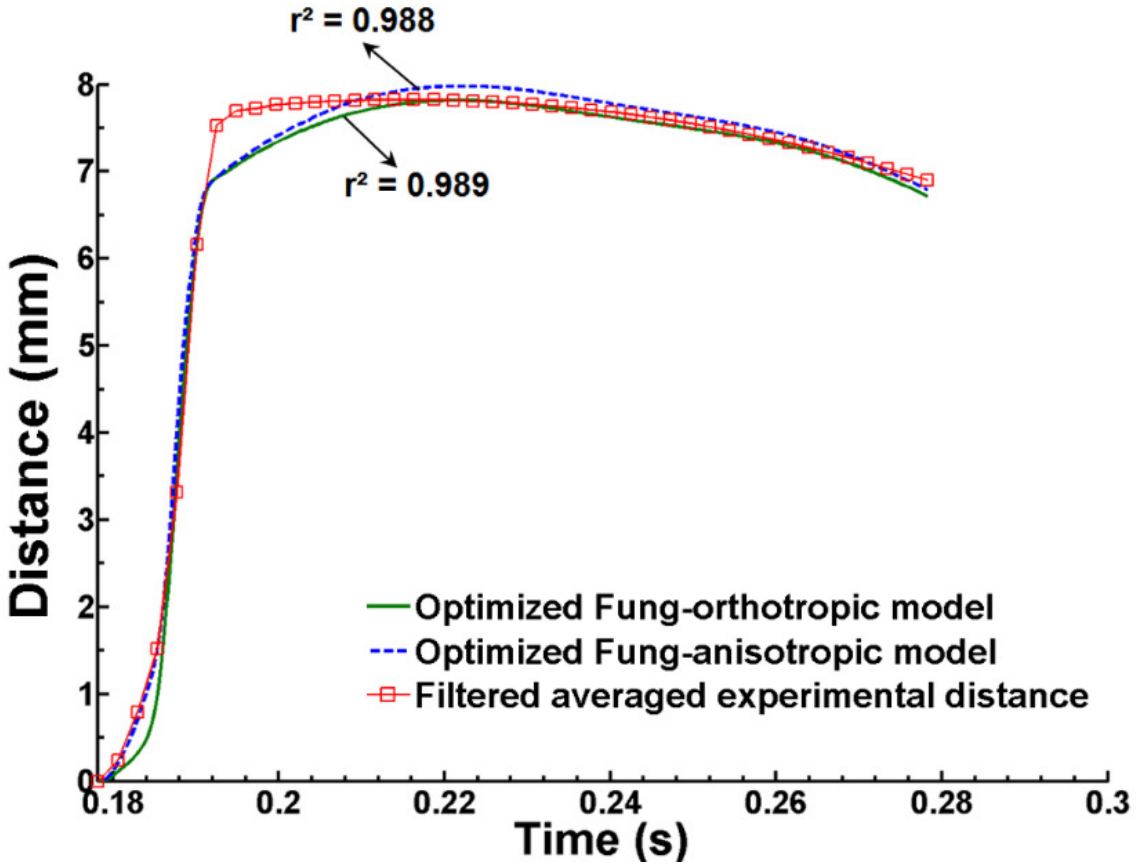

Figure 3.10: Middle point displacement of bioprosthetic leaflet; comparing optimized FE simulations with the experimental data, adapted from (Abbasi et al. 2016).

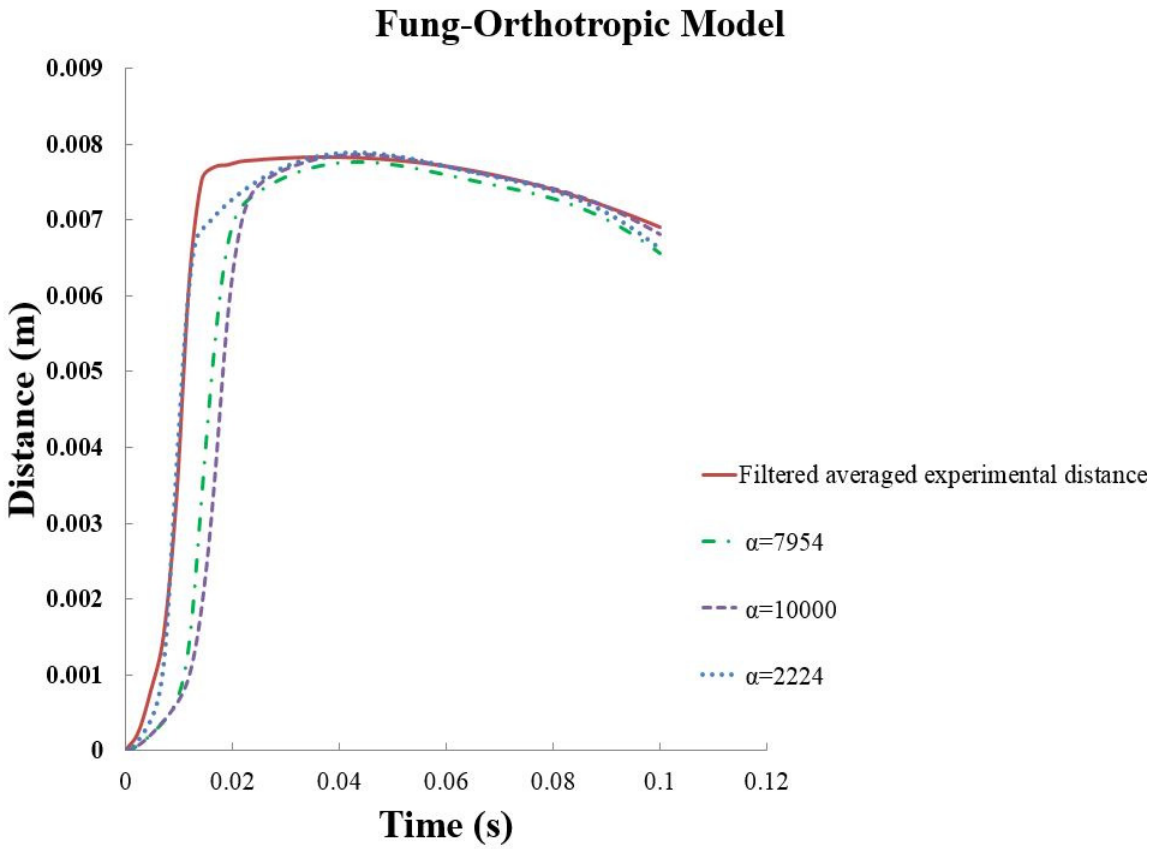

Figure 3.11: Middle point displacement of bioprosthetic leaflet; comparing optimized FE simulations with the experimental data for different viscous damping coefficients.

3.3.4 Leaflet Stress Distribution of the Carpentier-Edwards Bioprosthesis

Using the optimized material parameters and viscous damping coefficient, the maximum principal stress distribution of the 23 mm bioprosthesis during a cardiac cycle is shown in Fig. 3.12. The left-side column depicts the images of valve opening and closing in the pulse duplicator captured by the high-speed camera. The middle- and right-column of Fig. 3.12 show FE simulation results based on the estimated values for the orthotropic and generalized anisotropic Fung models, respectively. During systole, high stress regions were primarily observed in the fixed boundary edge. The peak stress value at the maximum

transvalvular pressure gradient, t = 0.215 s, reached to 3.28 and 3.17 MPa in the orthotropic and generalized anisotropic models, respectively.

In the fully closed position, however, high stress regions were primarily observed in the commissures. The peak stress value during diastole reached to 2.33 and 1.17 MPa in the orthotropic and generalized anisotropic models respectively. As shown in Figure 3.12, in comparison to the experimental data, the anisotropic model simulated the in-vitro leaflet deformation and shape significantly better than the orthotropic model. Furthermore, asymmetric leaflet stress patterns were observed in the generalized anisotropic model in contrast to the orthotropic model where the stress patterns were nearly symmetrical with respect to the leaflet midlines. The asymmetric leaflet stress pattern was due to the non-fully-symmetric leaflet geometry of the bioprosthesis commonly seen in a handmade manufacturing process.

3.4 Discussion

3.4.1 Summary

In this study, we presented an approach to obtain material parameters of a generalized Fung hyperelastic constitutive model used to model bovine pericardial leaflets of a bioprosthetic valve under dynamic loading conditions. Through an iterative optimization algorithm, the middle point distance of the leaflets with respect to the center of the valve in the FE simulations was matched with experimental data obtained from pulse duplicator measurements. Using inverse parameter estimation process, generalized anisotropic Fung model parameters were estimated for the bioprosthetic leaflets. Furthermore, the Rayleigh damping coefficient that was introduced to FE simulations to simulate viscous damping

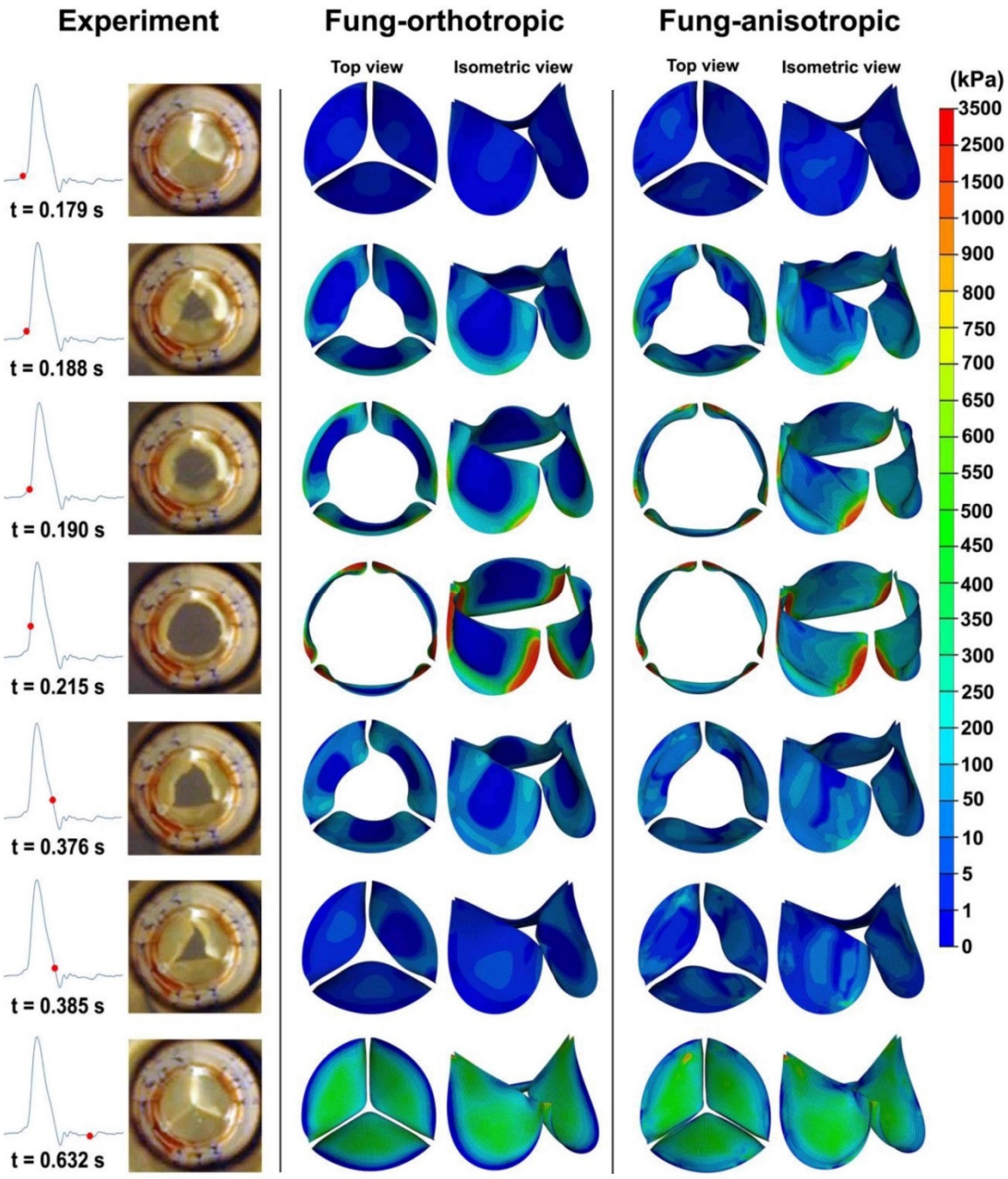

Figure 3.12: Comparison of in-vitro leaflet motion with FE simulations throughout a complete cardiac cycle. (Left column) Experimental data (Middle column) the maximum principal stress distributions on the bioprosthetic heart valve based on Fung-orthotropic model (Right column) the maximum principal stress distributions on the bioprosthetic heart valve based on Fung-anisotropic model, adapted from (Abbasi et al. 2016).

effects of surrounding fluid was assessed in the inverse parameter estimation. The anisotropic model accurately simulated the leaflet shape and deformation during valve opening and closing, significantly better than the orthotropic model. The highest stress values were found during the systole in the anisotropic model and the peak stress reached to 3.17 MPa at the leaflet boundaries. During diastole, however, high stress regions were primarily observed in the commissures and the peak stress reached to 1.17 MPa. The maximum leaflet stress at the peak of systole was 63% higher than the maximum principal stress during diastole.

3.4.2 Impact of Material Models on Leaflet Stress Distribution

During the past few decades, several investigations have been carried out to determine stress distribution of bioprosthetic leaflets and correlate high stress regions to the regions of calcification and tissue degeneration. However, the accuracy of the simulations may be affected using simplified material models for bovine pericardial leaflets, e.g. isotropic or partially anisotropic material models, or using simplified loading conditions, e.g. quasi-static loading instead of dynamic loading condition. In several computational studies, material properties of bovine pericardial leaflets have been assumed to be isotropic. Patterson et al. (Patterson, Howard, and Thornton 1996) investigated the impact of linear and nonlinear elastic material models on leaflet stress distribution of a bicuspid bioprosthetic heart valve. The leaflet material properties were isotropic, and a time-varying pressure differential was applied to the leaflets. Their results showed that the nonlinear properties of the leaflets have a profound effect on the deformation of the leaflets, and a maximum stress value of 2 MPa was reported in the commissures at the peak of diastole.

In addition, Hsu et al. (Hsu et al. 2014) and Kamensky et al. (Kamensky et al. 2015) developed fluid-structure interaction simulations of a bioprosthetic heart valve immersed in the lumen of a flexible artery wall under dynamic loading. They considered an isotropic St. Venant–Kirchhoff material, which assumes a linear stress–strain relationship, for the leaflets. The peak of maximum in-plane leaflet principal Green strain was 0.483 in the commissures at the peak of diastole. Recently, Hsu et al. (Hsu et al. 2015) combined an isotropic Fung model with a neo-Hookean model to capture the exponential stiffening behavior of soft tissues in the fluid-structure interaction simulations. The peak of maximum in-plane principal Green strain diminished significantly to 0.319 compare to the St. Venant–Kirchhoff material used in the previous study.

3.4.3 Out-of-plane Material Properties of Soft Tissue

Biaxial mechanical evaluations of chemically treated bovine pericardium tissues have shown an anisotropic mechanical behavior (Sacks and Chuong 1998) and (Sacks 2000). To implement the tissue anisotropy, Sun et al. (Sun, Abad, and Sacks 2005, Sun and Sacks 2005a) incorporated a seven parameter modified Fung model into the ABAQUS through its user subroutine UMAT to determine leaflet stress distribution of a pericardial bioprosthesis under quasi-static loading condition. The modified two-dimensional Fung model only incorporated the in-plane material parameters, as shown in Equation 3.11. The material parameters were estimated by fitting the model to experimental biaxial data. Under a quasi-static pressure of 120 mmHg, the highest leaflet stress region was observed in the vicinity of commissures with a maximum principal stress of 0.92 MPa. Unlike the quasi-static loading, under dynamic loading, the simplified in-plane Fung material model

resulted in physiologically unrealistic crimping of the leaflets in the free edge and belly regions (Kim et al. 2007). To solve the problem, Kim et al. (Kim et al. 2007), (Kim et al. 2008) included a bending moment in the simulation that was calculated based on an isotropic moment-curvature relationship. In three-dimensional FE simulations as presented here, although the out-of-plane normal and shear stresses of shell elements in FE simulations are zero, the out-of-plane coefficients related to strains of E_{13} and E_{23} have a constructive role to impose convexity on the material parameter tensor.

Lack of three-dimensional constitutive models for soft tissue limits the effectiveness of computational simulations. To compare the results from the optimized properties to the initial material properties, we would like to discuss about two recent studies in which arbitrary (random) values were used for the out-of-plane material coefficients. First, (Jermihov, Jia, Sacks, Gorman, Gorman III, et al. 2011) used the following anisotropic Fung constitutive model in their computational study. The authors used random small values for the out-of-plane coefficients in related to strains of E_{13} and E_{32} in the Fung model.

$$\mathbb{b}_{\text{anisotropic (Jermihov et al.,2011)}} = \begin{bmatrix} 49.558 & -3.124 & 24.779 & -0.002 & 24.779 & -0.004 \\ & 5.287 & -1.56 & -0.01 & -1.56 & -0.02 \\ & & 24.779 & -0.002 & 24.779 & -0.002 \\ & & & 8.02 & -0.002 & 8.016 \\ & & \text{Symmetric} & & 24.779 & 8.016 \\ & & & & & 16.031 \end{bmatrix}$$

Second, (Xuan et al. 2017) used the following orthotropic Fung model in ABAQUS to simulate TAVs. In-plane material coefficients were obtained from biaxial tensile tests and an arbitrary value of 0.01 was used for the out-of-plane material coefficients.

$$\mathbb{b}_{\text{orthotropic(Xuan et al.,2017)}} = \begin{bmatrix} 62.28 & 26.97 & 0.01 & 0 & 0 & 0 \\ & 132.12 & 0.01 & 0 & 0 & 0 \\ & & 0.01 & 0 & 0 & 0 \\ & & & 0.01 & 0 & 0 \\ & \text{Symmetric} & & & 0.01 & 0 \\ & & & & & 31.14 \end{bmatrix}$$

To show the importance of characterization of 3D valve-specific mechanical properties of the leaflets, we used the 9 coefficients of the orthotropic model presented by (Xuan et al. 2017) in the surgical valve model. As shown in Fig. 3.13, considering arbitrary small coefficients leads to dynamic instability and wrinkling of the leaflets in FE model, especially in the opening phase of the valve. Therefore, as discussed in this chapter, employing optimized material parameters to describe valve-specific mechanical behavior of the leaflets is essential in computational simulations.

3.4.4 Viscous Damping Coefficient

It has been demonstrated that neglecting viscous damping effects of blood flow in the finite element simulation of heart valves may cause instability. A wide range of viscous damping coefficients have been reported in the literature; however, the coefficients were not fully validated for bioprosthetic heart valves. Kim *et al* (Kim et al. 2008) considered a damping constant of 18.9 g/s in their dynamic FE analysis of bioprosthetic heart valves. However, the damping coefficient was reported in the literature for kinematic modeling of left ventricular filling (Oommen, Karamanoglu, and Kovács 2002). In a separate study, Patterson *et al.* (Patterson, Howard, and Thornton 1996) considered a damping coefficient of 0.995 in FE simulations of bicuspid bioprostheses in OASYS-LS DYNA3D (LSTC, Livermore, CA). The value was chosen by inexplicit comparison of leaflet displacements between FE model and pulse duplicator measurements. In addition, Jermihov *et al.*

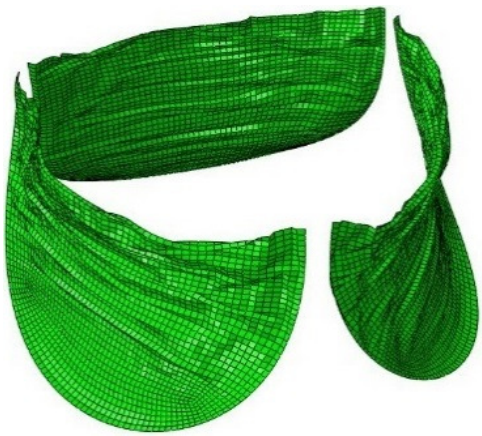

Figure 3.13: A sample of dynamic instability in FE model because of using random small values for the out-of-plane coefficients.

(Jermihov, Jia, Sacks, Gorman, Gorman, et al. 2011) applied a mass-proportional damping coefficient of 90,000 to the damping matrix to account for blood interactions with the surface of a congenital bicuspid aortic valve. However, no evidence was provided for validation the damping coefficient. Recently, Kamensky et al. (Kamensky et al. 2015) used damping constant per unit area of 80 g/(cm²s) in their bioprosthetic valve simulations to ensure that the valve opens at a physiologically reasonable time scale. Nevertheless, again no validation was provided for the damping coefficient. In this study, however, the viscous damping coefficient was estimated through inverse FE optimization analysis.

3.4.5 Viscoelasticity of Soft Tissue

Biological soft tissues are viscoelastic in nature and their mechanical behavior varies in response to the rate of deformation. Chemically treated bovine pericardium possess nonlinear viscoelastic behavior particularly in large deformations (Mavrilas et al. 2005), (Trowbridge and Crofts 1987) and (Lee et al. 1994). Lee et al. (Lee et al. 1994) used a servo-hydraulic testing system to evaluate the behavior of chemically treated bovine

pericardium under loading frequencies at 0.01, 0.1, 1, and 10 Hz. The corresponding strain rates of the samples in the testing protocol were approximately 0.45, 4.5, 45, and 400 1/s, respectively. The large deformation stress-strain response was nearly unaffected by loading frequency during tension, although the stress-strain curve was shifted slightly to the left at 10 Hz. Nevertheless, a significant increase in hysteresis was observed in stress-strain studies at 10 Hz compared to the lower frequencies. In our simulation, strain rate distribution was not uniform throughout the leaflets, and the maximum principle in-plane strain rate reached to 403 1/s during systole and 114 1/s during the diastole. Hence, by comparing our results with those of Lee et al. (Lee et al. 1994), the pseudo-elastic Fung model is a reasonable material model to use to simulate bovine pericardial leaflets. However, material parameters estimation should be based on the inverse parameter estimation rather than parameter fitting to experimental biaxial data in order to closely approximate the viscoelastic behavior of bovine pericardial leaflets during dynamic loading.

3.4.6 Difficulties of Biaxial Tests

Direct use of material parameters obtained from biaxial tests in numerical simulation of non-linear anisotropic materials is not appropriate due to technical difficulties in interpreting biaxial test results (Eilaghi et al. 2009, Nolan and McGarry 2016, Waldman and Lee 2002). Biaxial testing is commonly used to investigate the mechanics of anisotropic soft tissues and biomaterials. Test specimens are commonly attached to the machine actuators using either clamps(Kanyanta and Ivankovic 2010, Waldman and Lee 2002), or rakes/sutures (Humphrey, Strumpf, and Yin 1990, Waldman and Lee 2002).

Nolan and McGarry (Nolan and McGarry 2016) recently described the fundamental problem that exist with the calculation of material stress from measured force in standard biaxial tests using clamps. They showed that localized unmeasured shear forces that occur at the clamps has significant implications for the calculation of material stress from simplified force–equilibrium relationships. Furthermore, they demonstrated that the calculation of a general correction factor for non-linear anisotropic materials that accounts for material non-linearity and anisotropy is not feasible. Likewise, the difficulties associated with sutured specimens have been demonstrated previously. Uniformity of the strain and stress fields is highly sensitive to the number of suture attachment points, the regularity of their spacing and alignment (Eilaghi et al. 2009, Sacks 2000). Additionally, it is unclear whether there is full recruitment of collagen fibers throughout the specimen when sutures are used (Billiar and Sacks 2000, Waldman and Lee 2002). Therefore, a rigorous inverse FE analysis of biaxial tests should be performed to determine material stress distribution and calibrate constitutive law material parameters in biaxial tests.

3.4.7 Particle Swarm Optimization (PSO) Algorithm

In this chapter, we used particle swarm optimization (PSO) algorithm, a global optimization method that is well suited for biomechanical problems(Schutte et al. 2005). This method has received increasing attention among other optimization algorithms due to its simplicity and having few algorithm parameters to control the convergence behavior. In addition, the PSO algorithm is a derivative free method that is less sensitive to objective functions as well as design variable scaling (Kumar and Minz 2014, Schutte et al. 2005, Schutte et al. 2004). However, the method possesses an important limitation; the PSO often

converges more slowly than the other global optimization methods such as genetic algorithm and sequential quadratic programming. Furthermore, biomechanical optimization problems are nonlinear and multiple local minima may exist. Therefore, to obtain a reliable solution, we utilized a two-step global optimization method in this chapter. The lower and upper bounds of the optimization variables were selected based on the initial values that were obtained from biaxial stretching tests of bovine pericardium samples. Therefore, by choosing appropriate initial values, the probability of reaching a global optimal solution that is physically feasible will be highly increased.

3.4.8 Study Limitations

Although intra-specimen and inter-specimen variations exist in mechanical properties of bovine pericardium(Sacks, Chuong, and More 1994), variability in the material properties of the three leaflets was not considered in the simulations to reduce computational cost. Furthermore, bioprosthetic leaflet motion with respect to the center of the valve was analyzed and an average distance value was used to match computational results with the experiment data. However, simultaneous matching of all the three leaflets with experimental data can be implemented in the optimization procedure. In addition, in this chapter, we used a two-step global optimization method based on the equibiaxial test data of bovine pericardium samples and by matching the middle point distance of leaflets in the FE simulation with the experimental measurements in the pulse duplicator. Although, a good agreement between the experimental data and FE simulation results was obtained during valve opening and closing, utilizing other experimental techniques such as high-speed dynamic strain measurement by advanced 3D photogrammetry would improve

the uniqueness of the solution. Finally, a Rayleigh damping coefficient was introduced to the simulations to mimic viscous damping effects of surrounding fluid. However, a more accurate simulation to consider blood flow shear stresses on the surface of the leaflets may involve fluid–structure interaction simulation.

3.5 Conclusions

In summary, we presented an approach to obtain material parameters of a pericardial surgical bioprosthesis based on generalized nonlinear Fung-type constitutive model under dynamic loading conditions. Using the inverse parameter estimation process, 3D generalized anisotropic and orthotropic Fung model parameters were estimated for the bioprosthetic leaflets. Furthermore, the Rayleigh damping coefficient that was introduced to FE simulations to simulate viscous damping effects of surrounding fluid was assessed. The generalized anisotropic model accurately simulated the leaflet deformation and coaptation during valve opening and closing. During systole, high stress regions were primarily observed at the boundary edge; however, during diastole, high stress regions were primarily observed in the commissures. The maximum leaflet stress at the peak of systole was significantly more than the maximum principal stress during diastole. Also, we presented a step-by-step instruction for employing commercial FE software packages to non-invasively estimate three-dimensional anisotropic material parameters of soft tissue and biomedical materials. Commercial FE software packages are widely available and can be utilized effectively for quantitative description of surgical and transcatheter heart valves to better understand mechanism of tissue degeneration and improve long-term valve durability.

CHAPTER 4: EFFECT OF REDUCED TISSUE THICKNESS IN TAVS

4.1 Introduction

Tissue heart valves in general degenerate through two distinct yet possibly synergistic processes: 1) calcification and 2) mechanical damage (Schoen 2012). TAV technology uses the same leaflet tissue as surgical bioprostheses, and therefore it can be postulated that the failure mechanisms in TAVs are similar to the surgical bioprostheses. Leaflet calcification is responsible for a significant percentage of surgical bioprosthetic valve degeneration. Calcification appears to originate mainly within residual connective tissue cells that were not removed by chemical pretreatment (Schoen 2012). Collagen and elastin fibers can also work as nucleation sites (Bailey et al. 2003, Schoen and Levy 2005). Furthermore, it is broadly accepted that mechanical stress accelerates calcification by disrupting tissue structure. It has been demonstrated that high stress regions correlate with regions of calcification in stented surgical bioprostheses (Schoen and Levy 1999a). Besides calcification, it has been demonstrated that mechanical damage due to fatigue could be a cause of failure in surgical bioprostheses (Sacks and Schoen 2002b). Due to tissue fixation procedure, the entire extracellular matrix is vastly bonded which eliminates the

ability for fibers to slide relative to each other (Sacks et al. 2006). As a result, non-calcific damage is high likely due to shearing and fiber debonding (Sacks and Schoen 2002b). It has been demonstrated that high stress regions in stented surgical bioprostheses correlate with regions of mechanical deterioration (Ferrans et al. 1978b, Sacks and Schoen 2002b).

TAVs are typically implanted using either the transfemoral or non-transfemoral approaches (left ventricular apex, aorta, axillary, carotid arteries) depending on arterial iliofemoral suitability. One of the most important design constraints in transfemoral TAVI is the diameter size of the delivery catheter. The larger diameter of the delivery catheter may increase the risk of vascular injuries and the occurrence of arterial dissection or perforation (Borz et al. 2014, Koehler et al. 2015). In the first generation of TAVs studied in clinical trials, e.g. the Edwards SAPIEN valve evaluated in the PARTNER clinical trial, 22-Fr sheath was used for 23mm valve and 24-Fr sheath was used for 26mm valve in the transfemoral approach. In the French sizing system, 3 Fr equals 1mm. With technological advances, newer low-profile systems were designed which were suitable for smaller catheter delivery systems (e.g., 20/23/26/29mm Edwards SAPEIN XT requires 16-/16-/18-/20-Fr, respectively, and 23/26/29/31mm Medtronic CoreValve devices are inserted through an 18-Fr Cook sheath). Among the new designs recently released, a further reduction in delivery profile has been observed (e.g., Edwards SAPIEN 3 valve requires 14-/14-/16-Fr for 23/26/29mm valve sizes respectively, and the 23/26/29 mm Medtronic Evolute R devices require 14-Fr sheath).

Although low-profile systems reduce the risk of vascular injuries and improve catheter maneuver for precise placement of TAV devices, the cross-sectional area reduction causes more constraints in the design of TAV devices. To use smaller cross-sectional areas of delivery catheters, the valve must be crimped into a small diameter which is less than the delivery catheter size. It has been shown that crimping may induce structural changes at the surface and deep layers of TAV leaflets (Alavi, Groves, and Kheradvar 2014a, Abbasi and Azadani 2015, Khoffi and Heim 2015, Dvir 2016). Therefore, to accommodate TAVs to the miniaturized catheters and minimize structural damage due to crimping, the pericardial leaflet thickness of a TAV needs to be reduced to a value which is typically thinner than a surgical valve leaflet thickness. For example, bovine pericardial leaflet thickness of a 23mm Carpentier-Edwards PERIMOUNT Magna surgical bioprosthesis is 0.4-0.55 mm, whereas for a similar size TAV the leaflet thickness may be in range of 0.14-0.18 mm (Li and Sun 2010). Such reductions in the thickness of leaflets may lead to a decrease in tissue strength to the physiological dynamic loading, and over time can negatively influence long-term valve durability.

The impact of thickness reduction on leaflet stress and strain distribution under dynamic physiological loading condition and in the long run on the long-term valve durability is not known. In the absence of long-term valve durability data, accurate structural simulations and computational modeling become an integral part of the evaluation. Therefore, the main objective of this chapter was to use finite element (FE) simulation to determine the impact of leaflet thickness on TAV leaflet stress and strain distribution under dynamic loading condition. Leaflet mechanical properties in this study

were characterized by a three-dimensional anisotropic nonlinear Fung-type constitutive model to accurately describe tissue mechanical behavior under physiological loading.

4.2 Methods

4.2.1 Constitutive Modeling

Accurate constitutive models are needed for the purpose of characterizing material behavior of soft tissue in computational modeling. Most native and chemically treated biological soft tissues are viscoelastic in nature, and often are considered as pseudo-hyperelastic materials (Fung 2013a). A material can be defined as hyperelastic if there is a stored (strain) energy function Ψ which is exclusively a function of the deformation gradient tensor. Fung strain-energy function has become a widespread strain energy function to describe nonlinear mechanical behavior of numerous biological soft tissues (Fung, Fronek, and Patitucci 1979). A generalized Fung strain-energy function in three-dimensional space is in the form of

$$\Psi = \frac{c}{2}\left(e^{\mathcal{Q}} - 1\right) + \frac{1}{\mathcal{D}}\left(\frac{{\mathcal{J}_{el}}^2 - 1}{2} - \ln J_{el}\right) \tag{4.1}$$

Details of the generalized Fung strain-energy function have been previously described in chapter 3. The number of components of $\mathbb{b}$ that have to be determined is similar to the elasticity tensor, namely 21 independent components for a three-dimensional generalized anisotropic Fung strain-energy function as shown below.

$$\mathbb{b}_{\text{anisotropic}} = \begin{bmatrix} b_{1111} & b_{1122} & b_{1133} & b_{1123} & b_{1113} & b_{1112} \\ & b_{2222} & b_{2233} & b_{2223} & b_{2213} & b_{2212} \\ & & b_{3333} & b_{3323} & b_{3313} & b_{3312} \\ & & & b_{2323} & b_{1323} & b_{1223} \\ & & \text{Symmetric} & & b_{1313} & b_{1213} \\ & & & & & b_{1212} \end{bmatrix} \tag{4.2}$$

4.2.2 Heart Valve Tissue Mechanical Properties

The majority of experimental testing used to estimate mechanical properties of soft tissue such as in-plane biaxial testing cannot capture the out-of-plane displacements required to determine three-dimensional anisotropic mechanical properties of tissue (Holzapfel and Ogden 2008). We have previously shown the use of inverse FE analysis to determine three-dimensional anisotropic mechanical properties of bovine pericardial leaflets of a surgical bioprosthesis under dynamic physiological loading condition (Abbasi et al. 2016). Briefly, a two-step global optimization technique was utilized by first simulating the equibiaxial test data of bovine pericardium samples to obtain initial estimate values for the out-of-plane material coefficients, and second by matching the middle point distance of bioprosthetic valve leaflets in the FE simulation with experimental measurements of bioprosthetic leaflet motion in a custom-built pulse duplicator. A heart rate of 70beat/min mean aortic pressure of 100mm-Hg, and cardiac outputs (COs) of 5.0, 3.5, and 2.0L/min were used as the pulse duplicator input parameters.

Using the inverse parameter estimation process previously described in chapter 3, three-dimensional generalized anisotropic Fung model parameters were estimated for the bioprosthetic leaflets (Equation 4.3). Furthermore, the Rayleigh damping coefficient (α), that was introduced to FE simulations to simulate viscous damping effects of surrounding fluid, and c, were determined, i.e. α = 2,148 (1/s) and c = 24.62 KPa for CO=5 L/min. In

addition, the α was determined as 1007 and 816 (1/s) for cardiac outputs of 3.5 L/min and 2 L/min, respectively. The generalized anisotropic Fung model accurately simulated the leaflet deformation and coaptation during valve opening and closing (Abbasi et al. 2016).

$$\mathbb{b}_{\text{anisotropic}} = \begin{bmatrix} 62.95 & 36.39 & 54.14 & 17.13 & 45.45 & 41.72 \\ & 61.88 & 45.64 & 68.15 & 67.97 & 23.42 \\ & & 65.98 & 38.70 & 63.95 & 56.17 \\ & & & 14.40 & 16.26 & 27.56 \\ & & \text{Symmetric} & & 42.57 & 17.61 \\ & & & & & 60.66 \end{bmatrix} \quad (4.3)$$

Using the obtained material properties, a good agreement between the experimental data and FE simulation results was obtained during valve opening and closing in CO=5 L/min (Fig. 4.1A). The simulation results were further validated for CO of 3.5 and 2.0 L/min and a good agreement was observed between leaflet displacement obtained from the experimental tests and FE simulations during valve opening and closing (Fig. 4.1B). Details of Rayleigh damping coefficient impact on heart valve tissues have been previously described (Abbasi and Azadani 2015, Abbasi et al. 2016). There are few papers in literature in which generalized anisotropic Fung model was used to characterize the three-dimensional anisotropic bovine pericardium mechanical properties in ABAQUS software (Jermihov, Jia, Sacks, Gorman, Gorman III, et al. 2011, Xuan et al. 2017). They considered a bunch of arbitrary or very small values for material coefficients which could not be found by biaxial stretching testing.

4.2.3 Finite Element Modeling

In this study, the three-dimensional geometry of the TAV was selected based on the Edwards SAPIEN XT valve design. Since the TAV leaflet geometry is similar to that of

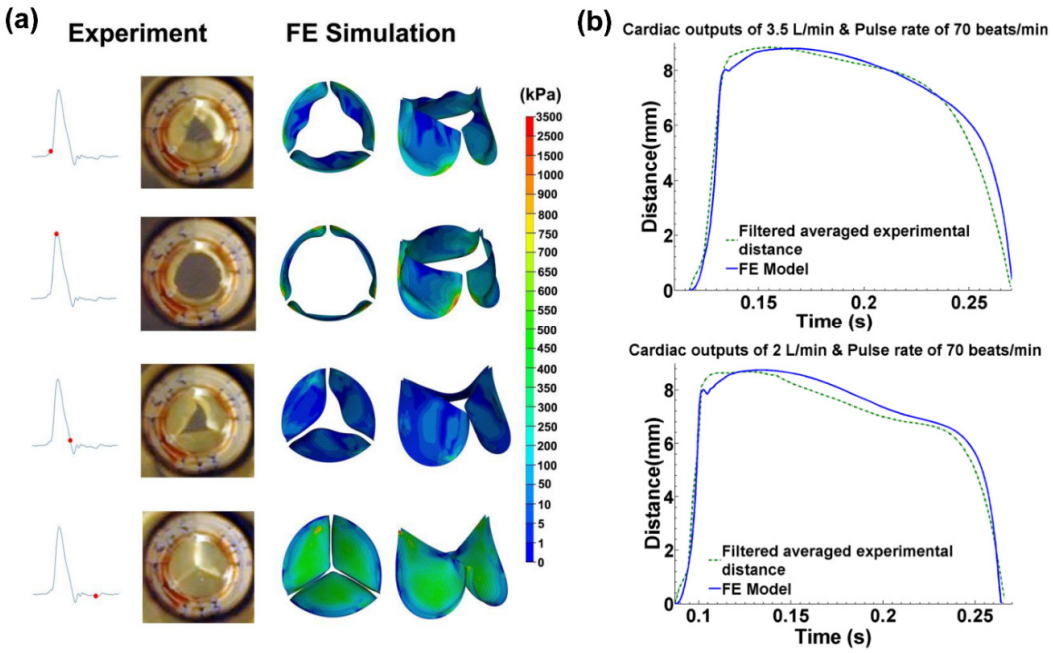

Figure 4.1: (A) Comparison of in-vitro leaflet motion with FE simulations throughout a complete cardiac cycle for cardiac output 5 L/min. (B) Leaflets displacement during systole for cardiac outputs of 3.5 and 2.0L/min. A good agreement was observed between the experimental data and FE simulations, adapted from (Abbasi and Azadani 2017).

the 23mm Carpentier-Edwards PERIMOUNT Magna bioprosthetic aortic valve, we obtained the leaflet geometry by three- dimensional scanning of the surgical valve.

Details of the Surface reconstruction of the leaflets, making the mesh pattern and FE models have been previously described in chapters 2 and 3.

Due to the relatively high stent radial force, leaflets were only modeled in the simulations and the stent was considered to be rigid. The leaflet thickness was assumed uniform and constant throughout the leaflet. To determine the impact of the thickness reduction on leaflet stress and strain distribution, five different thickness values were considered in the FE simulations, namely 0.18, 0.2, 0.3, 0.4, and 0.5mm. A transvalvular pressure gradient waveform obtained from the in-vitro test in the pulse duplicator was applied to the leaflets under dynamic loading (Fig. 4.2). Details of the in-vitro

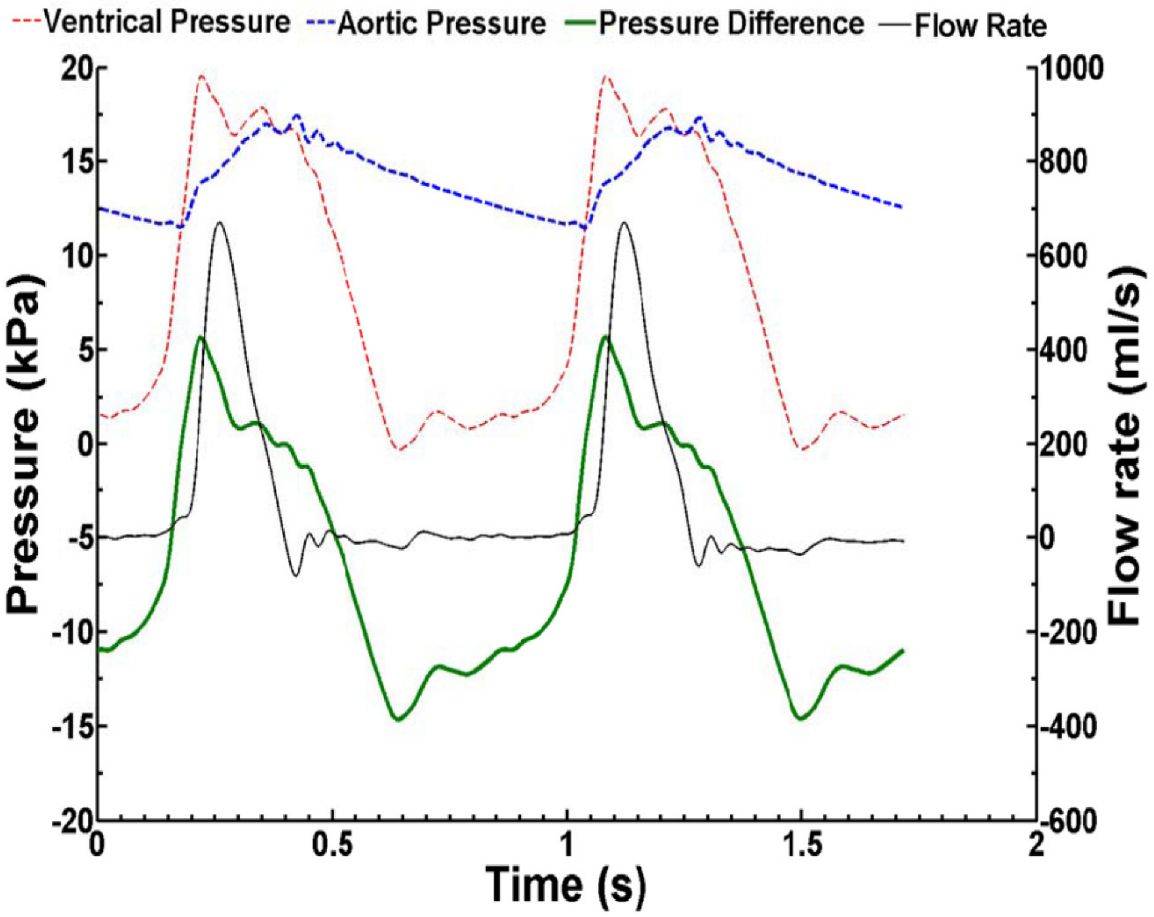

Figure 4.2: Bioprosthetic pressure and flow rate waveforms, adapted from (Abbasi and Azadani 2017).

experimental testing procedure have been previously described in chapters 2 and 3. In the dynamic analysis, density of 1,100 kg/m³ was used for the leaflet tissue. Moreover, a Rayleigh damping coefficient was considered in the simulations to mimic viscous damping effects of surrounding fluid. In post-processing, the surface of the leaflets was divided into four main zones as shown in Fig. 4.3 to evaluate stress and strain regions: zone 1: commissures; zone 2: free edge; zone 3: fixed edge; and zone 4: belly region.

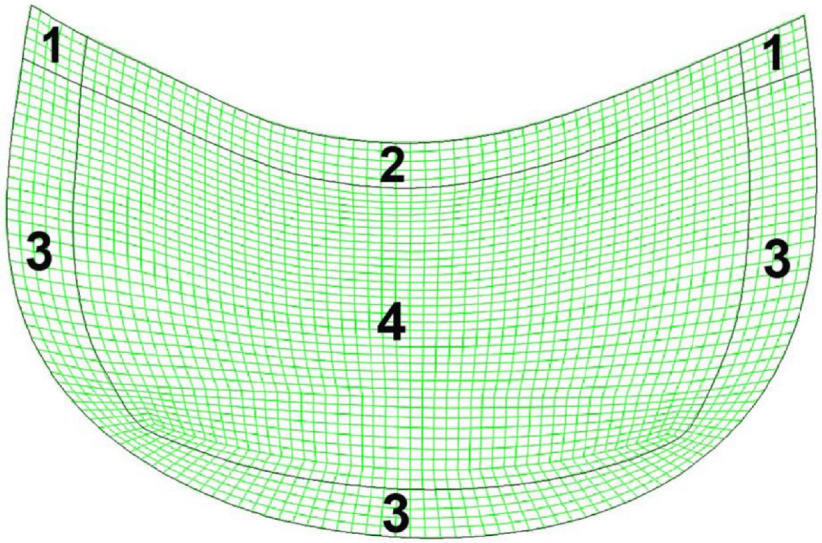

Figure 4.3: Surface of the leaflets were divided into four main zones for post-processing, adapted from (Abbasi and Azadani 2017).

4.3 Results

4.3.1 Leaflet Stress Distribution

The maximum principal stress distribution of the TAV leaflets at the peak of systole and at the peak of diastole (i.e., the largest pressure gradient across the valve) is shown in Figure 4.4 for leaflet thicknesses ranging from 0.18mm to 0.5mm. At the peak of systole, high stress regions were mainly observed at the leaflet fixed edge (zone 3). The maximum principal stress increased significantly with decreasing the leaflet thickness. During diastole, however, high stress regions were primarily observed at the commissures (zone 1). The maximum principal stress at the commissures of the leaflets increased as the leaflet thickness decreased. Furthermore, the maximum principal stress in the belly of the leaflets increased in the diastole with decreasing the leaflet thickness. Localized high stress regions were observed in the belly region as the leaflet thickness decreased due to bending of the tissue at the base of the leaflet contact area (Figure 4.4).

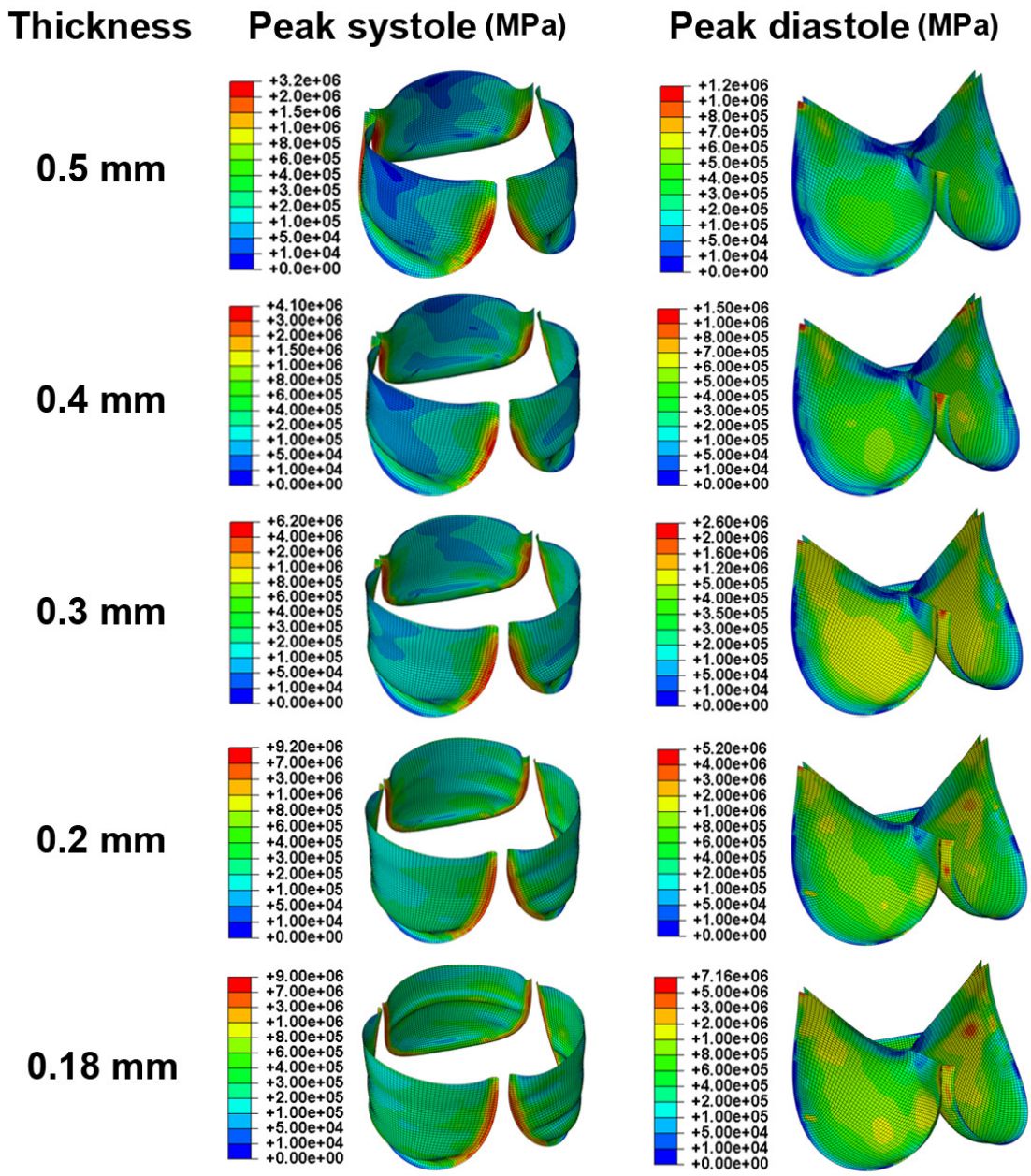

Figure 4.4: 1st principal stress of TAV leaflets at the peak of systole and at the peak of diastole for various leaflet thicknesses, adapted from (Abbasi and Azadani 2017).

Figure 4.5 shows the peak of maximum principal stress in the leaflets versus thickness at the peak of systole and diastole. Simulation results showed that the peak maximum

principal stress was increased at the peak of systole in an exponential manner from 3.17MPa to 9.17MPa after reducing the thickness from 0.5mm to 0.18mm. Furthermore, the peak maximum principal stress at the peak of diastole was increased from 1.17MPa to 7.11MPa in an exponential manner after reducing the thickness from 0.5mm to 0.18mm. In addition, stress history of the four zones was obtained during one cardiac cycle for all the thicknesses. As shown in Fig. 4.6, the local maximum stress history in all the zones was changing considerably during one cardiac cycle. The stress variation is important to be considered in fatigue assessment of the leaflets. At the peak of systole, a local maximum stress was observed in the stress history at the commissures (zone 1), the fixed edge (zone 3), and the belly region (zone 4). During diastole, an elevated stress level was observed in all the regions of the leaflets. The maximum principal stress of the leaflets increased as the leaflet thickness decreased.

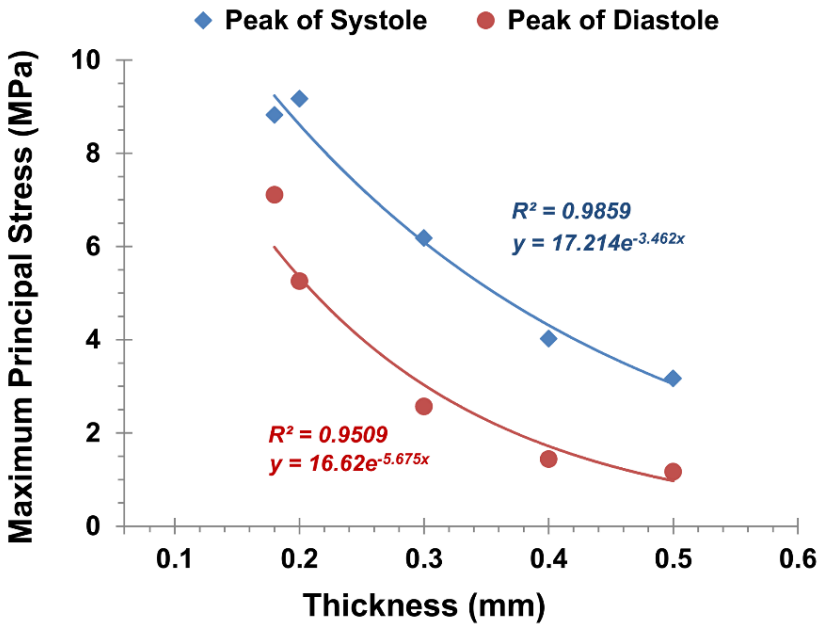

Figure 4.5: Maximum principal stress of TAV leaflets versus leaflet tissue thickness, adapted from (Abbasi and Azadani 2017).

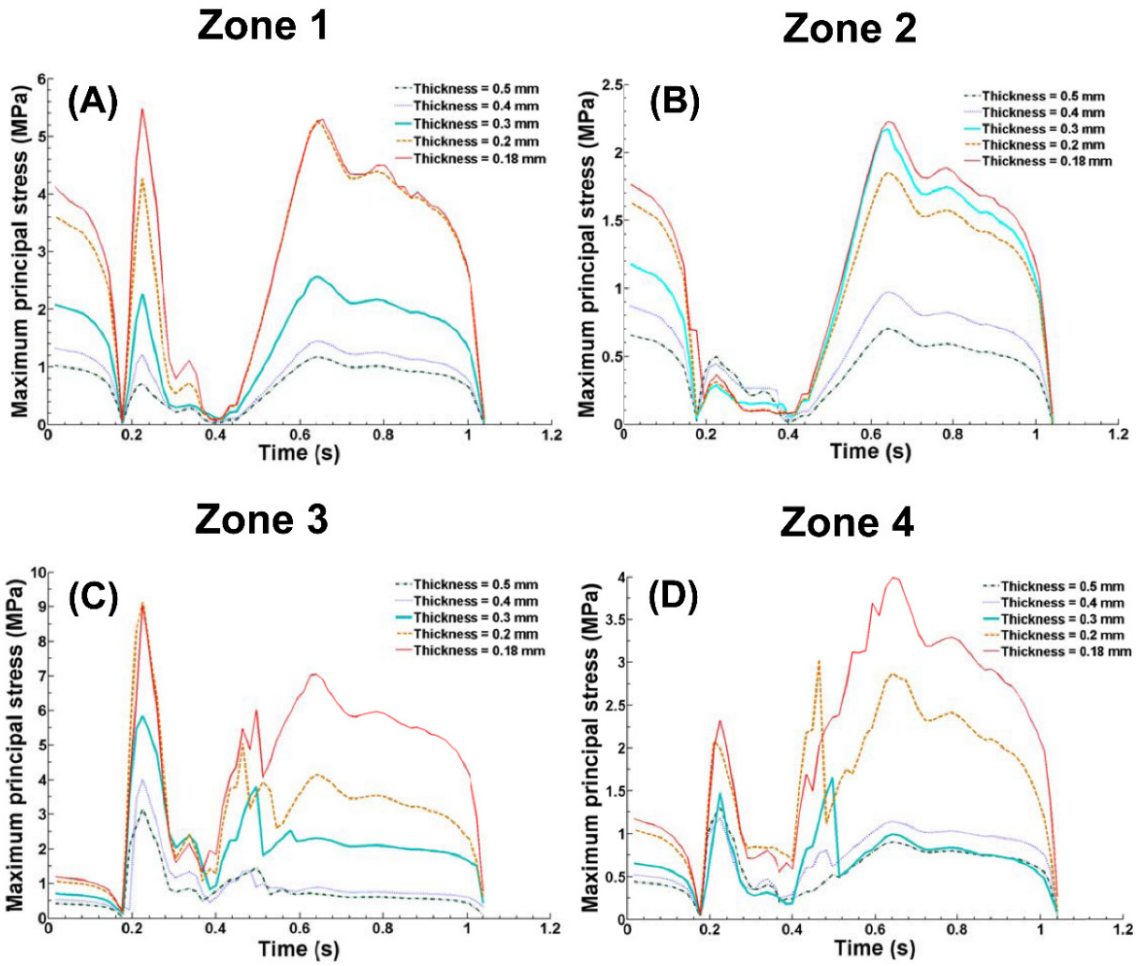

Figure 4.6: (A) The peak of 1st principal stress of TAV leaflets versus time in zone-1 (commissures). (B) The peak of 1st principal stress of TAV leaflets versus time in zone-2 (free edge). (C) The peak of 1st principal stress of TAV leaflets versus time in zone-3 (fixed edge). (D) The peak of 1st principal stress of TAV leaflets versus time in zone-4 (belly region), adapted from (Abbasi and Azadani 2017).

4.3.2 Leaflet Strain Distribution

Figures 4.7 and 4.8 show the distribution of normal and shear logarithmic strain (LE) components ($LE_{11}, LE_{22}, LE_{12}, LE_{33}$) within the leaflets of the TAV at the peak of systole and at the peak of diastole. The 1-, 2-, and 3-directions were aligned with circumferential, radial, and normal directions of the leaflets, respectively. As presented in Figure 4.7, TAV leaflet strain distributions at the peak of systole were dependent on the thickness of the

TAV leaflets. After employing thinner thicknesses in the FE simulation, the absolute value of in-plane and out-of-plane normal strain components were increased. The magnitude of shear strain (LE_{12}) was comparable to the normal in-plane strain valves at the peak of systole in all the simulations. Moreover, considerable negative normal strain values (LE_{33}) were observed at the leaflet fixed edge at the peak of systole due to deformation and tissue incompressibility. Similar to the peak of systole, at the peak of diastole, the absolute value of in-plane and out-of-plane strain components of the leaflets increased as the leaflet thickness decreased (Figure 4.8).

A considerable change in thickness (LE_{33}) and shear strain (LE_{12}) was observed in the leaflets, indicating the importance of using the three-dimensional anisotropic constitutive model in the simulations. In contrast to stress distribution which increased significantly as the thickness decreased, strain distribution did not change considerably as the thickness decreased due to the non-linear stress-strain characteristics of the soft tissue.

4.4 Discussion

4.4.1 Summary

In this chapter, we examined the impact of leaflet thickness on TAV leaflet stress and strain distribution under dynamic loading conditions. A generalized anisotropic Fung hyperelastic constitutive model was used to model bovine pericardial leaflets of a 23mm TAV. Through dynamic FE simulations, we found that the highest stress values were found during the systole in the leaflet fixed edge. On the other hand, at the peak of diastole, high stress regions were mainly observed in the commissures. The peak stress was increased by 178% and 507% within the leaflets after reducing the thickness of 0.5mm to

0.18mm at the peak of systole and diastole, respectively. In contrast to the stress distribution, the changes in the logarithmic strain components were not as significant as the stress distribution due to the non-linear stress-strain characteristics of the leaflets. All of the strain components were increased by less than 25% after reducing the thickness from0.5mm to 0.18mm, except for the in-plane shear strain component which was increased by 67%.

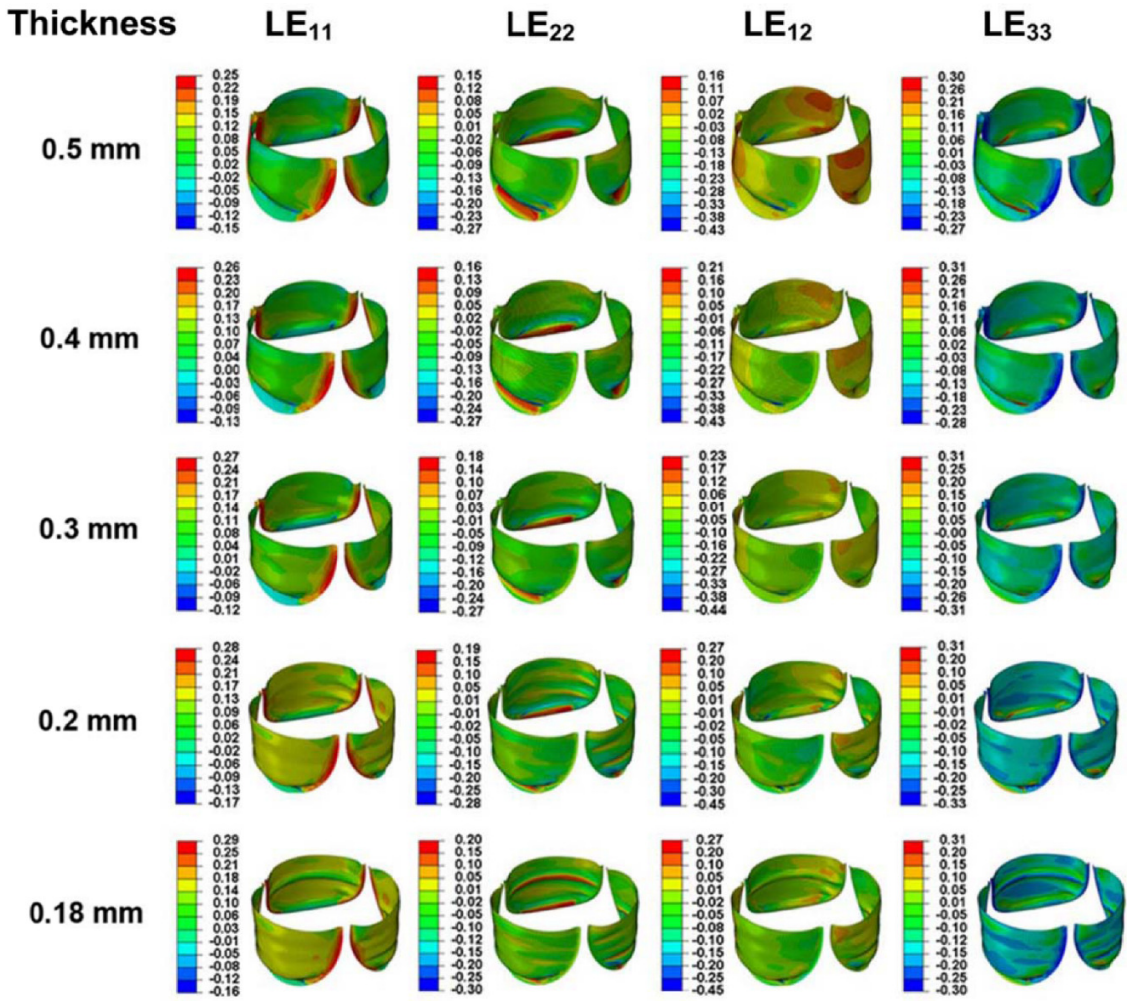

Figure 4.7. Distribution of normal and shear logarithmic strain components of TAV leaflets at the peak of systole for various leaflet thicknesses, LE_{11}: logarithmic strain in circumferential direction, LE_{22}: logarithmic strain in radial direction, LE_{12}: shear logarithmic strain, LE_{33}: logarithmic strain in normal direction, adapted from (Abbasi and Azadani 2017).

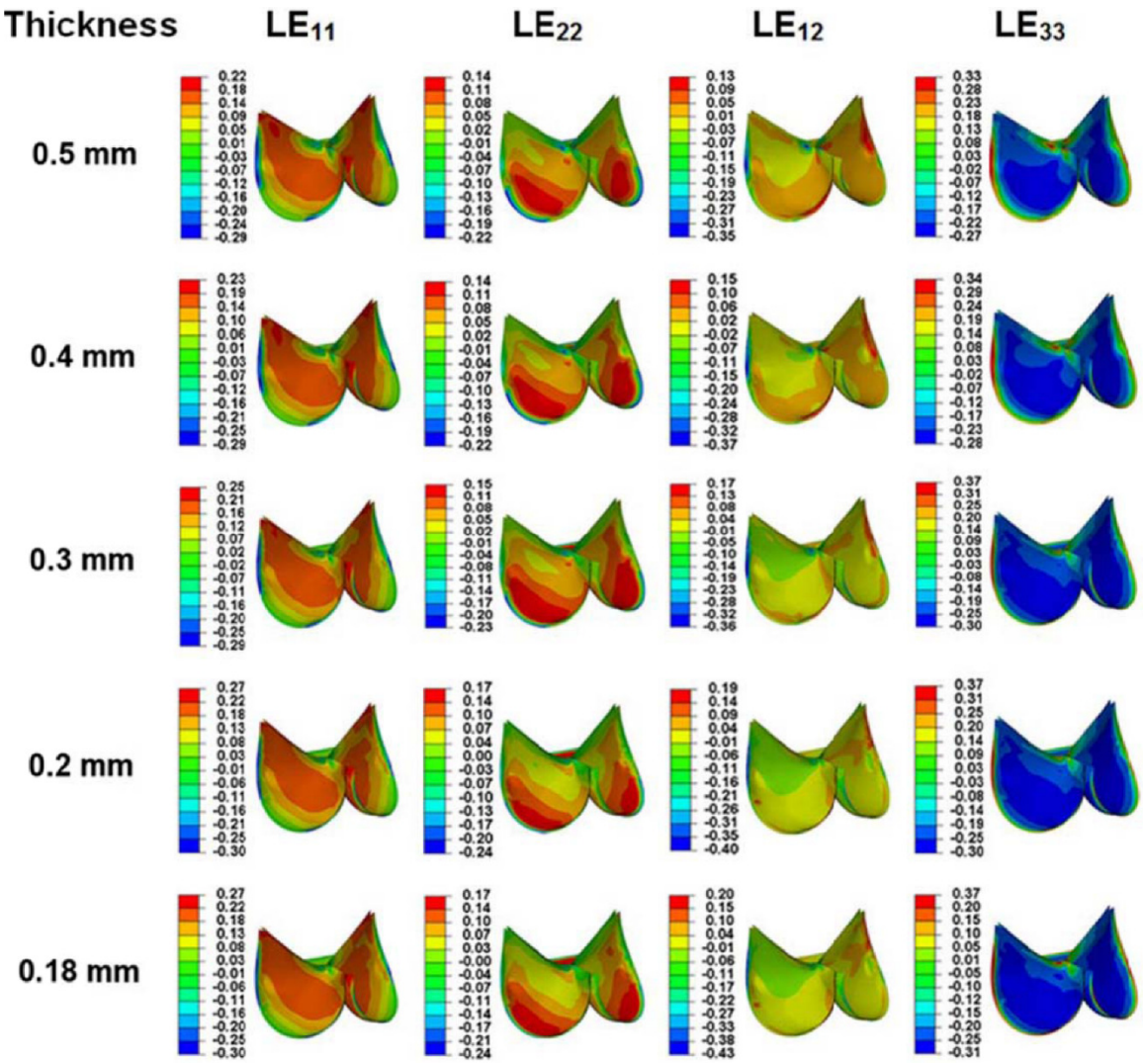

Figure 4.8: Distribution of normal and shear logarithmic strain components of TAV leaflets at the peak of diastole for various leaflet thicknesses, LE_{11}: logarithmic strain in circumferential direction, LE_{22}: logarithmic strain in radial direction, LE_{12}: shear logarithmic strain, LE_{33}: logarithmic strain in normal direction, adapted from (Abbasi and Azadani 2017).

4.4.2 Durability in TAVs

TAVR is uniquely different from surgical aortic valve replacement (SAVR) using bioprosthetic valves. TAVs are not sutured into place like surgical bioprostheses but crimped into delivery sheaths and re-expanded in the aortic annulus. In addition, TAV design is fundamentally different from surgical valves with thinner leaflets to fit within

delivery catheters. Recent randomized clinical trials have demonstrated TAVI was similar to SAVR in intermediate-risk patients with respect to the primary end point of death and disabling stroke, and superiority of transfemoral TAVI over SAVR (Leon et al. 2016b). With the data on intermediate-risk patients and the notion clinical trial showing equivalence of TAVI with SAVR in low-risk patients (Thyregod et al. 2015), TAVI with its percutaneous approach may dominate the SAVR market for the treatment patients with severe aortic stenosis. However, clinical data have durability demonstrated only to 10 years in few patients thus far, since most clinical trials were in patients >80 years old(Arora et al. 2017). In contrast, surgical bioprosthetic valves such as Carpentier-Edwards PERIMOUNT Magna Ease demonstrated excellent durability and hydrodynamic performance after an equivalent of 25 years in in-vitro accelerated durability tests (Raghav et al. 2016a).

4.4.3 Effect of Reduced Tissue Thickness on Leaflets Stress Distribution

Based on our dynamic FE simulations, higher stresses and strains have been witnessed within TAV leaflets due to using thinner leaflets compared to surgical bioprostheses. Therefore, TAVs can be expected to have reduced long-term durability compared to surgical valves. Previously, Li and Sun (Li and Sun 2010) performed a static simulation of a 23mm TAV under a static pressure-only loading condition of 120 mm-Hg. Bovine and porcine pericardium tissues were obtained from local abattoirs and were chemically treated with 0.625% glutaraldehyde. Mechanical properties of the tissue were obtained using a biaxial mechanical testing system. Subsequently, a two-dimensional Fung-type elastic model was used for constitutive modeling of the bovine and porcine pericardium

samples. The static FE simulation results showed that the highest stress regions on the valve leaflets were reported in the vicinity of the leaflet commissures. The peak of maximum principal stresses was reduced with the increase of leaflet tissue thickness by 36% and 59%, from the mean thickness of bovine pericardium samples (0.24 mm) and porcine (0.18 mm) pericardium samples to 0.35 mm, respectively. The peak of maximum principal stresses value for bovine and porcine pericardium samples with a thickness of 0.35 mm reached to 0.59 and 0.64 MPa, respectively. In addition, for the mean thickness of bovine pericardium samples (0.24 mm) and porcine (0.18 mm) pericardium samples, the peak of maximum principal stresses was 0.92 and 1.57 MPa. In this study, we examined the impact of leaflet thickness on TAV leaflet stress and strain distribution under dynamic loading conditions using three-dimensional anisotropic Fung model. Under dynamic loading, at the peak of systole, the highest stress region on the leaflets was found in the leaflet fixed boundary edge. During diastole, however, high stress regions were mainly observed at the commissures. Stress history diagrams of the leaflets were obtained for various thicknesses, necessary to be considered in fatigue assessment of the leaflets.

Although several constitutive models have been used to characterize mechanical properties of biological soft tissues under physiological loading conditions, only a few models were proposed as failure/damage models of soft tissue. In a pioneer work, Simo (Simo 1987) developed a fully three-dimensional finite-strain viscoelastic damage model based on irreversible thermodynamics with internal variables. Over the past decade, a few soft tissue damage models utilized the concept of Simo's model as the basis for their models (Rodríguez et al. 2006, Alastrué et al. 2007, Calvo et al. 2007, Peña 2011, Li and

Robertson 2009). In the models, soft tissue damage was dependent only upon the strain history and not on the number of loading cycles. Recently, Martin and Sun (Martin and Sun 2012) have proposed a phenomenological damage model to describe tissue fatigue damage of tissue heart valves due to strain history and number of loading cycles. Based on the fatigue model and static FE simulations, Martin and Sun reported that durability of TAVs may be considerably reduced under identical loading conditions compared to surgical valves to about 7.8 years (Martin and Sun 2015).

4.4.4 Study Limitations

In this chapter, leaflet mechanical properties were estimated through inverse FE optimization analysis of a 23mm Carpentier-Edwards surgical bioprosthesis with an average thickness of 0.513 mm (Abbasi et al. 2016). Alteration in mechanical properties of bovine pericardium leaflets may exist for various thicknesses. The thinner tissue specimens might be more compliant. Although the absence of thickness-specific material properties of the leaflets was considered as a limitation of the present work, considering reduced mechanical property values, even higher stress values is expected to be obtained in leaflets with reduced thickness. Therefore, the results of this study are claimed to be valid and not affected by the simplification. Finally, we assumed the same material properties in all three leaflets in order to reduce computational cost. However, intra-specimen and inter-specimen variations may exist in material properties of bovine pericardium as highlighted by Sacks et al. (Sacks, Chuong, and More 1994).

4.5 Conclusions

In summary, FE simulations were developed to study the impact of thickness reduction on leaflet stress and strain distributions. We found that TAV leaflet stress and strain distributions were dependent on the tissue thickness of the TAVs. By reducing TAV leaflet thickness to minimize the cross-sectional area of crimped TAVs, higher leaflet stress distribution is expected. Increased mechanical stress on TAV leaflets due to thickness reduction may lead to diminished long-term valve durability. As a result, by using thinner leaflets, TAV durability may not match with that of surgical bioprostheses.

CHAPTER 5: STRAIN MAPPING OF BIOPROSTHESES USING DIGITAL IMAGE CORRELATION

5.1 Introduction

To assess longevity of the currently available TAVs and develop the next generation of heart valve prostheses, in-depth comparison and assessment of strain and stress of the leaflets is essential. Numerous computational models have been developed to determine stress and strain distribution of the bioprosthetic heart valve leaflets under physiological loading conditions (Abbasi et al. 2016, Gunning, Vaughan, and McNamara 2014, Hsu et al. 2015, Martin and Sun 2015). In the computational simulations, considering robust and accurate constitutive models for the leaflets is of the utmost importance (Humphrey 2003, Holzapfel and Ogden 2009). As a result, experimental validation of the computational models should be an indispensable step to confirm the accuracy and reliability of the simulations (Abbasi et al. 2016). Due to the limited temporal and spatial resolution of the currently available imaging modalities in real-world in vivo clinical cases as applied to bioprosthetic heart valves, in-vitro experimental testing of the bioprostheses provides a viable alternative to characterize soft tissue mechanical properties and validate the computational simulations. High-resolution optical measurements can be regarded as an appropriate non-invasive in vitro measurement technique to assess the deformation of the leaflets and determine the strain field. A suitable and accurate optical measurement

technique is three-dimensional digital image correlation (DIC) technique which becomes more readily available and more widely used in experimental mechanics (Chu, Ranson, and Sutton 1985, Palanca, Brugo, and Cristofolini 2015, Rogge et al. 2013, Luyckx et al. 2014, Sun, Abad, and Sacks 2005). The DIC technique is particularly suited for determination of TAV leaflet deformation due to its high temporal and spatial resolution (Heide-Jørgensen et al. 2016).

The goal of this chapter was to perform a side-by-side comparison of leaflet displacement and strain fields of three commonly used bioprosthetic heart valves: (i) Carpentier-Edwards PERIMOUNT Magna surgical bioprosthesis, (ii) Medtronic CoreValve, and (iii) Edwards SAPIEN 3 using a high-resolution DIC system. The obtained results can be used to characterize the anisotropic material behavior of the leaflets and validate computational models of the commercially available bioprosthetic valves.

5.2 Materials and Methods

5.2.1 Bioprosthetic Heart Valves

In this chapter, three different bioprosthetic heart valves with comparable size were investigated (Fig. 5.1). The first bioprosthetic valve was a 25-mm Carpentier-Edwards (CE) PERIMOUNT Magna aortic heart valve (Edwards Lifesciences, CA, USA). The surgical bioprosthetic valve consists of bovine pericardium leaflets mounted on an Elgiloy frame.

The internal diameter of the frame is 24 mm. The second bioprosthesis was a self-expanding 26-mm Medtronic CoreValve (Medtronic, Minneapolis, MN, USA), constructed from porcine pericardial leaflets mounted on a self-expanding Nitinol stent.

The third bioprosthetic valve examined in this study was a 26-mm Edwards SAPIEN 3 (Edwards Lifesciences, Irvine, CA, USA). The TAV is made from bovine pericardial leaflets mounted on a balloon-expandable cobalt-chromium stent. The thicknesses of the bioprosthetic heart valve leaflets were measured using a Mitutoyo Digital caliper. The average thickness of the leaflets of the PERIMOUNT Magna, Medtronic CoreValve, and Edwards SAPIEN 3 bioprostheses was 0.56 mm, 0.43 mm, and 0.32 mm, respectively.

5.2.2 Digital Image Correlation System

For DIC measurements, graphite (synthetic powder, < 20µm, Sigma-Aldrich, St. Louis, MO) was applied to the top side of the leaflets to achieve a speckled pattern (Fig. 5.2). Graphite was used due to its negligible effect on the mechanical properties of soft tissue as compared to ink dyes, verified by planar biaxial testing of bovine pericardial patch. To create a suitable stochastic pattern, graphite was applied multiple times to the top side of the leaflets. Subsequently, the valves were stored in normal saline solution at the

Figure 5.1: (Left) 25-mm surgical Carpentier-Edwards PERIMOUNT Magna Pericardial bioprosthetic aortic valve. (Center) 26-mm self-expanding Medtronic CoreValve. (Right) 26-mm ballooned expandable Edward SAPIEN 3 transcatheter heart valve, adapted from (Abbasi et al. 2018a).

room temperature prior to the DIC measurements. All the DIC measurements were conducted in an in-vitro test setup comprised of an optically clear acrylic chamber, peristaltic pump, pressure transducer, and data acquisition system (Fig.5.3). The valves were mounted inside the chamber using a silicone washer on a custom-made fixture fabricated by a U-Print SE Plus 3D printer (Stratasys Ltd., MN, USA). A Masterflex peristaltic pump (Cole Parmer Instrument Co., Chicago, IL, USA) was used to fill the valve housing and apply uniform pressure within the chamber. The bioprosthetic valves were submerged fully in the chamber and care was taken to make sure no air bubbles remained in the chamber. Pressure in the chamber was measured continuously by a pressure transducer (Deltran, Utah Medical Products Inc., UT, USA), which was calibrated prior to the tests using a Delta-Cal Pressure Transducer (Utah Medical Products Inc., UT, USA). The chamber pressure was monitored by StatysTM software (BDC Laboratories, Wheat Ridge, CO, USA) and recorded simultaneously by a data acquisition system (NI SCC-68, National instruments, TX, USA).

DIC imaging was performed using a GOM-ARAMIS stereovision system (GOM-Optical Measuring Techniques, Braunschweig, Germany) distributed by Trilion Quality Systems in the USA). The system consists of two high-speed cameras with a resolution of 5 megapixels (2448 x 2050 pixels) equipped with 50 mm focal length Titanar lenses (Fig. 5.4). To achieve a high contrast in the speckled pattern, the valve surface was lightened by two pattern, the valve surface was lightened by two integrated LED lights (Schneider Optische Werke, GmbH, Bad Kreuznach, Germany). The DIC system was calibrated prior to the tests to accommodate a measuring volume of 80 × 80 × 65 mm. The calibration

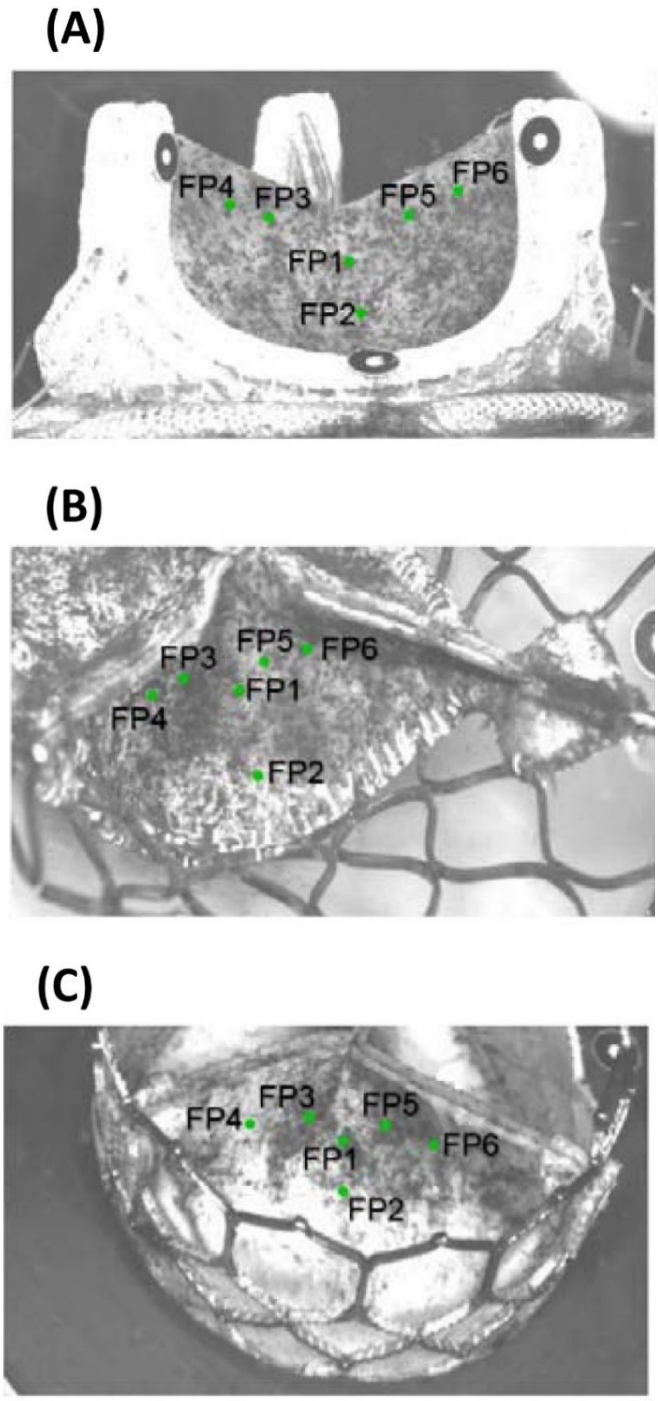

Figure 5.2: Example of speckled pattern and facets points that were used for post processing of the experimental data. (A) 25-mm surgical Carpentier-Edwards PERIMOUNT, (B) 26-mm Medtronic CoreValve, and (C) 26-mm Edward SAPIEN 3, adapted from (Abbasi et al. 2018a).

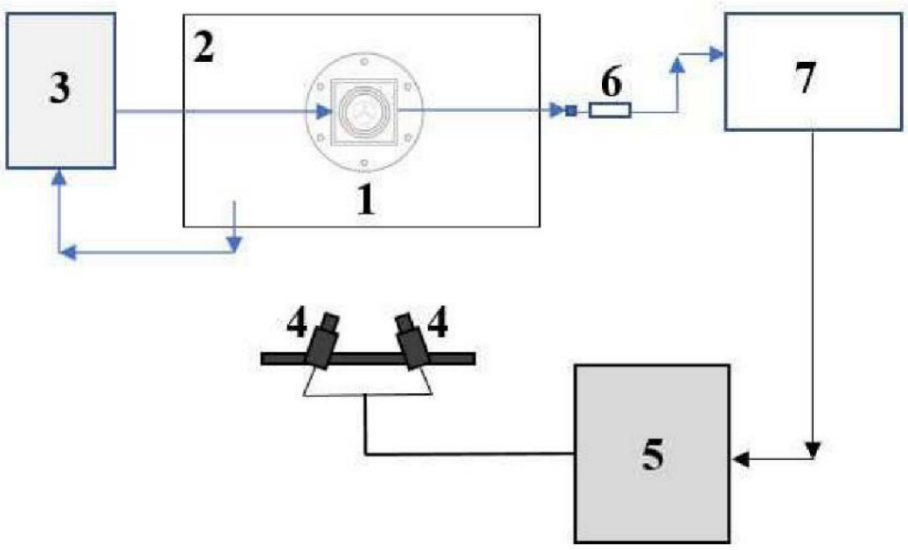

Figure 5.3: A schematic overview of the in-vitro DIC-based experiments consisting of (1) homemade valve housing, (2) water pool, (3) Masterflex peristaltic pump, (4) two high-speed cameras with two integrated LED light sources, (5) DIC system, (6) the pressure transducer, and (7) the data acquisition system, adapted from (Abbasi et al. 2018a).

procedure for the cameras was done based on the user manual of ARAMIS. The angle between the two cameras was ~25° and the distance between two cameras was 216 mm. Both cameras were placed at the measuring distance of 575 mm from the valve housing. For each one of the bioprostheses, DIC measurement was conducted both from top and side views in separate experiments.

A change in the pump speed resulted a corresponding change in the pressure within the testing chamber, and the chamber pressure was simultaneously monitored by StatysTM software. Prior to data collection, 10 preconditioning cycles were applied to the leaflets at a rate of 0.5 Hz. In each cycle, the pressure inside the chamber was cyclically changed from 20 mmHg to 30 mmHg. After preconditioning, the pump speed was increased from 120 rpm to 180, 300, and 480 rpm at a fixed rate of 1 Hz, corresponding to low, medium,

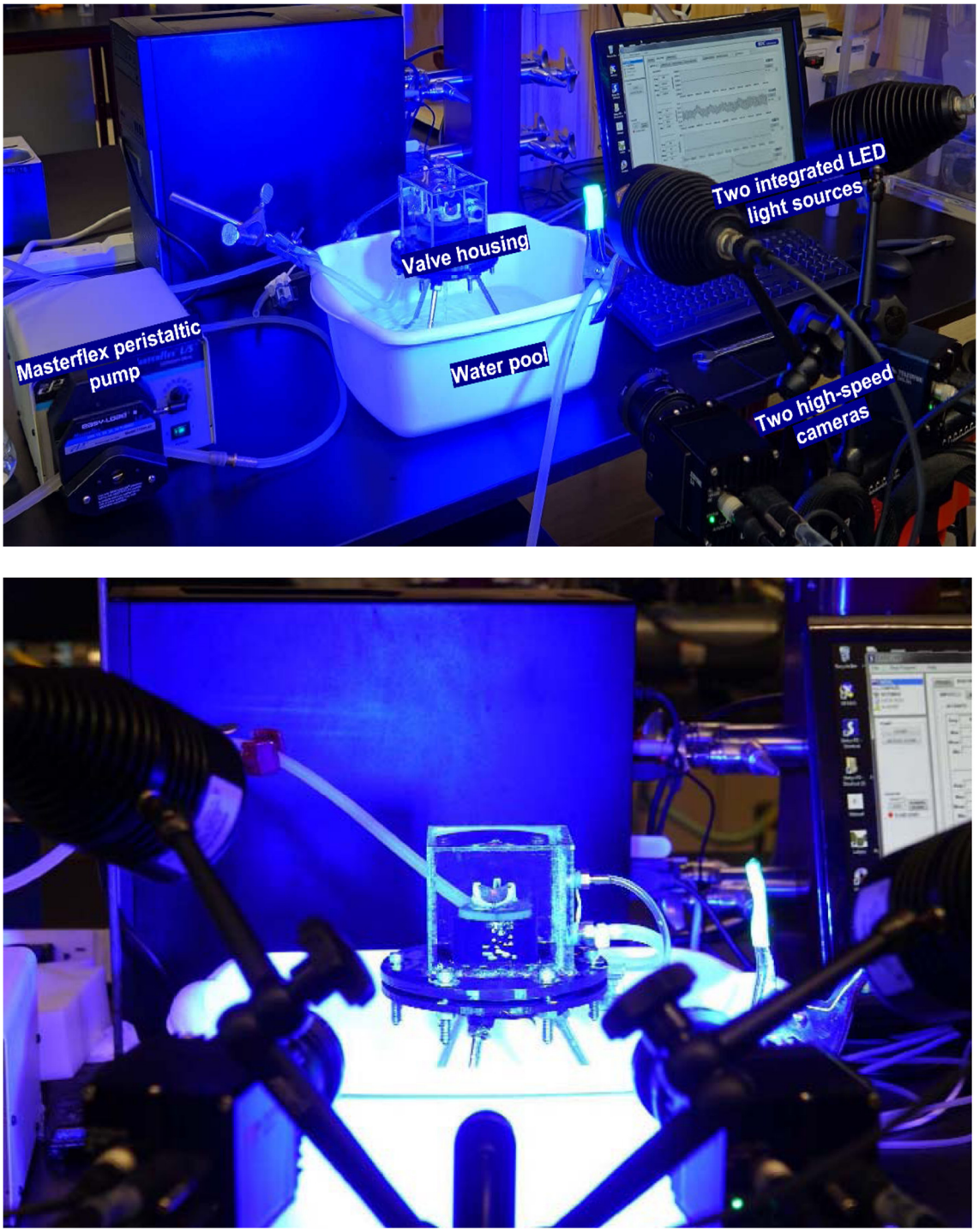

Figure 5.4: A photograph of the in-vitro experimental setup, adapted from (Abbasi et al. 2018a).

high loading frequencies, respectively. Separate experiments were conducted for each pump setting. Loading was followed by an unloading stage and the pump speed was reduced to 120 rpm at a fixed rate of 1Hz. Simultaneously with pressure alteration, image acquisition was triggered in the DIC system and image series were collected and stored using the ARAMIS DIC software (ARAMIS v2016, GOM, Braunschweig, Germany) at a frame rate of 10 frames per second. Following image acquisition, image processing was performed using the ARAMIS DIC software by discretizing all the images to a grid of square subsets of pixels called facet point (FP). A few sample FPs are shown in Fig. 5.2, e.g., FP 1 and FP 2 on the belly region and FP 3-6 parallel to the leaflet free edge. An identical facet size (19 pixels) was considered for all the three valves. Leaflet deformation was determined by tracking the movement of all the facet points. 3D surface contours of the displacement map and corresponding strain values were determined with respect to a reference configuration, i.e. chamber pressure of 30-mmHg.

5.3 Results

5.3.1 Pressure Curves

The obtained pressure curves in the in-vitro test setup for the three pump settings, i.e. 180, 300, 480 rpm, are presented in Fig. 5.5. Three distinct pressure curves were obtained for the three pump settings was expected. Pressure build-up magnitude and time were similar for the two TAV devices. However, the pressure build-up magnitude and time was higher and shorter, respectively, in the CE PERIMOUNT Magna surgical bioprosthesis compare to the two TAVs particularly in 300 and 480 rpm pump settings. For example, at pump speed of 480 rpm, the pressure build-up magnitude in the CE PERIMOUNT Magna

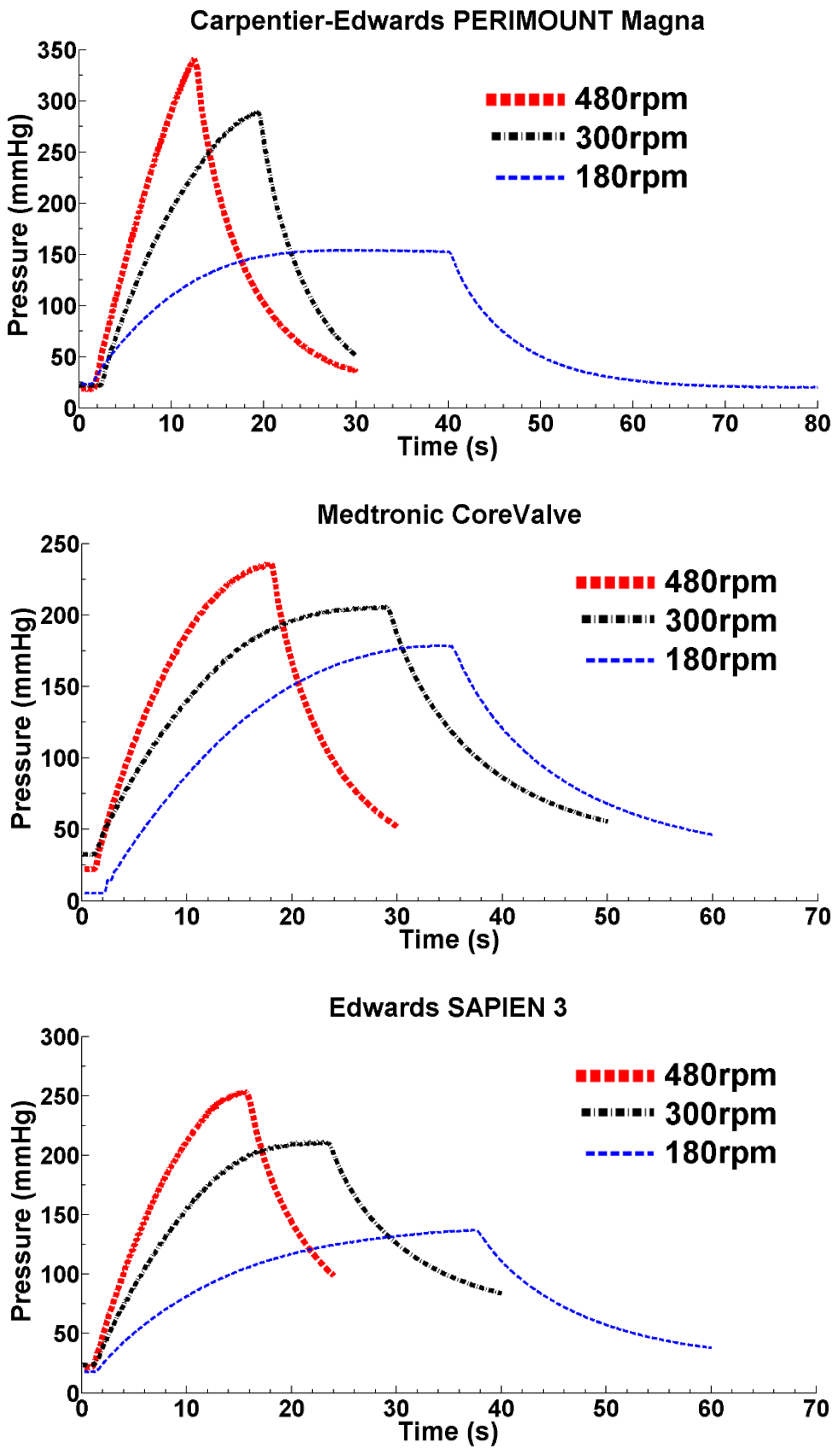

Figure 5.5: Pressure curves acquired from the in-vitro experimental setup during loading and unloading. (Top) 25-mm surgical Carpentier-Edwards PERIMOUNT Magna, (Middle) 26-mm Medtronic CoreValve, and (Bottom) 26-mm Edward SAPIEN 3, adapted from (Abbasi et al. 2018a).

surgical bioprosthesis was 44% and 34% higher than the Medtronic CoreValve and Edwards SAPIEN 3, respectively. At the same time, the CE PERIMOUNT Magna bioprosthesis reached to the peak pressure 30% and 19% faster than the CoreValve and SAPIEN 3, respectively. The main reason behind the difference in pressure curves between the SAV and the two TAVs was the perfectly closed leaflet geometry of the surgical bioprostheses at zero-loading condition which prohibits any central leakage upon small pressure applied to the leaflets of the surgical valve.

5.3.2 Displacement Map

The representative displacement contour plots of the bioprosthetic valve leaflets at pressures of 40, 80, and 120 mmHg are presented in Fig. 5.6. At 120 mmHg pressure, high displacement regions were observed at the leaflet belly region for the PERIMOUNT Magna, CoreValve, and SAPIEN 3 bioprostheses. The maximum leaflet displacement value for the PERIMOUNT Magna, Medtronic CoreValve, and Edwards SAPIEN 3 with respect to the reference configuration (chamber pressure of 30-mmHg) was 1.80, 0.80, and 0.92 mm, respectively. Unlike the CE PERIMOUNT Magna and SAPIEN 3 bioprostheses, the displacement contour for the CoreValve was not symmetric due to a subtle asymmetry in the geometry after leaflet cooptation under loading. In addition, the frame of the surgical bioprosthesis was found to be flexible under the loading conditions (Fig. 5.7). For instance, the maximum displacement of the frame reached to 0.63 mm at 120 mmHg pressure. However, the stent of CoreValve and SAPIEN 3 was found to be inelastic and rigid under similar loading conditions. It was observed that maximum displacement of the CoreValve and SAPIEN 3 stents at the commissures was 0.04 and 0.06 mm at 120 mmHg pressure,

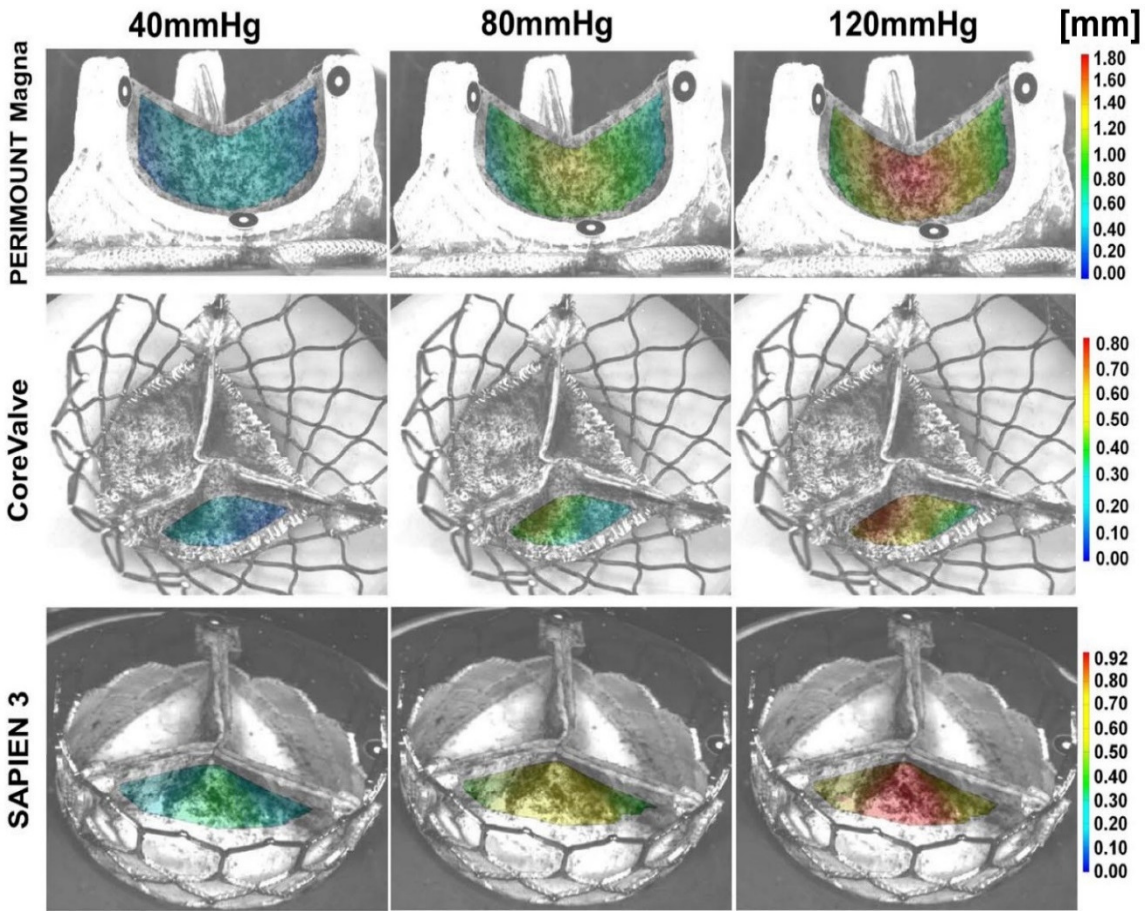

Figure 5.6: Displacement contour plots of the leaflets of bioprostheses valve leaflets at pressures of 40, 80, and 120 mmHg at the pump speed of 480 rpm, adapted from (Abbasi et al. 2018a).

respectively. Overall, the results of the experiments show that the stent deformation of TAVs was negligible compared to the surgical bioprosthesis. To evaluate the viscoelastic behavior of the pericardial leaflets, experimental pressure–displacement curves were obtained at the three pump speeds for the high displacement region,which was the belly region of the leaflets. Figure 5.8 shows the pressure–displacement curves of FP 1, as marked in Fig. 5.2, on the belly region of the three bioprosthetic valves. The FP 1

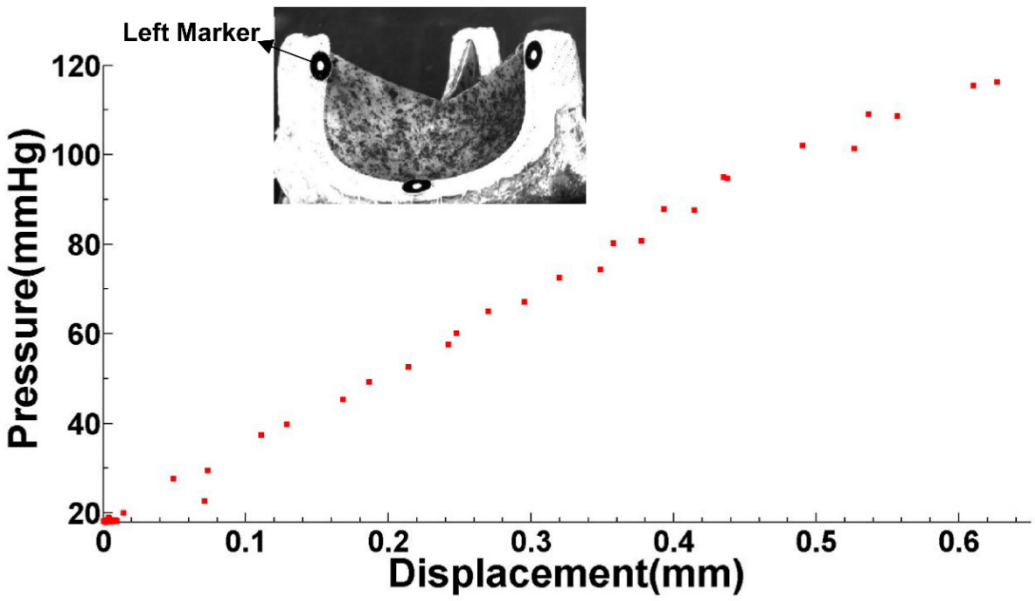

Figure 5.7: Pressure–displacement curves of the left marker mounted on the PERIMOUNT Magna frame close to the commissure at the pump speed of 480 rpm, adapted from (Abbasi et al. 2018a).

coordinates with respect to the commissures at the reference pressure configuration are given in the supplementary material. It was observed that the loading and unloading curves were of different shape. Moreover, the large deformation response was not fundamentally affected by the loading rate.

5.3.3 Strain Map

Strain can be calculated and determined from the obtained displacement field. The contour maps of the major (principal) in-plane Green strain of the three bioprostheses at pressure of 120 mmHg and pump speed of 480 rpm were depicted in Fig. 5.9. The contour maps were obtained from top view DIC measurements. Table 5.1 shows the major (principal) in-plane Green strain values in the belly region of the bioprosthetic valve leaflets in vicinity of FP1 at different pressure levels. It was observed that the maximum

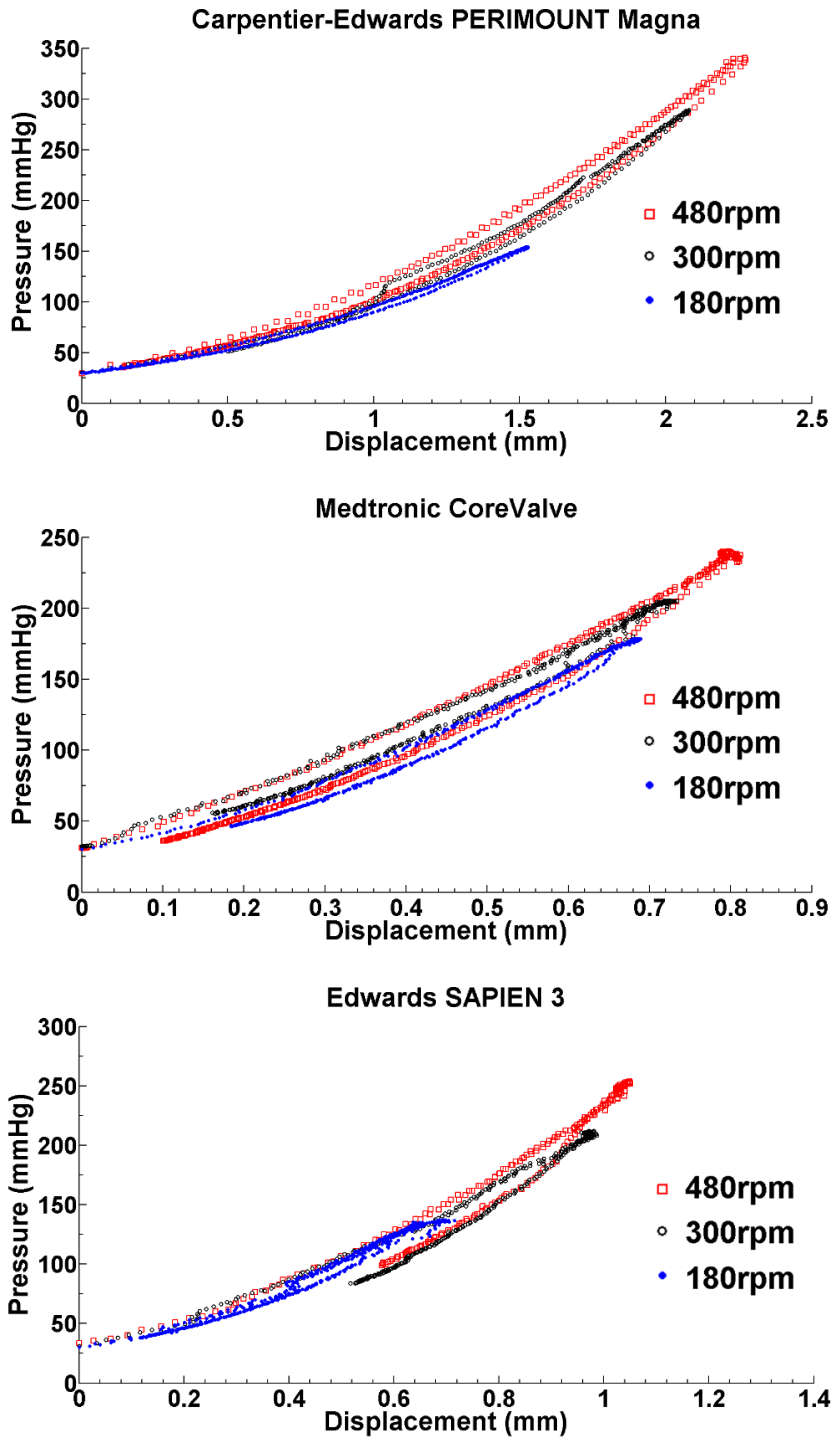

Figure 5.8: Experimental pressure–displacement curves of FP 1 (see Fig 5.2) on the belly region of (Top) 25-mm surgical Carpentier-Edwards PERIMOUNT Magna, (Middle) 26-mm Medtronic CoreValve, and (Bottom) 26-mm Edward SAPIEN 3 bioprosthesis, adapted from (Abbasi et al. 2018a).

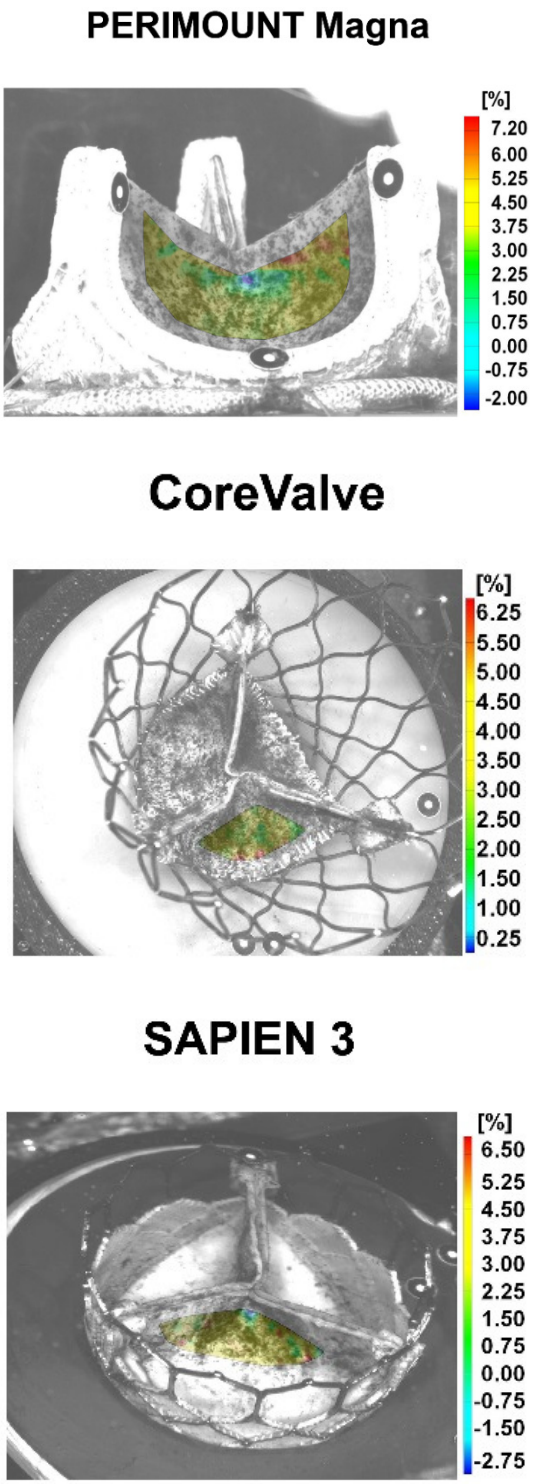

Figure 5.9: The Green major (principal) in-plane strain contour plots of the bioprosthetic valve leaflets at pressure of 120 mmHg at the pump speed of 480 rpm, adapted from (Abbasi et al. 2018a).

Table 5.1: Major (principal) in-plane Green strain in the belly region of the bioprosthetic valve leaflets in vicinity of FP1 of the bioprosthetic valve leaflets at different pressures (pump speed: 480 rpm).

Pressure	40 mmHg	60 mmHg	80 mmHg	100 mmHg	120 mmHg
PERIMOUNT Magna	1.6%	2.5%	3.3%	3.6%	4.0%
CoreValve	1.6%	2.2%	3.2%	4.0 %	4.6%
SAPIEN 3	1.6%	2.1%	2.7%	3.1%	3.3%

in-plane principal strain was increased as the chamber pressure was raised. In addition, Table 5.2 shows the principal Green strain values at different pressure settings for a region close to the commissures as shown by red markers in Fig. 5.10. For PERIMOUNT Magna and Edwards SAPIEN 3, the principal strain values were higher in the region close to the commissures than the belly region. For Medtronic CoreValve, however, the strain values were lower in the commissure region than the belly region. Nevertheless, the maximum strain value on CoreValve leaflets were found below the commissure region close to the fixed boundary edge, as marked by a blue marker in Fig 5.10. The principal strain values for the region below the commissure and close to the fixed boundary edge were 1.5%, 2.3%, 3.1%, 4.6 %, and 5.3%, at a pressure of 40, 60, 80, 100, and 120 mmHg, respectively.

Table 5.2: Major (principal) in-plane Green strain at different pressure settings for a region close to the commissure shown by red markers in Fig 5.10 (pump speed: 480 rpm).

Pressure	40 mmHg	60 mmHg	80 mmHg	100 mmHg	120 mmHg
PERIMOUNT Magna	2.1%	3.4%	4.3%	4.5%	5.8%
CoreValve	1.1%	1.8%	2.3%	3.0 %	3.2%
SAPIEN 3	1.1%	2.4%	4.1%	4.8%	5.9%

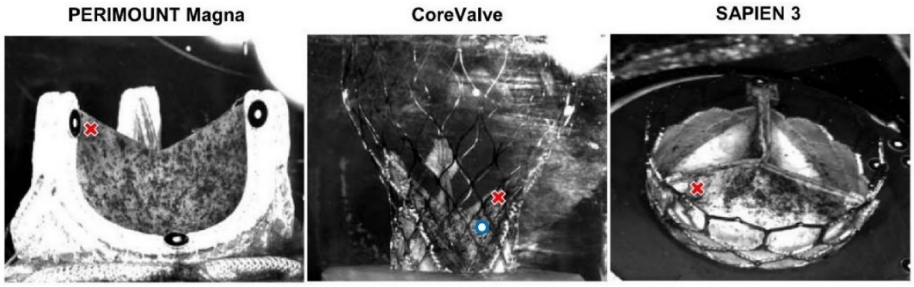

Figure 5.10: Location of facet points close to the commissure region in the three bioprosthetic heart valves identified by red cross markers. The maximum strain value on CoreValve leaflets were found below the commissure region close to the fixed boundary edge as marked by a blue circle marker, adapted from (Abbasi et al. 2018a).

5.4 Discussion

5.4.1 Summary

In this chapter, we presented an experimental framework to determine leaflet displacement field of CE PERIMOUNT Magna surgical bioprosthesis, Medtronic CoreValve, and Edwards SAPIEN 3 using 3D DIC measurements. A time-dependent uniform pressure was applied to the leaflets of the bioprosthetic valves mounted in a custom-made testing system. Through the in-vitro experiments, we found that in all the three bioprosthetic heart valves the maximum leaflet displacement was generally in the upper part of the belly region. However, higher displacement values were observed in the CE PERIMOUNT Magna than CoreValve and SAPIEN 3 bioprostheses. In addition, the frame of the surgical bioprosthesis was found to be markedly flexible under the loading conditions. However, the stent of CoreValve and SAPIEN 3 was found to be rigid under the same loading condition. Frame flexibility and higher leaflet displacement magnitude of the SAV as compared to those for the two TAVs can potentially alter leaflet stress distribution and may be related to the altered long-term durability among different

bioprostheses. The acquired experimental data can be used to characterize the 3D anisotropic mechanical properties of the leaflets and validate computational models of the commercially available bioprosthetic heart valves. Moreover, the experimental observations underline the fact that there are significant differences between geometry and deformation characteristics of TAVs and SAVs, which may lead to altered long term durability of the bioprostheses.

5.4.2 Long-term durability of SAVs

Long-term durability assessment of tissue heart valves is crucial to choose the right prosthetic heart valve for aortic valve replacement. Particularly, to expand TAVR into low-risk younger patients, TAV durability must match with that of surgical bioprostheses. Although there is no unified definition of structural valve degeneration, the rate of structural valve degeneration in surgical bioprostheses is known to be less than 15% at 10 years (Rodriguez-Gabella et al. 2017). Forcillo and colleagues (Forcillo et al. 2013) in a retrospective cohort study studied 2,405 patients with a mean age of 71 ± 9 years old who underwent aortic valve replacement with Carpentier-Edwards surgical pericardial bioprostheses. They found that the overall freedom rate of valve reoperation for valve dysfunction averaged 96% ± 1% and 67% ± 4% at 10 and 20 years, respectively. It is also well known that the rate of reoperation for surgical valve dysfunction is strongly affected by age. As an example, Bourguignon and colleagues (Bourguignon, El Khoury, et al. 2015) demonstrated that the freedom from reoperation rates attributable to structural valve deterioration in patients aged 60 or younger who received Carpentier-Edwards PERIMOUNT aortic valve were 88.3% ± 2.4% and 38.1% ± 5.6% at 10 and 20 years,

respectively. Besides clinical studies, an in-vitro experiment was recently conducted in accordance with ISO 5840:2005 heart valve standard to assess the long-term durability of the CE PERIMOUNT Magna Ease Bioprostheses (Raghav et al. 2016b). In the study, the long-term mechanical durability and hydrodynamic performance of the valve were evaluated through 1 billion cycles (equivalent to 25 years) considering mechanical wear and tear in the absence of calcification. The results showed that the Carpentier-Edwards Magna Ease valves are able withstand the mechanical environment of aortic valves for up to 25 years and perhaps even longer.

5.4.3 Long-term durability of TAVs

In contrary to SAVs, there is a paucity of clinical data regarding long-term durability of TAVs. Recently, Dvir and colleagues (Dvir et al. 2016) conducted a study to evaluate long-term durability of TAVs including Cribier-Edwards, Edwards SAPIEN, and Edwards SAPIEN XT for 378 patients followed for up to 10 years. Based on their results, the estimated structural valve degeneration rate was approximately 50% at 8 years. Beside the clinical observations, several finite element computational simulations have been performed to obtain stress and strain distributions of TAV leaflets (Abbasi and Azadani 2015, Abbasi et al. 2016, Li and Sun 2010, Martin and Sun 2015, Hsu et al. 2015, Xuan et al. 2017, Abbasi and Azadani 2017). The simulation results showed higher mechanical stress in TAVs compare to SAVs, affected by leaflet mechanical properties, design, and thickness. As shown in this study, the pericardial leaflet thickness employed in TAVs is less than that of surgical bioprostheses to accommodate TAVs to miniaturized catheters. A reduction in leaflet thickness increases mechanical stress on the tissue and over time can

negatively influence long-term durability of the TAVs. The increased mechanical stress on TAV leaflets may explain the relatively higher rate of accelerated tissue degeneration and diminished long-term durability in TAVs. However, the simulation results must be validated by in-vivo clinical studies and by non-invasive in-vitro techniques such as DIC measurements as presented in this study. In addition, it is important to note that in vitro studies, such as the one presented here, only investigate the potential modes of valve failure inherent to the design and materials used, and less towards the potential clinical modes of failure.

5.4.4 Viscoelastic Behavior of Tissue Heart Valves

Biological soft tissue, including glutaraldehyde fixed bovine and porcine pericardial tissues, are viscoelastic in nature and demonstrate a number of features including hysteresis, creep, and force relaxation (Lee, Courtman, and Boughner 1984, Lee et al. 1994, Talman and Boughner 1995). Considering the results of our experiments, the leaflets showed viscoelastic behavior as manifested by different loading and unloading paths. Histological characterization of the bovine and porcine pericardium has been carried out in the past showing that the architecture of the pericardiums are similar consisting of multiple layers of collagen bundles holding some degrees of fiber orientations (Gauvin et al. 2013). In addition, it has been demonstrated that the large deformation response of pericardial bioprosthetic materials is virtually unaffected by loading frequency (Lee et al. 1994), a phenomenon that we also observed in this study. As a result in computational modeling, the viscoelastic behavior of tissue heart valves is often approximated by pseudo-hyperelastic material models (Fung 2013b). Although pseudo-elastic models seem

reasonable to simulate biological soft tissues, high-quality experimental data from DIC measurements are still needed to characterize the 3D anisotropic materiel models used in the computational simulations.

5.5 Conclusions

In summary, an in-vitro DIC-based experiment was conducted to map displacement and measure strain values on three different bioprosthetic heart valves, i.e., Carpentier-Edwards PERIMOUNT Magna surgical bioprosthesis, Medtronic CoreValve, and Edwards SAPIEN 3. High displacement regions were found at the leaflet belly region of the three valves. In addition, frame of the surgical bioprosthesis was found to be noticeably flexible, in contrary to CoreValve and SAPIEN 3, in which the stent was rigid. High strain regions were found at the leaflet commissures in PREIMOUNT Magna and SAPIN 3. However, the maximum strain value on CoreValve leaflets were found below the commissure region close to the fixed boundary edge. The results of optical measurements in the DIC system can be utilized to characterize the anisotropic materiel behavior of the leaflets and validate computational simulations. The simulations would enable one to compare side-by-side different bioprosthetic heart valves and to obtain high resolution stress and strain values particularly close to the fixed boundary edge of the leaflets, a region which displacement and strain measurements are not feasible by DIC measurements. Moreover, further studies are motivated to measure leaflet deformation and strain fields under dynamic loading conditions.

Chapter 6: Material Characterization Framework for Commercial bioprostheses

6.1 Introduction

Pre-clinical assessment and verification of life sustaining implantable medical devices such as prosthetic heart valves are essential and required by regulatory agencies. As a result, in vitro bench-top and pre-clinical animal testing have been employed to verify safety and improve design features of prosthetic heart valves . However, the pre-clinical studies are time-consuming and costly, and therefore, the tests may potentially inhibit exploration and use of novel materials and designs in prosthetic heart valves. In the past few years, computational modeling and simulation have been widely employed to expedite design and optimization of new medical devices (Fries 2016, Morris et al. 2016). Computational simulations can play a pivotal role in design and development of prosthetic heart valves by reducing the need to perform expensive pre-clinical tests. Furthermore, regulatory agencies such as the U.S. Food and Drug Administration (FDA) and EU Medical Device Regulatory System currently accept validated computational modeling and simulation as a scientific evidence in regulatory submissions (Food and Administration 2014).

In the past decade, use of bioprosthetic heart valves for aortic valve replacement has increased significantly (Mack and Holmes 2016). The trend was due to promising improvements in the long-term durability of surgical aortic valves (SAVs) and the advent

of transcatheter aortic valves (TAVs) (Cribier et al. 2002, Isaacs et al. 2015). Randomized clinical trials proved transcatheter aortic valve replacement (TAVR) improved survival over medical therapy for inoperable patients with severe symptomatic aortic stenosis (Kapadia et al. 2015, Leon et al. 2010, Makkar et al. 2012, Nishimura et al. 2014, Popma et al. 2014). Furthermore, transfemoral TAVR showed equivalent or superior outcomes when compared to surgical aortic valve replacement (SAVR) for the high-risk (Adams et al. 2014, Kodali et al. 2012, Mack et al. 2015, Smith et al. 2011) and intermediate-risk (Leon et al. 2016a, Reardon et al. 2016) patients. At present, large randomized clinical trials are underway for low-risk surgical patients with aortic stenosis. However, durability is the Achilles heel of bioprosthetic heart valves (Arsalan and Walther 2016, Bourguignon, Bouquiaux-Stablo, et al. 2015, Dvir et al. 2016, Grunkemeier et al. 2012, Johnston et al. 2015).

Accurate and validated computational simulations can be effectively used to improve structural and hemodynamic performance of bioprosthetic heart valves. The commercially available bioprosthetic heart valves are made from materials such as metals (e.g., stainless steel, cobalt alloys, and titanium-nickel alloy (Nitinol), polymers (e.g., Dacron and Teflon), and fixed biological soft tissue (e.g., bovine and porcine pericardium). To have a reliable computational model, considering accurate mechanical properties for the bioprosthetic materials is a crucial step. In the past few decades, mechanical properties of bovine and porcine pericardium have been obtained primarily using experimental methods such as uniaxial and biaxial tensile tests(Abbasi and Azadani 2015, Sacks 2000, Sun, Abad, and Sacks 2005). However, the planar tests cannot capture the out-of-plane mechanical

behavior of the soft tissue (Holzapfel and Ogden 2008). In addition, due to extensive intra-specimen and inter-specimen variations (Hiester and Sacks 1998), mechanical properties of examined materials in the pre-clinical tests may be significantly different from the actual materials used in the implanted bioprosthetic valves. Consequently, employing optimized material parameters to describe valve-specific mechanical behavior of the leaflets is essential in computational simulations.

In the present chapter, we aimed to develop a non-invasive material characterization framework using integrated experimental and numerical methods to determine mechanical propertied of soft tissue employed in bioprosthetic heart valves. Accordingly, we characterized three-dimensional anisotropic mechanical properties of leaflets used in two commercially available TAVs (i.e., Edwards SAPIEN 3 and Medtronic CoreValve), and compared the results to that of a commonly used and well-examined surgical bioprosthesis (i.e., Carpentier-Edwards PERIMOUNT Magna aortic heart valve). In addition, the present chapter presents a reliable approach to compare leaflet stress distribution among different bioprostheses under physiological loading condition.

6.2 Materials and Methods

6.2.1 Commercial bioprostheses

In the present study, two commercially available TAVs and one surgical bioprosthesis with comparable size were evaluated (Fig. 6.1). The first bioprosthetic valve was a 25-mm Carpentier-Edwards (CE) PERIMOUNT Magna aortic heart valve (Edwards Lifesciences, CA). The surgical bioprosthetic valve was made from bovine pericardium leaflets mounted on an Elgiloy frame with an internal diameter of 24 mm. The second bioprosthesis was a

self-expanding 26-mm Medtronic CoreValve (Medtronic, Minneapolis, MN), consists of porcine pericardial leaflets mounted on a self-expanding Nitinol stent. The third bioprosthetic valve investigated in this study was a 26-mm Edwards SAPIEN 3 (Edwards Lifesciences, Irvine, CA). The TAV was constructed from bovine pericardial leaflets mounted on a balloon-expandable cobalt-chromium stent. The thickness of the leaflets was measured using Mitutoyo Digital caliper (Mitutoyo Corp, Kanogawa, Japan) and the average thickness was 0.56 mm, 0.43 mm, and 0.32 mm for CE PERIMOUNT Magna bioprosthesis, CoreValve, and SAPIEN 3, respectively.

Figure 6.1. (Left) 25-mm Carpentier-Edwards PERIMOUNT Magna surgical bioprosthetic aortic valve. (Center) 26-mm Medtronic CoreValve. (Right) 26-mm Edwards SAPIEN 3 transcatheter heart valve.

6.2.2 Experimental Setup

6.2.2.1 Digital image correlation measurements

Due to the limited temporal and spatial resolution of the currently available in vivo imaging modalities, in vitro tests play a central role in characterizing mechanical properties of soft tissue and validate computational simulations. In view of that, high-resolution optical techniques such as digital image correlation (DIC) can be utilized to quantify

bioprosthetic valve leaflet displacement non-invasively under a well-defined loading condition. In this chapter, a high-resolution GOM-ARAMIS stereovision DIC system (GOM-Optical Measuring Techniques, Braunschweig, Germany) was used to obtain displacement map of the bioprosthetic heart valves. The system consists of two high-speed cameras with a resolution of 5 megapixels (2448 x 2050 pixels) equipped with 50 mm focal length Titanar lenses. The top side of the leaflets were sprinkled with graphite to create a speckled pattern (Fig. 6.2). Details of the DIC imaging and measurements have been previously described in chapter 5. Briefly, the bioprosthetic valves were mounted inside an optically clear acrylic chamber on a custom-made fixture. The valves were submerged fully in the chamber and the leaflets were pressurized uniformly from 20 mmHg to 120 mmHg using a peristaltic pump. Pressure in the chamber was measured continuously by a pressure transducer, monitored by StatysTM software, and recorded simultaneously by a data acquisition system. Pressure curves acquired from the DIC tests were shown in the Fig 5.5. In addition, image acquisition was triggered simultaneously, and image series were collected and stored using the ARAMIS DIC software at a frame rate of 10 frames per second. Following image acquisition, image processing was performed using the ARAMIS DIC software by discretizing all the images to a grid of square subsets of pixels called facet point (FP). An identical facet size (19 pixels) was considered for all the three valves. A few sample FPs (FP1 - FP6) are shown in Fig.6.2. Leaflet deformation was determined by tracking the movement of the FPs. Three-dimensional surface contours of the displacement map were determined with respect to a reference pressure configuration, i.e. chamber pressure of 30-mmHg.

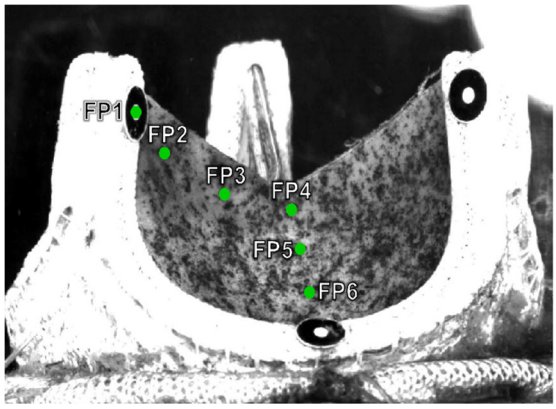

Carpentier-Edwards PERIMOUNT Magna

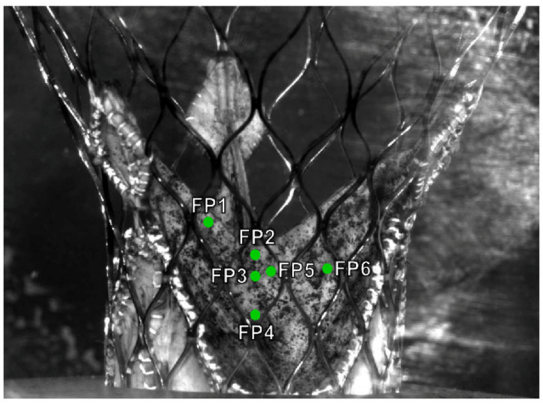

Medtronic CoreValve

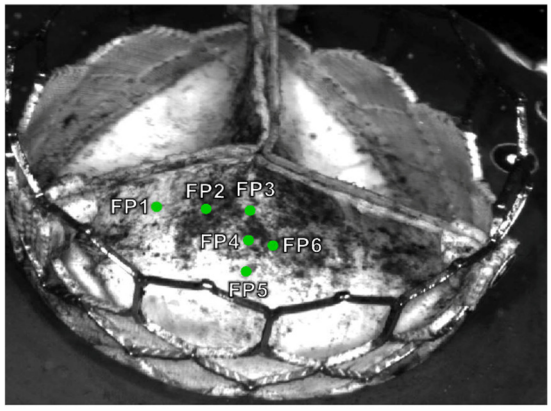

Edwards SAPIEN 3

Figure 6.2: Example of speckled pattern and facets points that were used for post processing of the experimental data.

6.2.2.2 In-vitro pulse duplicator system

The three bioprosthetic heart valves were also examined under dynamic physiological loading condition in a custom-built pulse duplicator system (BDC Labs, Wheat Ridge, CO). Details of the in vitro tests have been previously described in chapter 3. The pulse duplicator input parameters matched the international standard ISO 5840: 2015 recommendations for testing prosthetic heart valves, i.e., heart rate of 70 beats/min, mean atrial and aortic pressures of 10 and 100 mmHg, and cardiac output of 5 L/min. The physiological flow condition was simulated by controlling local compliance and peripheral resistance in the pulse duplicator. Recirculating fluid of 45% by volume glycerin solution (99% glycerin, The Science Company, Denver, CO) in phosphate buffered normal saline solution (PBS 100ml tablets, Research Products International, Mount Prospect, IL) was used as a blood analog fluid at 37 °C. Transvalvular pressure waveform and flow rate of the three bioprosthetic valves were measured from the in-vitro tests in Fig. 6.3. Furthermore, the leaflet motion for the valves was captured by a using a high-speed camera, SONY DSC-RX10M3 high-speed camera, at a rate of 960 frames per second. The images were digitized in MATLAB, and the center of each leaflet was tracked and its distance with respect to the center of the three valves was calculated through the entire cardiac cycle.

6.2.3 Computational Simulation

6.2.3.1 Finite element modeling

Leaflet geometry of the three bioprosthetic valves was obtained using NextEngine 3D Laser Scanner with a resolution of 100 micrometers (NextEngine, Inc., Santa Monica, CA). Surface reconstruction of valves was performed using RapidWorks and SOLIDWORKS

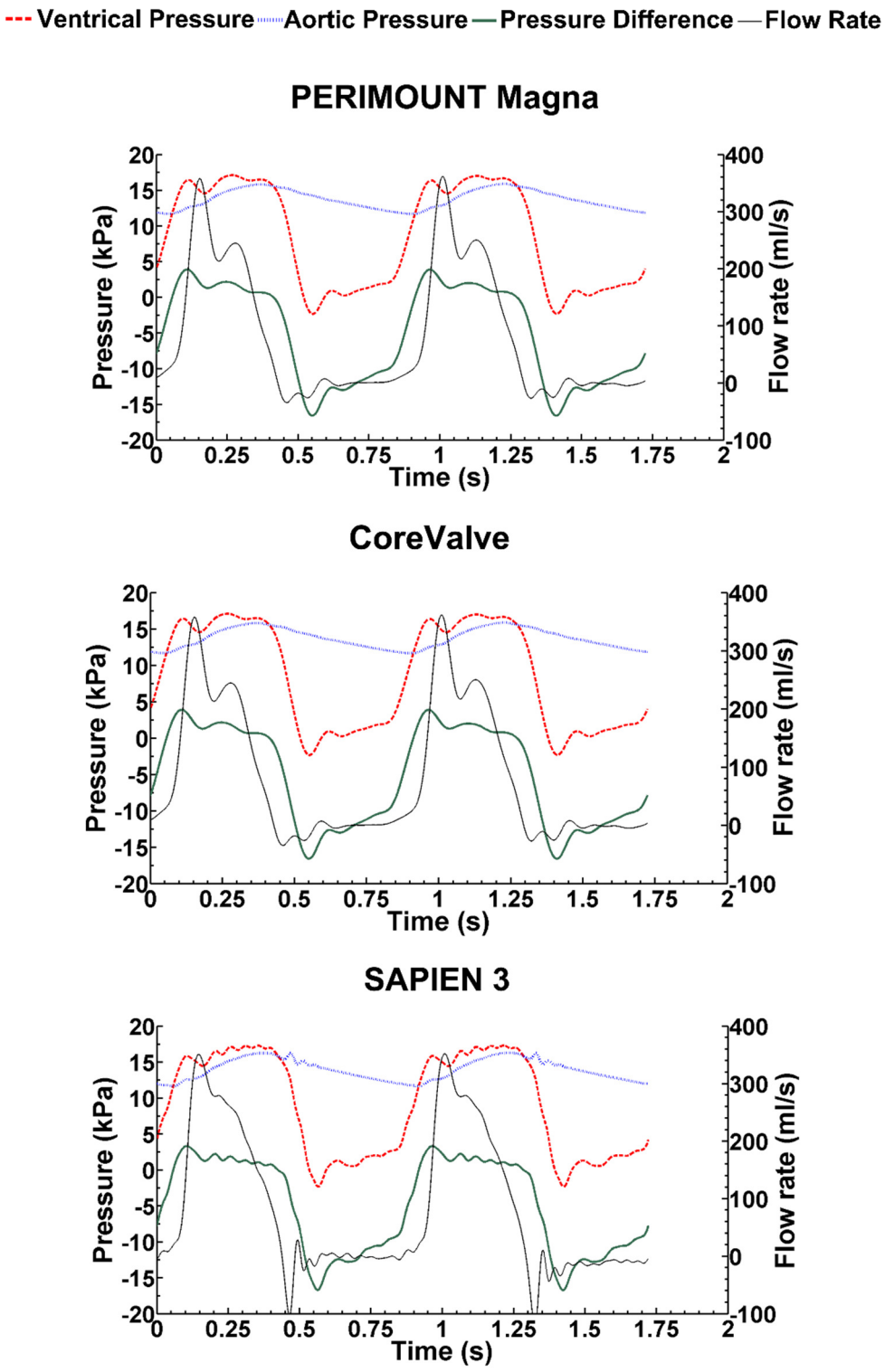

Figure 6.3: Bioprosthetic pressure and flow rate waveforms, (Top) Carpentier-Edwards PERIMOUNT Magna, (Middle) Medtronic CoreValve, (Bottom) Edward SAPIEN 3.

packages, and IGES format of the leaflets were obtained for finite element (FE) simulations. For mesh generation, the leaflets were imported to HyperMesh (Altair Engineering, Inc., Troy, MI), and the geometry was discretized using a mapped mesh. The mesh was subsequently imported to ABAQUS/Explicit solver. The leaflet thickness was assumed uniform and constant throughout the leaflet. Material orientation was assigned to the shell elements using a home-developed MATLAB code. Density of the leaflets was considered to be 1,100 kg/m³ (Kim et al. 2008). Frame of the surgical bioprosthetic valve was found to be flexible in the DIC tests in chapter 5. Therefore, a flexible frame with a uniform diameter, measured by the caliper to be 0.89 mm, and density of 8,300 kg/m^3 (Roy and Chanda 2014) was considered in the FE simulations for the surgical bioprosthesis (Fig. 6.4). Due to the high radial strength of TAV frames, the stent of CoreValve and SAPIEN 3 was considered to be rigid. The rigidity of the TAV frames was confirmed by the DIC measurements. The geometry of CE PERIMOUNT Magna bioprosthesis was meshed using 7,674 ABAQUS S4 shell elements and 345 B31 beam elements. The beam elements of the surgical valve frame were connected to the leaflet using multi-point constraints. 11,166 and 8,250 ABAQUS S4 shell elements were used to discretize CoreValve and SAPIEN 3 bioprostheses, respectively. The number of elements in the simulations was adequate to assure that the results are independent of mesh density.

To make sure the FE results are independent of mesh density, for each one of the bioprosthetic heart valves, four mesh densities were evaluated by comparing the maximum displacement of the middle point of the leaflet's free-edge and its maximum principle stress

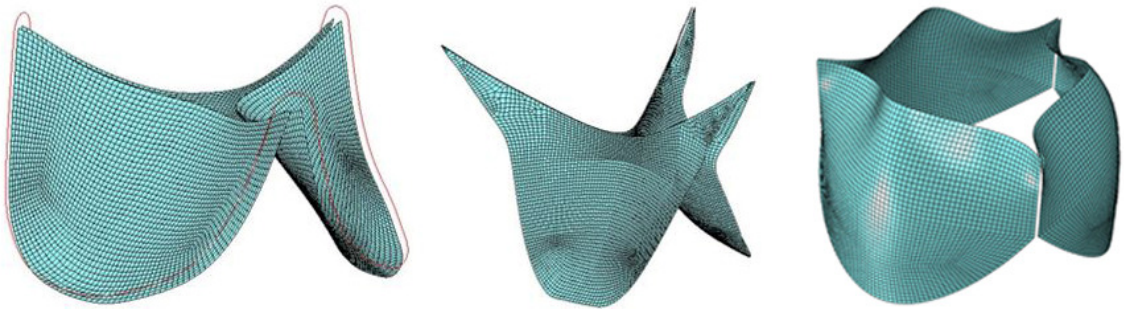

Figure 6.4: Representative FE models for (Left) Carpentier-Edwards PERIMOUNT Magna, (Center) Medtronic CoreValve, (Right) Edward SAPIEN 3.

value. As an example, please see below in Table 6.1 and Fig. 6.5, analysis of mesh density for SEIPEN 3 at a point in the systole. The difference in normal displacement and maximum stress between mesh density (#3) and (#4) was less than 0.14% and 0.5%, respectively. Therefore, mesh density (#3) was considered in the FE simulations. A similar analysis was conducted for the CoreValve and the CE PREIMOUNT Magna bioprosthesis.

Transvalvular pressure gradient waveforms obtained from the in-vitro tests were applied to the ventricular side of the leaflets. Moreover, a Rayleigh damping coefficient α was introduced to the simulations to mimic viscous damping effects of surrounding fluid.

Table 6.1: Independence of the FE simulation of SAPIEN 3 from computational grid density.

Number	Number of elements (one leaflet)	Displacement (m)	Maximum principal stress(Pa)
1	1008	0.00340988	1171250
2	2238	0.00342635	1262410
3	2750	0.00345985	1280560
4	4040	0.00345501	1287020

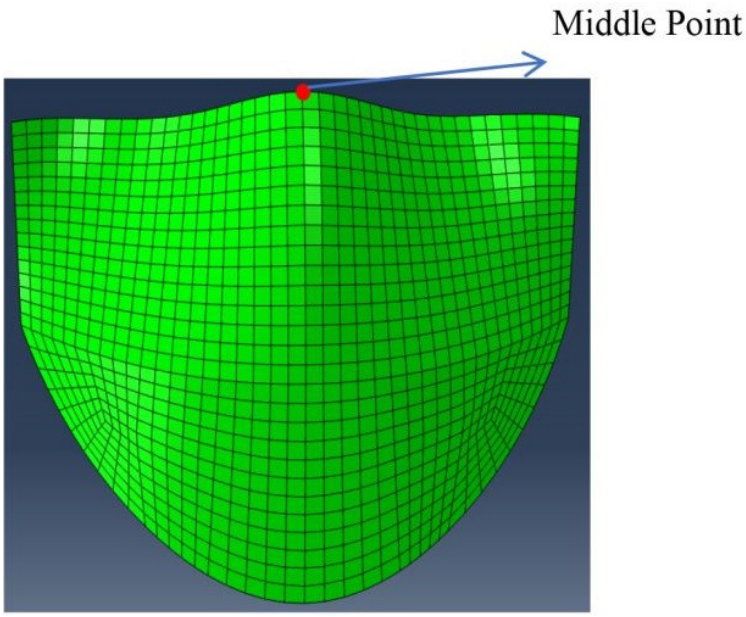

Figure 6.5: Maximum displacement of the middle point of the SAPIEN 3 leaflet's free-edge.

In the FE simulations, bioprosthetic leaflets were considered to be pseudo-hyperelastic anisotropic materials (Abbasi and Azadani 2015, Abbasi and Azadani 2017). There are two forms of strain energy potentials available in ABAQUS/Explicit to characterize anisotropic materials: (i) generalized three-dimensional Fung strain-energy function proposed by Humphrey (Humphrey 1995) and (ii) Holzapfel-Gasser-Ogden (HGO) strain energy function which was developed as a framework to model arterial layers with distributed collagen fiber orientation(Holzapfel 2000). A generalized Fung strain-energy function is in the form

$$\Psi = \frac{c}{2}(e^{Q} - 1) + \frac{1}{\mathcal{D}}\left(\frac{{J_{el}}^{2} - 1}{2} - \ln J_{el}\right) \tag{6.1}$$

where Ψ is the strain energy per unit of reference volume. Details of the generalized Fung strain-energy function have been previously described in chapter 3. On the other hand, the

strain energy function for HGO model also known as Holzapfel model in ABAQUS consists of two terms: (i) isochoric and (ii) volumetric parts. The isochoric part is further decomposed into distinct matrix and fiber material terms with the following function

$$\Psi = \underbrace{\underbrace{C_{10}(\bar{I}_1 - 3)}_{matrix} + \underbrace{\frac{k_1}{2k_2}\sum_{\alpha=1}^{N}\{exp[k_2\langle\bar{E}_\alpha\rangle^2] - 1\}}_{fiber}}_{isochoric} + \underbrace{\frac{1}{\mathcal{D}}\left(\frac{{J_{el}}^2 - 1}{2} - \ln J_{el}\right)}_{volumetric} \tag{6.2}$$

With

$$\bar{E}_\alpha \overset{\text{def}}{=} \kappa(\bar{I}_1 - 3) + (1 - 3\kappa)\left(\bar{I}_{4(\alpha\alpha)} - 1\right) \tag{6.3}$$

where C_{10} is the parameter of the isotropic neo-Hookean term which affects the stiffness of the isotropic hyperelastic matrix; k_1 , k_2 are temperature-dependent material parameters which determine the stiffness and exponential response of the collagen fiber networks in the material, respectively; $\mathcal{D}$ is the compressibility parameter; κ describes the level of dispersion in the fiber directions ($0 \leq \kappa \leq 1/3$); N is the number of families of fibers ($N \leq 3$); $\bar{I}_1$ is the first deviatoric strain invariant; and $\bar{I}_{4(\alpha\alpha)}$ are pseudo-invariants of the right Cauchy Green tensor and a set of unit vectors for the fiber directions. The structural anisotropy induced by the fiber network originates from $\bar{I}_{4(\alpha\alpha)}$. The HGO model can be defined by five parameters (C_{10}, k_1 , k_2, κ, $\mathcal{D}$). In this study, $\mathcal{D}$ was assumed to be a constant value of 10^{-5} for the bioprosthetic valve leaflets(Martin and Sun 2015).

6.2.3.2 Optimization framework

To determine 3D mechanical properties of the leaflets, a two-step global optimization approach was utilized. The flowchart in Fig. 6.6 shows how the optimization technique

was implemented to find the material parameters. We used leaflet material properties reported in Abbasi and colleagues (Abbasi et al. 2016) and Martin and Sun (Martin and Sun 2015) as initial estimate values of the optimization for Fung and HGO models, respectively. In the first step, the DIC measurements were utilized to determine leaflet material coefficients in both Fung and HGO models. The stent of CoreValve and SAPIEN 3 was considered to be rigid. However, for the surgical bioprosthesis a linear elastic frame was considered in the simulations. The Young's modulus of the frame was taken as an adjustable parameter in the optimization to match displacement of the frame obtained from the DIC tests. The Poisson's ratio of the frame was considered to be 0.226 (Roy and Chanda 2014). The material coefficients were obtained by minimizing the error norm of displacement field between DIC measurements and FE simulations for the six facet points, selected in the belly region and region close to the free edge of the leaflets as shown in Fig. 6.2, using particle swarm optimization (PSO) (Banks, Vincent, and Anyakoha 2008) method implemented in Isight (Simulia, Providence, RI). Six facet points provided a reasonable balance between the complexity of the analysis (i.e., computational cost) and accuracy of the computational model. Equal weight was considered for all the facet points. The optimization process terminated when the change of the objective function was less than the set tolerance of 10^{-5}. Approximately, 500 iterations were performed to achieve convergence. The displacement contour plots obtained by the optimized material coefficients were then compared with experimental displacement contours obtained from the DIC tests. A material model that showed a good agreement with the experimental data was then considered for the second step of optimization. In the second step, the leaflet

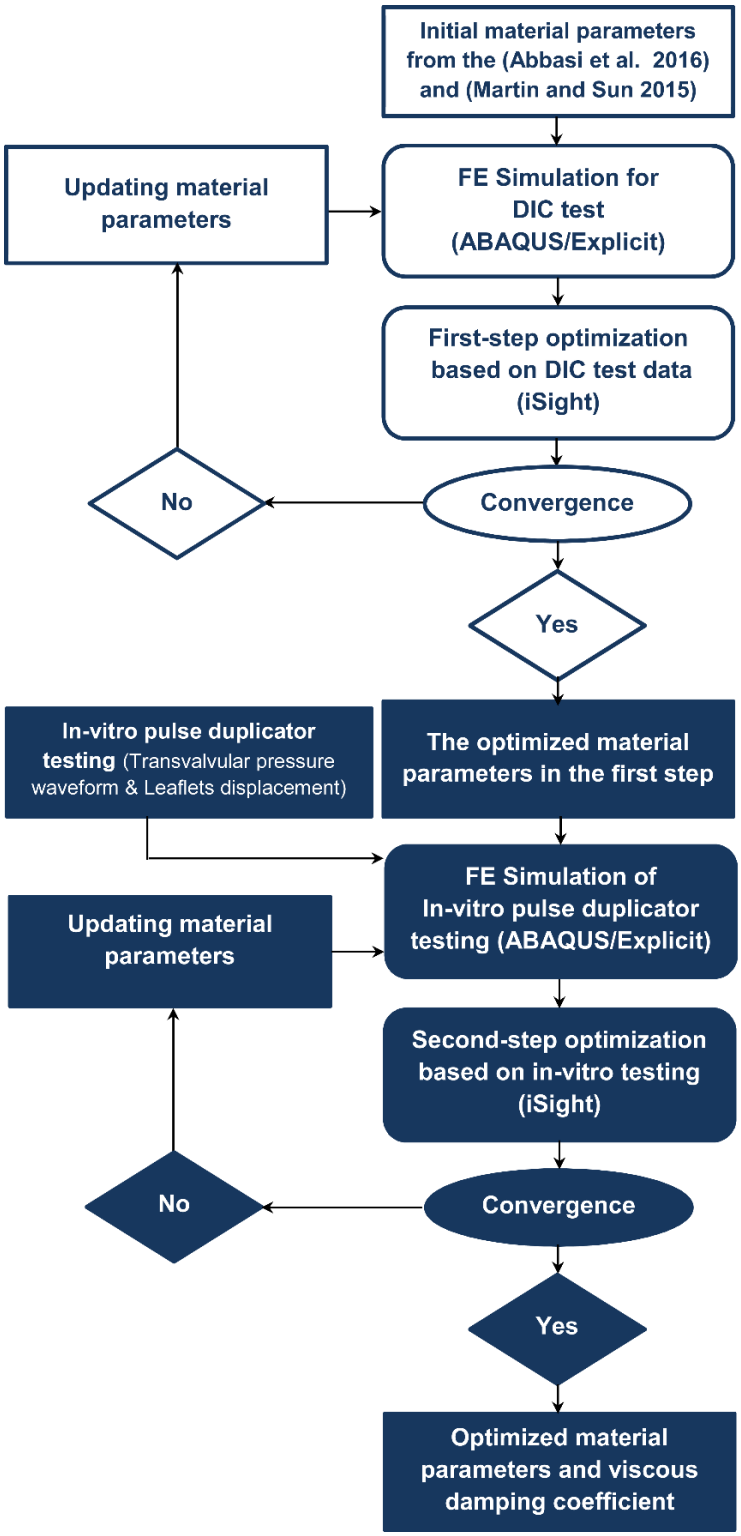

Figure 6.6: Flowchart for parameter estimation algorithm.

material parameters plus the viscous damping coefficient were optimized based on the raw (unfiltered) hemodynamic data (i.e., pressure waveforms) obtained from the pulse duplicator system using PSO method in Isight. The middle point distance of leaflets with respect to the center of the valve in the FE simulation was matched with the experimental measurements in the pulse duplicator system. To reduce computational cost, only one cardiac cycle was simulated, and one leaflet motion was considered in the optimization procedure during valve opening and closing. The optimization process was set to be terminated when the change of the objective function was less than the set tolerance of 10^{-5}.

6.3 Results

6.3.1 Estimated Material Parameters of Leaflets

The two-step optimization procedure was used to determine 3D mechanical properties of the bioprosthetic valve leaflets. First, DIC tests were simulated to obtain appropriate initial estimate values for the material coefficients in both Fung and HGO models. Material coefficients were obtained by minimizing the simulated and measured displacement vectors of the six facet points (Figs. 6.7-6.9). The results of material optimization are shown below for 3D anisotropic Fung model. Furthermore, the estimated values for c coefficient in the Fung model are presented in Table 6.2. In addition, the results of material optimization for HGO model are shown in Table 6.3. For the three bioprosthetic heart valves, the curve fit of the generalized Fung model was to some extent better than the HGO model (Figures 6.7-6.9 and Table 6.4). In addition to the six facet points, to evaluate the overall accuracy of the two constitutive models, displacement contour plots of the leaflets

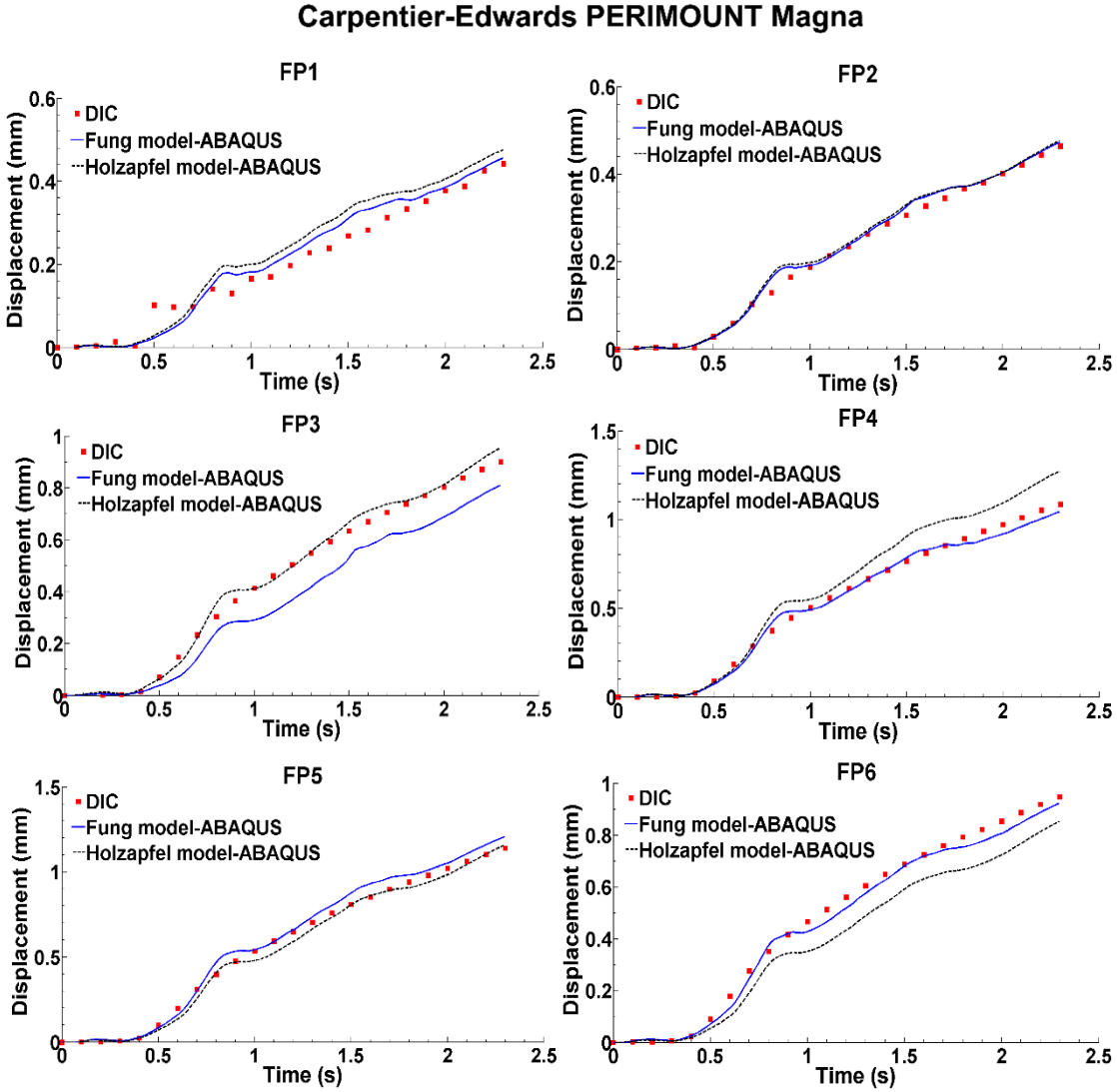

Figure 6.7: Displacement-time curves of the six facet points on the leaflets of Carpentier-Edwards PERIMOUNT Magna.

$$\mathbb{b}_{\text{PERIMOUNT Magna (First-step optimization estimate)}} = \begin{bmatrix} 65.24 & 32.75 & 52.28 & 17.47 & 48.74 & 38.88 \\ & 62.51 & 46.69 & 67.17 & 65.73 & 20.02 \\ & & 61.28 & 38.03 & 62.67 & 53.36 \\ & & & 14.89 & 15.58 & 27.96 \\ & & \text{Symmetric} & & 45.49 & 14.26 \\ & & & & & 69.73 \end{bmatrix},$$

$$\mathbb{b}_{\text{CoreValve (First-step optimization estimate)}} = \begin{bmatrix} 64.10 & 38.52 & 57.15 & 18.84 & 45.21 & 47.59 \\ & 63.35 & 46.36 & 61.87 & 60.38 & 25.54 \\ & & 71.17 & 41.68 & 70.03 & 58.04 \\ & & & 15.90 & 14.90 & 28.00 \\ & & \text{Symmetric} & & 44.06 & 17.75 \\ & & & & & 66.33 \end{bmatrix},$$

$$\mathbb{b}_{\text{SAPIEN 3 (First-step optimization estimate)}} = \begin{bmatrix} 87.27 & 38.19 & 56.26 & 18.40 & 45.47 & 37.23 \\ & 83.97 & 43.50 & 70.21 & 71.65 & 25.72 \\ & & 92.84 & 43.70 & 62.41 & 58.98 \\ & & & 14.25 & 14.90 & 27.96 \\ & & \text{Symmetric} & & 44.84 & 17.70 \\ & & & & & 68.76 \end{bmatrix}.$$

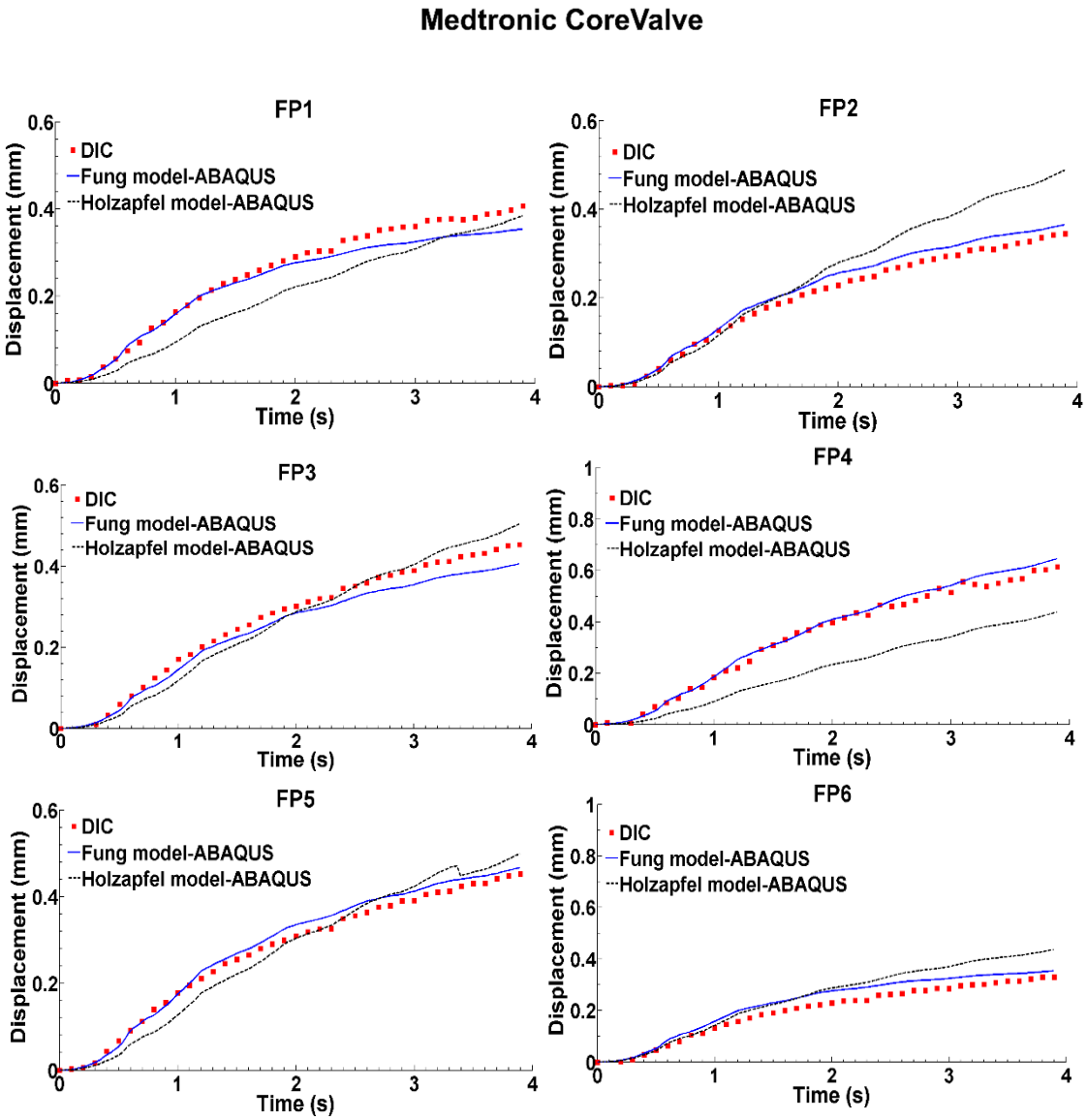

Figure 6.8: Displacement-time curves of the six facet points on the leaflets of Corevalve.

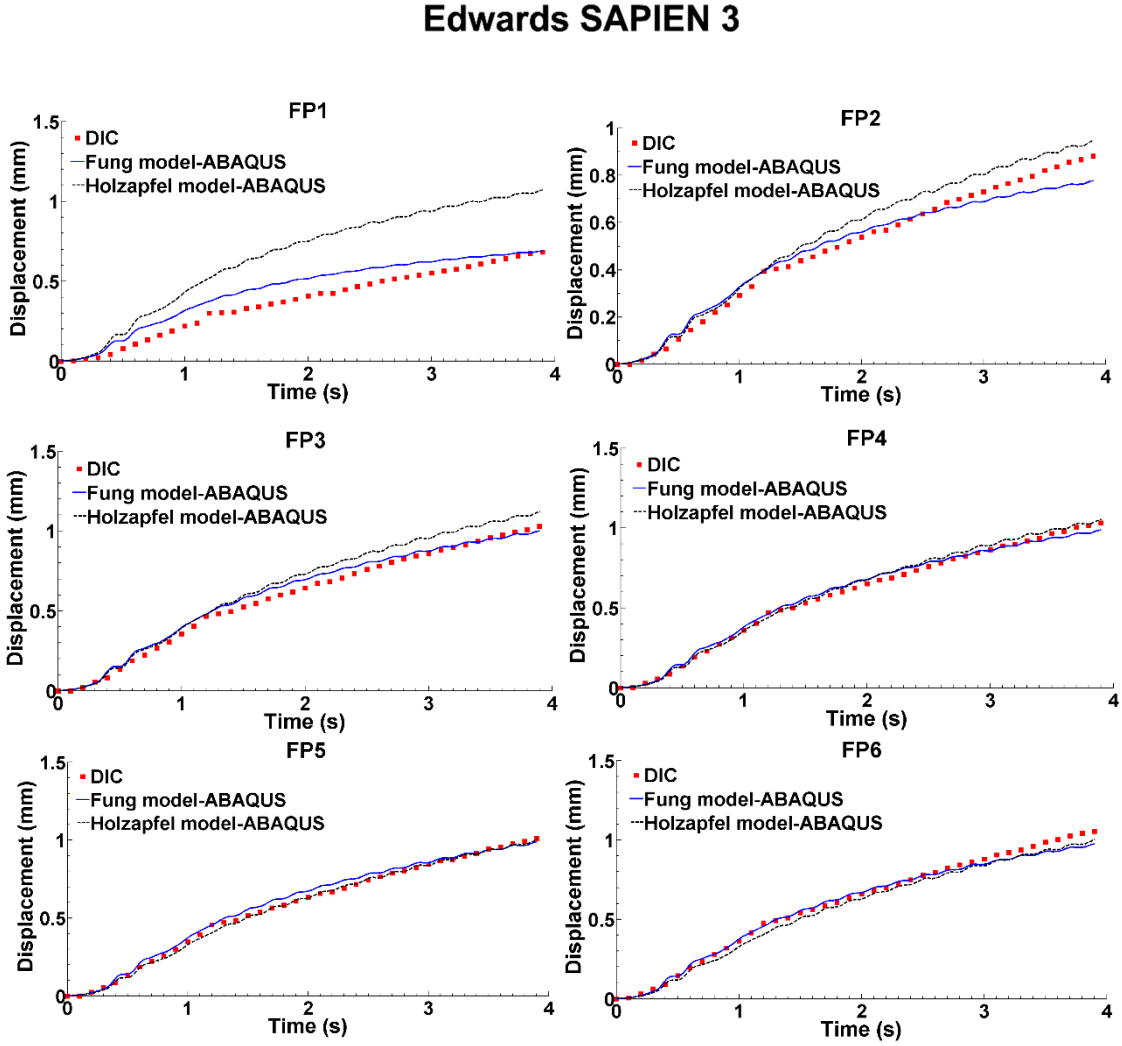

Figure 6.9: Displacement-time curves of the six facet points on the leaflets of Edward SAPIEN 3.

were obtained from the FE simulations and compared with the displacement contour plots obtained from the DIC tests. As shown in Figure 6.10, the anisotropic Fung model simulated the surgical valve leaflet displacement better than the HGO model. Therefore, at the end of first step of the optimization, between the two constitutive models, the 3D anisotropic Fung model was chosen for the second step of the optimization procedure.

Table 6.2: Material parameter (c) coefficient for the Fung model after the first-step of the optimization procedure.

Bioprosthesis	c (kPa)
CE PERIMOUNT Magna	171.10
CoreValve	105.53
SAPIEN 3	52.32

Table 6.3: Optimized Holzapfel-Gasser-Ogden model parameters after the first-step of the optimization procedure.

Bioprosthesis	C_{10} (kPa)	k_1 (kPa)	k_2	κ
CE PERIMOUNT Magna	1457.56	584.76	820.64	0.299
CoreValve	764.27	1166.40	3986.86	0.292
SAPIEN 3	1772.98	1058.47	984.19	0.287

Table 6.4: Optimization objective functions based on the DIC measurements.

Bioprosthesis	Fung	Holzapfel-Gasser-Ogden
CE PERIMOUNT Magna	5.43E-06	1.43 E-05
CoreValve	1.55 E-06	4.41 E-06
SAPIEN 3	3.77 E-06	1.92 E-05

In the second step, bioprosthetic leaflet deformation was simulated under dynamic physiological loading condition that was obtained from in vitro tests in the pulse duplicator system. The range of initial values in the second step of the optimization was $0.8 \times \mathbb{b}_{(First-step\ optimization\ estimate)} \leq \mathbb{b} \leq 1.2 \times \mathbb{b}_{(First-step\ optimization\ estimate)}$, $0.9 \times c_{(First-step\ optimization\ estimate)} \leq c \leq 1.1 \times c_{(First-step\ optimization\ estimate)}$, and $1000 \leq \alpha \leq 11000$. Three-dimensional generalized anisotropic Fung model parameters of the leaflets and Rayleigh damping coefficient for the three bioprostheses were estimated

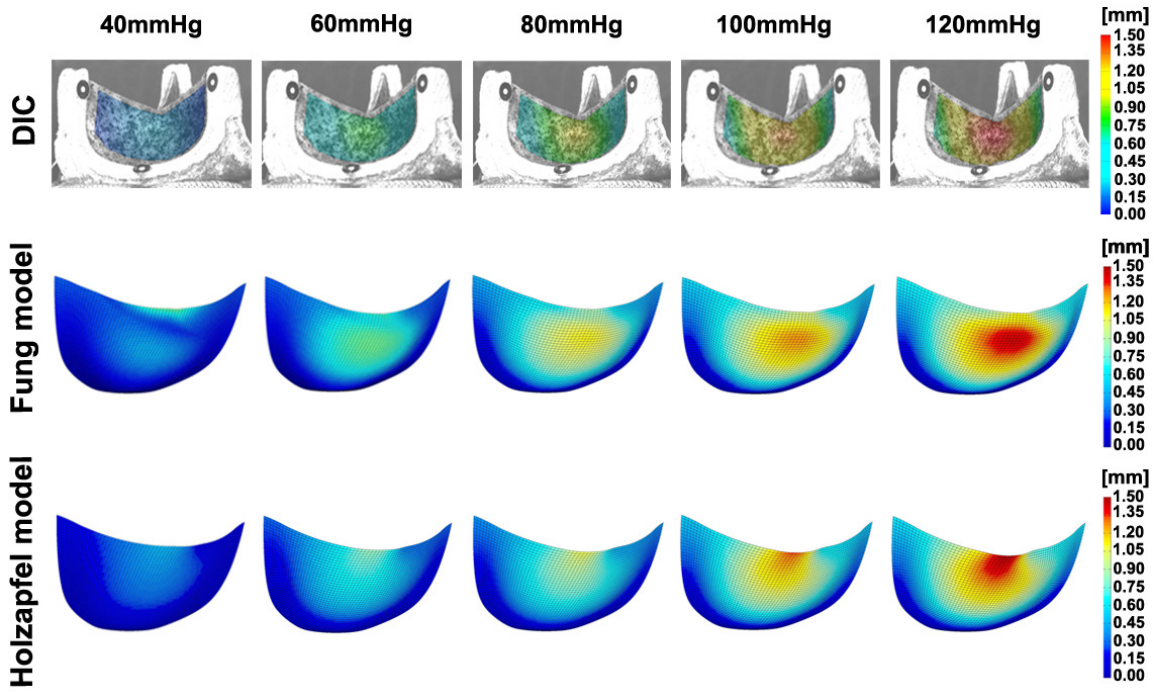

Figure 6.10: Comparison of displacement contour plots of PERIMOUNT Magna leaflets obtained from the FE simulations and DIC test at pressures of 40, 60, 80,100 and 120 mmHg.

using PSO method in Isight by matching the middle point distance of one leaflet in the FE simulations with the averaged experimental data (Fig. 6.11). After another 500 iterations, the optimization results showed a reasonable agreement with the experimental data. The estimated material parameters of the leaflets for the three heart valves are listed below for the 3D anisotropic Fung model. In addition, the estimated values for c and the viscous damping coefficient are presented in Table 6.5.

$$\mathbb{b}_{\text{PERIMOUNT Magna (estimated values)}} = \begin{bmatrix} 63.42 & 31.84 & 51.29 & 17.37 & 49.02 & 39.39 \\ & 63.74 & 46.75 & 68.38 & 63.09 & 19.22 \\ & & 62.82 & 38.51 & 60.17 & 55.50 \\ & & & 14.30 & 15.47 & 28.04 \\ & & \text{Symmetric} & & 47.30 & 13.69 \\ & & & & & 67.53 \end{bmatrix},$$

$$\mathbb{b}_{\text{CoreValve (estimated values)}} = \begin{bmatrix} 64.10 & 38.51 & 57.14 & 18.89 & 44.91 & 47.58 \\ & 63.25 & 45.96 & 62.37 & 61.13 & 25.19 \\ & & 71.65 & 42.18 & 69.83 & 58.04 \\ & & & 15.45 & 14.33 & 27.93 \\ & & \text{Symmetric} & & 43.87 & 17.01 \\ & & & & & 66.12 \end{bmatrix},$$

$$\mathbb{b}_{\text{SAPIEN 3 (estimated values)}} = \begin{bmatrix} 87.45 & 37.88 & 56.25 & 18.49 & 45.47 & 37.23 \\ & 83.97 & 43.50 & 70.21 & 71.65 & 25.72 \\ & & 89.93 & 43.70 & 62.41 & 58.98 \\ & & & 13.92 & 15.12 & 27.96 \\ & & \text{Symmetric} & & 43.54 & 16.47 \\ & & & & & 68.56 \end{bmatrix}.$$

In addition, after completing the second optimization step, the optimized material coefficients were double checked to make sure both convergence criteria are met. As an example, in the CE PERIMOUNT Magna bioprosthesis, the displacement of three facet points in the commissure (FP1), free edge (FP4), and belly region (FP6) are shown below in Fig. 6.12 based on the coefficients obtained from the first- and second-step of the optimization procedure.

6.3.2 Leaflet stress distribution

Using the optimized parameters, the maximum in-plane principal stress distribution of 25-mm CE PERIMOUNT Magna, 26-mm CoreValve, and 26-mm SAPIEN 3 were obtained and shown separately in Figure 6.13, 6.14, and 6.15, respectively. Two cardiac cycles were simulated to guarantee cycle invariance. The left-side columns depict the images of valve opening and closing in the pulse duplicator, captured by the high-speed camera. In the systole, high stress regions were primarily observed in the fixed boundary edges of the three bioprostheses. The peak leaflet stress value during systole for the CE PERIMOUNT Magna, CoreValve, and SAPIEN 3 reached to 3.29, 7.25 and 7.53 MPa, respectively. During diastole, the peak stress value of the PERIMOUNT Magna,

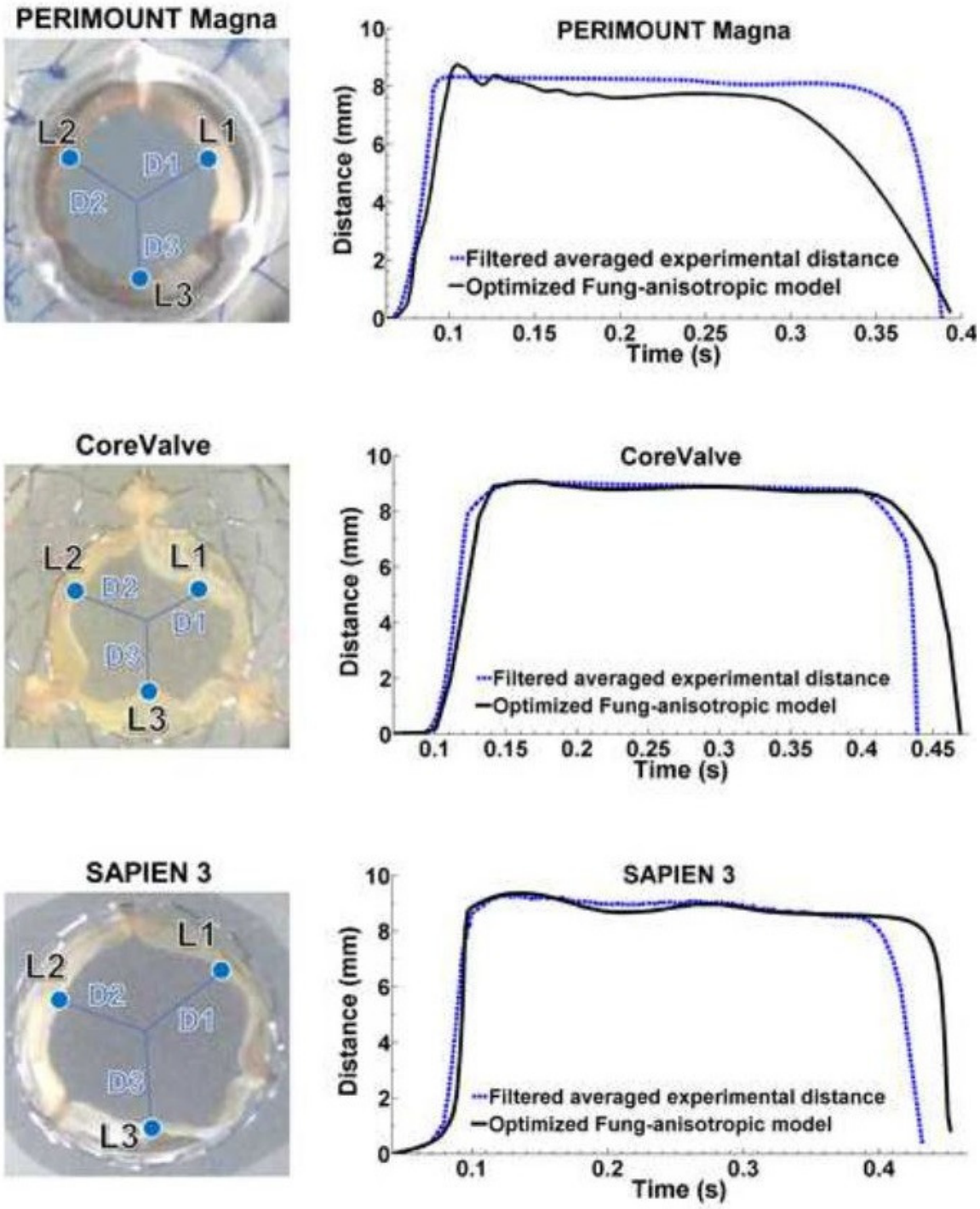

Figure 6.11: Middle point displacement of the leaflet for the three valves; comparing optimized FE simulations with the experimental data. The average standard deviation for the three leaflets based on the experimental data was ± 0.38, ± 0.35, and ± 0.18 mm for the CE PERIMOUNT Magna, CoreValve, and SAPIEN 3, respectively.

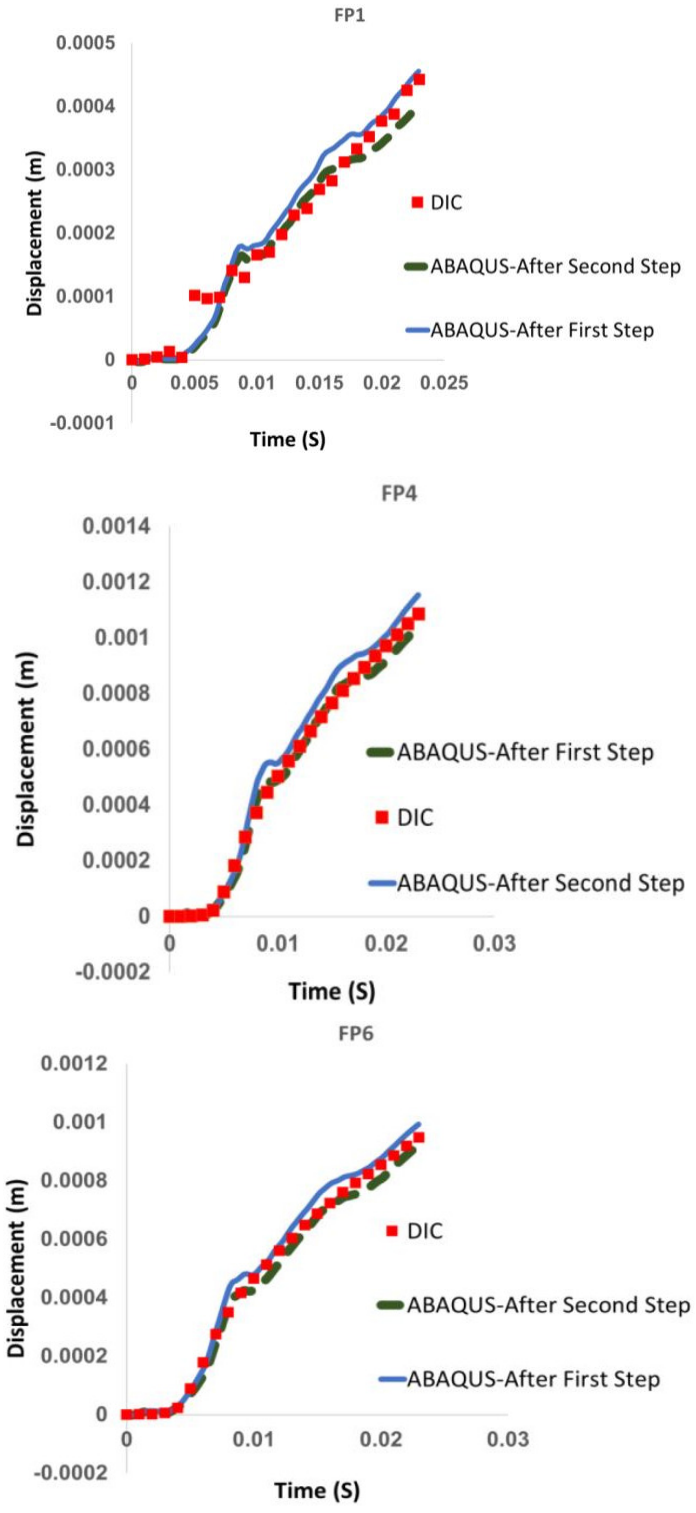

Figure 6.12: Displacement of three facet points in the commissure (FP1), free edge (FP4), and belly region (FP6) of Magna bioprosthesis based on coefficients obtained from the first- and second-step of the optimization procedure.

Table 6.5: Material parameter and viscous damping coefficient for 3D anisotropic Fung model.

Bioprosthesis	c (Material parameter, kPa)	α (Viscous damping, $1/s$)
CE PERIMOUNT Magna	90.72	10642
CoreValve	100.29	8313
SAPIEN 3	47.53	4800

CoreValve, and SAPIEN 3 leaflets reached to 0.99, 1.01 and 2.53 MPa, respectively. In CE PERIMOUNT Magna and Edwards SAPIEN 3, the high stress regions were observed close to the commissures in the fully closed position. For Medtronic CoreValve, however, the maximum stress values were observed in the lower leaflet belly region.

To compare the leaflet stress distribution among the three bioprostheses, contours of maximum in-plane principal stress of the leaflets were determined at an identical pressure gradient in the diastole and systole (i.e., 16kPa and 3.3kPa). As shown in Figure 6.16A, the peak of maximum in-plane principal stress in the diastole was 0.98, 0.96 and 2.95 MPa for the CE PERIMOUNT Magna, CoreValve, and SAPIEN 3, respectively. It can be seen that CoreValve had the lowest peak stress value at the identical pressure value during diastole. Figure 6.16B, further demonstrates that the value of peak stress reached to 1.64, 4.14, and 6.87 MPa at the pressure gradient 3.3kPa (≈ 25 mmHg) in the systole for the PERIMOUNT Magna, CoreValve, and SAPIEN 3 valves, respectively. Unlike diastole, the peak stress in the PERIMOUNT Magna valve was significantly lower than the CoreValve and SAPIEN 3 bioprostheses. Moreover, to quantify the difference in stress distribution among the three valves at the identical pressure gradient, the maximum in-plane principal stress histogram of the leaflets was presented in Figure 6.17. SAPIEN 3 had significantly more elements with stress values higher than 600 kPa (35.7%) compared to the PERIMOUNT Magna and

CoreValve. In addition, 12.7% of elements in SAPIEN 3 had stress values higher than 1,000 kPa (1MPa). On the other hand, 94.9% and 98.7% of elements in the CE PERIMOUNT Magna and CoreValve had stress values of less than 600 kPa, respectively. At the systole, 7.5%, 8.0 % and 12.7% of elements in the PERIMOUNT Magna, CoreValve and SAPIEN 3 models reached to stress values higher than 600 kPa, respectively. This observation demonstrates many elements with high stress values during diastole may affect long-term valve durability more than the systole phase. However, the maximum leaflet stress during diastole was 40%, 77% and 57% less than the maximum principal stress during systole for the PERIMOUNT Magna, CoreValve, and SAPIEN 3 valves, respectively.

6.4 Discussion

6.4.1 Summary

In the present chapter, we presented a non-invasive material characterization framework to determine mechanical propertied of soft tissue employed in bioprosthetic heart valves. We characterized three-dimensional anisotropic mechanical properties of leaflets used in two commercially available TAVs (i.e., Edwards SAPIEN 3 and Medtronic CoreValve), and compared the results to that of a commonly used and well-examined surgical bioprosthesis (i.e., Carpentier-Edwards PERIMOUNT Magna aortic heart valve). High resolution DIC was used to quantify bioprosthetic valve leaflet displacement under a well-defined loading condition. In addition, the bioprosthetic valves were examined under dynamic physiological loading condition in a pulse duplicator system. A two-step iterative optimization approach was then utilized to determine 3D anisotropic mechanical properties

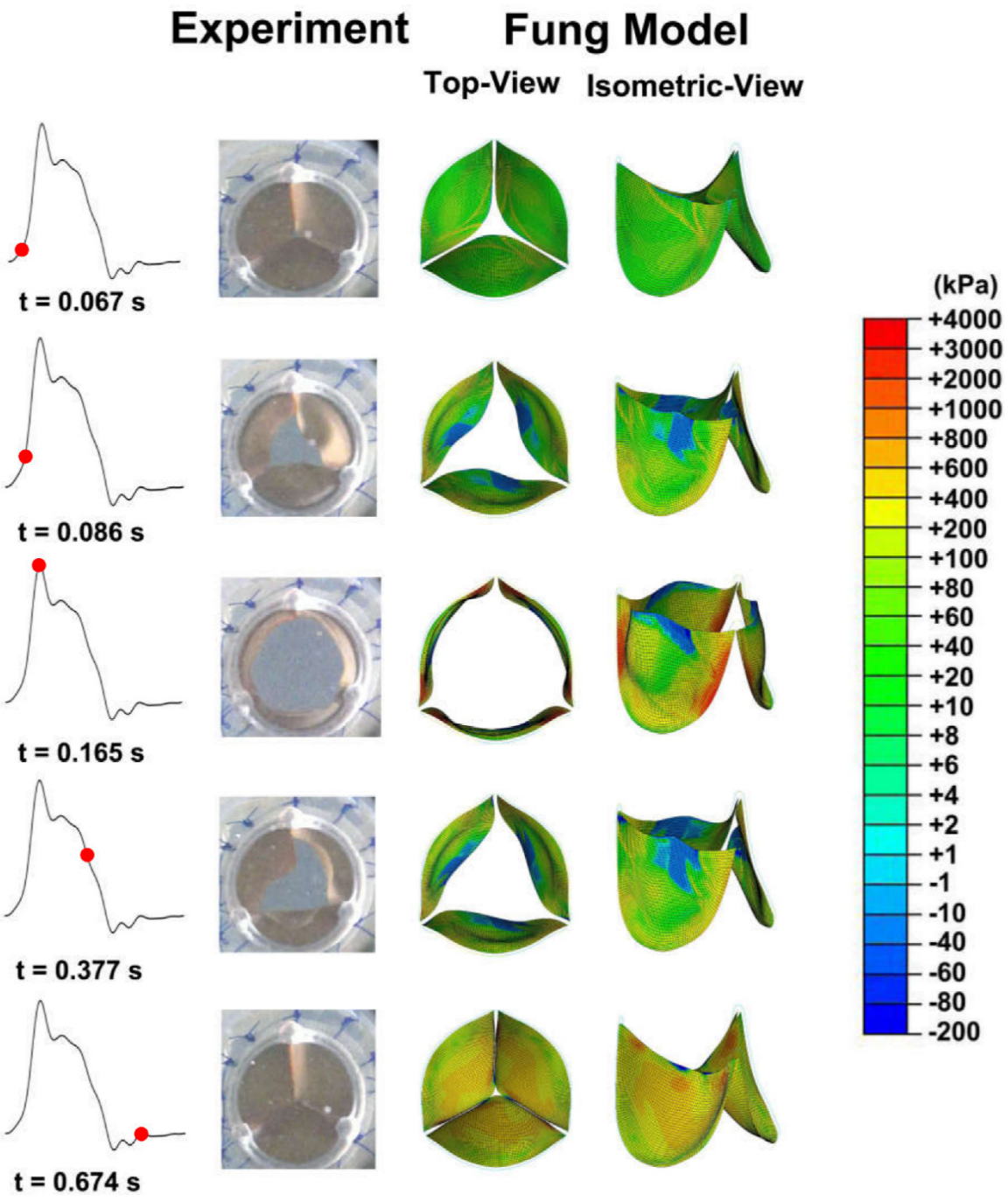

Figure 6.13: Comparison of in-vitro leaflet motion with FE simulations throughout a complete cardiac cycle for the valves. The left plot represents flow curve. (Left column) Experimental data (Middle and right columns) the maximum principal stress distributions on the valve based on Fung-anisotropic model, Carpentier-Edwards PERIMOUNT Magna.

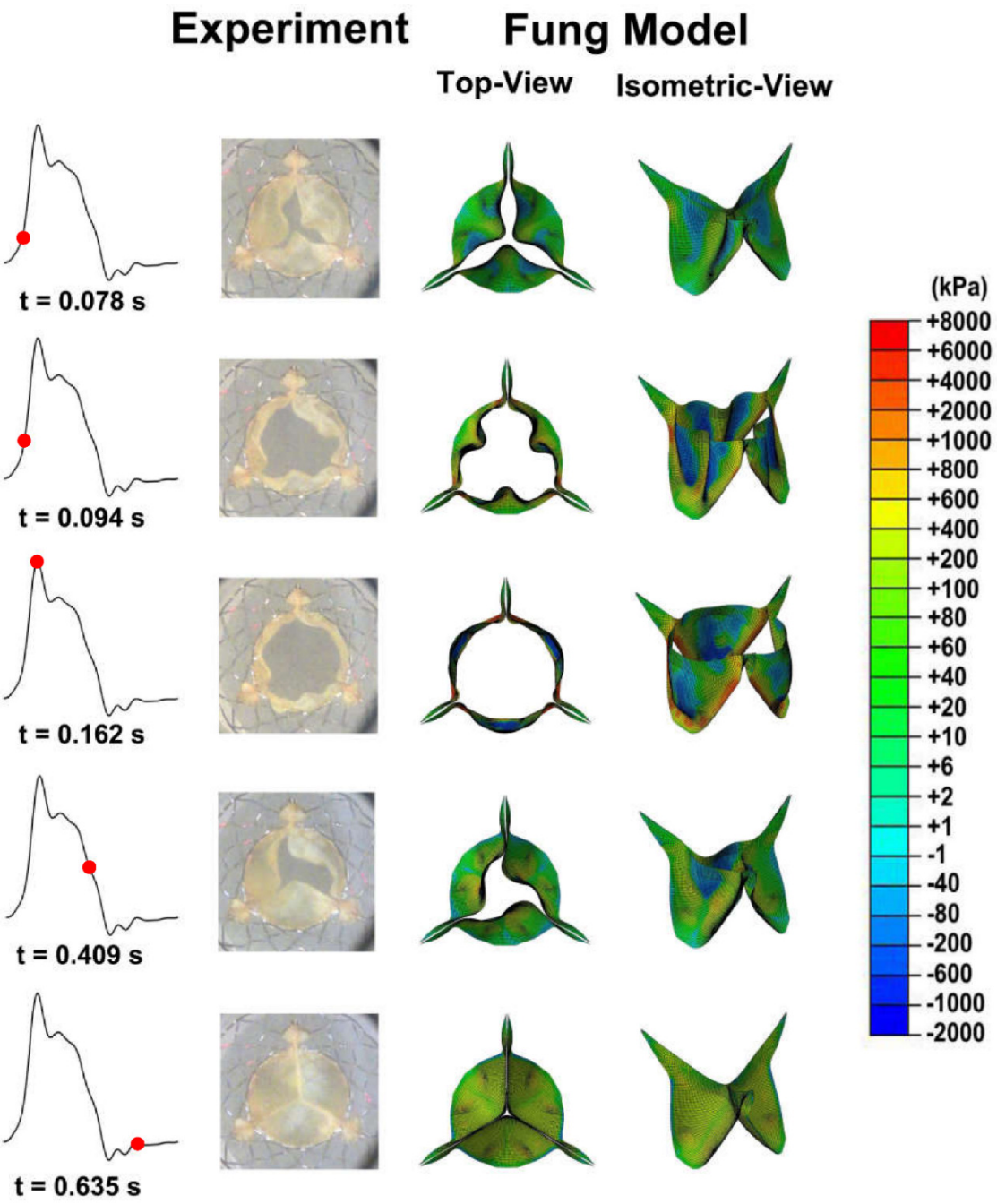

Figure 6.14: Comparison of in-vitro leaflet motion with FE simulations throughout a complete cardiac cycle for the valves. The left plot represents flow curve. (Left column) Experimental data (Middle and right columns) the maximum principal stress distributions on the valve based on Fung-anisotropic model, Medtronic CoreValve.

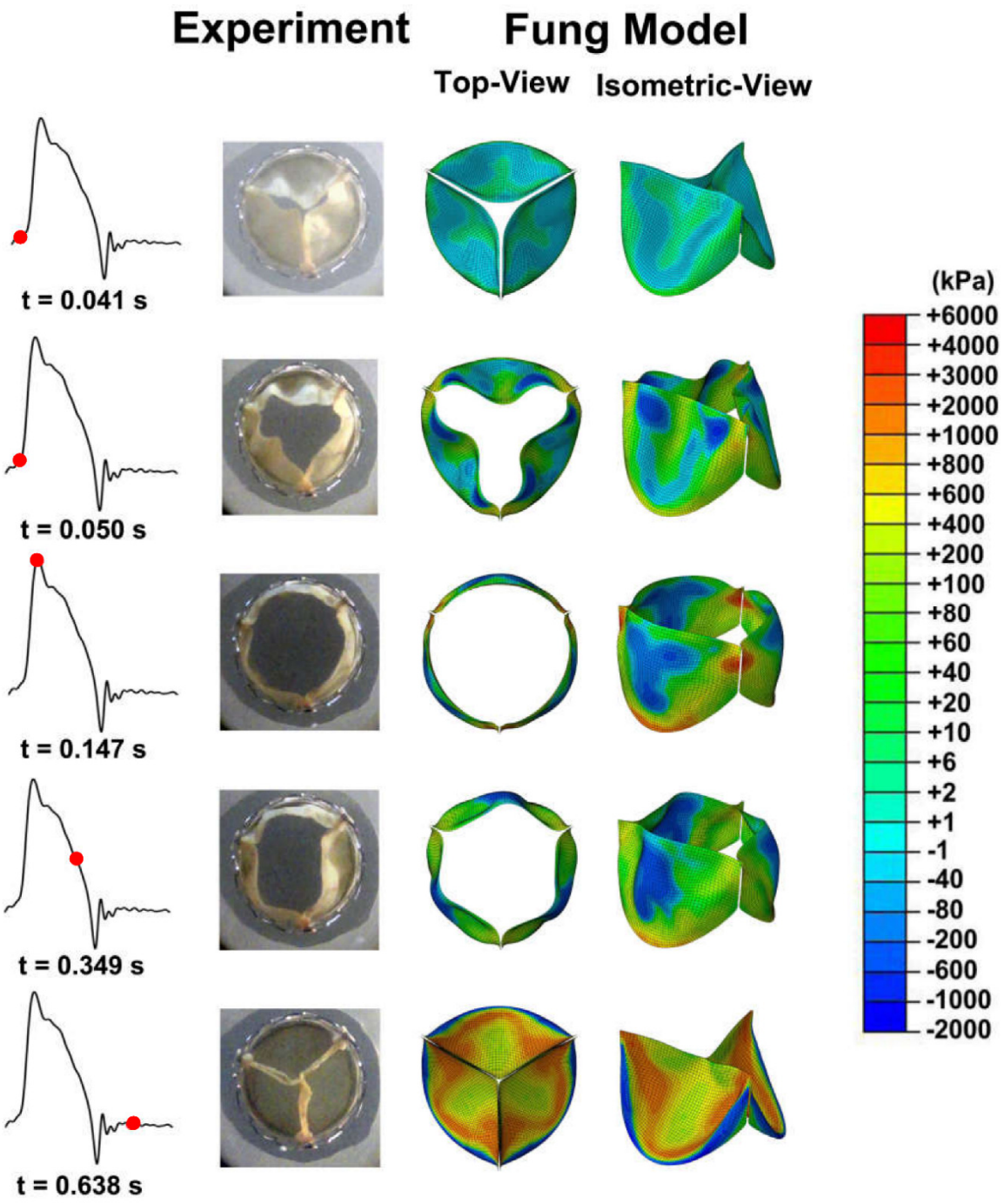

Figure 6.15: Comparison of in-vitro leaflet motion with FE simulations throughout a complete cardiac cycle for the valves. The left plot represents flow curve. (Left column) Experimental data (Middle and right columns) the maximum principal stress distributions on the valve based on Fung-anisotropic model, Edward SAPIEN 3.

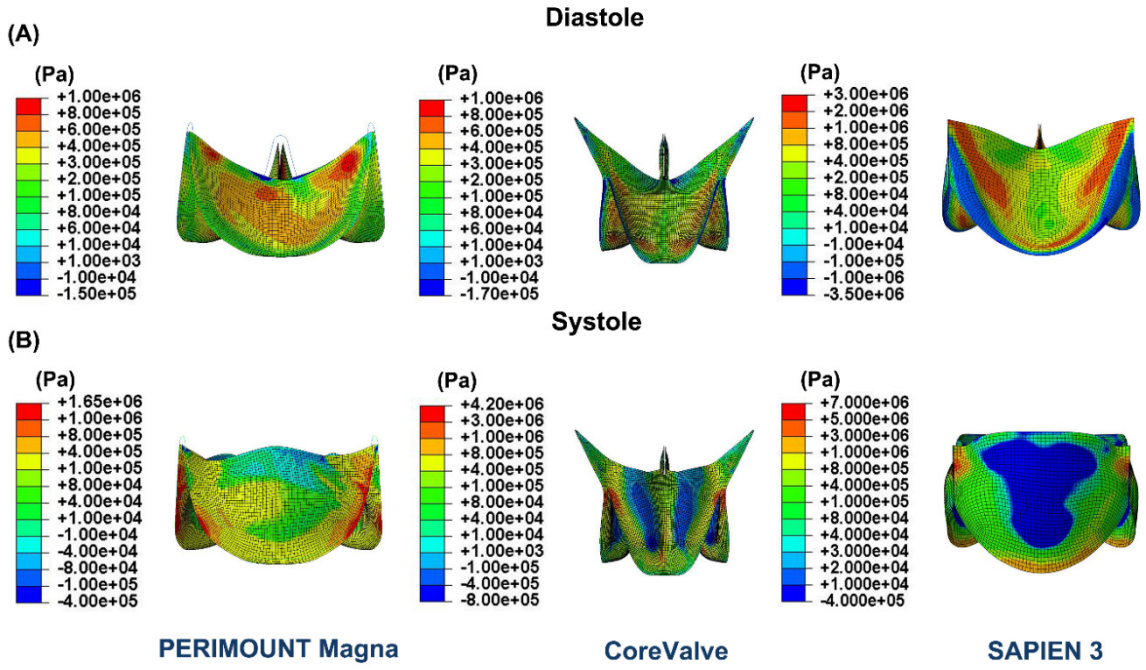

Figure 6.16: Maximum in-plane principal stress contour plots of (Left) Carpentier-Edwards PERIMOUNT Magna, (Center) Medtronic CoreValve, (Right) Edward SAPIEN 3 (A) Diastole at the pressure gradient 16kPa (≈ 120 mmHg) (B) Systole at the pressure gradient 3.3kPa (≈ 25 mmHg).

of the leaflets. Using the optimized material parameters, the maximum in-plane principal stress distribution of the three bioprostheses were obtained and compared during both systole and diastole.

6.4.2 Long-term Durability

In the past few years, use of bioprosthetic valves for aortic valve replacement has increased considerably (Mack and Holmes 2016). To choose an appropriate bioprosthetic heart valve for aortic valve replacement, long-term durability of tissue heart valves is an important factor. Especially, to expand the reach of TAVR into low-risk younger patients, long-term durability of TAVs must be comparable to surgical bioprostheses. In surgical bioprosthetic valves, leaflets degenerate through two distinct but potentially synergistic

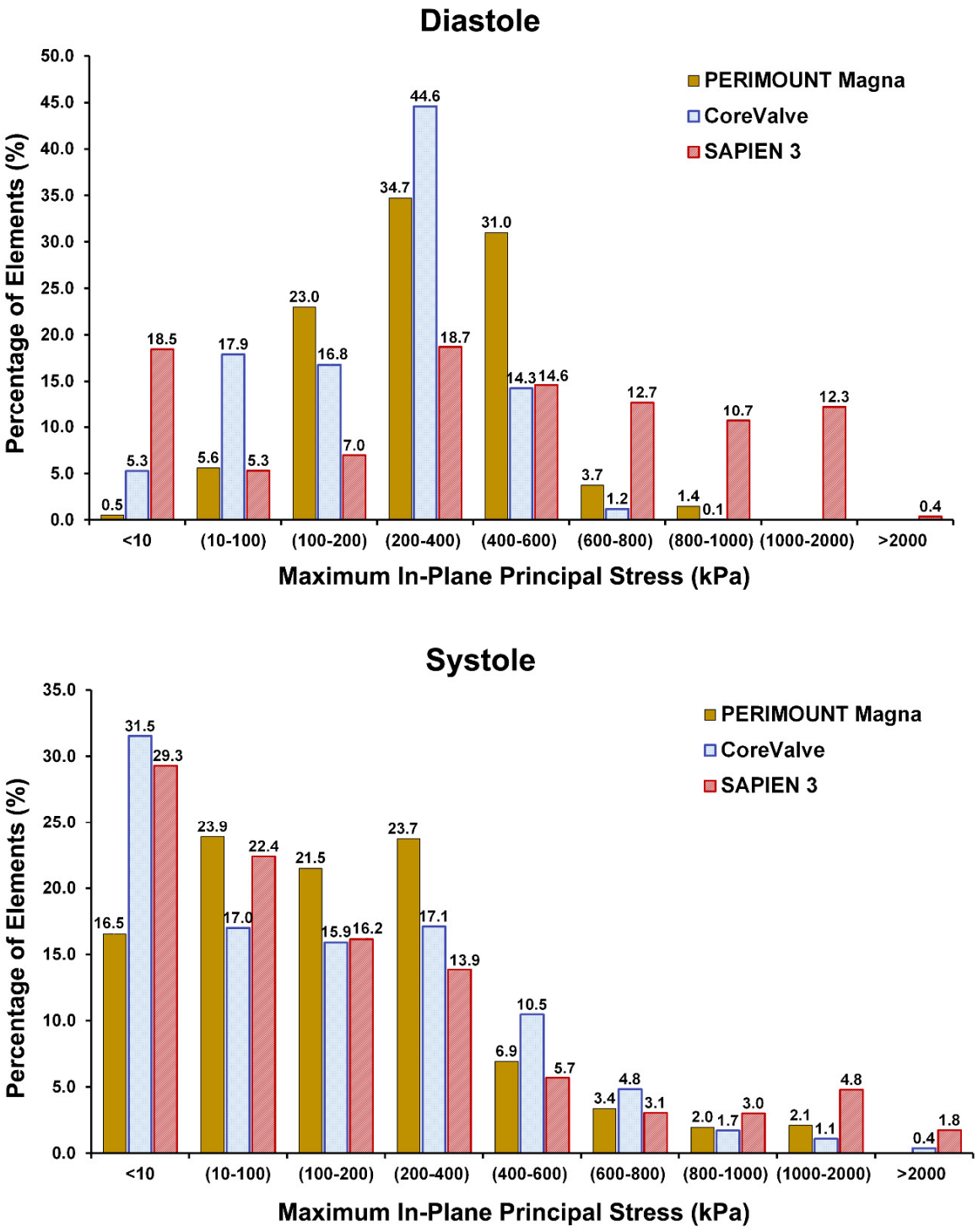

Figure 6.17: The maximum in-plane principal stress histogram of the leaflets.

mechanisms: (i) calcification and (ii) fatigue-induced structural deterioration (Schoen et al. 1985, Schoen 2012). Since the commercially available TAV leaflets are made from chemically treated bovine or porcine pericardium tissue, it can be postulated that the structural deterioration of TAVs occurs via the two failure mechanisms. Although, a unified definition of structural valve degeneration does not exist in the literature, the rate of structural valve degeneration in surgical bioprostheses is known to be less than 15% at 10 years (Rodriguez-Gabella et al. 2017). In a retrospective cohort study, Forcillo and colleagues (Forcillo et al. 2013) studied 2,405 patients with a mean age of 71 ± 9 years old who underwent aortic valve replacement with Carpentier-Edwards surgical pericardial bioprostheses. They found that the overall freedom rate of valve reoperation for valve dysfunction averaged 96% ± 1% and 67% ± 4% at 10 and 20 years, respectively. In addition, it is well known that the rate of reoperation for surgical valve dysfunction is strongly affected by age. Bourguignon and colleagues (Bourguignon, El Khoury, et al. 2015) showed that the freedom from reoperation rates attributable to structural valve deterioration in patients aged 60 or younger who received CE PERIMOUNT aortic valve were 88.3% ± 2.4% and 38.1% ± 5.6% at 10 and 20 years, respectively. On the other hand, clinical data regarding long-term durability of TAVs beyond 5 years is still limited. Dvir and colleagues (Dvir et al. 2016) recently demonstrated the estimated structural valve degeneration rate of Cribier-Edwards, Edwards SAPIEN, and Edwards SAPIEN XT was approximately 50% at 8 years. In addition, Toggweiler and colleagues (Toggweiler et al. 2013) reported that 9.7% of living patients in the study had moderate prosthetic valve

failure after 5 years. On the other hand, the 5-year rate of prosthesis failure was 1.4% with the Medtronic CoreValve device (Barbanti et al. 2015).

6.4.3 Computational Modeling

Computational modeling and simulation can provide qualitative and quantitative insights into the durability of bioprosthetic heart valves (Rabkin and Hsu 1975, Sacks, Zhang, and Wognum 2016, Soares et al. 2016, Zhang and Sacks 2017, Zioupos and Barbenel 1994). In the presence of limited clinical follow-up data for TAVs, several computational simulations have been performed to obtain stress and strain distributions of TAV leaflets (Abbasi and Azadani 2017, Abbasi and Azadani 2015, Abbasi et al. 2016, Hsu et al. 2015, Jermihov, Jia, Sacks, Gorman, Gorman III, et al. 2011, Martin and Sun 2015, Xuan et al. 2017). The simulation results showed higher mechanical stress in TAVs compare to surgical bioprosthetic valves. The increased mechanical stress on the leaflets may explain the relatively higher rate of accelerated tissue degeneration and diminished long-term valve durability. Considering the results presented in this study, there might also be a difference in the long-term durability of different TAV models and designs, as previously observed in clinical studies (Barbanti et al. 2015, Toggweiler et al. 2013). However, due to the limited number of valves examined in this study, it is prudent not to over-interpret the simulation results. The results must be validated by retrospective cohort studies to confirm the findings in presence of calcification and other patient related factors.

Accuracy of computational modeling and simulations depends on the accuracy of the prescribed material properties for the fixed bovine and porcine pericardium leaflets (Humphrey 2003). Regional structural and compositional heterogeneity has been observed

in pericardium leaflets (Billiar and Sacks 2000, Sacks 2000, Simionescu, Simionescu, and Deac 1993). 3-D anisotropic constitutive models should therefore be considered for the fixed-biological tissue to fully describe the three-dimensional mechanical properties of the leaflets. Non-invasive material characterization methods, such as the one presented in this chapter and other published studies (Abbasi et al. 2016, Murdock, Martin, and Sun 2018, Aggarwal and Sacks 2016, Lee et al. 2014), can be used to determine the out-of-plane and shear coefficients of the bioprosthetic heart valve leaflets. In addition, it is imperative to evaluate bioprosthetic heart valves under dynamic loading condition to elucidate failure mechanism in bioprostheses. Simplified loading conditions, e.g. quasi-static loading, may not represent the true loading condition that the valves are exposed to following replacement in clinical practice. Moreover, experimental validation of the computational simulations should be an indispensable part of evaluation.

6.5 Conclusions

In summary, we developed a two-step optimization procedure to determine 3D anisotropic mechanical properties of pericardial valves under physiological loading conditions. Three different bioprosthetic heart valves with comparable size were investigated. The optimized material parameters for each valve were implemented in FE simulations to assess the leaflet deformation and stress distribution. During systole, high stress regions were primarily observed at the boundary edge for the bioprostheses. However, during diastole, high stress regions were primarily observed in the commissures for CE PERIMOUNT Magna and Edwards SAPIEN 3. In contrary to the two other bioprostheses, the maximum stress values for the CoreValve were seen in the lower leaflet

belly region. In addition, the CoreValve had the lowest peak stress value at the identical pressure value during diastole compared to the CE PERIMOUNT Magna and Edwards SAPIEN 3. The present work presents a reliable approach to compare leaflet stress distribution among different bioprostheses. Further studies are also motivated to obtain 3D anisotropic mechanical properties of pericardial leaflets under physiological loading condition using fluid-solid interaction simulations.

CHAPTER 7: GEOMETRY OPTIMIZATION FRAMEWORK FOR TAV LEAFLET SHAPE

7.1 Introduction

Durability of tissue heart valves results primarily from their ability to resist two distinct yet potentially synergistic failure mechanisms (i) calcification and (ii) fatigue-induced structural deterioration (Schoen and Levy 1999b). Since most of the TAV devices are fabricated from chemically treated bovine or porcine pericardium tissue, it can be postulated that the structural deterioration of TAVs occurs via the two failure mechanisms. It has been shown that mechanical stress on bioprosthetic heart valve leaflets can be linked with the leaflet degeneration (Levy et al. 1983, Schoen et al. 1985, Schoen and Levy 1999b, Sacks and Schoen 2002b). There is a correlation between the regions of tissue rupture in bioprosthetic heart valves and excessive mechanical stress on the leaflets (Sacks and Schoen 2002a, Ferrans et al. 1978a, Sacks 2001, Schoen et al. 1987). Moreover, it is widely accepted that high stress regions initiate calcification by damaging the structural integrity of tissue (Levy et al. 1983, Schoen and Levy 1999b, Schoen et al. 1985). Therefore, proper evaluation of the leaflet stress distribution is essential to assess long-term durability of TAV devices (Zhang and Sacks 2017, Soares et al. 2016, Abbasi et al. 2016, Abbasi and Azadani 2015).

Minimizing the peak stress valve in bioprosthetic heart valve leaflets is a crucial to maximize long-term durability of the tissue heart valves (Vesely 2003). Therefore, parametric studies on the effect of leaflet geometry on valve peak stress have been inspired and developed (Li and Sun 2017, Hsu et al. 2015, Xu et al. 2017). In the present chapter, we aimed to develop an automatic optimization framework using commercially available software packages to assess the impact of TAV leaflet design on the maximum stress value of the leaflets under dynamic physiological loading conditions. Optimized leaflet designs were achieved for two different commonly-used TAV sizes (i.e., 23 mm and 26 mm). Subsequently, the optimized leaflet designs were compared with two commercially available bioprostheses (i) Carpentier-Edwards PERIMOUNT Magna surgical bioprosthesis and (ii) Edwards SAPIEN 3 transcatheter heart valve, both are considered as gold-standard devices in today's practice of heart valve replacement.

7.2 Materials and Methods

7.2.1 Parameterization and Optimization of The TAV Leaflet Geometry

An automated geometry optimization framework was developed to reduce TAV leaflet stress under physiological loading condition. TAV leaflets with uniform thickness (t) were considered to be attached to a frame with a uniform thickness of 0.5 mm and an external diameter of D. Two different external diameters (D) were considered in this study (i) 23 mm and (ii) 26 mm. Design variables were defined using two second-order Non-uniform rational B-splines (NURBS) curves. As shown in Fig. 7.1, the approach provides effective and reliable method to explore all possible geometrical configurations for the TAVs with only 6 parameters: valve height (H), leaflet coaptation height (h), and two control points

for each one of the two second-order B-splines (i.e., X_s and Y_s for B-spline 1 in the plane of symmetry (Plane 1), and X_f and Y_f for B-spline 2 in Plane 2 which is tangent to the TAV frame as shown in Fig. 7.1). In parameterization procedure, B-spline 2 was subsequently projected on the cylinder, the TAV frame, to create a fixed-boundary edge for the leaflet.

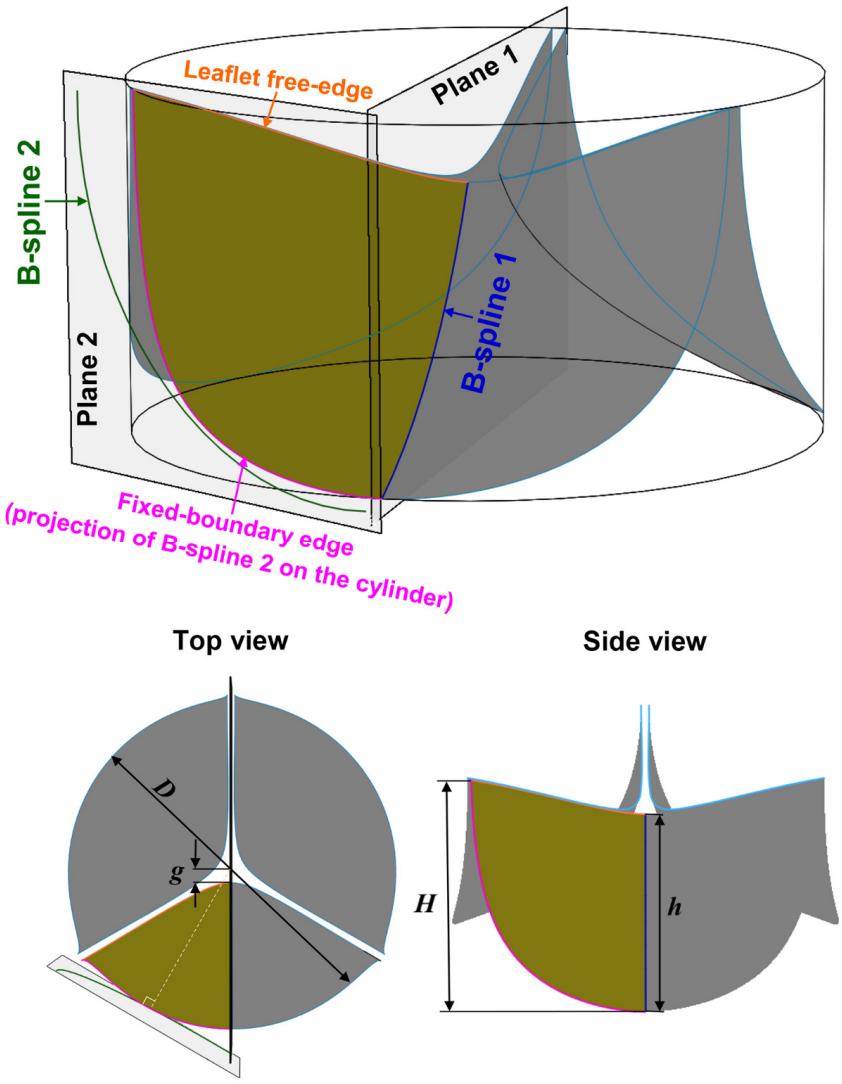

Figure 7.1. Design variables in parameterization of the TAV leaflet geometry.

The B-splines control points determine the shape of the fixed-boundary edge and the symmetric curve. Afterward, the leaflet free-edge that connects the commissure to the point of leaflet coaptation was reconstructed automatically based on the fixed-boundary edge and the symmetric curve. A small gap (g) with a constant value of 0.6 mm was considered at the center of the leaflets at the load-free initial configuration (Fig. 7.1). For mathematical formulation and further details of the parameterization in MATLAB, please refer to the supplementary materials.

The flowchart shown in Fig. 7.2 shows how the optimization procedure was implemented in this study. Using an ABAQUS Python script, the curves generated in MATLAB were imported into SolidWorks. Due to the symmetry of the TAV leaflet design, the fixed-boundary edge and the leaflet free-edge were mirrored with respect to the plane of symmetry (Plane 1). Then, a surface was created based on the boundary curves of the leaflet using Filled Surface command in SolidWorks (Fig. 7.3). The symmetric curve was used as a constraint curve in the procedure. Subsequently, the constructed leaflet was rotated ± 120° about the center of the TAV frame to create the other two leaflets (Fig. 7.3). Then using an ABAQUS Python script, the valve geometry was imported to ABAQUS and discretized using S4 and S3 shell elements. In the Python script, the average size of mesh in finite element (FE) simulations was set to be 0.3 mm. Due to high radial strength of TAV frames that is needed to provide positional stability of the valves (Abbasi et al. 2018b), the stent frame was considered to be rigid. As a result, all nodes along the fixed-edge curve were considered to be fixed in the FE simulations. In addition, a uniform leaflet thickness of 0.5 mm was considered in the simulations. Furthermore, a physiological transvalvular

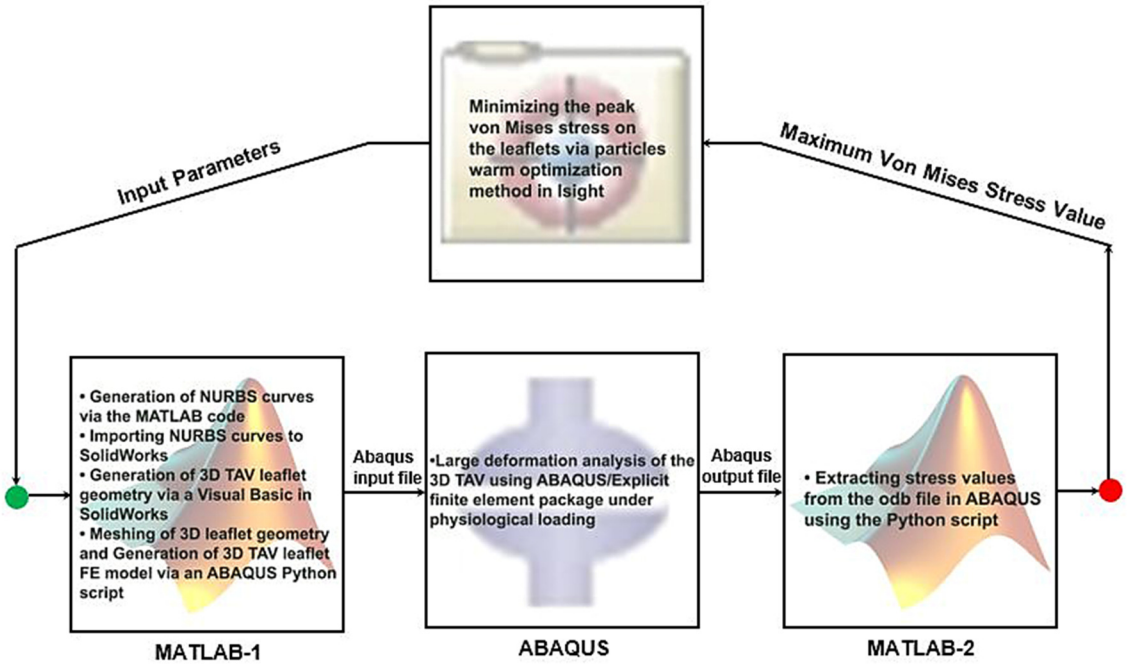

Figure 7.2. Flowchart for the optimization framework of the TAV leaflet geometry.

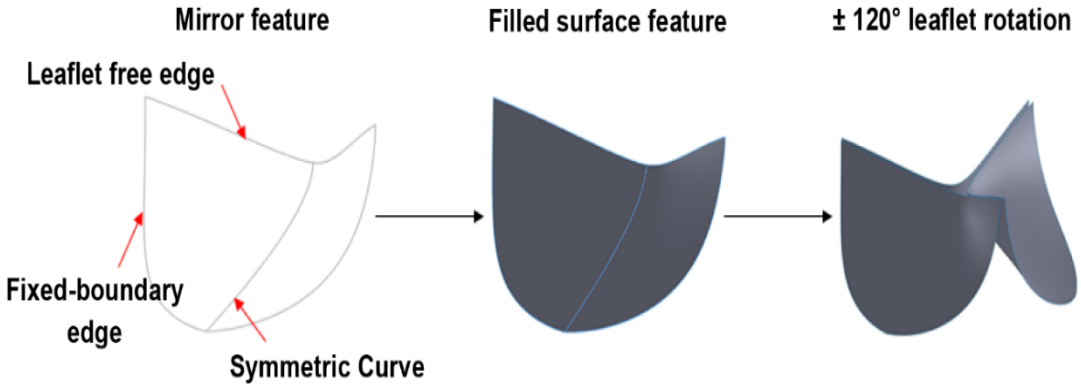

Figure 7.3. Reconstruction of the leaflet geometry in SolidWorks.

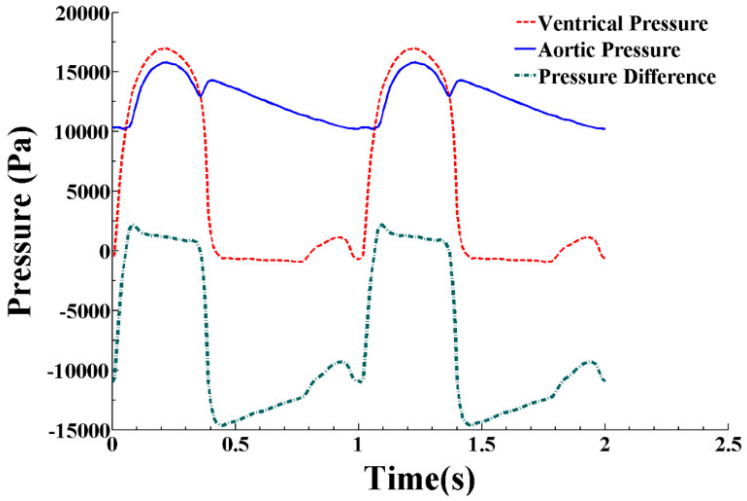

Figure 7.4. Variation in pressure in the left ventricle (red dashed line) and the aorta (blue solid line). The wave pressure (green dash-dot line) is defined as the pressure difference between the left ventricle and the aorta.

pressure gradient was applied to the leaflets as a loading condition (Fig. 7.4) (Abbasi and Azadani 2015).

In the optimization process, TAV leaflets were considered to be isotropic nonlinear hyperplastic material. A fourth-order reduced polynomial strain-energy function was fitted to experimental raw data obtained from biaxial testing of bovine pericardium samples, previously reported by our group (Abbasi and Azadani 2015).

$$W = \sum_{i=1}^{4} C_{i0} \, (\bar{I}_1 - 3)^i \qquad (1)$$

Where C_{i0} are constants and $\bar{I}_1$ is the first principal invariant of the left Cauchy–Green deformation tensor (See Table 7.1).

Table 7.1: Coefficients of fourth-order reduced polynomial strain-energy function.

C10	C20	C30	C40
1.56941E+5	8.59024E+5	-6.50847E+5	5.59565E+6

The objective of the optimization technique was minimization of the squared root of maximum von Mises stress S_{max}, defined based on the following equation:

$$S_{max} = \sqrt{S_{systole}{}^2 + S_{diastole}{}^2} \quad (2)$$

Where $S_{systole}$ and $S_{diastole}$ were the maximum Von Mises stress at the peak of systole and the peak diastolic pressure, respectively. To reduce the bending stress including tensile and compressive stresses within the leaflets of TAVs, the maximum Von Mises stress is the most appropriate objective value to be minimized in the optimization procedure. Particle swarm optimization method, a built-in algorithm in Isight, was used in the optimization procedure. Range of design parameters for two TAV sizes is listed in Table 7.2. Approximately, 500 iterations were required to reach convergence for each one of the TAV sizes.

Table 7.2: Range of design parameters in the optimization procedure.

Parameters	H **(mm)**	h **(mm)**	X_f **(mm)**	Y_f **(mm)**	X_s **(mm)**	Y_s **(mm)**
D **= 23 mm**	10.3 ~ 12.3	7.0 ~ 9.0	9.0 ~ 12.7	0.0 ~ 1.0	7.0 ~ 11.0	0.0 ~ 6.0
D **= 26 mm**	14.0 ~ 16.00	10.0 ~ 12.5	9.0 ~ 12.7	0.0 ~ 1.0	7.0 ~ 11.0	0.0 ~ 6.0

7.2.2 Comparison with The Commercially Available Bioprosthetic Heart Valves

After completing the optimization procedure, the optimized 23-mm and 26-mm leaflet geometries were compared with comparable size Carpentier-Edwards PERIMOUNT Magna surgical bioprostheses. In addition, the 26-mm optimized leaflet geometry was compared with 26-mm Edwards SAPIEN 3 transcatheter heart valve. To compare leaflet

stress distribution, a 3-D generalized anisotropic Fung-type hyperelastic material model was used to characterize the anisotropic behavior of the leaflets. A generalized Fung strain-energy function in 3-D space is in the form

$$\Psi = \frac{c}{2}(e^{\mathcal{Q}} - 1) + \frac{1}{\mathcal{D}}(\frac{{J_{el}}^2 - 1}{2} - \ln J_{el}) \tag{3}$$

where Ψ is the strain energy per unit of reference volume. $\mathcal{D}$ and c describe the temperature-dependent material parameters, J_{el} stands for the elastic volume ratio which is equal to J in the absence of thermal strains, and $\mathcal{Q}$ is given by

$$\mathcal{Q} = \boldsymbol{E}:(\mathbb{b}\boldsymbol{E}) \tag{4}$$

where $\mathbb{b}$ is a non-dimensional symmetric fourth-order tensor of anisotropic material constants, and $\boldsymbol{E}$ is the Green-Lagrange strain tensor, under the assumption of tissue incompressibility. Considering the incompressibility assumption ($J_{el} = 1$), the Fung strain energy function is reduced to

$$\Psi = \frac{c}{2}(e^{\mathcal{Q}} - 1) \tag{5}$$

The number of components of that must be determined is similar to the elasticity tensor, namely 21 independent components for a 3-D generalized anisotropic Fung strain-energy function as shown below.

$$\mathbb{b}_{\text{anisotropic}} = \begin{bmatrix} b_{1111} & b_{1122} & b_{1133} & b_{1123} & b_{1113} & b_{1112} \\ & b_{2222} & b_{2233} & b_{2223} & b_{2213} & b_{2212} \\ & & b_{3333} & b_{3323} & b_{3313} & b_{3312} \\ & & & b_{2323} & b_{1323} & b_{1223} \\ & & \text{Symmetric} & & b_{1313} & b_{1213} \\ & & & & & b_{1212} \end{bmatrix} \quad (6)$$

The following material coefficients previously reported in the literature for the bioprostheses were considered in this study (Abbasi et al. 2016, Abbasi and Azadani 2017) and chapter 6 in this dissertation.

$$\mathbb{b}_{23\text{mm}-\text{PERIMOUNT Magna}} = \begin{bmatrix} 62.95 & 36.39 & 54.14 & 17.13 & 45.45 & 41.72 \\ & 61.88 & 45.64 & 68.15 & 67.97 & 23.42 \\ & & 65.98 & 38.70 & 63.95 & 56.17 \\ & & & 14.40 & 16.26 & 27.56 \\ & & \text{Symmetric} & & 42.57 & 17.61 \\ & & & & & 60.66 \end{bmatrix},$$

$$\mathbb{b}_{25\text{mm}-\text{PERIMOUNT Magna}} = \begin{bmatrix} 63.42 & 31.84 & 51.29 & 17.37 & 49.02 & 39.39 \\ & 63.74 & 46.75 & 68.38 & 63.09 & 19.22 \\ & & 62.82 & 38.51 & 60.17 & 55.50 \\ & & & 14.30 & 15.47 & 28.04 \\ & & \text{Symmetric} & & 47.30 & 13.69 \\ & & & & & 67.53 \end{bmatrix},$$

$$\mathbb{b}_{26\text{mm}-\text{SAPIEN 3}} = \begin{bmatrix} 87.45 & 37.88 & 56.25 & 18.49 & 45.47 & 37.23 \\ & 83.97 & 43.50 & 70.21 & 71.65 & 25.72 \\ & & 89.93 & 43.70 & 62.41 & 58.98 \\ & & & 13.92 & 15.12 & 27.96 \\ & & \text{Symmetric} & & 43.54 & 16.47 \\ & & & & & 68.56 \end{bmatrix}.$$

In addition, the estimated values for *c* is presented in Table 7.3. For the surgical bioprostheses, a flexible frame with a uniform diameter (0.89 mm) and density (8,300 kg/m^3) was considered in the FE simulations. To compare the leaflet stress distribution between the commercially available bioprostheses and the optimized leaflet geometry, it was assumed that the leaflets have identical mechanical properties and thickness in each pair of comparisons. Contours of maximum in-plane principal stress of the leaflets were

Table 7.3: Material parameter for the 3D anisotropic Fung models.

Bioprosthesis	c (kPa)
23-mm PERIMOUNT Magna	24.62
25-mm PERIMOUNT Magna	90.72
26-mm SAPIEN 3	47.53

then determined at an identical pressure gradient across the valve (i.e., 16kPa ~120 mmHg). To avoid the mesh density sensitivity, the number of elements in the FE simulations were comparable for each pair of comparison groups.

7.3 Results

7.3.1 Optimization Results

The objective of the optimization procedure was to minimize the square root of maximum Von Mises stress (S_{max}) on the TAV leaflets. As shown in Fig. 7.5, there was a significant difference in the magnitude of S_{max} within the design domain. The maximum value of S_{max} was 2.46 and 2.41 MPa, while the minimum value of S_{max} was 1.30 and 1.29 MPa for the 23-mm and 26-mm TAVs, respectively. S_{max} reached to its minimum value after 451 and 477 iterations for 23-mm TAV and 26-mm TAV, respectively. The minimum value of S_{max} , hereafter referred to as the best leaflet design, was 47.2% and 46.5% less than maximum value of S_{max}, hereafter referred to as the worst leaflet design, for the 23-mm and 26-mm TAVs, respectively. In addition, for the best and the worst leaflet design configurations, the maximum Von Mises stress at the peak of systole ($S_{systole}$) and peak of diastolic pressure ($S_{diastole}$) are listed in Table 7.4.

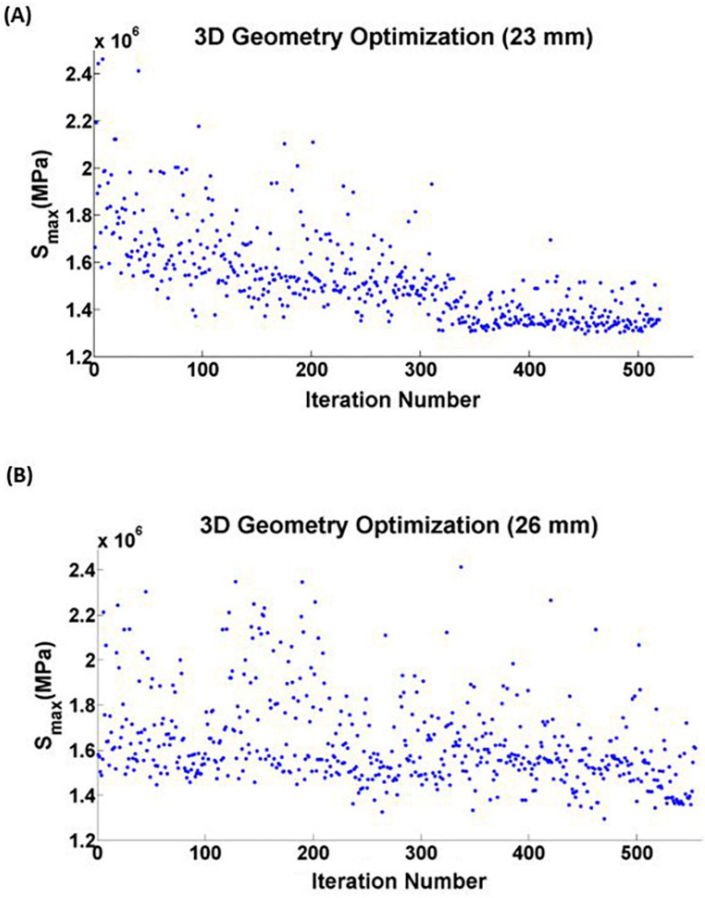

Figure 7.5. An overview of the optimization process. The square root of maximum von Mises stress (S_max) versus the number of iterations for (A) 23-mm TAV (B) 26-mm TAV.

Table 7.4: The stress values for the best and worst designs of 23 and 26 mm TAVs.

	$S_{systole}$ (MPa)	$S_{diastole}$ (MPa)	S_{max} (MPa)
23-mm TAV (best leaflet design)	0.92	0.91	1.30
23-mm TAV (worst leaflet design)	1.22	2.14	2.46
26-mm TAV (best leaflet design)	0.97	0.86	1.29
26-mm TAV (worst leaflet design)	1.02	2.19	2.41

7.3.2 The Best Design and Commercial Bioprostheses

After completing the optimization procedure, to compare leaflet stress distribution between the commercially available bioprostheses and the best leaflet design configuration, contours of the maximum in-plane principal stress of the leaflets were obtained and presented in Fig. 7.6. As shown in Fig. 7.6A, high stress regions were observed close to the commissures. The peak leaflet stress value for the 23-mm Carpentier-Edwards with a flexible frame reached to 0.98 MPa. However, the maximum in-plane stress of the best leaflet design with rigid stent was 0.9 MPa. In other words, there was an 8.2% reduction in the peak in-plane maximum principal stress in the optimized TAV geometry. An identical uniform thickness of 0.5 mm and material property were considered for the two models. Stress in the belly region was also lower in the best leaflet design than the 23-mm Carpentier-Edwards PERIMOUNT Magna surgical bioprosthesis.

A similar trend was observed with the 26-mm TAV (Fig. 7.6B). The maximum in-plane stress of the best leaflet design with rigid frame was 0.69 MPa, while the maximum in-plane stress for the 25-mm Carpentier-Edwards PERIMOUNT Magna surgical bioprosthesis with flexible frame was 0.99 MPa. In other words, there was a 30.3% reduction in the peak in-plane maximum principal stress in the optimized TAV geometry. Both models had an identical leaflet thickness of 0.56 mm and leaflet mechanical properties. Stress in the belly and commissure regions was lower in the best leaflet design compare to the 25-mm Carpentier-Edwards PERIMOUNT Magna surgical bioprosthesis (Fig. 7.6B). Lastly, the optimized 26-mm TAV was compared with 26-mm Edwards SAPIEN 3 with rigid frame (Fig. 7.6C). Identical material property and leaflet thickness

(0.32 mm) were considered for the two models. The in-plane stress distribution of the optimized geometry was considerably different from that of the 26-mm Edwards SAPIEN 3 (Fig. 7.6C). A peak leaflet stress of 0.86 MPa was found in the best design of TAV 26 mm close the fixed boundary edge. However, the peak in-plane maximum principal stress for the SAPIEN 3 was 3.42 MPa close to the commissures. In other words, there was an 74.8% reduction in the peak in-plane maximum principal stress in the optimized TAV geometry.

7.4 Discussion

7.4.1 Summary

In the present chapter, we presented an automated optimization framework to reduce TAV leaflet stress under dynamic physiological loading condition. Commercially available software packages such as MATLAB, SolidWorks, and ABAQUS/Explicit were linked together using Isight to develop the optimization framework. In addition, particle swarm optimization method was used to examine and explore the design space to obtain optimized leaflet geometry for 23-mm and 26-mm TAVs. The optimized leaflet designs were compared with two commercially available bioprostheses, i.e., Carpentier-Edwards PERIMOUNT Magna surgical bioprosthesis and Edwards SAPIEN 3 transcatheter heart valve. A considerable reduction in the peak maximum in-plane principal stress was observed in the optimized TAV geometries than the commercially available bioprostheses.

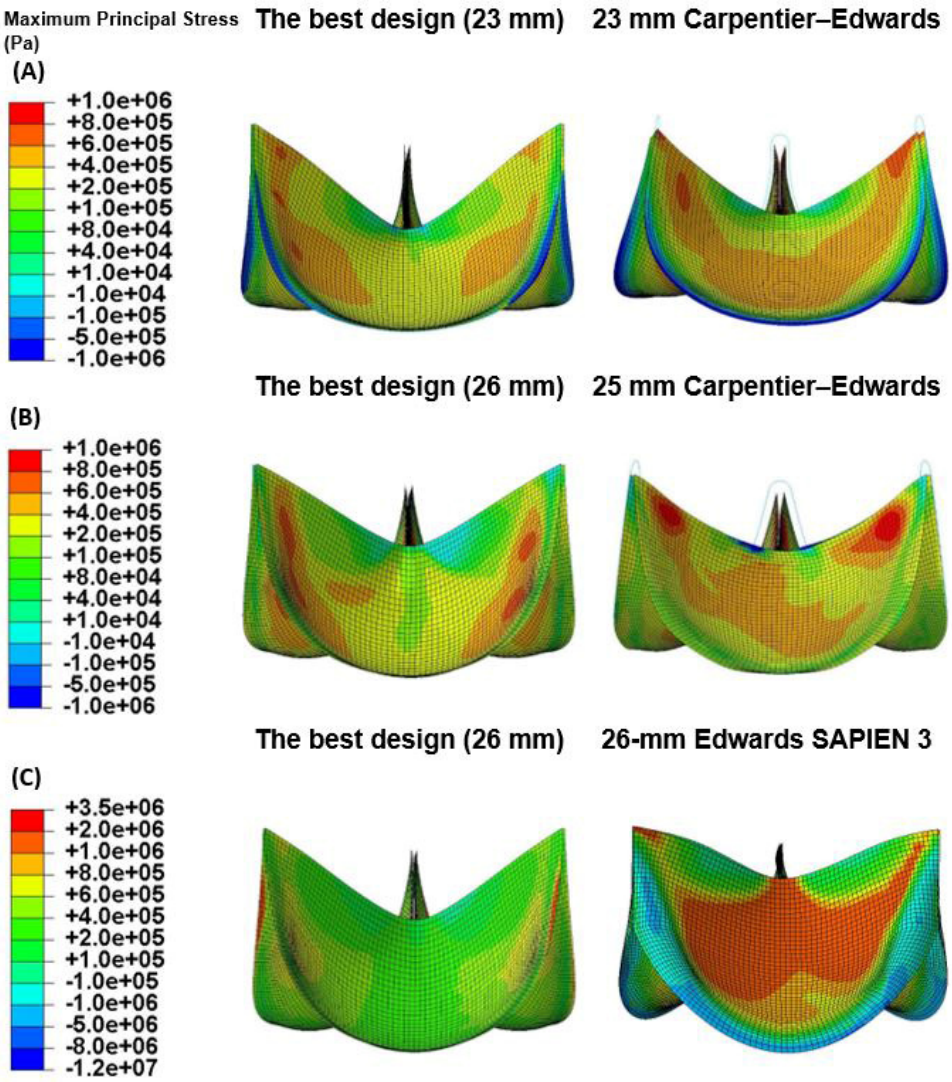

Figure 7.6: Comparison of leaflet stress distribution between the commercially available bioprostheses and the best leaflet design configuration. Contours of the maximum in-plane principal stress of (A) 23-mm Carpentier-Edwards PERIMOUNT Magna versus the best TAV leaflet design with nominal size of 23 mm (B) 25-mm Carpentier-Edwards PERIMOUNT Magna versus the TAV leaflet design with nominal size of 26 mm (C) 26-mm Edward SAPIEN 3 versus the best TAV leaflet design with nominal size of 26 mm.

7.4.2 Optimization Framework for TAV Leaflet Design

During the past couple of years, a few computational frameworks has been developed to optimize the design of bioprosthetic aortic valves leaflets to minimize the peak stress

within the leaflets and achieve a better hemodynamic performance. Recently, Li and Sun (Li and Sun 2017) performed an optimization framework to assess the impact of TAV leaflet geometry on the leaflet stress distribution and to minimize its peak stress in both circular and elliptical configurations. In the study, all initial 3D TAV geometries were generated from 2D leaflet designs and were virtually assembled automatically in ABAQUS using a Python script. A semilunar shaped 2D leaflet design consists of one leaflet–stent attachment edge and one free edge that were parameterized by two exponential functions. The computational parametric study was carried out to minimize the peak maximum principal stress on the leaflets under quasi static pressure loading. The authors found a range of leaflet peak stress between 0.87 MPa and 2.77 MPa under the nominal circular configuration. The peak stress on the optimal leaflet design was 5% lower than the nominal design derived from (Li and Sun 2010). In addition, the analysis showed that increasing the free edge width had the highest overall impact on decreasing the peak stress value of the leaflets (Li and Sun 2017). In a separate parametric study, Xu and colleagues (Xu et al. 2017) developed a computational framework to design patient-specific bioprosthetic heart valves to analyze the impact of the leaflets geometry on valve hemodynamics. Two NURBS curves were defined to parameterize the leaflets design, one free-edge curve and one belly-region curve. The suturing line length and shape were kept constant and fixed in the study. By changing the location of two control points of the NURBS curves, the valve design was parametrically and manually altered. The study showed the potential of parametric studies to create more effective design of bioprosthetic heart valves and reduce patent-prosthesis mismatch (Xu et al. 2017). In this study, we introduced an effective

approach to use commercially available software and explore a vast range of leaflet shapes with only 6 parameters: valve height, leaflet coaptation height, and two control points for the fixed-edge and free-edge B-splines. The framework creates three-dimensional leaflet geometries efficiently and eliminate any residual stress that will be created by transforming 2D planer mesh into its 3D configuration, observed in previous studies (Li and Sun 2017). The framework has the potential to determine optimized leaflet design for a wide range of TAV design parameters and control variables. In addition, it is important to determine the optimized leaflet geometry under dynamic loading condition. Simplified loading conditions, e.g. quasi-static loading in the optimization procedure, may not represent the true loading condition that the leaflets will experience following heart valve replacement in clinical practice.

7.4.3 The Impact of Leaflets Design on TAVs Long-term Durability

In the past few decades, several computational simulations have been performed to assess stress and strain distributions of bioprosthetic heart valves (Abbasi and Azadani 2015, Jermihov, Jia, Sacks, Gorman, Gorman III, et al. 2011, Abbasi et al. 2016, Abbasi and Azadani 2017, Martin and Sun 2015, Wu et al. 2018) Computational modeling can provide qualitative and quantitative insights into the durability of bioprostheses. The increased mechanical stress on TAV leaflets may lead to accelerated tissue degeneration and diminished long-term valve durability. Besides leaflet geometry, there are additional factors such as TAV crimping (Alavi, Groves, and Kheradvar 2014b) and incomplete transcatheter aortic valve expansion (Abbasi and Azadani 2015) that might affect the long-term durability of TAVs. Nevertheless, the results presented by our group and others

underline the opportunity to improve TAV leaflet design in the next generation of TAVs to enhance long-term durability of the bioprostheses.

Some limitations were inherent in this study. A major limitation associated with this study was that the effect of TAV leaflet geometry was not studied on the valve hemodynamics. Further studies are motivated to determine optimized TAV leaflet geometry under physiological loading condition using fluid-solid interaction simulations. In addition, in the optimization procedure, an isotropic nonlinear hyperplastic material was assumed for the mechanical properties of the leaflets. Further studies are motivated to use anisotropic material model for the leaflets in the optimization procedure and discretize the 3D model with structured mesh. Nevertheless, the optimized leaflet designs were compared with Carpentier-Edwards PERIMOUNT Magna surgical bioprosthesis and Edwards SAPIEN 3 using anisotropic material models. A considerable reduction in the peak in-plane maximum principal stress was observed in the optimized TAV geometry in comparison to the commercially available bioprostheses.

7.4.4 Study limitations

In FE simulations, we assumed a fixed value for Rayleigh damping coefficient to mimic viscous damping effects of surrounding fluid in TAVs. In addition, the viscous damping coefficient depends on the transvalvular pressure waveform and valve geometry in TAVs (Abbasi et al. 2016, Abbasi and Azadani 2017). Therefore, a slight change in design parameters in the optimization framework might alter the opening and closing time of simulated TAVs in FE simulations. A future study implementing fluid-structure interaction into the TAV models may improve optimization results. For the sake of

simplicity in the optimization framework, isotropic nonlinear hyperplastic material was assumed for mechanical properties of the TAV materials. Since the optimization framework was a side-by-side comparison study, our best designs should still be valid without considering the impact of leaflet tissue anisotropy. Furthermore, the best TAV designs in our optimization process showed a significant stress reduction compared to commercially available valves.

7.5 Conclusions

In summary, we developed an automatic computational framework using commercially available software to optimize the TAV leaflet shape under physiological loading conditions. Optimized leaflet designs for two different TAV sizes (23-mm and 26-mm) were obtained using particle swarm optimization algorithm. Furthermore, the impact of leaflet design parameters was evaluated on leaflet maximum stress. The results showed that increasing the ratio of valve height to leaflet coaptation height decreases the maximum Von Mises stress of the leaflets. Furthermore, increasing the curvature of the fixed-boundary edge could potentially reduce the maximum stress of the TAV leaflets. In addition, the optimized leaflet designs were compared with Carpentier-Edwards PERIMOUNT Magna surgical bioprostheses and Edwards SAPIEN 3 transcatheter heart valve. A considerable reduction in the peak in-plane maximum principal stress was observed in the optimized TAV geometry in comparison to the commercially available bioprosthetic heart valves. The framework has the potential to determine optimized leaflet design for a wide range of TAV design parameters and control variables (e.g., different frame designs and leaflet properties). In addition, the results presented in this study

underline the opportunity to improve leaflet design in the next generation of TAVs which could potentially increase long-term durability of transcatheter heart valves.

CHAPTER 8: CONCLUSIONS AND FUTURE WORK

TAVR is an established therapy alternative to surgical valve replacement in high-risk and intermediate-risk patients with severe aortic stenosis. TAVR could potentially be applied to lower-risk younger patients if the indications can be safely expanded to the patients and TAV long-term durability can match with that of surgical bioprostheses. In contrary to SAV, there have been limited clinical data on the long-term durability of TAV devices. In the absence of enough long-term valve durability data, accurate structural simulations and computational modeling become an integral part of the evaluation. Thus, the objectives of this dissertation were to employ in-vitro experiments and inverse finite element (FE) analyses obtain the accurate material properties of soft tissue employed in commercial available TAVs and then to implement them in computational simulations to determine leaflet stress and strain distributions for proper of the TAVs long-term durability assessment. Therefore, the main goal of this study was to develop an automated computational framework to minimize the peak stress on the leaflets under and optimize the TAV leaflet shape under physiological loading conditions. In addition, the impact of incomplete TAV expansion and thickness reduction on leaflet stress and strain distribution

was assessed in this dissertation. Based on the context of this dissertation, the main conclusions of the previous chapters are summarized in this chapter. Then we will propose the future works related to the studies of this dissertation.

8.1 Conclusions

8.1.1 Incomplete TAV Expansion

The current guidelines for TAVR are to upsize the TAV relative to the native annulus to secure the device and minimize paravalvular leakage. We have developed computational models to assess the impact of incomplete TAV stent expansion on leaflet stress and strain distributions. It was found that TAV leaflet stress and strain distributions were dependent on the diameter of the inflated TAV. We found that 2-3mm incomplete TAV stent expansion induced localized high stress regions within the TAV commissures, while 4-5mm incomplete stent expansion induced localized high stress regions within the belly of the TAV leaflets during the diastolic phase of the cardiac cycle. In TAVR, valve oversizing is essential to secure the valve and prevent paravalvular aortic regurgitation. However, if oversizing leads to incomplete expansion of the stent, it will induce localized high stress regions within the TAV leaflets which overtime may lead to premature tissue degeneration.

8.1.2 Material Characterization of Heart Valve Tissue

Constitutive models in computational simulations are needed to accurately predict and simulate mechanical response of biomedical materials under a verity of multi-axial loading conditions that may exist under physiological conditions. We developed an approach to obtain material parameters of a pericardial surgical bioprosthesis based on generalized nonlinear Fung-type constitutive model under dynamic loading conditions. Using the

inverse parameter estimation process, 3D generalized anisotropic and orthotropic Fung model parameters were estimated for the bioprosthetic leaflets. Furthermore, the Rayleigh damping coefficient that was introduced to FE simulations to simulate viscous damping effects of surrounding fluid was assessed. The generalized anisotropic model accurately simulated the leaflet deformation and coaptation during valve opening and closing. During systole, high stress regions were primarily observed at the boundary edge; however, during diastole, high stress regions were primarily observed in the commissures. The maximum leaflet stress at the peak of systole was significantly more than the maximum principal stress during diastole. Commercial FE software packages are widely available and can be utilized effectively for quantitative description of surgical and transcatheter heart valves to better understand mechanism of tissue degeneration and improve long-term valve durability.

8.1.3 Effect of Reduced Tissue Thickness in TAVs

Although low-profile systems reduce the risk of vascular injuries and improve catheter maneuver for precise placement of TAV devices, the cross-sectional area reduction causes more constraints in the design of TAV devices. To use smaller cross-sectional areas of delivery catheters, the valve must be crimped into a small diameter which is less than the delivery catheter size. We developed FE simulations to assess the impact of thickness reduction on leaflet stress and strain distributions. It was found that TAV leaflet stress and strain distributions were dependent on the tissue thickness of the TAVs. By reducing TAV leaflet thickness to minimize the cross-¬sectional area of crimped TAVs, significantly higher leaflet stress distribution is expected. Increased mechanical stress on TAV leaflets

due to thickness reduction may lead to diminished long-term valve durability. As a result, by using thinner leaflets, TAV durability may not match with that of surgical bioprostheses.

8.1.4 Strain Mapping of Bioprosthetic Heart Valves using DIC

To assess longevity of the currently available TAVs and develop the next generation of heart valve prostheses, in-depth comparison and assessment of strain and stress of the leaflets is essential. We developed an in-vitro DIC-based experiment to map displacement and measure strain values on three different bioprosthetic heart valves, i.e., Carpentier-Edwards PERIMOUNT Magna surgical bioprosthesis, Medtronic CoreValve, and Edwards SAPIEN 3. High displacement regions were found at the leaflet belly region of the three valves. In addition, the frame of the surgical bioprosthesis was found to be noticeably flexible, in contrary to CoreValve and SAPIEN 3, in which the stent was rigid. We found that high strain regions at the leaflet commissures in PREIMOUNT Magna and SAPIN 3. However, the maximum strain value on CoreValve leaflets were found below the commissure region close to the fixed boundary edge. The results of optical measurements in the DIC system can be utilized to characterize the anisotropic materiel behavior of the leaflets and validate computational simulations.

8.1.5 Material Characterization Framework for Commercial bioprostheses

Computational simulations can play a pivotal role in design and development of prosthetic heart valves by reducing the need to perform expensive pre-clinical tests. To have a reliable computational model, considering accurate mechanical properties for the bioprosthetic materials is a crucial step. We developed a two-step optimization procedure to determine 3D anisotropic mechanical properties of pericardial valves under

physiological loading conditions. Three different bioprosthetic heart valves with comparable size were investigated. The optimized material parameters for each valve were implemented in FE simulations to assess the leaflet deformation and stress distribution. During systole, high stress regions were primarily observed at the boundary edge for the bioprostheses. However, during diastole, high stress regions were primarily observed in the commissures for CE PERIMOUNT Magna and Edwards SAPIEN 3. In contrary to the two other bioprostheses, the maximum stress values for the CoreValve were seen in the lower leaflet belly region. In addition, the CoreValve had the lowest peak stress value at the identical pressure value during diastole compared to the CE PERIMOUNT Magna and Edwards SAPIEN 3.

8.1.6 TAV Leaflet Design

It is well-known that leaflet shape has a key role in hemodynamic performance and durability of bioprosthetic valves. Excessive mechanical stress on transcatheter aortic valve (TAV) leaflets may lead to accelerated tissue degeneration and diminished long-term valve durability. We developed an automatic computational framework to optimize the TAV leaflet shape under physiological loading conditions. The curves of the leaflet geometry, fixed edge, free edge and symmetry curves, were parameterized using NURBS. The best designs for two different diameters (23 and 26 mm) of TAVs were obtained using particle swarm optimization (PSO) algorithm in Isight software. It was observed that high stress regions were primarily observed at the boundary edge for the TAV designs at the peak of systole. However, during diastole, high stress regions typically occurred near the commissures. Among various perturbations of the leaflet design, increasing the ratio of

commissure height to coaptation point height generally decreases the maximum stress. Within the chosen design parameters, we have achieved new designs for TAVs leaflet geometry in which the peak stress was 8.2% and 30.3% less than the corresponding surgical valves for 23 and 26 mm diameters, respectively. In addition, the leaflet peak stress of best TAV design obtained from the optimization framework showed the leaflet peak stress was 74.8% lower than the Edwards SAPIEN 3 TAV. The developed optimization framework may provide a more reliable TAV design with longer valve durability in comparison to the currently available TAVs.

8.2 Future Works

There are a few limitations in incomplete TAV expansion study which should be addressed in future works. In this study, we only used the leaflet geometry which was like the SAPIEN XT. Therefore, precise leaflet geometry of SAPIEN 3 valve or CoreValve which are widely used in clinics can be considered in future works to assess leaflet stress and strain distributions under incomplete TAV expansion. In addition, the effects of crimping on the mechanical properties of tissue can be assumed in future FE models. Additionally, we used a fixed value for Rayleigh damping coefficient to mimic viscous damping effects of surrounding fluid in bioprostheses. However, the viscous damping coefficient depends on fluid dynamics in bioprostheses. Therefore, a more accurate simulation may involve FSI simulation in future works. Furthermore, to characterize material parameters of soft tissue employed in bioprosthetic heart valves, FSI simulations are also motivated under physiological loading condition in further studies. In this way, the accuracy of material characterization can be increased, and the leaflets motion can be

captured perfectly. In addition, we believe that the inverse FE simulations can be used to obtain the in-vivo material model responses for human heart valves.(Lee et al. 2014, Lee et al. 2016, Aggarwal and Sacks 2016)

In this dissertation, the in-vitro DIC-based experiment was conducted to map displacement and measure strain values on commercially available bioprosthetic heart valves under quasi-static loading. To obtain displacement and measure strain values within bioprosthetic leaflets under dynamic loading conditions, pulse duplicator in-vitro system and DIC system can be used simultaneously in future works. Accordingly, the displacement and strain distribution of bioprosthesis leaflets can be obtained during one cardiac cycle under physiological conditions.

We used the optimization technique to minimize the stress distribution within the leaflet geometry in TAVs. However, implementing FSI simulation into the TAV models may improve optimization results in future studies. Besides minimizing leaflet peak stress, hemodynamic performance improvement and reduction of the incidence thrombosis can be considered in future optimization frameworks for TAVs design. Moreover, the new TAV design presented in this dissertation can be fabricated as a valve prototype and its hydrodynamic performance can be assessed by in-vitro valve testing in the pulse duplicator system. Accordingly, the optimized valve prototype can be hemodynamically comparable with commercially available TAVs. Therefore, subsequent in-vitro studies should be conducted to verify the best TAV design for different sizes in this study.

BIBLIOGRAPHY

Abbasi, M, and AN Azadani. 2017. "Stress Analysis of Transcatheter Aortic Valve Leaflets Under Dynamic Loading: Effect of Reduced Tissue Thickness." The Journal of heart valve disease 26 (4):386-396.

Abbasi, M., and A. N. Azadani. 2015. "Leaflet stress and strain distributions following incomplete transcatheter aortic valve expansion." J Biomech. doi: 10.1016/j.jbiomech.2015.08.012.

Abbasi, Mostafa, M.S. Barakat, K. Vahidkhah, and A. N. Azadani. 2016. "Characterization of three-dimensional anisotropic heart valve tissue mechanical properties using inverse finite element analysis." J Mech Behav Biomed 62:33-44.

Abbasi, Mostafa, Dong Qiu, Yashar Behnam, Danny Dvir, Chadd Clary, and Ali N Azadani. 2018a. "High resolution three-dimensional strain mapping of bioprosthetic heart valves using digital image correlation." Journal of biomechanics 76:27-34.

Abbasi, Mostafa, Dong Qiu, Yashar Behnam, Danny Dvir, Chadd Clary, and Ali N Azadani. 2018b. "High resolution three-dimensional strain mapping of bioprosthetic heart valves using digital image correlation." Journal of biomechanics.

Adams, David H, Jeffrey J Popma, Michael J Reardon, Steven J Yakubov, Joseph S Coselli, G Michael Deeb, Thomas G Gleason, Maurice Buchbinder, James Hermiller Jr, and Neal S Kleiman. 2014. "Transcatheter aortic-valve replacement with a self-expanding prosthesis." N Engl J Med 370 (19):1790-1798.

Aggarwal, Ankush, and Michael S Sacks. 2016. "An inverse modeling approach for semilunar heart valve leaflet mechanics: exploitation of tissue structure." Biomechanics and modeling in mechanobiology 15 (4):909-932.

Alastrué, V, JF Rodríguez, B Calvo, and M Doblare. 2007. "Structural damage models for fibrous biological soft tissues." Int J Solids Struct 44 (18):5894-5911.

Alavi, S Hamed, Elliott M Groves, and Arash Kheradvar. 2014a. "The effects of transcatheter valve crimping on pericardial leaflets." The Annals of thoracic surgery 97 (4):1260-1266.

Alavi, S Hamed, Elliott M Groves, and Arash Kheradvar. 2014b. "The effects of transcatheter valve crimping on pericardial leaflets." Ann Thorac Surg 97 (4):1260-1266.

Alavi, S. H., E. M. Groves, and A. Kheradvar. 2014c. "The effects of transcatheter valve crimping on pericardial leaflets." Ann Thorac Surg 97 (4):1260-6. doi: 10.1016/j.athoracsur.2013.11.009.

Aranki, Sary F, Robert J Rizzo, Gregory S Couper, David H Adams, Jr JJ Collins, Jennifer S Gildea, Nancy M Kinchla, and Lawrence H Cohn. 1993. "Aortic valve replacement in the elderly. Effect of gender and coronary artery disease on operative mortality." Circulation 88 (5 Pt 2):II17-23.

Arora, Sameer, Cassandra J Ramm, Jacob A Misenheimer, and John P Vavalle. 2017. "Early transcatheter valve prosthesis degeneration and future ramifications." Cardiovascular diagnosis and therapy 7 (1):1.

Arsalan, Mani, and Thomas Walther. 2016. "Durability of prostheses for transcatheter aortic valve implantation." Nature Reviews Cardiology 13 (6):360.

Auricchio, F, M Conti, A Ferrara, S Morganti, and A Reali. 2014. "Patient-specific simulation of a stentless aortic valve implant: the impact of fibres on leaflet performance." Comput Methods Biomech Biomed Engin 17 (3):277-285.

Azadani, A. N., N. Jaussaud, L. Ge, S. Chitsaz, T. A. Chuter, and E. E. Tseng. 2011. "Valve-in-valve hemodynamics of 20-mm transcatheter aortic valves in small bioprostheses." Ann Thorac Surg 92 (2):548-55. doi: 10.1016/j.athoracsur.2011.04.009.

Azadani, A. N., N. Jaussaud, P. B. Matthews, T. A. Chuter, L. Ge, T. S. Guy, J. Guccione, and E. E. Tseng. 2009. "Aortic valve-in-valve implantation: impact of transcatheter-bioprosthesis size mismatch." J Heart Valve Dis 18 (4):367-73.

Azadani, A. N., N. Jaussaud, P. B. Matthews, L. Ge, T. A. Chuter, and E. E. Tseng. 2010. "Transcatheter aortic valves inadequately relieve stenosis in small degenerated bioprostheses." Interact Cardiovasc Thorac Surg 11 (1):70-7. doi: 10.1510/icvts.2009.225144.

Azadani, A. N., N. Jaussaud, P. B. Matthews, L. Ge, T. S. Guy, T. A. Chuter, and E. E. Tseng. 2009. "Valve-in-valve implantation using a novel supravalvular transcatheter aortic valve: proof of concept." Ann Thorac Surg 88 (6):1864-9. doi: 10.1016/j.athoracsur.2009.08.004.

Azadani, A. N., and E. E. Tseng. 2011. "Transcatheter heart valves for failing bioprostheses: state-of-the-art review of valve-in-valve implantation." Circ Cardiovasc Interv 4 (6):621-8. doi: 10.1161/CIRCINTERVENTIONS.111.964478.

Bailey, Michael T, Swadeep Pillarisetti, Hui Xiao, and Naren R Vyavahare. 2003. "Role of elastin in pathologic calcification of xenograft heart valves." J Biomed Mater Res Part A 66 (1):93-102.

Banks, Alec, Jonathan Vincent, and Chukwudi Anyakoha. 2008. "A review of particle swarm optimization. Part II: hybridisation, combinatorial, multicriteria and constrained optimization, and indicative applications." Natural Computing 7 (1):109-124.

Bapat, Vinnie N, Rizwan Q Attia, Fortunata Condemi, Ravi Visagan, Maya Guthrie, Shelina Sunni, and Martyn Thomas. 2013. "Fluoroscopic guide to an ideal implant position for Sapien XT and CoreValve during a valve-in-valve procedure." JACC: Cardiovascular Interventions 6 (11):1186-1194.

Barbanti, Marco, Anna Sonia Petronio, Federica Ettori, Azeem Latib, Francesco Bedogni, Federico De Marco, Arnaldo Poli, Carla Boschetti, Marco De Carlo, and Claudia Fiorina. 2015. "5-year outcomes after transcatheter aortic valve implantation with CoreValve prosthesis." JACC: Cardiovascular interventions 8 (8):1084-1091.

Barbanti, Marco, John G Webb, Martine Gilard, Davide Capodanno, and Corrado Tamburino. 2017. "Transcatheter aortic valve implantation in 2017: state of the art." EuroIntervention: journal of EuroPCR in collaboration with the Working Group on Interventional Cardiology of the European Society of Cardiology 13 (AA):AA11-AA21.

Billiar, Kristen L, and Michael S Sacks. 2000. "Biaxial mechanical properties of the natural and glutaraldehyde treated aortic valve cusp—part I: experimental results." Journal of biomechanical engineering 122 (1):23-30.

Binder, R. K., J. G. Webb, S. Toggweiler, M. Freeman, M. Barbanti, A. B. Willson, D. Alhassan, C. J. Hague, D. A. Wood, and J. Leipsic. 2013. "Impact of post-implant SAPIEN XT geometry and position on conduction disturbances, hemodynamic performance, and paravalvular regurgitation." JACC Cardiovasc Interv 6 (5):462-8. doi: 10.1016/j.jcin.2012.12.128.

Borz, Bogdan, Eric Durand, Christophe Tron, Matthieu Godin, Alexandre Canville, Camille Hauville, Alain Cribier, and Hélène Eltchaninoff. 2014. "Expandable sheath for transfemoral transcatheter aortic valve replacement: procedural outcomes and complications." Catheter Cardiovasc Interv 83 (6):E227-E232.

Bourantas, Christos V, and Patrick W Serruys. 2014. "Evolution of transcatheter aortic valve replacement." Circulation research 114 (6):1037-1051.

Bourguignon, Thierry, Anne-Lorraine Bouquiaux-Stablo, Pascal Candolfi, Alain Mirza, Claudia Loardi, Marc-Antoine May, Rym El-Khoury, Michel Marchand, and Michel Aupart. 2015. "Very long-term outcomes of the Carpentier-Edwards Perimount valve in aortic position." The Annals of thoracic surgery 99 (3):831-837.

Bourguignon, Thierry, Rym El Khoury, Pascal Candolfi, Claudia Loardi, Alain Mirza, Julie Boulanger-Lothion, Anne-Lorraine Bouquiaux-Stablo-Duncan, Fabien Espitalier, Michel Marchand, and Michel Aupart. 2015. "Very long-term outcomes of the Carpentier-Edwards Perimount aortic valve in patients aged 60 or younger." The Annals of thoracic surgery 100 (3):853-859.

Calvo, B, E Pena, MA Martinez, and M Doblaré. 2007. "An uncoupled directional damage model for fibred biological soft tissues. Formulation and computational aspects." Int J Numer Meth Eng 69 (10):2036-2057.

Chu, TC, WF Ranson, and Mr A Sutton. 1985. "Applications of digital-image-correlation techniques to experimental mechanics." Experimental mechanics 25 (3):232-244.

Cribier, Alain, Helene Eltchaninoff, Assaf Bash, Nicolas Borenstein, Christophe Tron, Fabrice Bauer, Genevieve Derumeaux, Frederic Anselme, François Laborde, and Martin B Leon. 2002. "Percutaneous transcatheter implantation of an aortic valve prosthesis for calcific aortic stenosis first human case description." Circulation 106 (24):3006-3008.

Delgado, V., A. C. Ng, N. R. van de Veire, F. van der Kley, J. D. Schuijf, L. F. Tops, A. de Weger, G. Tavilla, A. de Roos, L. J. Kroft, M. J. Schalij, and J. J. Bax. 2010. "Transcatheter aortic valve implantation: role of multi-detector row computed tomography to evaluate prosthesis positioning and deployment in relation to valve function." Eur Heart J 31 (9):1114-23. doi: 10.1093/eurheartj/ehq018.

Dvir, D. 2016. Half of transcatheter heart valves show degeneration within 10 years of TAVI. EuroPCR.

Dvir, D, H Eltchaninoff, J Ye, A Kan, E Durand, A Bizios, A Cheung, M Aziz, M Simonato, and C Tron. 2016. "First look at long-term durability of transcatheter heart valves: assessment of valve function up to 10 years after implantation." Eur J Cardiothorac Surg.

Dvir, Danny, Thierry Bourguignon, Catherine M Otto, Rebecca T Hahn, Raphael Rosenhek, John G Webb, Hendrik Treede, Maurice E Sarano, Ted Feldman, and Harindra

C Wijeysundera. 2018. "Standardized Definition of Structural Valve Degeneration for Surgical and Transcatheter Bioprosthetic Aortic Valves." Circulation 137 (4):388-399.

Eilaghi, Armin, John G Flanagan, G Wayne Brodland, and C Ross Ethier. 2009. "Strain uniformity in biaxial specimens is highly sensitive to attachment details." Journal of biomechanical engineering 131 (9):091003.

Ferrans, V. J., T. L. Spray, M. E. Billingham, and W. C. Roberts. 1978a. "Structural changes in glutaraldehyde-treated porcine heterografts used as substitute cardiac valves. Transmission and scanning electron microscopic observations in 12 patients." Am J Cardiol 41 (7):1159-84.

Ferrans, Victor J, Thomas L Spray, Margaret E Billingham, and William C Roberts. 1978b. "Structural changes in glutaraldehyde-treated porcine heterografts used as substitute cardiac valves: transmission and scanning electron microscopic observations in 12 patients." Am J Pathol 41 (7):1159-1184.

Food, and Drug Administration. 2014. "Reporting of Computational Modeling Studies in Medical Device Submissions—Draft Guidance for Industry and Food and Drug Administration Staff only." Food and Drug Administration, Rockville, MD.

Forcillo, Jessica, Michel Pellerin, Louis P Perrault, Raymond Cartier, Denis Bouchard, Philippe Demers, and Michel Carrier. 2013. "Carpentier-Edwards pericardial valve in the aortic position: 25-years experience." The Annals of thoracic surgery 96 (2):486-493.

Fries, Richard C. 2016. Reliable design of medical devices: CRC Press.

Fung, Y. C., K. Fronek, and P. Patitucci. 1979. "Pseudoelasticity of arteries and the choice of its mathematical expression." Am J Physiol 237 (5):H620-31.

Fung, Y., and P. Tong. 2001. Classical and Computational Solid Mechanics: World Scientific.

Fung, Y.C. 1993. " Biomechanics: Mechanical Properties of Living Tissues." Springer-Verlag, New York.

Fung, Y.C. 2013a. Biomechanics: Mechanical Properties of Living Tissues: Springer New York.

Fung, Yuan-cheng. 2013b. Biomechanics: mechanical properties of living tissues: Springer Science & Business Media.

Gauvin, Robert, Georgi Marinov, Yayhe Mehri, Julianne Klein, Bin Li, Danielle Larouche, Randolph Guzman, Ze Zhang, Lucie Germain, and Robert Guidoin. 2013. "A comparative study of bovine and porcine pericardium to highlight their potential advantages to manufacture percutaneous cardiovascular implants." Journal of biomaterials applications 28 (4):552-565.

Grunkemeier, Gary L, Anthony P Furnary, YingXing Wu, Lian Wang, and Albert Starr. 2012. "Durability of pericardial versus porcine bioprosthetic heart valves." The Journal of thoracic and cardiovascular surgery 144 (6):1381-1386.

Gunning, Paul S, Ted J Vaughan, and Laoise M McNamara. 2014. "Simulation of self expanding transcatheter aortic valve in a realistic aortic root: implications of deployment geometry on leaflet deformation." Annals of biomedical engineering 42 (9):1989-2001.

Heide-Jørgensen, Simon, Sellaswasmy Kumaran Krishna, Jonas Taborsky, Tommy Bechsgaard, Rachid Zegdi, and Peter Johansen. 2016. "A Novel Method for Optical High

Spatiotemporal Strain Analysis for Transcatheter Aortic Valves In Vitro." Journal of biomechanical engineering 138 (3):034504.

Hiester, Erik D, and Michael S Sacks. 1998. "Optimal bovine pericardial tissue selection sites. I. Fiber architecture and tissue thickness measurements." Journal of Biomedical Materials Research: An Official Journal of The Society for Biomaterials, The Japanese Society for Biomaterials, and the Australian Society for Biomaterials 39 (2):207-214.

Holzapfel, G.A. 2000. Nonlinear Solid Mechanics: A Continuum Approach for Engineering: Wiley.

Holzapfel, Gerhard A, and Ray W Ogden. 2008. "On planar biaxial tests for anisotropic nonlinearly elastic solids. A continuum mechanical framework." Mathematics and mechanics of solids.

Holzapfel, Gerhard A, and Ray W Ogden. 2009. "On planar biaxial tests for anisotropic nonlinearly elastic solids. A continuum mechanical framework." Mathematics and mechanics of solids 14 (5):474-489.

Hsu, Ming-Chen, David Kamensky, Yuri Bazilevs, Michael S Sacks, and Thomas JR Hughes. 2014. "Fluid–structure interaction analysis of bioprosthetic heart valves: significance of arterial wall deformation." Computational mechanics 54 (4):1055-1071.

Hsu, Ming-Chen, David Kamensky, Fei Xu, Josef Kiendl, Chenglong Wang, Michael CH Wu, Joshua Mineroff, Alessandro Reali, Yuri Bazilevs, and Michael S Sacks. 2015. "Dynamic and fluid–structure interaction simulations of bioprosthetic heart valves using parametric design with T-splines and Fung-type material models." Computational mechanics 55 (6):1211-1225.

Humphrey, J. D. 1995. "Mechanics of the arterial wall: review and directions." Crit Rev Biomed Eng 23 (1-2):1-162.

Humphrey, J. D. 2003. "Continuum biomechanics of soft biological tissues." Proceedings of the Royal Society a-Mathematical Physical and Engineering Sciences 459 (2029):3-46.

Humphrey, JD, RK Strumpf, and FC Yin. 1990. "Biaxial mechanical behavior of excised ventricular epicardium." American Journal of Physiology-Heart and Circulatory Physiology 259 (1):H101-H108.

Isaacs, Abby J, Jeffrey Shuhaiber, Arash Salemi, O Wayne Isom, and Art Sedrakyan. 2015. "National trends in utilization and in-hospital outcomes of mechanical versus bioprosthetic aortic valve replacements." The Journal of thoracic and cardiovascular surgery 149 (5):1262-1269. e3.

Jamieson, WR Eric, Lawrence H Burr, Robert T Miyagishima, Eva Germann, Joan S MacNab, Elizabeth Stanford, Florence Chan, Michael T Janusz, and Hilton Ling. 2005. "Carpentier-Edwards supra-annular aortic porcine bioprosthesis: clinical performance over 20 years." The Journal of Thoracic and Cardiovascular Surgery 130 (4):994-1000.

Jermihov, P. N., L. Jia, M. S. Sacks, R. C. Gorman, J. H. Gorman, 3rd, and K. B. Chandran. 2011. "Effect of Geometry on the Leaflet Stresses in Simulated Models of Congenital Bicuspid Aortic Valves." Cardiovasc Eng Technol 2 (1):48-56. doi: 10.1007/s13239-011-0035-9.

Jermihov, Paul N, Lu Jia, Michael S Sacks, Robert C Gorman, Joseph H Gorman III, and Krishnan B Chandran. 2011. "Effect of geometry on the leaflet stresses in simulated models of congenital bicuspid aortic valves." Cardiovasc Eng Technol 2 (1):48-56.

Jilaihawi, Hasan, Derek Chin, Tomasz Spyt, Mohamed Jeilan, Mariuca Vasa-Nicotera, Noor Mohamed, Johan Bence, Elaine Logtens, and Jan Kovac. 2011. "Comparison of complete versus incomplete stent frame expansion after transcatheter aortic valve implantation with Medtronic CoreValve bioprosthesis." The American journal of cardiology 107 (12):1830-1837.

Johnston, Douglas R, Edward G Soltesz, Nakul Vakil, Jeevanantham Rajeswaran, Eric E Roselli, Joseph F Sabik III, Nicholas G Smedira, Lars G Svensson, Bruce W Lytle, and Eugene H Blackstone. 2015. "Long-term durability of bioprosthetic aortic valves: implications from 12,569 implants." The Annals of thoracic surgery 99 (4):1239-1247.

Kamensky, David, Ming-Chen Hsu, Dominik Schillinger, John A Evans, Ankush Aggarwal, Yuri Bazilevs, Michael S Sacks, and Thomas JR Hughes. 2015. "An immersogeometric variational framework for fluid–structure interaction: Application to bioprosthetic heart valves." Computer methods in applied mechanics and engineering 284:1005-1053.

Kanyanta, Valentine, and Alojz Ivankovic. 2010. "Mechanical characterisation of polyurethane elastomer for biomedical applications." Journal of the mechanical behavior of biomedical materials 3 (1):51-62.

Kapadia, Samir R, Martin B Leon, Raj R Makkar, E Murat Tuzcu, Lars G Svensson, Susheel Kodali, John G Webb, Michael J Mack, Pamela S Douglas, and Vinod H Thourani. 2015. "5-year outcomes of transcatheter aortic valve replacement compared with standard treatment for patients with inoperable aortic stenosis (PARTNER 1): a randomised controlled trial." The Lancet 385 (9986):2485-2491.

Keefe, Daniel F, Fotis Sotiropoulos, Victoria Interrante, H Birali Runesha, Dane Coffey, Molly Staker, Chi-Lun Lin, Yi Sun, Iman Borazjani, and Trung Le. 2010. "A process for design, verification, validation, and manufacture of medical devices using immersive VR environments." Journal of Medical Devices 4 (4):045002.

Kheradvar, Arash, Elliott M Groves, Craig J Goergen, S Hamed Alavi, Robert Tranquillo, Craig A Simmons, Lakshmi P Dasi, K Jane Grande-Allen, Mohammad RK Mofrad, and Ahmad Falahatpisheh. 2015. "Emerging Trends in Heart Valve Engineering: Part II. Novel and Standard Technologies for Aortic Valve Replacement." Ann Biomed Eng 43 (4):844-857.

Khoffi, Foued, and Frederic Heim. 2015. "Mechanical degradation of biological heart valve tissue induced by low diameter crimping: an early assessment." Journal of the mechanical behavior of biomedical materials 44:71-75.

Kim, H., J. Lu, M. S. Sacks, and K. B. Chandran. 2006. "Dynamic simulation pericardial bioprosthetic heart valve function." J Biomech Eng 128 (5):717-24. doi: 10.1115/1.2244578.

Kim, Hyunggun, Krishnan B Chandran, Michael S Sacks, and Jia Lu. 2007. "An experimentally derived stress resultant shell model for heart valve dynamic simulations." Annals of biomedical engineering 35 (1):30-44.

Kim, Hyunggun, Jia Lu, Michael S Sacks, and Krishnan B Chandran. 2008. "Dynamic simulation of bioprosthetic heart valves using a stress resultant shell model." Annals of biomedical engineering 36 (2):262-275.

Kodali, Susheel K, Mathew R Williams, Craig R Smith, Lars G Svensson, John G Webb, Raj R Makkar, Gregory P Fontana, Todd M Dewey, Vinod H Thourani, and Augusto D Pichard. 2012. "Two-year outcomes after transcatheter or surgical aortic-valve replacement." New England Journal of Medicine 366 (18):1686-1695.

Koehler, Till, Michael Buege, Heinrich Schleiting, Melchior Seyfarth, Klaus Tiroch, and Marc Vorpahl. 2015. "Changes of the eSheath Outer Dimensions Used for Transfemoral Transcatheter Aortic Valve Replacement." Biomed Res Int 2015.

Kumar, Vipin, and Sonajharia Minz. 2014. "Multi-objective particle swarm optimization: an introduction." SmartCR 4 (5):335-353.

Laflamme, Jérôme, Rishi Puri, Marina Urena, Louis Laflamme, Hugo DeLarochellière, Omar Abdul-Jawad Altisent, Maria Del Trigo, Francisco Campelo-Parada, Robert DeLarochellière, and Jean-Michel Paradis. 2015. "Incidence and risk factors of hemolysis after transcatheter aortic valve implantation with a balloon-expandable valve." The American journal of cardiology 115 (11):1574-1579.

Lai, W.M., D.H. Rubin, D. Rubin, and E. Krempl. 2009. Introduction to Continuum Mechanics: Elsevier Science.

Lee, CH, K Feaver, W Zhang, RC Gorman, JH Gorman, and MS Sacks. 2016. "Inverse Modeling Based Estimation of In-Vivo Stresses and Their Relation to Simulated Layer-Specific Interstitial Cell Deformations in the Mitral Valve." Summer Biomechanics, Bioengineering and Biotransport Conference (SB3C), National Harbor, MD, June.

Lee, Chung-Hao, Rouzbeh Amini, Robert C Gorman, Joseph H Gorman III, and Michael S Sacks. 2014. "An inverse modeling approach for stress estimation in mitral valve anterior

leaflet valvuloplasty for in-vivo valvular biomaterial assessment." Journal of biomechanics 47 (9):2055-2063.

Lee, J Michael, David W Courtman, and Derek R Boughner. 1984. "The glutaraldehyde-stabilized porcine aortic valve xenograft. I. Tensile viscoelastic properties of the fresh leaflet material." Journal of Biomedical Materials Research Part A 18 (1):61-77.

Lee, J Michael, Sean A Haberer, Christopher A Pereira, Wendy A Naimark, David W Courtman, and Gregory J Wilson. 1994. "High strain rate testing and structural analysis of pericardial bioprosthetic materials." In Biomaterials' Mechanical Properties. ASTM International.

Leon, Martin B, Craig R Smith, Michael J Mack, Raj R Makkar, Lars G Svensson, Susheel K Kodali, Vinod H Thourani, E Murat Tuzcu, D Craig Miller, and Howard C Herrmann. 2016a. "Transcatheter or surgical aortic-valve replacement in intermediate-risk patients." New England Journal of Medicine 374 (17):1609-1620.

Leon, Martin B, Craig R Smith, Michael J Mack, Raj R Makkar, Lars G Svensson, Susheel K Kodali, Vinod H Thourani, E Murat Tuzcu, D Craig Miller, and Howard C Herrmann. 2016b. "Transcatheter or surgical aortic-valve replacement in intermediate-risk patients." N Engl J Med 2016 (374):1609-1620.

Leon, Martin B, Craig R Smith, Michael Mack, D Craig Miller, Jeffrey W Moses, Lars G Svensson, E Murat Tuzcu, John G Webb, Gregory P Fontana, and Raj R Makkar. 2010. "Transcatheter aortic-valve implantation for aortic stenosis in patients who cannot undergo surgery." N Engl J Med 363 (17):1597-1607.

Levy, RJ, FJ Schoen, JT Levy, AC Nelson, SL Howard, and LJ Oshry. 1983. "Biologic determinants of dystrophic calcification and osteocalcin deposition in glutaraldehyde-preserved porcine aortic valve leaflets implanted subcutaneously in rats." Am J Pathol 113 (2):143.

Li, Dalong, and Anne M Robertson. 2009. "A structural multi-mechanism damage model for cerebral arterial tissue." J Biomech Eng 131 (10):101013.

Li, Kewei, and Wei Sun. 2010. "Simulated thin pericardial bioprosthetic valve leaflet deformation under static pressure-only loading conditions: implications for percutaneous valves." Ann Biomed Eng 38 (8):2690-2701.

Li, Kewei, and Wei Sun. 2017. "Simulated transcatheter aortic valve deformation: A parametric study on the impact of leaflet geometry on valve peak stress." International journal for numerical methods in biomedical engineering 33 (3):e02814.

Luyckx, Thomas, Matthias Verstraete, Karel De Roo, Wim De Waele, Johan Bellemans, and Jan Victor. 2014. "Digital image correlation as a tool for three-dimensional strain analysis in human tendon tissue." Journal of experimental orthopaedics 1 (1):7.

Mack, Michael, and David Holmes. 2016. "Bioprosthetic valve thrombosis: the harder one looks, the more one finds." The Journal of thoracic and cardiovascular surgery 152 (4):952-953.

Mack, Michael J, Martin B Leon, Craig R Smith, D Craig Miller, Jeffrey W Moses, E Murat Tuzcu, John G Webb, Pamela S Douglas, William N Anderson, and Eugene H Blackstone. 2015. "5-year outcomes of transcatheter aortic valve replacement or surgical

aortic valve replacement for high surgical risk patients with aortic stenosis (PARTNER 1): a randomised controlled trial." The Lancet 385 (9986):2477-2484.

Makkar, Raj R, Gregory P Fontana, Hasan Jilaihawi, Samir Kapadia, Augusto D Pichard, Pamela S Douglas, Vinod H Thourani, Vasilis C Babaliaros, John G Webb, and Howard C Herrmann. 2012. "Transcatheter aortic-valve replacement for inoperable severe aortic stenosis." New England Journal of Medicine 366 (18):1696-1704.

Martin, Caitlin, and Wei Sun. 2012. "Modeling of Soft Tissue Property Changes Induced by Fatigue Loading." ASME 2012 Summer Bioengineering Conference.

Martin, Caitlin, and Wei Sun. 2015. "Comparison of transcatheter aortic valve and surgical bioprosthetic valve durability: A fatigue simulation study." J Biomech Eng 48 (12):3026-3034.

Matsumoto, Takeo, Tomohiro Fukui, Toshihiro Tanaka, Naoko Ikuta, Toshiro Ohashi, Kiichiro Kumagai, Hiroji Akimoto, Koichi Tabayashi, and Masaaki Sato. 2009. "Biaxial tensile properties of thoracic aortic aneurysm tissues." Journal of Biomechanical Science and Engineering 4 (4):518-529.

Mavrilas, Dimosthenis, EA Sinouris, DH Vynios, and N Papageorgakopoulou. 2005. "Dynamic mechanical characteristics of intact and structurally modified bovine pericardial tissues." Journal of biomechanics 38 (4):761-768.

Mohammadi, S., R. Baillot, P. Voisine, P. Mathieu, and F. Dagenais. 2006. "Structural deterioration of the Freestyle aortic valve: mode of presentation and mechanisms." J Thorac Cardiovasc Surg 132 (2):401-6. doi: 10.1016/j.jtcvs.2006.03.056.

Morganti, S, M Conti, M Aiello, A Valentini, A Mazzola, A Reali, and F Auricchio. 2014. "Simulation of transcatheter aortic valve implantation through patient-specific finite element analysis: two clinical cases." Journal of biomechanics 47 (11):2547-2555.

Morris, Paul D, Andrew Narracott, Hendrik von Tengg-Kobligk, Daniel Alejandro Silva Soto, Sarah Hsiao, Angela Lungu, Paul Evans, Neil W Bressloff, Patricia V Lawford, and D Rodney Hose. 2016. "Computational fluid dynamics modelling in cardiovascular medicine." Heart 102 (1):18-28.

Mozaffarian, Dariush, Emelia J Benjamin, Alan S Go, Donna K Arnett, Michael J Blaha, Mary Cushman, Sandeep R Das, Sarah de Ferranti, Jean-Pierre Després, and Heather J Fullerton. 2015. "Heart disease and stroke statistics—2016 update: a report from the American Heart Association." Circulation:CIR. 0000000000000350.

Murdock, Kyle, Caitlin Martin, and Wei Sun. 2018. "Characterization of mechanical properties of pericardium tissue using planar biaxial tension and flexural deformation." Journal of the mechanical behavior of biomedical materials 77:148-156.

Nishimura, Rick A, Catherine M Otto, Robert O Bonow, Blase A Carabello, John P Erwin, Robert A Guyton, Patrick T O'gara, Carlos E Ruiz, Nikolaos J Skubas, and Paul Sorajja. 2014. "2014 AHA/ACC guideline for the management of patients with valvular heart disease: a report of the American College of Cardiology/American Heart Association Task Force on Practice Guidelines." Journal of the American College of Cardiology 63 (22):e57-e185.

Nolan, DR, and JP McGarry. 2016. "On the correct interpretation of measured force and calculation of material stress in biaxial tests." Journal of the mechanical behavior of biomedical materials 53:187-199.

Oommen, Brian S, Mustafa Karamanoglu, and Sándor J Kovács. 2002. "Can Analysis of Transmitral Flow-Velocity Contours Differentiate Between Alternative Diastolic Pressure–Volume Relations?" Cardiovascular Engineering: An International Journal 2 (2):67-72.

Palanca, Marco, Tommaso Maria Brugo, and Luca Cristofolini. 2015. "Use of digital image correlation to investigate the biomechanics of the vertebra." Journal of Mechanics in Medicine and Biology 15 (02):1540004.

Patterson, EA, IC Howard, and MA Thornton. 1996. "A comparative study of linear and nonlinear simulations of the leaflets in a bioprosthetic heart valve during the cardiac cycle." Journal of medical engineering & technology 20 (3):95-108.

Peña, Estefanía. 2011. "Prediction of the softening and damage effects with permanent set in fibrous biological materials." J Mech Phys Solids 59 (9):1808-1822.

Piazza, Nicolo, Sabine Bleiziffer, Gernot Brockmann, Ruge Hendrick, Marcus-André Deutsch, Anke Opitz, Domenico Mazzitelli, Peter Tassani-Prell, Christian Schreiber, and Rüdiger Lange. 2011. "Transcatheter aortic valve implantation for failing surgical aortic bioprosthetic valve: from concept to clinical application and evaluation (part 1)." JACC: Cardiovascular Interventions 4 (7):721-732.

Popma, JJ, DH Adams, MJ Reardon, SJ Yakubov, NS Kleiman, D Heimansohn, J Hermiller Jr, GC Hughes, JK Harrison, and J Coselli. 2014. "CoreValve United States

Clinical I. Transcatheter aortic valve replacement using a self-expanding bioprosthesis in patients with severe aortic stenosis at extreme risk for surgery." J Am Coll Cardiol 63 (19):1972-81.

Rabkin, SIMON W, and Ping Hwa Hsu. 1975. "Mathematical and mechanical modeling of stress-strain relationship of pericardium." American Journal of Physiology-Legacy Content 229 (4):896-900.

Raghav, Vrishank, Ikechukwu Okafor, Michael Quach, Lynn Dang, Salvador Marquez, and Ajit P Yoganathan. 2016a. "Long-term durability of Carpentier-Edwards Magna Ease valve: a one billion cycle in vitro study." The Annals of thoracic surgery 101 (5):1759-1765.

Raghav, Vrishank, Ikechukwu Okafor, Michael Quach, Lynn Dang, Salvador Marquez, and Ajit P Yoganathan. 2016b. "Long-Term Durability of Carpentier-Edwards Magna Ease Valve: A One Billion Cycle In Vitro Study." The Annals of Thoracic Surgery.

Reardon, Michael J, Neal S Kleiman, David H Adams, Steven J Yakubov, Joseph S Coselli, G Michael Deeb, Daniel O'Hair, Thomas G Gleason, Joon Sup Lee, and James B Hermiller. 2016. "Outcomes in the randomized CoreValve US pivotal high risk trial in patients with a Society of Thoracic Surgeons risk score of 7% or less." JAMA cardiology 1 (8):945-949.

Roberts, William C, and Jong M Ko. 2005. "Frequency by decades of unicuspid, bicuspid, and tricuspid aortic valves in adults having isolated aortic valve replacement for aortic stenosis, with or without associated aortic regurgitation." Circulation 111 (7):920-925.

Rodes-Cabau, J. 2012. "Transcatheter aortic valve implantation: current and future approaches." Nat Rev Cardiol 9 (1):15-29. doi: 10.1038/nrcardio.2011.164.

Rodriguez-Gabella, Tania, Pierre Voisine, Rishi Puri, Philippe Pibarot, and Josep Rodés-Cabau. 2017. "Aortic Bioprosthetic Valve Durability: Incidence, Mechanisms, Predictors, and Management of Surgical and Transcatheter Valve Degeneration." Journal of the American College of Cardiology 70 (8):1013-1028.

Rodríguez, José F, Fernando Cacho, José A Bea, and Manuel Doblaré. 2006. "A stochastic-structurally based three dimensional finite-strain damage model for fibrous soft tissue." J Mech Phys Solids 54 (4):864-886.

Rogge, Renee D, Scott R Small, Derek B Archer, Michael E Berend, and Merrill A Ritter. 2013. "Validation of Digital Image Correlation Techniques for Strain Measurement in Biomechanical Test Models." Proceedings of the ASME Summer Bioengineering Conference.

Roy, Trina, and Abhijit Chanda. 2014. "Computational modelling and analysis of latest commercially available coronary stents during deployment." Procedia Materials Science 5:2310-2319.

Sacks, M. S. 2001. "The biomechanical effects of fatigue on the porcine bioprosthetic heart valve." J Long Term Eff Med Implants 11 (3-4):231-47.

Sacks, M. S., and C. J. Chuong. 1998. "Orthotropic mechanical properties of chemically treated bovine pericardium." Ann Biomed Eng 26 (5):892-902.

Sacks, M. S., C. J. Chuong, and R. More. 1994. "Collagen fiber architecture of bovine pericardium." ASAIO J 40 (3):M632-7.

Sacks, M. S., A. Mirnajafi, W. Sun, and P. Schmidt. 2006. "Bioprosthetic heart valve heterograft biomaterials: structure, mechanical behavior and computational simulation." Expert Rev Med Devices 3 (6):817-34. doi: 10.1586/17434440.3.6.817.

Sacks, M. S., and F. J. Schoen. 2002a. "Collagen fiber disruption occurs independent of calcification in clinically explanted bioprosthetic heart valves." J Biomed Mater Res 62 (3):359-71. doi: 10.1002/jbm.10293.

Sacks, Michael S. 2000. "Biaxial mechanical evaluation of planar biological materials." Journal of elasticity and the physical science of solids 61 (1-3):199.

Sacks, Michael S, and Frederick J Schoen. 2002b. "Collagen fiber disruption occurs independent of calcification in clinically explanted bioprosthetic heart valves." J. Biomed. Mater. Res. 62 (3):359-371.

Sacks, Michael S, Will Zhang, and Silvia Wognum. 2016. "A novel fibre-ensemble level constitutive model for exogenous cross-linked collagenous tissues." Interface focus 6 (1):20150090.

Sacks, MS. 1999. "A method for planar biaxial mechanical testing that includes in-plane shear." J Biomech Eng 121 (5):551-555.

Sarazan, R Dustan. 2014. "Cardiovascular pressure measurement in safety assessment studies: technology requirements and potential errors." Journal of pharmacological and toxicological methods 70 (3):210-223.

Schoen, F. J., and R. J. Levy. 1999a. "Founder's Award, 25th Annual Meeting of the Society for Biomaterials, perspectives. Providence, RI, April 28-May 2, 1999. Tissue heart

valves: current challenges and future research perspectives." J Biomed Mater Res 47 (4):439-65.

Schoen, FJ, RJ Levy, AC Nelson, WF Bernhard, A Nashef, and M Hawley. 1985. "Onset and progression of experimental bioprosthetic heart valve calcification." Lab Invest 52 (5):523-532.

Schoen, Frederick J. 2012. "Mechanisms of function and disease of natural and replacement heart valves." Annu Rev Pathol: Mechanisms of Disease 7:161-183.

Schoen, Frederick J, Javier Fernandez, Lorenzo Gonzalez-Lavin, and Aurel Cernaianu. 1987. "Causes of failure and pathologic findings in surgically removed Ionescu-Shiley standard bovine pericardial heart valve bioprostheses: emphasis on progressive structural deterioration." Circulation 76 (3):618-627.

Schoen, Frederick J, and Robert J Levy. 1999b. "Tissue heart valves: current challenges and future research perspectives." J. Biomed. Mater. Res. 47 (4):439-465.

Schoen, Frederick J, and Robert J Levy. 2005. "Calcification of tissue heart valve substitutes: progress toward understanding and prevention." Ann Thorac Surg 79 (3):1072-1080.

Schultz, C. J., A. Weustink, N. Piazza, A. Otten, N. Mollet, G. Krestin, R. J. van Geuns, P. de Feyter, P. W. Serruys, and P. de Jaegere. 2009. "Geometry and degree of apposition of the CoreValve ReValving system with multislice computed tomography after implantation in patients with aortic stenosis." J Am Coll Cardiol 54 (10):911-8. doi: 10.1016/j.jacc.2009.04.075.

Schutte, Jaco F, Byung-Il Koh, Jeffrey A Reinbolt, Raphael T Haftka, Alan D George, and Benjamin J Fregly. 2005. "Evaluation of a particle swarm algorithm for biomechanical optimization." Journal of Biomechanical Engineering 127 (3):465-474.

Schutte, Jaco F, Jeffrey A Reinbolt, Benjamin J Fregly, Raphael T Haftka, and Alan D George. 2004. "Parallel global optimization with the particle swarm algorithm." International journal for numerical methods in engineering 61 (13):2296-2315.

Simionescu, Dan, Agneta Simionescu, and Radu Deac. 1993. "Mapping of glutaraldehyde-treated bovine pericardium and tissue selection for bioprosthetic heart valves." Journal of biomedical materials research 27 (6):697-704.

Simo, JC. 1987. "On a fully three-dimensional finite-strain viscoelastic damage model: formulation and computational aspects." Comput Methods Appl Mech Eng 60 (2):153-173.

Smith, Craig R, Martin B Leon, Michael J Mack, D Craig Miller, Jeffrey W Moses, Lars G Svensson, E Murat Tuzcu, John G Webb, Gregory P Fontana, and Raj R Makkar. 2011. "Transcatheter versus surgical aortic-valve replacement in high-risk patients." N Engl J Med 364 (23):2187-2198.

Soares, Joao S, Kristen R Feaver, Will Zhang, David Kamensky, Ankush Aggarwal, and Michael S Sacks. 2016. "Biomechanical behavior of bioprosthetic heart valve heterograft tissues: Characterization, simulation, and performance." Cardiovascular engineering and technology 7 (4):309-351.

Stewart, S. F., P. Hariharan, E. G. Paterson, G. W. Burgreen, V. Reddy, S. W. Day, M. Giarra, K. B. Manning, S. Deutsch, and M. R. Berman. 2013. "Results of fda's first

interlaboratory computational study of a nozzle with a sudden contraction and conical diffuser." Cardiovasc. Eng. Technol. 4:374–391.

Sun, Wei, Ajay Abad, and Michael S Sacks. 2005. "Simulated bioprosthetic heart valve deformation under quasi-static loading." Journal of biomechanical engineering 127 (6):905-914.

Sun, Wei, Kewei Li, and Eric Sirois. 2010. "Simulated elliptical bioprosthetic valve deformation: implications for asymmetric transcatheter valve deployment." Journal of biomechanics 43 (16):3085-3090.

Sun, Wei, and Michael S Sacks. 2005a. "Finite element implementation of a generalized Fung-elastic constitutive model for planar soft tissues." Biomechanics and modeling in mechanobiology 4 (2-3):190-199.

Sun, Wei, and Michael S Sacks. 2005b. "Finite element implementation of a generalized Fung-elastic constitutive model for planar soft tissues." Biomech Model Mechanobiol 4 (2-3):190-199.

Talman, Eric A, and Derek R Boughner. 1995. "Glutaraldehyde fixation alters the internal shear properties of porcine aortic heart valve tissue." The Annals of thoracic surgery 60:S369-S373.

Thourani, Vinod H, Chun Li, Chandan Devireddy, Hanna A Jensen, Patrick Kilgo, Bradley G Leshnower, Kreton Mavromatis, Eric L Sarin, Tom C Nguyen, and Mihir Kanitkar. 2015. "High-risk patients with inoperative aortic stenosis: use of transapical, transaortic, and transcarotid techniques." The Annals of thoracic surgery 99 (3):817-825.

Thubrikar, ManoJ. 2018. The aortic valve: Routledge.

Thubrikar, MJ, JD Deck, J Aouad, and SP Nolan. 1983. "Role of mechanical stress in calcification of aortic bioprosthetic valves." J Thorac Cardiovasc Surg 86 (1):115-125.

Thyregod, Hans Gustav Hørsted, Daniel Andreas Steinbrüchel, Nikolaj Ihlemann, Henrik Nissen, Bo Juel Kjeldsen, Petur Petursson, Yanping Chang, Olaf Walter Franzen, Thomas Engstrøm, and Peter Clemmensen. 2015. "Transcatheter versus surgical aortic valve replacement in patients with severe aortic valve stenosis: 1-year results from the all-comers NOTION randomized clinical trial." Journal of the American College of Cardiology 65 (20):2184-2194.

Toggweiler, Stefan, Karin H Humphries, May Lee, Ronald K Binder, Robert R Moss, Melanie Freeman, Jian Ye, Anson Cheung, David A Wood, and John G Webb. 2013. "5-year outcome after transcatheter aortic valve implantation." Journal of the American College of Cardiology 61 (4):413-419.

Trowbridge, EA, and CE Crofts. 1987. "The extension rate independence of the hysteresis in glutaraldehyde-fixed bovine pericardium." Biomaterials 8 (3):201-206.

Vahanian, Alec, and Catherine M Otto. 2010. "Risk stratification of patients with aortic stenosis." European heart journal 31 (4):416-423.

van Nooten, G., S. Ozaki, P. Herijgers, P. Segers, P. Verdonck, and W. Flameng. 1999. "Distortion of the stentless porcine valve induces accelerated leaflet fibrosis and calcification in juvenile sheep." J Heart Valve Dis 8 (1):34-41.

Vesely, I. 2003. "The evolution of bioprosthetic heart valve design and its impact on durability." Cardiovascular Pathology 12 (5):277-286.

Waldman, Stephen D, and J Michael Lee. 2002. "Boundary conditions during biaxial testing of planar connective tissues. Part 1: dynamic behavior." Journal of materials science: Materials in medicine 13 (10):933-938.

Walther, Thomas, Johannes Blumenstein, Arnaud van Linden, and Jörg Kempfert. 2012. "Contemporary management of aortic stenosis: surgical aortic valve replacement remains the gold standard." Heart 98 (Suppl 4):iv23-iv29.

Webb, John G, Ronald G Carere, and Sam V Lichtenstein. 2007. "Percutaneous transarterial aortic valve replacement in selected high-risk patients with aortic stenosis." Circulation.

Willson, A. B., J. G. Webb, M. Freeman, D. A. Wood, R. Gurvitch, C. R. Thompson, R. R. Moss, S. Toggweiler, R. K. Binder, B. Munt, A. Cheung, C. Hague, J. Ye, and J. A. Leipsic. 2012. "Computed tomography-based sizing recommendations for transcatheter aortic valve replacement with balloon-expandable valves: Comparison with transesophageal echocardiography and rationale for implementation in a prospective trial." J Cardiovasc Comput Tomogr 6 (6):406-14. doi: 10.1016/j.jcct.2012.10.002.

Wu, Michael CH, Rana Zakerzadeh, David Kamensky, Josef Kiendl, Michael S Sacks, and Ming-Chen Hsu. 2018. "An anisotropic constitutive model for immersogeometric fluid–structure interaction analysis of bioprosthetic heart valves." Journal of biomechanics 74:23-31.

Xu, Fei, Simone Morganti, Rana Zakerzadeh, David Kamensky, Ferdinando Auricchio, Alessandro Reali, Thomas JR Hughes, Michael S Sacks, and Ming-Chen Hsu. 2017. "A framework for designing patient-specific bioprosthetic heart valves using

immersogeometric fluid–structure interaction analysis." International journal for numerical methods in biomedical engineering.

Xuan, Yue, Kapil Krishnan, Jian Ye, Danny Dvir, Julius M Guccione, Liang Ge, and Elaine E Tseng. 2017. "Stent and leaflet stresses in a 26-mm first-generation balloon-expandable transcatheter aortic valve." The Journal of thoracic and cardiovascular surgery 153 (5):1065-1073.

Zegdi, R., V. Ciobotaru, M. Noghin, G. Sleilaty, A. Lafont, C. Latremouille, A. Deloche, and J. N. Fabiani. 2008. "Is it reasonable to treat all calcified stenotic aortic valves with a valved stent? Results from a human anatomic study in adults." J Am Coll Cardiol 51 (5):579-84. doi: 10.1016/j.jacc.2007.10.023.

Zhang, Will, and Michael S Sacks. 2017. "Modeling the response of exogenously crosslinked tissue to cyclic loading: The effects of permanent set." Journal of the mechanical behavior of biomedical materials 75:336-350.

Zioupos, P, and JC Barbenel. 1994. "Mechanics of native bovine pericardium: II. A structure based model for the anisotropic mechanical behaviour of the tissue." Biomaterials 15 (5):374-382.

APPENDIX

In the present study, non-uniform rational B-splines (NURBS) curves were used to create transcatheter aortic valve (TAV) leaflet geometry. A NURBS curve is defined (Hughes, Cottrell, and Bazilevs 2005)

$$\boldsymbol{C}(t) = \frac{\sum_{i=0}^{n} N_{i,p}\,(t) w_i \boldsymbol{P}_i}{\sum_{i=0}^{n} N_{i,p}(t) w_i} \tag{A.1}$$

where p is the order of a NURBS curve, $N_{i,p}$ are the B-spline basis functions, $\boldsymbol{P}_i$ are control points, n is the number of control points and $w_i > 0$ is a weighting factor. B-spline basis functions given by (Hughes et al., 2005)

$$N_{i,0}(t) = \begin{cases} 1 & if\ t_i \le t \le t_{i+1}\ and\ t_i < t_{i+1} \\ 0 & otherwise \end{cases}$$

$$N_{i,j}(t) = \frac{t - t_i}{t_{i+j} - t_i} N_{i,j-1}(t) + \frac{t_{i+j+1} - t}{t_{i+j+1} - t_{i+1}} N_{i+1,j-1}(t) \tag{A.2}$$

where t_i are the knots forming a knot vector. The knot vector $\boldsymbol{T}$ is a set of $m + 1$ non-decreasing numbers.

$$\boldsymbol{T} = \{t_0, t_1, \ldots, t_m\} \tag{A.3}$$

Also, the degree of the basis functions p can be defined as

$$p = m - n - 1 \tag{A.4}$$

In this study, TAV leaflets with uniform thickness (t) were considered to be attached to a frame with a uniform thickness of 0.5 mm and an external diameter of D. The 3D leaflet geometry consists of two NURBS curves (i) the symmetric curve and (ii) the fixed-boundary edge. The leaflet free-edge, that connects the commissure to the point of leaflet coaptation, was subsequently reconstructed based on the symmetric curve and the fixed-boundary edge. The symmetric curve was generated using a second order NURBS curve (B-spline 1) in the plane of symmetry. The three controlling points of the B-spline, $P_{s1}(x_{s1}, y_{s1})$, $P_{s2}(x_{s2}, y_{s2})$ and $P_{s3}(x_{s3}, y_{s3})$, are shown in Fig. A.2. x_{s2} and y_{s2} were considered as the two design parameters for B-spline 1 in the plane of symmetry, X_s and Y_s, respectively. In addition, y_{s3} was taken as a parameter of h (leaflet coaptation height) to change coaptation height of the leaflets. As a result, the shape of the belly region was controlled by three parameters, i.e., X_s, Y_s and h.

B-spline 2 controls the shape of the fixed-boundary edge. To create a fixed-boundary edge for the leaflet, B-spline 2 was projected on the cylinder (the TAV frame) in the MATLAB code. The three controlling points of B-spline 2, $P_{f1}(x_{f1}, y_{f1})$, $P_{f2}(x_{f2}, y_{f2})$ and, $P_{f3}(x_{f3}, y_{f3})$ are shown in Fig. A.2. x_{f2} and y_{f2} were considered as the two design parameters for B-spline 2, X_f and Y_f, respectively. In addition, y_{f3} was taken as a parameter of H (valve height) to change the TAV height. As a result, the shape of the fixed-boundary edge was controlled by three parameters, i.e., X_f, Y_f and H.

As shown in Fig. A.1, the leaflet free-edge that connects the commissure to the point of leaflet coaptation was reconstructed based on projection of two B-splines with degree of 5 defined in Plane 3, the top plane of the TAV, and Plane 4, passing through TAV centerline and perpendicular to the plane of symmetry (Plane 1). Five control points, i.e., $P_{r1}(x_{r1}, y_{r1})$, $P_{r2}(x_{r2}, y_{r2})$, $P_{r3}(x_{r3}, y_{r3})$, $P_{r4}(x_{r4}, y_{r4})$, $P_{r5}(x_{r5}, y_{r5})$, $and\ P_{r6}(x_{r6}, y_{r6})$, determine the shape of B-spline in Plane 3. In addition, another Five control points, i.e., $P_{e1}(x_{e1}, y_{e1})$, $P_{e2}(x_{e2}, y_{e2})$, $P_{e3}(x_{e3}, y_{e3})$, $P_{e4}(x_{e4}, y_{e4})$, $P_{e5}(x_{e5}, y_{e5})$, $and\ P_{e6}(x_{e6}, y_{e6})$, determine the shape of B-spline in Plane 4.

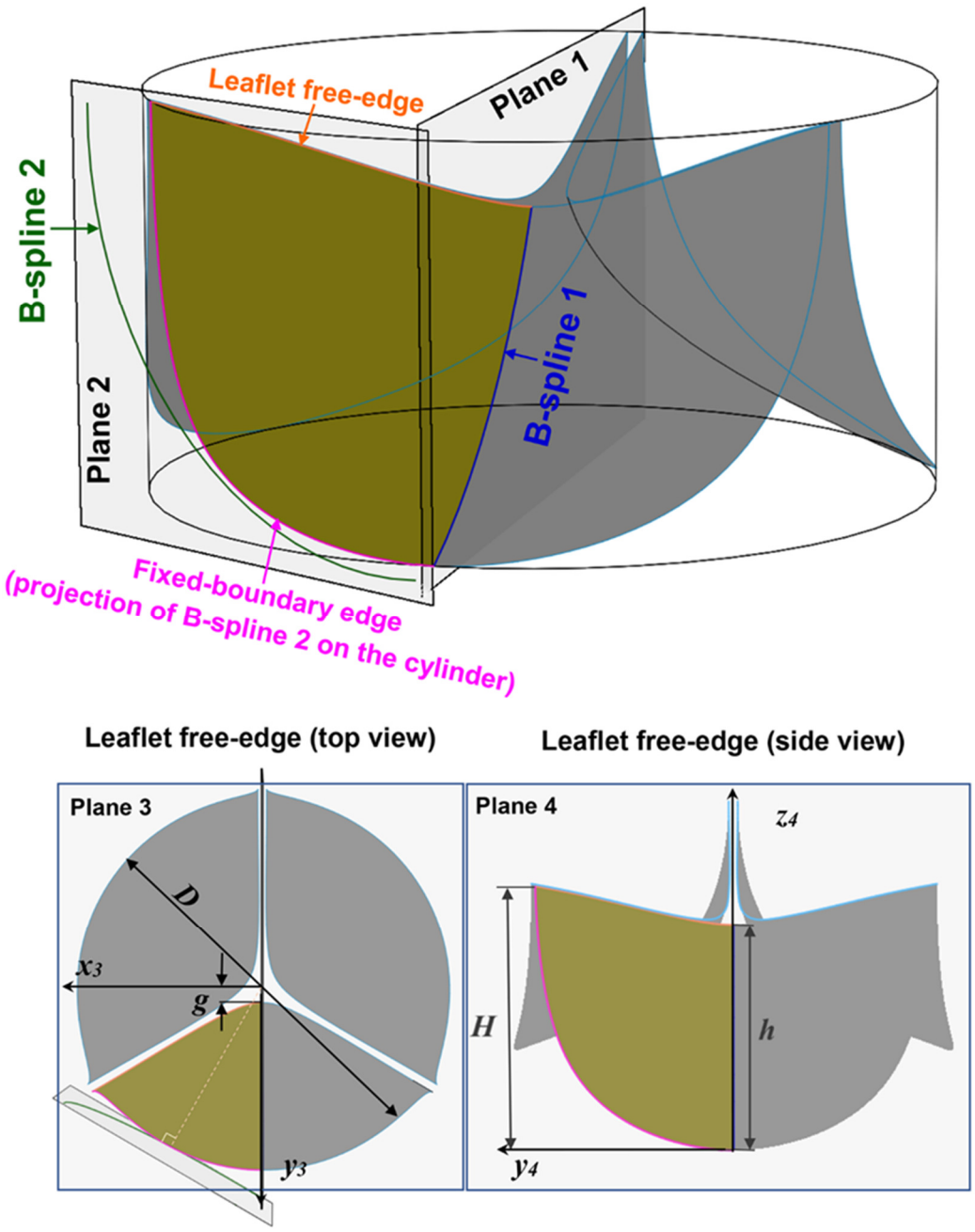

Figure A.1: Design variables in parameterization of the TAV leaflet geometry.

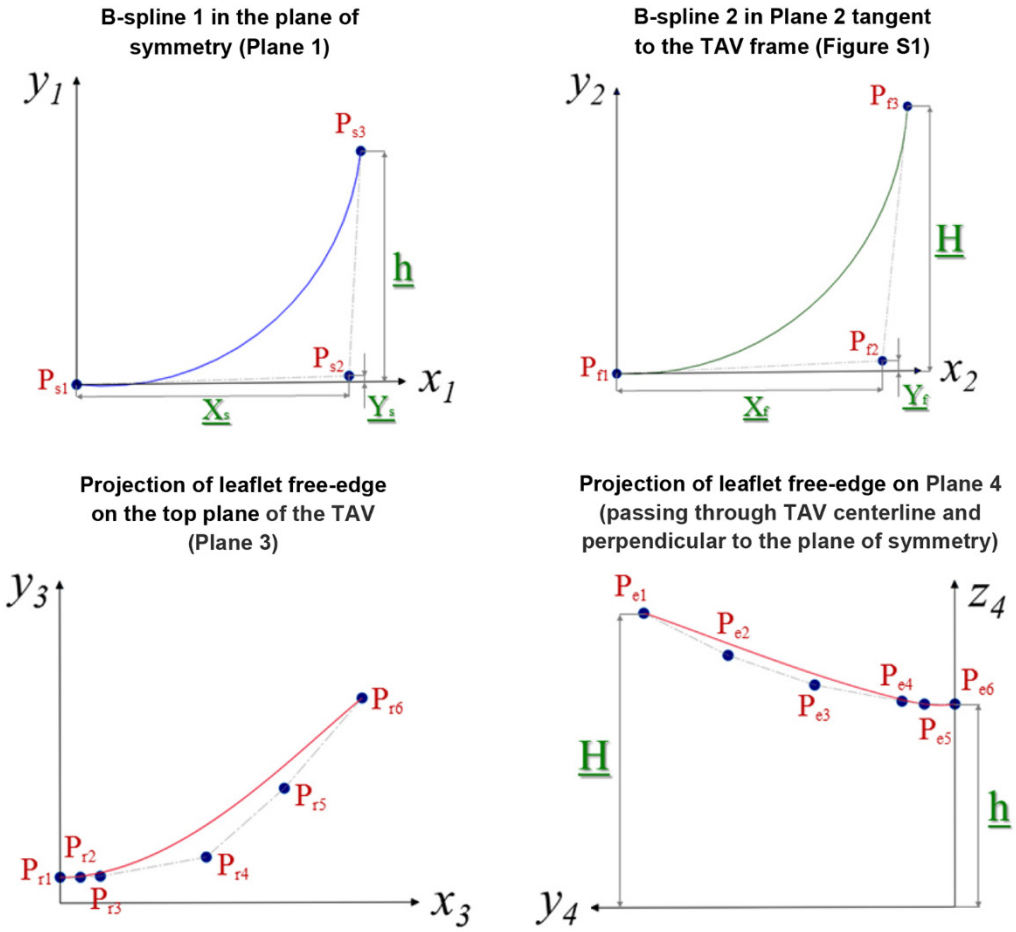

Figure A.2: Design variables and control points for generation of the NURBS curves. On each plane, a local coordinate system was defined.